Impact of the exposure to ultraviolet light on the nanomechanical properties of collagen probed by atomic force microscopy and Raman spectroscopy

Einfluss von ultraviolettem Licht auf die nano-mechanischen Eigenschaften von Kollagen gemessen mittels Rasterkraftmikroskopie und Raman Spektroskopie

Zur Erlangung des Grades eines Doktors der Naturwissenschaften (Dr. rer. nat.)

genehmigte Dissertation von Marcus Schulze aus Görlitz

Tag der Einreichung: 26.09.2019, Tag der Prüfung: 29.11.2019

Darmstadt — D 17

1. Gutachten: Prof. Dr. Robert W. Stark

2. Gutachten: Prof. Dr. Regine von Klitzing

TECHNISCHE UNIVERSITÄT DARMSTADT

Fachbereich Material- und Geowissenschaften

Fachgebiet Physics of Surfaces

Impact of the exposure to ultraviolet light on the nanomechanical properties of collagen probed by atomic force microscopy and Raman spectroscopy

Einfluss von ultraviolettem Licht auf die nano-mechanischen Eigenschaften von Kollagen gemessen mittels Rasterkraftmikroskopie und Raman Spektroskopie

Genehmigte Dissertation von Marcus Schulze aus Görlitz

1. Gutachten: Prof. Dr. Robert W. Stark

2. Gutachten: Prof. Dr. Regine von Klitzing

Tag der Einreichung: 26.09.2019

Tag der Prüfung: 29.11.2019

Darmstadt — D 17

Bitte zitieren Sie dieses Dokument als:

URN: urn:nbn:de:tuda-tuprints-114873

URL: http://tuprints.ulb.tu-darmstadt.de/id/eprint/11487

Dieses Dokument wird bereitgestellt von tuprints,

E-Publishing-Service der TU Darmstadt

http://tuprints.ulb.tu-darmstadt.de

tuprints@ulb.tu-darmstadt.de

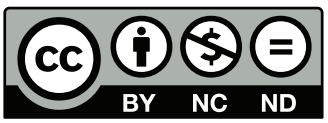

Die Veröffentlichung steht unter folgender Creative Commons Lizenz:

Attribution-NonCommercial-NoDerivatives 4.0 International (CC BY-NC-ND 4.0)

http://creativecommons.org/licenses/by-nc-nd/4.0/

Abstract

Collagen is a body own protein that, due to its outstanding biocompatibility, is applicable as substrate for cell seeding in tissue engineering. Creating a substrate that mimics the characteristics of human tissue and, thus, allows for a sustainable proliferation of biological cells, requires a well-directed design of its mechanical properties. In the case of collagen, the exposure to ultraviolet (UV) light is a promising method for inducing stabilising or destabilising reactions that modify the mechanical properties, as for example, the tensile modulus. For enabling a targeted substrate design, the reaction of the collagen samples towards the UV light treatment needs to be understood and made predictable. Collagen fibrils, as small units of the collagen's hierarchical structure, gained attention and are investigated regarding the response of their mechanical properties due to the exposure to UV light dependent on the kind of surrounding liquid.

Atomic force microscopy (AFM) and Raman spectroscopy were applied to monitor the impact of UV light on collagen fibrils and hydrogels. Changes in the indentation modulus of single collagen fibrils were recorded for the exposure to UVA, UVB, or UVC light while being immersed in varied liquid environments *in situ*. Next, an experimental procedure for an AFM-based eased extraction of the tensile modulus from fibrillar structures as small as collagen fibrils was proposed, which was used for the acquisition of the changes in the tensile modulus of collagen fibrils, dependent on the combination of the applied kind of UV light and liquid environment. The observed modifications of the mechanical properties should be complemented by a description of structural changes induced by UV light irradiation for which Raman spectroscopy was used.

Collagen fibrils responded to the exposure to UV light with a change in their mechanical properties and exhibited repeated patterns of behaviour dependent on the applied combination of UV light and the kind of liquid environment. A decrease in stability of up to 90 % (tensile modulus) was detected for the immersion of the samples in deionised water. For gaining an increase in stability with advancing exposure time, the application of phosphate-buffered saline (PBS) was a necessary condition. A maximum averaged increase in indentation modulus of approximately 60 % was seen during exposure of single collagen fibrils to UVB or UVC light. For the tensile tests, a fourfold increase of the tensile modulus was recorded as maximum value. The depicted dependence of the mechanical properties on the kind of liquid environment was confirmed by Raman spectroscopy on collagen hydrogels. The observed proliferation of biological cells on UV light exposed collagen hydrogels showed the applicability of the method.

Kurzbeschreibung

Kollagen ist ein körpereigenes Protein, das aufgrund seiner hervorragenden Biokompatibilität als Substrat beim *Tissue Engineering* eingesetzt wird. Bei der Herstellung eines Substrates, das die Eigenschaften menschlichen Gewebes imitiert und dadurch eine nachhaltige Proliferation der biologischen Zellen ermöglicht, müssen unter anderem die mechanischen Eigenschaften angepasst werden. Im Fall von Kollagen bietet die Bestrahlung mit ultraviolettem (UV) Licht eine vielversprechende Möglichkeit, mechanische Eigenschaften, wie z.B. den Zugmodul, durch photochemische Prozesse zu modifizieren. Für ein gezieltes Substrat-Design mit UV-Bestrahlung muss man deshalb den Einfluss von UV-Licht auf Kollagenproben besser verstehen.

Der Einfluss von UV-Licht auf Kollagenfibrillen und -hydrogele wurde mittels Rasterkraftmikroskopie (englisch: *atomic force microscopy*, AFM) und Raman Spektroskopie an gequollenem Kollagen untersucht. UVA-, UVB-, oder UVC-Strahlungs-induzierte Änderungen des Indentationsmoduls von Kollagenfibrillen wurden für unterschiedliche Salzkonzentrationen aufgezeichnet. Für diese Untersuchungen waren vor allem Kollagenfibrillen von Interesse, da sie eine der kleinsten Kollageneinheiten darstellen. Anschließend wurde ein Vorgehen für eine AFM-basierte Messung des Zugmoduls von nanofibrillären Strukturen etabliert. Die so nachgewiesenen UV-Licht-induzierten Veränderungen der mechanischen Eigenschaften wurden durch eine Untersuchung der strukturellen Änderungen mittels Raman Spektroskopie ergänzt.

Im Zuge der Bestrahlung mit UV-Licht veränderte sich die Elastizität der Kollagenfibrillen in Abhängigkeit der verwendeten Kombination von UV-Licht und Umgebungsflüssigkeit. Dabei konnten sowohl stabilisierende als auch destabilisierende Effekte beobachtet werden. Eine Abnahme der Stabilität von bis zu 90 % (Zugmodul) wurde für Proben ermittelt, die in deionisiertem Wasser behandelt wurden. Eine Zunahme der Steifigkeit wurde dagegen bei UV-Bestrahlung in phosphatgepufferter Salzlösung (PBS) erreicht. Hier konnte für den Indentationsmodul von einzelnen Kollagenfibrillen eine mittlere Erhöhung der Steifigkeit um etwa 60 % gemessen werden. Dagegen konnte in Zugversuchen ein bis zu vierfacher Anstieg des Zugmoduls nachgewiesen werden. Die gemessene Abhängigkeit der mechanischen Eigenschaften von der Umgebungsflüssigkeit wurde durch die Raman Spektroskopie-Ergebnisse unterstützt. Eine Proliferation von Zellen auf Kollagenhydrogelen, die mit UV-Licht bestrahlt waren, zeigte das Anwendungspotential der Methode auf.

Erklärung zur Dissertation

Hiermit versichere ich, die vorliegende Dissertation ohne Hilfe Dritter nur mit den angegebenen Quellen und Hilfsmitteln angefertigt zu haben. Alle Stellen, die aus Quellen entnommen wurden, sind als solche kenntlich gemacht. Diese Arbeit hat in gleicher oder ähnlicher Form noch keiner Prüfungsbehörde vorgelegen.

Darmstadt, den 26.09.2019

(Marcus Schulze)

Contents

List of Figures

List of Tables

List of Abbreviations

AFM atomic force microscopy

COS CV-1 in Origin and carrying the SV40 genes

DHT dehydrothermal

DMT Derjaguin-Muller-Toporov

DNA deoxyribonucleic acid

ECM extracellular matrix

EMCCD electron multiplying charge-coupled device

DMEM Dulbeccos's modified essential medium

FBS fetal bovine serum

FE finite element

FEA finite element analysis

FTIR Fourier-transform infrared spectroscopy

FWHM full-width half maximum

HP hematoporphyrin

InvOLS inverse optical lever sensitivity

IR infrared

JKR Johnson-Kendall-Roberts

MEMS microelectromechanical systems

NADPH nicotinamide adenine dinucleotide phosphate

NEAA non-essential amino acid solution

PBS phosphate buffered saline

PDMS polydimethylsiloxane

PFQNM Peak Force Quantitative Nanomechanical Mapping

RFUVA riboflavin and UVA light

ROI region of interest

ROS reactive oxygen species

SAM self-assembled monolayer

SEM scanning electron microscopy

SERS Surface Enhanced Raman Spectroscopy

SPM scanning probe microscopy

STM scanning tunneling microscopy

TEM transmission electron microscopy

TERS Tip Enhanced Raman Spectroscopy

UV ultraviolet

Amino Acids

Ala alanine

Arg arginine

Asn asparagine

Asp aspartic acid

Cys cysteine

Gln glutamine

Glu glutamic acid

Gly glycine

His histidine

Ile isoleucine

Leu leucine

Lys lysine

Met methionine

Phe phenylalanine

Pro proline

Ser serine

Thr threonine

Trp tryptophan

Tyr tyrosine

Val valine

1 Motivation

The human body is an intricate and unique entity. Evolved in millions of years, it is host to an uncountable number of interlocking processes (chemical as well as biological), a highly educated immune system, a brain that is an unrivalled construct whose secrets have not been fully decrypted yet, and many more miracles. As the vivid and permanently working engine that it is, the human body may not be the fastest, tallest, or strongest among all animals, but it is a show-piece of evolution and it is unique to every individual; but after all it is vulnerable. Coming with age or by external influences, tissue and organs can be destroyed. To heal wounds the body cannot heal by itself, it might be necessary to replace these parts. For successful and longterm replacements, the body's complexity does not prefer rather simple solutions as transplants. Biological, chemical, and mechanical properties have to be met so that a transplantation can be considered promising and side effects such as rejection or inflammation, can be reduced. Introducing artificial materials into the body increases the risk of the side effects. Instead, biomaterials are favourable. The applied material should be able to perfectly imitate the conditions around the wound site and integrate itself smoothly. For this purpose, parts of the extracellular matrix (ECM) are a promising matter. Following this argumentation, collagen was moved into the spotlight of extensive research due to its distinguished properties. The excellent biocompatibility, as well as the possibility of being processed in several shapes, made collagen a useful material for several disciplines, like tissue engineering or drug delivery applications,[1] as well as pharmacy and cosmetics[2]. The ability to please the increasing need in more complex collagen-based structures that serve the purpose of wound healing or function as substrate for tissue growth[3] is build up on the understanding of the single units they are composed of: the collagen fibrils.[4–10] Regarding that, the properties of the single collagen fibril are not sufficiently investigated yet.[11,12] The functionality of the product is closely linked to its mechanical strength, whether it is about the stability of the substrate[13,14] or the influence of its stiffness on the behaviour of eventually attached cells.[15–18] Thus, the modification and tailoring of the collagens mechanics is the objective of a great research effort. Chemical and physical treatment are available for adjusting the mechanics but the chemical approaches, especially, carry the possibility of introducing cytotoxicity into the material.[19,20] Among the physical treatments, the irradiation with ultraviolet (UV) light has gained attention. Studying the interaction of UV light and collagen is obvious due to its sterilising effect[21] and the exposition of the skin to sunlight which results in ageing, or, in the worst case, skin cancer.[22] Beyond that, UV light influences the mechanical properties of the collagen and a fine tuning of the multiplicity of exposure parameters has to be conducted for being able to control underlying processes and balancing the occurring photodegradation and

photocrosslinking reactions.[2,21–27] Before it comes to controlling, an understanding of the impact of UV light on collagen and the resulting reactions, as well as analysis of the influencing environmental conditions has to be created. If all this knowledge eventually leads to the design of collagen-based substrates or implants that are accepted by the body and provide a more successful healing, then it is worth the effort.

2 Fundamentals

2.1 Collagen

2.1.1 Occurrence and functionality

Collagen is the most abundant protein in mammals[28–31] or even in all animals.[32,33] By providing 25[27] to 30 %[34] of the total protein mass of the body, collagen is found in a variety of organs and tissues, *e.g.*, skin, tendons, muscles, bones, cornea, and structural tissue. While mostly being responsible for the mechanical integrity of its application site, in every organ or tissue, collagen provides special properties. Together with glycoproteins and further proteins, it is part of the ECM of the connective tissue and provides its mechanical and biological properties.[30,35] Collagen, among many things, is responsible for elasticity[22] and rigidity, thickness of the heart wall,[13] or scaffolding bones[8] and is also involved in angiogenesis and tissue repair.[36,37] In general, collagen is known and investigated due to characteristics like an outstanding biocompatibility and biodegradability, being nontoxic and serving as promising substrate for cell adhesion, inducing immune responses, and supporting wounds to stop bleeding.[1,38] Using the comparison of bone to mineralised tendon fibres, Zhang *et al.*[39] display how the number of hierarchical levels in the setup of organs can define different mechanical qualities even if it is built from the same basic component. All in all, the application of collagen in the human body is not only the application of a single protein but an interplay between influences as, for example, environment, application site, and hierarchical setup that form individual properties. Currently, 28 different types of collagen are known: type I to XXVIII.[40] They do not only differ in the sequence of amino acids but also, for example, in the appearance of non-helical domains and purpose.[30] While type I is mostly found in bone, tendon, and ligaments, type XIV, for example, is predominantly found in the lungs and liver. Gelse *et al.*[30] provide a comprehensive overview on collagen types, their function, and where to find them. About 90 % of the collagen found in the human body is of type I, which is also why most of the research is focused on it.[30,41] But type II[42,43] and type III[44] are also under investigation. The behaviour of biological cells in contact with collagen is dependent on special amino acid sequences, as well as structure,[45] mechanics,[46] and topography[47] of the collagen. Defective collagen can result in diseases like the Ehlers-Danlos syndrome,[48] the Alport syndrome,[49] and osteogenesis imperfecta.[50] The most famous representative might be osteoporosis,[51] in which a loss of bone mass can eventually lead to fractures. Most of these diseases are linked to the mechanics

of the collagen,[52] as are changes in the mechanical properties of the ECM seen as a cause of vascular diseases and cancer.[53–56] Diabetes also leads to the formation of further crosslinks in collagen and thereby changes its mechanics.[2] Thus, the investigation of the mechanical properties of collagen should move into the spotlight of collagen research.

2.1.2 Structure

The first proposals of the structure of collagen were released in the 1950s based on data from X-ray diffraction experiments.[57,58] During the years, these findings were expanded and refined. The structure of collagen shows a hierarchy that goes from the smallest building blocks in the nanometre-range up to tendons in the millimetre- or even centimetre-range. At the lowest level, amino acids form polypeptide chains that are called α-chains. The series of the incorporated amino acids is referred to as primary structure. In the simplest case, an amino acid consists of an amine group (NH_2) and a carboxyl group (COOH) with one methylene group (CH_2) as a linker between them (glycine (Gly)). There are more than 140 amino acids found in natural proteins, yet, only 20 count as canonical amino acids from which the others are derived.[59] An overview of these 20 canonical or proteinogenic (protein building) amino acids is shown in Table 2.1.

For proteins in general, the appearance of the polypeptide chains is known as secondary structure and the most common forms are the left-handed collagen-helix, the right-handed α-helix, or the β-sheet.[62] In the case of collagen, the predominantly chosen form for an α-chain is the left-handed collagen-helix. For most regions, the α-chains have a repetitive pattern of amino acids that is $[\text{-Gly-X-Y-}]_n$. Every third position is occupied by Gly while the positions X and Y can be occupied with any other amino acid. However, some amino acids are more likely to be found at the X or Y positions, *i.e.*, proline (Pro) and hydroxyproline.[63,64] Table 2.2 lists the amino acids that occur in rat tail tendon with their corresponding fraction. The nomenclature of a left-handed α-chain states its number and the collagen type it is part of. For example, the α1-chain of type I collagen is described by α1(I). For the collagen type I, II, and III, the left-handed helix is extended by a non-helical (non-collagenous) part that is called the telopeptide. Some amino acids, *e.g.*, tyrosine (Tyr),[25] are only present in the telopeptides and the ends are referred to as the N- and the C-terminus according to the amine or the carboxyl group of the amino acid that is last at the respective end of the chain. The overall arrangement is the 180° hairpin-turn that enables a crosslinking between the tropocollagen molecules.[65] The presence of certain amino acids differs with the type of collagen and so does the number of amino acids one α-chain consists of. Hudson *et al.*[66] present general numbers for the length of an α-chain with approximately 1400 amino acid residues, approximately 15 residues at the non-collagenous N-terminal, and approximately 230 residues at the non-collagenous C-terminal. Hostikka and Tryggvason,[67] for example, name the length of the collagenous part of a human type IV collagen α2(IV)-chain with 1428 amino acid residues.

Table 2.1.: Chemical structures of canonical amino acids based on a compilation by Vnucec *et al.*[60].

Proline, Pro, P	Serine, Ser, S	Asparagine, Asn, N	Aspartic acid, Asp, D
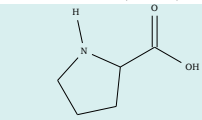	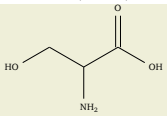	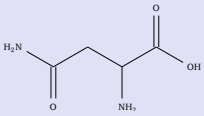	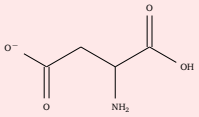
Valine, Val, V	Threonine, Thr, T	Glutamine, Gln, Q	Glutamic Acid, Glu, E
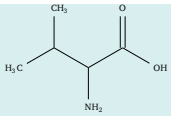	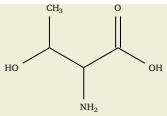	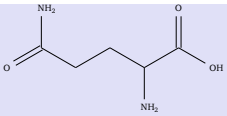	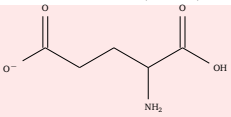
Leucine, Leu, L	Cysteine, Cys, C	Histidine, His, H	Phenylalanine, Phe, F
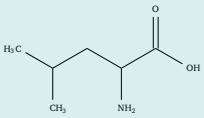	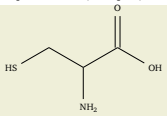	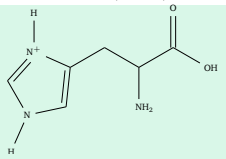	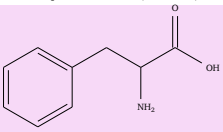
Isoleucine, Ile, I	Glycine, Gly, G	Lysine, Lys, K	Tyrosine, Tyr, Y
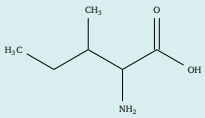	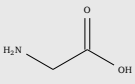	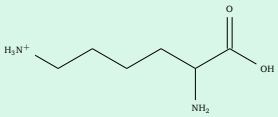	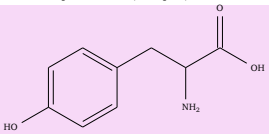
Methionine, Met, M	Alanine, Ala, A	Arginine, Arg, R	Tryptophan, Trp, W
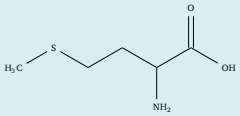	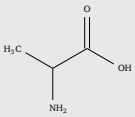	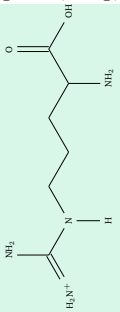	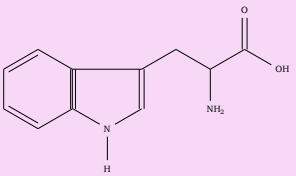

hydrophobic - nucleophilic - small - amide - basic - acidic - aromatic

Table 2.2.: Overview on the types of amino acids occurring in rat tail tendon with the respective fraction. The table is adapted from Gullekson *et al.*[61].

Amino acid	Gly	Pro	Ala	Arg	Glu	Ser	Lys	Asp	Gln
Fraction	32.8 %	22.3 %	10.9 %	5.0 %	4.6 %	4.2 %	3.6 %	3.2 %	2.9 %
Amino acid	Leu	Thr	Val	Phe	Asn	Met	Ile	Tyr	His
Fraction	1.9 %	1.9 %	1.9 %	1.3 %	1.3 %	0.8 %	0.7 %	0.5 %	0.2 %

Three α-chains form a right-handed triple helix where the residue of the Gly is directed into the middle of the helix and the residues of the amino acids at the X- and Y-positions are directed to the outside of this newly formed helix. This structure is called the procollagen and it is referred to as tertiary structure. During the next steps in the biosyntheses of collagen, the telopeptide chains are shortened (for some collagen types they are completely removed), resulting in a structure that is referred to as (tropo)collagen molecule. The collagen molecule has a length of 300 nm and a width of 1.5 nm. The nomenclature of the right-handed triple helices is based on the incorporated α-helices and states the type of collagen, as well as the number of the α-chain. For three identical α-chains, as it is the case for collagen type II, the label is written as $[\alpha 1(\mathrm{II})]_3$. Configurations that contain three non-identical α-chains, as is possible for collagen type V, can be described as $\alpha 1(\mathrm{V})\alpha 2(\mathrm{V})\alpha 3(\mathrm{V})$.[68]

The collagen molecules aggregate to form collagen fibrils with a length of several micrometres and a width of up to several hundreds of nanometres. A lot of research was dedicated to the identification of the arrangement of the collagen molecules within a fibril. After all, there is only a limited number of possible arrangements since the molecules do have a distinct structure.[69] Packaging units of five molecules[70] were suggested, as well as quasi-hexagonal molecule packaging[71] and a combination of both.[72] The Hodge-Petruska scheme, saying that collagen molecules are parallelly staggered, which leads to the formation of gap and overlap regions,[73] is generally accepted. The three-dimensional composition of the collagen molecule, according to Erickson *et al.*,[74] is revealed by the work of Orgel *et al.*[75] and Hulmes *et al.*[76] whose result is *"that a fibril is composed of five-stranded microfibrils that are super-twisted in the axial direction and quasi-hexagonally packed in the equatorial plane"*[74]. With a stagger between the molecules of 64 to 67 nm, or an integer multiple of this, the collagen fibrils exhibit a characteristic structure of alternating regions with high and low electron density along the axis. These areas are referred to as gap and overlap regions, as already mentioned. The gap regions exhibit a 20 % lower packing density than the overlap regions. Additionally, X-ray investigations show that the molecules in the overlap regions are highly ordered while being less ordered in the gap regions.[77] The resulting structure is referred to as D-band pattern and has a periodicity of 60 to 73 nm.[74] Varying properties of the gap and overlap regions can lead to differences in mechanics of the fibrils.[78] Fibrils aggregate to fibres and

fibre bundles assemble to tendons that have a diameter with up to 500 µm. In the case of rat tail tendon, a crystalline lateral packing order is seen differing from other sources, as for example skin that exhibits a closed packed structure with liquid like disorder.[2]

The formation of collagen in biological cells is a multi-step process that is reviewed in detail elsewhere.[30,79] In short, mRNA is translated into pre-procollagen that, after moving to the endoplasmic reticulum, undergoes a series of post-translational modifications, including a partial hydroxylation of Pro and lysine (Lys) residues. 4-hydroxyproline is involved in the formation of intramolecular hydrogen bonds and hydroxylysine participates in intermolecular crosslinks. The formed procollagen is released into extracellular space *via* the Golgi compartment with the subsequent (partial) cleavage of the C- and N-propeptides. Outside of the cell, the collagen molecules start their aggregation process to form fibrillar structures.[30] It shall be mentioned, that some collagen types, *e.g.*, type IV and VI, do not form fibrils after being released into the extracellular space. These non-fibrillar collagens form a network of microfibrils[80] and also take part in processes as differentiation or proliferation.[81]

2.1.3 Crosslinks in collagen

The number and kind of crosslinks in collagen structures is manifold and comprehensively reviewed elsewhere.[33,57,58,63,79,82] Yet, relevant features shall be summarised here. The primary structure consists of chained amino acids that are linked by peptide bonds. Connecting the α-chains, stabilisation of the triple helix is (predominantly) based on hydrogen bonds.[22] Hydrogen bonds between the carbonyl group (C=O) of a Pro from one α-chain and the N–H group of a Gly residue from another α-chain of the same triple helix are formed in a fixed pattern.[83,84] This pattern leaves some carbonyl groups left without the possibility of a formation of direct hydrogen bonds to a N–H group. These sites are involved in intra- and interchain water mediated hydrogen bonds resulting in an ordered water network.[63,85] This is also observed by Berisio *et al.*,[86] agreeing that in the triple helix, singly and doubly hydrated residues, mostly Gly and Pro respectively, act as anchor points for water bridges. Additionally, these water bridges also influence interactions with other molecules in the crystal, as well as they shield the triple helix. Other binding mechanisms are covalent bonds between Lys residues of telopeptides and adjacent triple helical chains that create intermolecular crosslinks between collagen molecules.[87] To spatially enable this link, it is suggested that the telopeptides fold in the so-called hairpin-turn, to get closer to the triple helical part of the next collagen molecule.[88] The hairpin-turn enables the crosslink between Lys and hydroxylysine that, *via* a condensation reaction, forms the Schiff base dihydroxylysinonorleucine. This link is considered to participate in the stabilisation of collagen.[89] Other amino acids can be involved in amide or ester bonds, as there are the reaction of Lys with aspartic acid (Asp) or glutamic acid (Glu) or the interplay between serine (Ser) and hydroxyproline or hydroxylysine.[90] The parti-

cipation of Tyr and phenylalanine (Phe) in crosslinking events for collagen is discussed in Section 2.1.5. The importance of the telopeptides for crosslinking of collagen molecules is also emphasised elsewhere.[87,90,91]

2.1.4 Applications in tissue engineering

The term *tissue engineering* describes an interdisciplinary approach to develop functional substitutes for damaged tissue. After the isolation of cells, a biodegradable substrate is used for tissue growth *in vitro* before an implantation *in vivo* takes place. The methods provided by tissue engineering shall diminish or even abolish drawbacks of conventional transplantations as, *e.g.*, inflammations or rejection.[14,92] Materials scientists contribute in focusing on the material the substrates are made of. Providing a high biocompatibility, synthetic, as well as natural materials have been tested, reaching from hydroxyapatite over polystyrene to collagen.[14] Chen *et al.*[93] provide a comprehensive review of elastomeric biomaterials for tissue engineering. The widespread presence of collagen in the body gives reason to embrace this material in the discipline of tissue engineering and makes it a promising material for replacements of various kinds of organs, *e.g.*, like heart valves and eye implants.[32] Lee *et al.*[94] state that it is feasible to shape collagen into hydrogels and further forms like films, discs, and powders and Rubin *et al.*[32] mention the creation of tubes and membranes. Thus, the range of possible applications is manifold, as the collagens characteristics reach from drug and gene delivery systems[95–97] to wound dressings and skin substitutions.[98] For tissue engineering, the application of collagen for the synthesis of substrates is in the focus of research.[99–103] Other fields of application are formation of membranes,[104] bone substitutes,[105,106] and recovery of articular cartilage,[107] to name a few.[i] Another characteristic is the possible modification of the mechanical characteristics of collagen, enabling great potential for its applications.[108] Type I collagen is under research especially for the tasks of tissue engineering.[109,110]

Collagen hydrogels were proposed for surgical use[3] and the first collagen-based scaffolds for the regeneration of skin in burn patients found their way into application[111]. Research shows that special attention has to be directed to the surface properties of the collagen-based materials since properties such as roughness, hydrophilicity, and stiffness directly influence the behaviour of the cells.[1]

[i] The listed examples are found in the work of Skopinska-Wisniewska *et al.*[1].

2.1.5 Crosslinking with ultraviolet light

The interaction of UV light and collagen has been a subject of research since at least the middle of the 20$^{\text{th}}$ century. Not only have the beneficial effects of the UV light in the field of tissue engineering been a motivation for these investigations, but also the impact of sunlight on skin and the thereby caused damage. In 1965, Fujimori[112] already discovered occurring photopolymerisation in a collagen solution, due to the irradiation with light of a wavelength of 253.7 nm, as well as an inhibited fibril formation. The observations were related to photoabsorption-induced transitions from Phe to Tyr under the creation of new crosslinks. Photolysis of the peptide bonds was only expected for wavelengths smaller than 240 nm,[113] but, also, a degradation of soluble collagen into low-molecular-weight fragments with wavelengths beneath 400 nm was reported when irradiated for several hours. This meant the loss of the helical structure, as well as the breaking of weak peptide bonds.[114] At an early stage, it was obvious that crosslinking and denaturation are mutually induced by UV light and that the telopeptides, due to the involvement of the UV-absorbing Tyr and Phe, play a major role in these processes.[25] The processes, especially the intra- and intermolecular crosslinking, are triggered by the creation of free radicals[114] and so, presumably, is the scission of the peptide bonds.[23,115–118] A major role seems to be played by reactive oxygen species (ROS).[119] Ryu *et al.*[120] specified this by stating that only singlet oxygen supports the crosslinking in collagen. The application of an aerobic environment is considered to be necessary for crosslinking to occur. These insights sum up the major information on how UV light interacts with collagen samples. Nevertheless, further effort has been taken to optimise and control these interactions. Sionkowska *et al.*[121] confirmed the absorbance of light with a wavelength of 253.7 nm by Tyr, Phe, and peptide bonds and identified the Tyr photoproduct as dityrosine, which is the result of the reaction between two Tyr radicals. Additionally, β-carotene was identified to reduce the UV light-induced effects. The same holds true for vitamin E as UV absorber.[117] Additives might also be useful for enabling the UV light-induced crosslinking as, *e.g.*, glucose.[21] One of the most prominent examples is the combination of UVA light with riboflavin (riboflavin and UVA light (RFUVA)). When irradiated with UVA light, riboflavin generates singlet oxygen radicals that interact with the amino acids.[120,122] This involves Tyr residues forming dityrosine, but also histidine (His) residues forming crosslinks.[123,124] Again, additives can influence the outcome, as sodium azide decreases the effect and deuterium oxide enhances it.[125] For the *in vivo* case of RFUVA treatment, McCall[125] suggests three types of crosslinks that can be developed: intrafibrillar bonds within individual collagen fibrils between amino acid residues of different collagen molecules, fibrillar-ECM bonds between amino acid residues and proteins of the surrounding, and interlamellar bonds between collagen fibrils. Then the mechanical strength is increased. Its application for the treatment of corneal diseases has been comprehensively investigated.[126] It also holds true for the RFUVA treatment that aerobic conditions are necessary for the initiation of the crosslinking that results in an increase of the mechanical strength.[127] An UV-induced increase in the mechanical strength is a

time-dependent process with a maximal yield. Weadock *et al.*[128] report a beneficial influence of light with a wavelength of 254 nm on the mechanical strength of collagen for up to 30 min of exposure. It is proposed that all possible crosslinks have built up within this time and a further increase in strength is not achievable in this way. As stated earlier, the process was connected with the impact of free radicals on the Tyr and Phe residues forming crosslinks. Additionally, a fragmentation of the collagen is shown by findings of a higher amount of smaller fractions within the exposed sample in comparison to the unexposed sample. Considering the applications of collagen in modern science, questions have to be answered concerning the influence of UV light on the biocompatibility and the cell reactivity of the collagen. While other crosslinking methods like, *e.g.*, the zero-link carbodiimide treatment, may use acidic and basic side chains of the collagen that are involved in cell recognition processes and, therefore, disrupt these, the unimpaired cell reactivity of UV light exposed collagen samples confirms the involvement of less important (regarding the cell reactivity) aromatic sites as Tyr and Phe. Involvement of amino acids with side chains containing carboxylate (for example Glu) and amine groups (for example Lys, hydroxylysine) during UV exposure is not considered based on the stable amount of free primary amine groups that has been detected during UV exposure. This also means that the level of crosslinking that can be achieved by UV exposure is low in comparison to other methods due to the small amount of aromatic residues in a collagen molecule that is less than 2 %.[21]

Crosslinking in collagen happens during natural ageing or photodegradation, but it also has to be considered that the level of crosslinks influences the biodegradability.[129] Apart from the beneficial effects of the mechanical strength, the impact of UVC light suppresses the formation of new fibrils and may lead to breaking of peptide bonds.[130] Additionally, the helical structures may get transformed into random coil structures due to the formation of secondary free radicals that interact with, *e.g.*, Gly residues.[131,132]

2.1.6 Interactions with biological cells

After all the shaping and treatment, the collagen still needs to be a favourable environment for biological cells to attach, proliferate, differentiate, and migrate. Thus, any treatment of the collagen needs to avoid an introduction of cytotoxic chemicals. It is also important that the binding sites of the collagen with the cells are not blocked or shielded. An example for such a binding site are free primary amino groups and carboxylate anions, *e.g.*, the acidic E in the GFOGER sequence.[21] Another example is the RGD sequence.[133] Again, type I collagen is very promising for cell applications since it carries several sequences that can function as binding sites. In general, the availability of certain binding sites on a substrate applied for cell growth - among other quantities - influences whether a cell can bind to this substrate or not. The arrangement of these binding sites influences the cell behaviour as well. Collagen is used as substrate and, thus, the arrangement of collagen has been a topic of research. An example of collagen films attached to different supporting structures with

varying densities shows the influence on cell shape, adhesion, and spreading.[47] Several more research groups have been involved in the investigation of supporting structure influences on the attached collagen films to be able to control the outcome.[134–137] Yet, this is just the first step. Apart from creating collagen-based surfaces and matrices that sustain a prosperous cell life with a homogeneously distributed population, modern substrates for tissue engineering require a more sophisticated structuring of these surfaces that provide guided cell adhesion and growth. Strategies have to be developed that allow for a controlled and patterned adjustment of the substrates parameters that, in turn, influence the cell behaviour. For that it has to be learned what substrate-qualities the cell reacts to. Apart from the mentioned availability of binding sites, roughness,[138–140] hydrophobicity,[141] presentation of receptors,[142] micro-structures[143] and, especially, the stiffness[17,46,144,145] of the substrate directly influence the cell behaviour. To describe the meaning of 'cell behaviour' Wells[17] published a scheme regarding the influence of the substrate stiffness. In most cases, the cells are rounder, minimally adhesive, growth arrested, and tend to apoptosis on softer[ii] areas, while on stiffer areas, cells increase their contact area with the substrate and are proliferative and fibrogenic. Even migration from softer to stiffer areas can take place. The elastic modulus that is considered 'soft' or 'stiff' depends on the cell type.[18]

Modification of the substrate stiffness can be achieved by variation of, *e.g.*, thickness,[145] state of hydration,[16] or crosslinking density by chemical or physical approaches. The gained knowledge about the general control of the cell behaviour still has to be extended by the introduction of patterning techniques that allow for the design of substrates with controlled adhesion patterns of the cells. While any kind of cells can be grown outside the body, mimicking natural organs *in vitro* requires the right architecture too. The pattern needs to mimic the morphology of the tissue and create its organisation characteristics.[146] In the case of muscles a linearly aligned structure would be beneficial and a radial arrangement is suggested for liver lobule tissues.[147–149] Generating these structures was investigated by spatial variation of the hydrophobicity,[141] cell growth along nodal position of resonance vibration,[147] lithography,[150] inkjet printing,[151] and photo patterning with UV light[152,153] to name a few. Collagen often takes its part throughout these studies and it is also shown that large collagen fibrils and unpolymerised fibrils induce different reactions of cells, leading to the conclusion that the properties of collagen fibrils also affect the cell response.[154,155]

[ii] The quantification of "soft" and "stiff" in the context of biological cells is owing.

2.2 Atomic Force Microscopy

2.2.1 Functionality

With the first successfully conducted experiment in 1981, the scanning tunneling microscopy (STM) founded the scanning probe microscopy (SPM) family. Later, the atomic force microscopy (AFM) was added. The first references to STM and AFM in scientific publications were made in 1982[156] and 1986,[157] respectively. In 1986, the German physicist Gerd Binnig (*1947) and the Swiss physicist Heinrich Rohrer (*1933; †2013) were awarded with the Noble prize for their invention of the STM.

Nowadays, AFM can characterise a sample surface not only by displaying its topography but correlating it with mechanical[158,159] or electrical[160] properties, as well as extracting information from single molecules.[161] The sample kind is barely limited by more than a maximum roughness depending on the type of microscope. Soft samples down to a modulus of a few kilopascals can be measured, as well as stiff samples up to hundreds of gigapascals. The measurement environment can be varied between ambient conditions, vacuum, and varied humidity up to measurements within a liquid. Sample preparation is not required as long as the sample surface is accessible and the variety of available probes allows for conducting experiments that are specifically tailored to satisfy the operator‘s needs. AFM is a a powerful technique that found its purpose in several disciplines, *e.g.*, nanobiotechnology,[162] microbiology,[163–165] nanofabrication,[166] crystallography,[167] and materials science.[168] This offer of possibilities has to be looked at more closely.

Unlike optical microscopy methods, AFM is not bound to the Abbe diffraction limit describing the minimal distance d that can be resolved between two objects depending on the applied wavelength λ. For AFM instead, a solid probe is brought in close proximity or in contact with the sample, sensing the forces interacting between this probe and the sample. Butt *et al.*[169] provide a comprehensive introduction into force measurement techniques with the atomic force microscope. Usually, the probe is referred to as tip and can have different shapes, but for an image with a resolution in the lower nanometre-range, the sample-facing end of a tip has a radius of a few nanometres. The tip is attached to the foremost end of a cantilever and from the back of this cantilever a Laser beam is reflected to a segmented photodiode placed at a certain distance. A deflection of the cantilever is recorded on the photodiode as a shift of the signal. The distance between the cantilever and the photodiode makes it possible that even tiny deflections of the cantilever induce a measurable shift of the electric signal. Even vibrations of the cantilever due to Brownian motion can be detected by this setup. Important characteristics of the cantilever are the force constant k and the resonant frequency f_0. The cantilever is attached to a piezoelectric crystal-steerage unit, *i.e.*, a piezo-tube or a tripod scanner, that can move the cantilever in x-, y-, and z-direction. The positioning in x- and y-direction enables a controlled scanning movement of the probe on the sample. The photodiode is connected to this unit via a feedback loop that compares the

measured deflection of the cantilever to a beforehand chosen set point of this deflection. In fact, several ways of detecting the deflection are available as, *e.g.*, capacitive or interferometric, but the described optical method is most conventionally applied. In case of a deviation between detected deflection and set point, the feedback loop signals the steerage unit to change its z-position re-adjusting the deflection of the cantilever. The essence of nearly every AFM mode is the choice of a set point value that has to be kept constant throughout the entire measurement by the help of the feedback loop. This measurement principle is best illustrated with an example: the most straightforward way of operating an atomic force microscope is in the constant force mode that belongs to the static contact modes. In constant force mode, the probe is engaged towards the sample surface and brought in contact with it until a chosen force, acting between tip and sample, is reached. The probe is scanned across the sample line by line at which each line is usually scanned twice (trace and retrace). If the probe encounters a change in height, elevated as deepened, the deflection of the cantilever will change, increase or decrease, and this deviation in relation to the set point is detected by the feedback loop instantly. The consequence is a feedback loop-induced change in z-position of the cantilever, up or down, to maintain the initial deflection. From these collected data, the height profile of the sample is recalculated and displayed in two- or three-dimensional images.

A large number of modes requires the introduction of an oscillatory cantilever movement excited by a piezoelectric shaker crystal or other methods like pulsed Laser irradiation. A very common mode is the intermittent contact mode, also referred to as tapping mode, in which the tip is only touching the surface at the lower reverse point of every oscillation cycle. In comparison to the constant force mode, the lateral forces are reduced which preserves tip and sample. In this mode, the parameter that is kept constant is the amplitude of the damped cantilever oscillation. The frequency of the oscillation is at or close to the resonant frequency of the cantilever. In the unperturbed state where no forces are acting between sample surface and tip, the cantilever is oscillating according to a harmonic oscillator with a free amplitude A_0. During engagement, forces start acting and the model changes to a harmonic oscillator with damping, which results in the shift of the resonant frequency to f_1; but since the excitation still happens at f_0, the force-induced shift of the resonant frequency leads to a decrease of the amplitude until the set point amplitude A_1 is reached. Starting the measurement, changes in topography will again vary the resonant frequency and, therefore, create changes in the amplitude that have to be balanced by the feedback loop and the consequent adjustment of the cantilever's z-position.

2.2.2 Force versus distance curves

A further way to extract information from a surface is the application of so-called force versus distance curves. Butt *et al.*[169] provide a comprehensive overview on the analysis of force curves. From a distance without any forces acting, the probe is approached towards the surface until it gets in contact. The cantilever is

further moved towards the surface until the thereby induced bending of the cantilever reaches a beforehand chosen set point. After that has happened, the cantilever is retracted to the initial position (cf. Figure 2.1a). Tracking the deflection signal during this engage and retract cycle on the photodiode delivers a characteristic curve that, without further recalculations, is a deflection versus piezo displacement curve. To obtain the force out of the deflection value that is given in volts, the force constant k and the inverse optical lever sensitivity (InvOLS) of the cantilever have to be determined. The InvOLS is the slope of the contact part of the acquired deflection versus piezo displacement curve. Several techniques are available for the estimation of k like the Sader method[170] or the thermal noise method.[171] The acting force F depending on the deflection can be calculated by

$$F = deflection \cdot InvOLS \cdot k. \tag{2.1}$$

The piezo displacement can be transferred into distance or indentation by identifying the contact point of the probe on the sample surface. The resulting force versus indentation curve carries much information on the relationship between tip and sample (cf. Figure 2.1b): there is the adhesion force, as vertical distance between the lowest point of the retract curve and the line of zero force, the dissipative energy, as area between trace and retrace curve, and the indentation, as horizontal distance between the contact point and the reverse point of the trace and retrace curve. With indentation experiments, the elasticity of a sample can be estimated by fitting the slope of the curve in the contact area (Figure 2.1). Force versus indentation curves can be obtained with an oscillating or a non-oscillating cantilever.

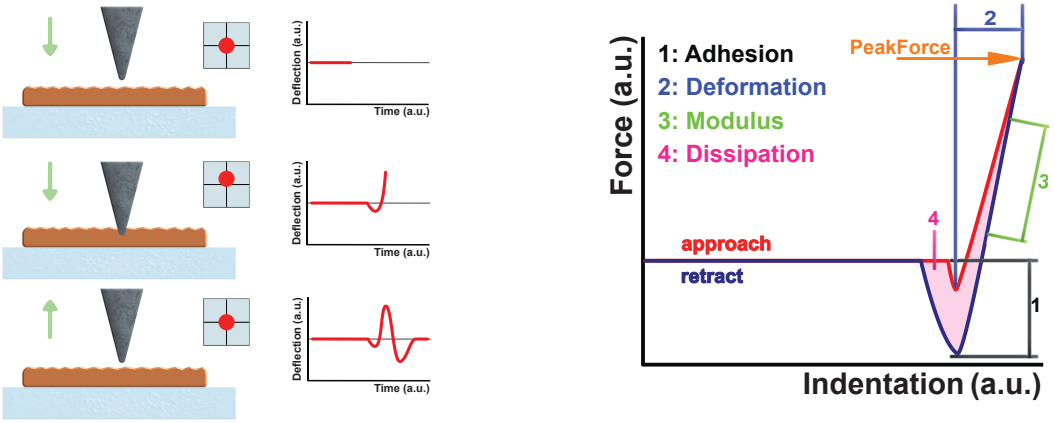

Figure 2.1.: Schematics of the formation and the evaluation of force versus indentation curves showing (a) the approach of an AFM tip towards a surface supported collagen fibril with the corresponding deflection versus time signal. As soon as the applied force reaches the set point the tip is retracted and the deflection reaches the initial state again. The resulting (b) force versus indentation curves holds several quantities like adhesion, deformation, modulus, and dissipation.

2.2.3 Peak force tapping mode

An AFM mode that combines the scanning nature of the imaging and the information obtained from force versus indentation curves is the Peak Force Quantitative Nanomechanical Mapping (PFQNM) tapping mode by Bruker presented in 2009 and described in the application notes # 128[172] and # 141.[173] The cantilever oscillates with a sinusoidal trajectory and a frequency of 0.125 to 2 kHz while scanning the sample. For this mode, the set point variable is the peak force, which is the maximal force that acts in the lower reverse point of the oscillatory cycle. This enables the precise control of the force that is applied on the sample, which, especially for soft samples or delicate tips, means that damage can be reduced to minimum and the load on the sample can be quantified. With this method, the peak forces can be as small as several tens of piconewtons. Every oscillatory cycle can be evaluated, as discussed in Section 2.2.2, and several cycles are averaged for each data point. By that, property maps are generated that carry the information on the elastic modulus of the sample and the topography at the same time. For the evaluation, the software offers the application of the Derjaguin-Muller-Toporov (DMT) or the Sneddon model (cf. Section 2.2.3.1). The Sneddon model is well suited for the application on very soft samples (*e.g.* biological samples) since, in these cases, the indentation of the probe may exceed the very tip radius and, thus, the contact is of conical nature rather than represented by a sphere. A minimum indentation of 30 nm is suggested for the acquisition of reliable results. The DMT modulus, in general, can also be applied to harder materials and is well suited for small indentation depths.

2.2.3.1 Contact mechanics

Classical contact mechanics is inevitably linked to Heinrich Hertz (*1857; †1894) who developed the famous Hertz model.[174] The model describes the contact between two elastically isotropic bodies with a contact area that is very small in comparison to the dimensions of the bodies, no adhesive contact, and a finite pressure. A further requirement is the assumption of an ideal flat surface so that friction forces can be neglected and only vertical forces are considered. The geometry of the bodies can be varied. For AFM measurements, the indentation of a rigid sphere into an elastic, flat surface is important. In that case the force[175] reads

$$F = \frac{4}{3} \cdot \sqrt{R} \cdot E_{eff} \cdot \delta^{\frac{3}{2}} \tag{2.2}$$

with the radius of the indenter R, the effective Young's modulus E_{eff}, and the indentation depth δ. As useful as the Hertz model is, it has to be expanded by the description of adhesion during contact. In 1971, Johnson, Kendall, and Roberts[176] proposed a model, known as Johnson-Kendall-Roberts (JKR) model, for the description of surface energy on the contact of elastic solids and supported their theoretical findings with

experiments of rubber and gelatine spheres. For the JKR model it is assumed that the contact between an elastic sphere and rigid surfaces results in a "neck" between two bodies, leading to an adhesive force in their contact area. The model can be applied best for large, flexible spheres. Only four years later, in 1975, Derjaguin, Muller, and Toporov[177] proposed an alternative model for the description of adhesion during contact (DMT model) which holds for small, rigid spheres. The DMT model considers that tensile forces between the bodies take place at the edge of the contact area, which shifts the area of adhesion beyond the contact area and results in

$$F = \frac{4}{3} \cdot \sqrt{R} \cdot E_{eff} \cdot \delta^{\frac{3}{2}} + F_{adh} \tag{2.3}$$

for a contact between spherical indenter and flat surface with the adhesion force F_{adh}. Changing the indenter shape to a conus, Sneddon[178] developed a model to describe this contact with a flat surface leading to

$$P = \frac{4 \cdot \mu \cdot \cot \alpha}{\pi \cdot (1 - \eta)} \cdot D^2, \tag{2.4}$$

with the total load P, the rigidity modulus μ described by

$$\mu = E/2 \cdot (1 + \nu), \tag{2.5}$$

the Poisson ratio ν, the semivertical angle of the cone α, and the penetration D.

2.3 Raman spectroscopy[iii]

2.3.1 Functionality

In 1923, the German physicist Adolf Smekal (*1895, †1959) predicted the existence of inelastically scattered light, but it was the Indian physicist Chandrasekhara Venkata Raman (*1888, †1970) who, in 1928, was able to experimentally prove this phenomenon. Only two years later, in 1930, Raman received the Noble prize for his work on the scattering of light and the discovery of the inelastically scattered light which was called Raman effect. Soon, the effect was used for spectroscopic purposes and created the Raman spectroscopy. This tool is mainly used for structural determination. The sample is irradiated with monochromatic light (Laser) and the scattered light is analysed. The main part of the detected light is scattered elastically, which is called Rayleigh scattering, named after John William Strutt, third Baron Rayleigh (*1842, †1919). The rest is inelastically scattered light, meaning that the detected wavelength differs from the excitation wavelength. In this case, the frequency can either be lower (Stokes scattering) or higher (Anti-Stokes scattering) than the initial wavelength. Thus, energy transfer from the incident light to the scattering atom or molecule or an energy transfer vice versa takes place. The thereby induced shift is characteristic for the scattering centrum of the photon which gives the Raman spectroscopy the potential of identifying systems by their fingerprint spectrum.
The requirement for the occurrence of the Raman effect is the change in polarisability α of the molecule during its vibrations described by

$$\left(\frac{\partial \alpha}{\partial q}\right)_0 \neq 0 \tag{2.6}$$

where q is the normal coordinate of the vibration.[181] These vibrations are called to be Raman active and are mostly symmetric and the corresponding bond is non-polar. With that, Raman spectroscopy provides a complement to infrared (IR) spectroscopy for which a change in dipole moment during the vibration is required. When the photon interacts with a particle, the particle is excited to a virtual state that is between the ground state and the first electrical state. Subsequently, the molecule drops back to a vibrational state in the ground state. In case of Rayleigh scattering, which happens in $> 99\,\%$ of the scattering events, the initial and the final vibrational state are the same resulting in no energy transfer. For the Stokes scattering, the initial state is the vibrational ground state, but after the scattering process the particle is left in a higher vibrational state,

[iii] The information displayed in Section 2.3 is partially extracted from *Practical Raman Spectroscopy - An Introduction* by Peter Vandenabelle,[179] *Modern Raman Spectroscopy - A Practical Approach* by Ewen Smith and Geoffrey Dent,[180] and *Raman and SERS Investigations of Pharmaceuticals* by Monica Baia, Simion Astilean, and Traian Iliescu.[181]

meaning that energy has been transferred from the photon to the particle. In the more unlikely event of Anti-stokes scattering, the process is opposed with the particle being in the vibrational ground state after the scattering while it was in a higher vibrational state before.

In the Raman spectrum, the resulting signals are represented as bands with intensity, position, symmetry, and a full-width half maximum (FWHM) as describing quantities. Bands can represent a single state of vibration or a superposition of several bands leading to the appearance of shoulders or a splitting of the peak. The position of the bands is approximately described by

$$\psi = \frac{1}{2 \cdot \pi} \sqrt{\frac{K}{m_r}} \tag{2.7}$$

with the vibration frequency ψ, the force constant K, and the reduced mass m_r.[179] It can be seen that the band position depends on K which, for example, allows for the distinction between single and multiple bonds. If a vibrating molecule changes its substituents, it will shift the resulting Raman band position according to the variation in mass. Further parameters influence the band position because even if a Raman spectrum is a fingerprint spectrum of a certain sample, this spectrum is also unique in its dependence on the chemical environment of the sample and, *e.g.*, its history, temperature, and changes in concentrations. The spectral resolution of the spectrometer also influences the bandwidth and the applied wavelength of the excitation Laser influences the spectrum. A poorly chosen Laser changes the relative intensities of the Raman bands and can introduce a fluorescence that makes an evaluation of the Raman spectrum impossible.[182]

In combination with a confocal microscope, Raman spectroscopy cannot only perform scans of a single point, but can also provide two-dimensional map scans, or depth scans. The Raman spectroscopy exhibits little scattering in water, which allows for the measurement of samples in a H_2O environment. As long as the sample material is Raman active, it can be solid, liquid, or gaseous. The limiting factor is a sufficient amount of particles within the excitation volume of the excitation light beam because statistically only 1 out of 10^6 to 10^8 photons is scattered inelastically. In case of Raman spectroscopy of a small sample volume, signal enhancement is required.

2.3.2 Surface Enhanced Raman Spectroscopy

A method to amplify the Raman signal is Surface Enhanced Raman Spectroscopy (SERS) that can be used to investigate samples whose volume is not sufficient for producing a signal with regular Raman spectroscopy.[183] For that, gold, silver, or platinum is used to enhance the signal intensity. Further metals were investigated as well.[184] In general, there are two ways how to contact the sample with the noble metal: in the form of nanoparticles or with especially designed substrates. In both cases, the excitation of the sample requires a close

coupling between noble metal and sample that, in turn, implies that the penetration depth is rather limited (3 nm) and the method is very surface-sensitive.[185,186] In the best case, the investigation of single molecules is enabled.[187,188] Nanoparticles of the noble metal can be incorporated into the sample by mixing them into the polymerisation solution and attach the nanoparticles to the sample,[61] the sample to the nanoparticles,[189] or cover a substrate with nanoparticles.[190] In case of the SERS substrate glass slides can be covered with a thin layer of the noble metal. Roughness, structure, and thickness of this layer are very important factors influencing the quality of the signal enhancement, as it is the size of the nanoparticles for the first approach.

For the explanation of the underlying processes, two major mechanisms have been under debate: the electromagnetic enhancement and the charge transfer mechanism. It seems that the full enhancement achieved with SERS is founded in both explanations.[191–193] The charge transfer mechanism is based on the formation of an adsorbate-metal complex of chemi- or physisorbed molecules. For the electromagnetic enhancement the amplification comes from the scattering due to the excitation of the plasmon resonance.

In addition to all the advantages of SERS, it shall also be mentioned that the method suffers drawbacks such as, *e.g.*, a poor quantitative reproducibility. A further technique that is based on the amplification of the Raman signal due to the application of silver or gold is Tip Enhanced Raman Spectroscopy (TERS) using an AFM setup.

2.4 State of the art

2.4.1 Application of atomic force microscopy on biological materials

AFM was established as an indispensable method for the characterisation of a variety of material types in the field of micro- and nanotechnology. This also holds true for the investigation of biomaterials. Imaging of viruses[194–196] is as much possible as displaying deoxyribonucleic acid (DNA) in ambient conditions[197] and liquid environments.[198,199] Apart from mastering these challenges in capturing objects with nanometre-dimensions, AFM is also capable of imaging cells[200] that not only have an extent in the micrometre-range, but which are delicately soft with a modulus of a few kilopascal. Collagen fibrils are dimension- and moduluswise not as sensitive as the so far named examples. Thus, the application of the atomic force microscope on collagen is very well established. AFM was used to investigate, for example, the impact of UV light on the D-band periodicity,[201] to document the untwisting processes of swollen fibrils,[202] to image fibrillar sub-structures,[203] to identify varying dissipation behaviour between gap and overlap region,[78] and to record time-lapse videos of the self-assembling process of collagen.[204]

The estimation of the Young's modulus of collagen fibrils by indentation experiments,[205,206] and the implementation of bending[90,207,208] and tensile tests[209–213] in ambient air, as well as in a liquid environment, are of general interest. Thus, AFM provides the opportunity to measure the mechanical response of collagen fibrils towards loads for several directions. This is beneficial since the mechanical properties of collagen fibrils are expected to be anisotropic.[90,214] Regarding the indentation, the application of single force versus indentation curves can extract mechanical properties of collagen but it is more desirable to obtain two-dimensional maps of mechanical properties, which has already been done for collagen samples in various environments and with various treatments.[6,205,215–217] By comparison of treated and untreated samples, the impact of the applied conditioning is extracted. The acquired modulus of collagen fibrils is, at ambient conditions, in the single-digit gigapascal-range and for fibrils immersed in a liquid environment in the single-digit megapascal-range. In more detail, AFM based nanoindentation measurements show a Young's modulus obtained by nanoindentation of 3.2 ± 1.0 GPa for non-irradiated fibrils,[218] 2.2 GPa for the overlap and 1.2 GPa for the gap regions of dry fibrils,[78] 1.9 ± 0.5 GPa for collagen fibrils at ambient conditions and 1.2 ± 0.1 MPa in buffer solution.[205] The indentation modulus of air-dried osteogenesis imperfecta collagen fibril is 5.3 ± 2.2 GPa, in comparison to air-dried collagen fibrils of wild-type animals with 7.9 ± 2.8 GPa completed by 10.8 ± 3.7 MPa and 1.2 ± 0.4 MPa for these collagen species being hydrated.[52]

The sample preparation for AFM-based bending tests is straightforward as well as the measurement itself. The rod-shaped specimen is spanned over a substrate that contains some kind of cavities like pores or trenches. While the parts of the specimen that are in contact with the substrate need to have a firm attachment, the parts

crossing the cavities shall be freely suspended. The AFM probe is used to deflect the freely suspended part vertically. A quantity for the bending modulus can be extracted by the evaluation of the deflection signal in combination with knowledge on the dimensions of specimen and substrate and characteristics of the cantilever as it is shown for carbon nanotubes or single crystal silicon beams.[219–221] Generally, the evaluation is based on the assumption of the sample following the linear elastic theory of an isotropic material[207,220–222] with

$$E = \frac{L^3}{192 \cdot I} \cdot \frac{\mathrm{d}F}{\mathrm{d}x}, \tag{2.8}$$

where E is the elastic modulus, I is the moment of inertia, L is the suspended length, and $\frac{\mathrm{d}F}{\mathrm{d}x}$ is the gradient of the force versus displacement curve. Results for collagen fibrils range from 1 to 10 GPa in ambient conditions to 70 to 170 MPa in liquid media.[90,207,208]

The extraction of the tensile modulus for single collagen fibrils poses a special challenge due to the small dimensions of the sample. Bearing of tensile loads from collagen-based constructs has been researched for three-dimensional matrices,[223–225] as well as fibres or tendons, that produce dimensions in the micrometre- or even millimetre-range. Testing has taken place in ambient conditions with the report of tensile moduli from 1 to 8 GPa,[226–228] as well as in aqueous media in which a tensile modulus of 54 MPa has been indicated.[229] However, when it comes to smaller units of collagen, namely the fibrils, new approaches had to be installed. The small dimensions impede the attachment of their ends to any kind of suspension, which leads to enormous efforts during this task. Research has applied microelectromechanical systems (MEMS),[230–232] optical tweezers,[233,234] self-built systems,[235,236] and AFM to address this issue. MEMS-based tensile testing of single collagen fibrils immersed in a liquid environment has delivered tensile moduli from 0.47[230] to 0.86 GPa[231] and others even distinguish between a tensile modulus extracted for low strains with 0.4 to 0.5 GPa and high strains with 6 GPa.[232] In case of AFM, the most common method is to fix one end of a single fibril to the substrate and the other end to the AFM probe by the application of epoxy glue.[209,210] Further researchers report from the attachment of the fibril to the probe by pulling them out of an aggregation[211] or adsorbing the fibril by resting the tip on it[212]. Additionally, some experimental setups provide the combination with a visualisation technique like scanning electron microscopy (SEM).[236,237] The resulting tensile moduli for single collagen fibrils have been between 2 and 7 GPa for ambient conditions.[238] In an aqueous environment, the reported values diverge from 32 MPa,[212] over 250 to 450 MPa,[90,238] up to 2.2 to 3.5 GPa for small strains.[209]

2.4.2 Raman spectroscopy on collagen

Collagen has been identified by Raman spectroscopy in various forms.[61,239–241] Caetano *et al.*[242] compared dermis of photoexposed (dorsal forearm) and non-photoexposed (proximal medial arm) regions in different age groups by Raman spectra *in vivo*. They conclude that the Raman shift region between 798 and 994 cm^{-1} as well as the intensity ratio of the peaks at 1275 and 1450 cm^{-1}, are useful sites for the identification of photoageing effects. Similar experiments were performed by comparing skin samples of 40 and 70 years old test persons under varied relative environmental humidity, highlighting the interactions between collagen and water. [243] However, Raman spectroscopy on single amino acids or other proteins during denaturation and crosslinking events, not necessarily induced by UV light, has been done.[182,239,242,244–253] This information is used for the description of the obtained findings. Detailed identification of peaks and stabilisation or destabilisation markers based on this literature will be stated during the discussion of the presented results. Additionally, the applicability of SERS on collagen fibrils was already proven.[61]
However, the influence of different UV light sources on the molecular structure of collagen hydrogels or collagen fibrils in various liquid environments has not been studied by Raman spectroscopy.

2.4.3 The Raman spectrum of collagen

Raman spectroscopy was applied earlier for the identification of the fingerprint spectrum of collagen.[240,241] For evaluation, several regions can be highlighted according to their containing information. Prominent examples are the amide band region (1100 to 1800 cm^{-1}), the C–H region (2800 to 3150 cm^{-1}), and the O–H region (3150 to 3550 cm^{-1}).
The amide bands in the Raman spectrum describe the peptide bonds that are created by the carboxyl group and the amino group between two amino acids and thereby stabilise the collagen backbone. In the Raman spectrum, three bands are available for the description of these bonds: amide I, amide II, and amide III. Since vibrations in the peptide bonds are interconnected, they cannot be interpreted separately.[254] Between 1600 and 1690 cm^{-1} the amide I band can be found[182] and it is mainly dominated (80 %) by the C=O stretching. The various peaks within the amide I band are designated to different appearances of the collagens secondary structure as there are α-helix, β-sheet, turn, and unordered. Between 1450 and 1550 cm^{-1} the amide II band is located[182] and it represents the N–H bending (60 %) as well as the C–N stretch (40 %). The amide III band appears between 1230 and 1300 cm^{-1} and, again, is mainly formed by the N–H bending (30 %), as well as the C–N stretch (40 %).[255] Regarding the secondary structure, the amide III band carries complementary information to the amide I band. The O–H band that is located between approximately 3150 and 3550 cm^{-1} represents the water that is bound or free within the measurement volume. This can help in identifying

occurring reactions as condensation reactions. The region in which the C−H vibrations of amino acids are mostly found is between 2800 and 3150 cm^{-1}. It allows for the identification of amino acids. An amino acid induces several bands which may lead to band overlap and, thus, a more complicated band assignment. Some amino acids, however, have very characteristic peaks or exhibit signals at wave numbers higher than 3000 cm^{-1}, which eases their recognition.[256]

2.4.4 Patterning of biological substrates

As adumbrated in Section 2.1.6, the complex environment of biological cells *in vivo* requires more elaborated substrates to mimic these structures *ex vivo*. This includes the creation of areas on the substrate in which the cells tend to grow favourably or areas in which cells do not grow at all, as well as formation of structures that guide the cell growth. Thus, a certain patterning of the substrate has to be done for which several approaches have been applied utilising the different properties of a substrate that influence the cell behaviour (cf. Section 2.1.6). Photolithography in combination with cell-attractive zirconium,[257] electrochemical wet stamping of gold islands equipped with self-assembled monolayer (SAM)s enabling placement of single cells,[258] a combination of photolithography, etching, chemical vapour deposition, and polyethylene glycol treatment,[259] and the application of electroactive substrates,[260] to name a few, are used for the patterning of substrates. A more general perspective is summarised by Ayibaike *et al.*[259] stating the division of cell patterning techniques into top-down methods[261,262] and bottom-up methods.[263,264] The challenge of patterning can be expanded by moving from two- to three-dimensional substrates. Several approaches follow the idea that three-dimensional substrates are a composition of stacked two-dimensional substrates accomplished by 3D-printing. Thus, a modification of the substrate has to be applied only on the two-dimensional level[257]; but the invasion of cells in three-dimensional structures is also a research subject.[265]

2.4.5 Collagen

Section 2.1 gave a general introduction to collagen, covering its structure, application in tissue engineering, interaction with cells, and provided an overview on the research that has been dealing with the chemical interactions of collagen with UV light. The following section extends the information regarding the interaction of collagen with UV light, highlighting the changes in mechanical properties.

Since collagen is a major load-bearing component of the ECM,[207,209] its mechanical properties are always a characteristic of major interest with the collagen fibril generating a principle impact.[235] It is common that collagen-based specimens undergo a crosslink-promoting treatment to increase their stability or modify

them according to other requirements. Chemical approaches include the addition of, *e.g.*, sulphated glycosaminoglycans,[266] transglutaminase,[267] or glutaraldehyde.[268] The chemical based methods bear the possibility of introducing cytotoxicity to the collagen-based structures, which would limit or totally disable the later experiments with biological cells.[267] Even if the cytotoxicity, in case of glutaraldehyde addition, can be reduced by, *e.g.*, neutralisation[269] or the application of smaller amounts,[270] research also moved the physical methods into the spotlight. Representatives are dehydrothermal (DHT) treatment[128,271] and exposure to UV light.[2,21,22] DHT treatment has proven to modify the mechanics of collagen samples but the method requires an exposition of the sample to elevated temperatures (100 °C and more) for several hours or up to days at a reduced pressure.[272,273] The irradiation with UV light offers a faster and more effortless approach. Although destabilising events can be triggered,[274] cytotoxicity is most likely not introduced. The impact of UV light on collagen-based structures has become comprehensively investigated.

Apart from AFM measurements (cf. Section 2.4.1), differential scanning calorimetry, X-ray diffraction, and rheological methods have been applied for the investigation of changes in collagen during denaturation events.[275,276] It is shown that the exposure of collagen samples to UV light changes the mechanics as elongation, Young's modulus, and breaking strength.[2] It is also suspected that, not only are denaturation events induced by the irradiation of UV light, but also, denaturation and crosslinking events happen simultaneously.[21,22] Sample preparation and irradiation dose are crucial parameters for triggering photodegradation or photocrosslinking.[19,23,24,116,117,121,277] The variation of the collagen source may also lead to differing results.[2] As indicated by the dependence of the results on the dose, the time of irradiation plays a central role in the outcome, since stabilising effects can peak after a certain time of exposure and subsequently vanish again. A maximum increase in mechanical properties has been reported after 15 to 30 min for UVC irradiation of collagen fibres,[128] 30 min for the UVC irradiation of collagen-glycosaminoglycan matrices, and 30 min for UVC irradiation of collagen films.[19] Further influences are named that take their part in balancing stabilising and destabilising events. The pH and the addition of, *e.g.*, salts, do induce a change in modulus without any exposure to UV light. Ethanol and KCl are reported to increase the indentation modulus[217] and variations of other quantities do impact stabilisation and destabilisation as, *e.g.*, temperature,[128,244,278] mechanical stress,[34] and γ-radiation[246] tend to change the modulus as well. Even if these methods are not primarily linked to UV exposure, questions arise whether occurring stabilising and destabilising mechanisms can be used for the explanation of UV light-induced modifications or whether a combination with UV irradiation can lead to even higher changes.

Collagen is of central importance for the substrate design in the discipline of tissue engineering. Necessary modifications of the substrate regarding its mechanical properties is best done without introducing cytotoxicity; for this reason exposure to UV light is a method of choice. As presumably strongest unit in the hierarchical construct of collagen, the interaction of collagen fibrils with the UV light exposure is of major interest. For investigations, a method is required that can extract mechanical information from specimens as small as single collagen fibrils and extract these properties for different directions of load on the sample due to the mechanical anisotropy. AFM suits these requirements and allows for measurements in ambient air, as well as in liquid environments.

At the beginning, two-dimensional maps of mechanical information of single collagen fibrils were extracted for different combinations of UV light sources and liquid environments. The treatment of the specimen took place simultaneously to the acquisition of the mechanical properties providing experiments *in situ*. By measuring the same fibril during treatment, a high comparability of the results was achieved and the chronological sequence of the modifications could be tracked.

Due to the elaborate extraction of a tensile modulus from nanometre-sized objects, a new evaluation method was proposed combining the simplicity of a sample preparation for three point bending tests with the physical outcome of a conventional tensile test. Again, collagen fibrils were treated simultaneously to the measurement, which resulted in time-resolved evolutions of the tensile modulus dependent on the applied UV light source and the liquid environment the sample was immersed in.

Raman spectroscopy was applied to correlate observed changes in the mechanical properties to structural changes of the collagen. Underlying mechanisms should be revealed and help understanding of how UV light interacts with collagen dependent on wavelength and kind of liquid environment.

Bridging the gathered results and possible applications, three-dimensional structures of collagen were used as substrate for cell growth. The behaviour of the cells regarding the UV light exposure of the collagen substrate was investigated. By that, the ability of the UV light should be exploited to selectively expose a sample and, thus, create a pattern on it with varying mechanical properties.

The study of collagen fibrils and their reaction towards UV light exposure under application of different liquid environments should contribute to the comprehensive research on collagen as suitable material for tissue engineering. Providing experiments *in situ* shall support earlier findings elsewhere by the estimation of the temporal point of maximum change and expand them by, simultaneously, recording the course of the mechanical properties with time of exposure. The application of different UV light sources and liquid environments on the same experimental setup and the same source of collagen shall provide a comparison between the settings that, to the knowledge of the author, has not been performed yet. The introduction of a new evaluation method for

bending experiments with the aim of extracting the tensile modulus shall enable a faster and easier access of tensile moduli of nanometre-sized, rod-shaped specimens. The investigation of structural changes by Raman spectroscopy shall satisfy the need for a time-resolved recording of the evolution of the collagen structure during UV exposure enhancing the understanding of their interactions. Cultivating cells on only-collagen substrates and demonstrating the feasibility of UV light patterned surfaces shall dress the path for an easy access to more elaborated substrates living up to the requirements of tissue engineering.

3 Methodology

3.1 Materials and devices

List of chemicals

Accutase solution	Merck, Darmstadt (Germany)
Acetone	Carl Roth GmbH + Co. KG, Karlsruhe (Germany)
Collagen I rat protein, tail, 3 mg·ml^{-1}	Gibco, ThermoFisher Scientific, Waltham, Massachusetts (USA)
Deionised water	Milli-Q, Merck, Darmstadt (Germany)
Dulbeccos's modified essential medium (DMEM)	CLS Cell lines service GmbH, Eppelheim (Germany)
Methylated spirit	Carl Roth GmbH + Co. KG, Karlsruhe (Germany)
Nitrogen gas	Air Liquide, Paris (France)
1x/10xPBS	Carl Roth GmbH + Co. KG, Karlsruhe (Germany)
3D printer resin "Clear Resin-BV007"	Asiga, Sydney (Australia)
Silver coated substrates RAM-SERS-AG	Ocean Optics B.V, Duiven (Netherlands)
Silver nanoparticles, 20 nm	Merck, Darmstadt (Germany)
Silver paint 200, conductive	Ted Pella Inc., Redding, California (USA)
Sodium hydrogen carbonate, powder	Carl Roth GmbH + Co. KG, Karlsruhe (Germany)

List of devices

3D printer, Pico 2HD 27	Asiga, Sydney (Australia)
Atomic force microscope, Dimension Icon	Bruker, Billerica, Massachusetts (USA)
Bandpass filter 365 nm, 10 nm FWHM	Edmund Optics Ltd., York (United Kingdom)

Bandpass filter 313 nm, 10 nm FWHM	Edmund Optics Ltd., York (United Kingdom)
Calibration grating, TGZ-500	plano, Wetzlar (Germany)
Calibration sample RS-15M	Bruker, Billerica, Massachusetts (USA)
CO_2-Incubator, CB 53	Binder, Tuttlingen (Germany)
Confocal Raman microscope, alpha 300 RA	WITec, Ulm (Germany)
Light microscope, Axio Observer Z.1	Zeiss, Oberkochen (Germany)
Light microscope, Axio Imager.M2m	Zeiss, Oberkochen (Germany)
Microprocessor temperature regulator HT MC1	Horst, Lorsch (Germany)
Plasma chamber, Femto	Diener, Ebhausen (Germany)
Quartz glass cuvette QS, 2 mm	Hellma Analytics, Müllheim (Germany)
Thermomixer comfort	Eppendorf, Hamburg (Germany)
Ultrasonic cleaner	VWR, Radnor, Pennsylvania (USA)
UV-A light source N8-L	Benda, Wiesloch (Germany)
UV-B light source N8-M	Benda, Wiesloch (Germany)
UV-C light source	Osram, Munich (Germany)
UV spectrometer	Ocean Optics, Largo, Florida (USA)

List of cell types

Monkey kidney (SV 40 transformed) cells (COS-7)	CLS Cell lines service GmbH, Eppelheim (Germany)

List of consumables

Cell flask, 25 cm^2	Corning, New York (USA)
Microscope slides, soda-lime glass	Carl Roth GmbH + Co. KG, Karlsruhe (Germany)
Pipettes 2 ml, 5 ml	VWR, Radnor, Pennsylvania (USA)
Reaction vessel, 1.5 µl	Carl Roth GmbH + Co. KG, Karlsruhe (Germany)

Table 3.1.: List of the cantilever types that were applied throughout the course of the presented work, arranged accordingly to their occurrence in the text. The table contains the nominal characteristics of the cantilever as well as measured properties.

Property / Cantilever	Manufacturer	Force constant nominal	Force constant measured	Resonant frequency nominal	Tip radius nominal	Cantilever shape
	-	($N \cdot m^{-1}$)	($N \cdot m^{-1}$)	(kHz)	(nm)	-
ZEIHR	Nanosensors Neuchâtel, Switzerland	27	18 - 25	130	8	triangular
ScanAsyst Fluid	Bruker Billerica, MA, USA	0.7	0.6 - 1.0	100	20	rectangular
B300	nanotools Munich, Germany	0.2	0.1 - 0.3	13	300	triangular
MLCT-Bio-D	Bruker Billerica, MA, USA	0.015	0.01 - 0.04	10	20	rectangular
XNC12-A	µmasch Sofia, Bulgaria	0.08	0.08 - 0.15	17	10	triangular

3.2 Sample preparation

3.2.1 Single collagen fibrils

For the investigation of single collagen fibrils, microscope glass slides were used as substrates and the fibrils were spread on them. The glass slides were cut into pieces of approximately $2 \times 3\,\mathrm{cm}^2$ and cleaned with acetone and methylated spirit before being placed in the ultrasonic bath with methylated spirit and deionised water for 10 min each. Subsequently, the substrates were dried with nitrogen. Before the solution was placed on the cleaned substrates, the glass slides were treated with oxygen plasma at 35 W for 1 min. It is applied for removing organic residues by changing them to water and carbon dioxide and additionally forming O–H groups on the surface to increase its hydrophilicity. The solution for the single collagen fibril samples contained 100 µl of 10x phosphate buffered saline (PBS), 100 µl of the type I rat tail tendon collagen protein, 37 µl of $NaHCO_3$, and 763 µl of 1xPBS. All components were stored in the fridge before being gently mixed in a reaction vessel. Approximately 100 µl of the solution was placed on each glass substrate so that the glass was fully covered. The samples were stored in the incubator at a temperature of 37 °C for 60 min to accelerate the polymerisation. The residual solution was removed by rinsing each sample gently with deionised water three times. Until further use, the samples were stored in the fridge.

3.2.2 Collagen hydrogels

For the investigation of collagen hydrogels, microscope glass slides were used as substrates for AFM measurements and cell experiments while for the Raman measurements silicon wafers were used. The glass slides were cut, cleaned, and treated with oxygen plasma as described in Section 3.2.1. The solution for the collagen hydrogels contained 100 µl of 10xPBS, 670 µl of the collagen I rat protein, 17 µl of $NaHCO_3$, and 213 µl of deionised water. All components were stored in the fridge before being given in a reaction vessel. The single components were blended in a thermomixer, for 2 min at 500 pm. The solution was placed on a prepared substrate so that it was fully covered while the amount of deposited solution was varied in accordance with different layer thicknesses. After being stored in the incubator for 1 h, the samples were not rinsed with deionised water but residual solution was aspirated. For the Raman experiments, the silicon wafers were cut into pieces of approximately $1 \times 1\,\mathrm{cm}^2$. The substrates were fully covered with solution for the collagen hydrogels and then stored in the incubator for 2 to 4 h. As for the collagen hydrogels on the glass slides, residual solution was aspirated. Until further use, the samples were stored in the fridge.

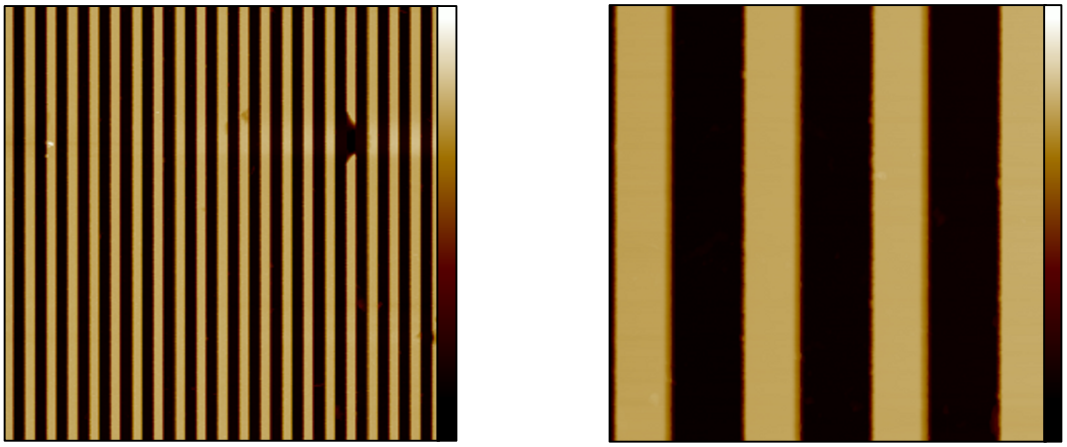

a b

Figure 3.1.: AFM height images of the TGZ-500 calibration grid with a scan size of (a) $60 \times 60\,\mu m^2$ and (b) $10 \times 10\,\mu m^2$ obtained in tapping mode with a ZEIHR cantilever (cf. Table 3.1). The calibration grid is shown after cleaning. Colour bar: 400 to 500 nm. Scan size: (a) $60 \times 60\,\mu m^2$ and (b) $10 \times 10\,\mu m^2$.

3.2.3 Freely suspended collagen fibrils

For the investigation of freely suspended single collagen fibrils, the TGZ-500 calibration grating was used as a substrate (Figure 3.1). The grating is a silicon wafer with periodically arranged rectangular SiO_2 steps on top, covered by a 10 nm thick Si_3N_4 layer. It was mounted on a metal plate. With a nominal step height of 490 to 520 nm and a pitch of 3 µm, an active area of $3 \times 3\,mm^2$ is provided on the substrate. According to the synthesis described in Section 3.2.1, a solution for single collagen fibrils was prepared. After gently mixing the single components in a reaction vessel, the solution was placed in the incubator promoting the polymerisation of collagen fibrils. Within 10 min in which the solution was kept at 37 °C, white streaks formed that were placed on the calibration grating and stored in the incubator for another 50 min. Residual solution was aspirated and the sample was stored in the fridge until further use. For the cleaning of the calibration grating after use, it was placed in 10xPBS for 2 h, rubbed with a tissue soaked in acetone, and put in the ultrasonic bath with methylated spirit before being dried with nitrogen.

3.2.4 Samples for Surface Enhanced Raman Spectroscopy

For the investigation of separated collagen fibrils with Raman spectroscopy, silver was used to amplify the Raman signal. Two ways were tested for the incorporation of the silver: the application of substrates coated with silver and the addition of silver nanoparticles ($\varnothing = 20$ nm, $0.02\,mg \cdot ml^{-1}$) to the collagen solution. In the first case, the glass substrates were replaced by the silver substrates and the sample separation followed the

protocol established in Section 3.2.1. In the latter case, 50 µl of the silver nanoparticles were added to the collagen solution (cf. Section 3.2.1) that, deviating from the established protocol, had 200 µl of collagen instead of 100 µl. The silver nanoparticles were added last and before the solution was placed in the incubator, the reaction vessel was mixed for 2 min at 400 rpm with the thermomixer. The subsequent procedure followed the established protocol (cf. Section 3.2.1).

All measurements took place in the fully hydrated state of the samples. The state of hydration has an impact on the mechanics of the collagen samples and slight variations change these.[85,279–282] Working in a partially hydrated state would introduce an uncertainty about the actual state of hydration of every individual sample and, therefore, affect the results on the measured mechanics.

All AFM experiments required a calibration of the cantilever which was done before the actual measurement. The InvOLS was measured by performing three to five deflection versus piezo displacement curves on a sapphire sample followed by the estimation of the force constant by the thermal noise method.[171] In case of a required tip estimation, the tip was scanned over the calibration sample RS-15M and from the obtained image the radius was estimated with the help of the provided tip characterisation function. The synchronisation distance was calibrated on the sapphire sample for the applied measurement frequency. For quantitative measurements of the indentation modulus without estimation of the tip radius, a polydimethylsiloxane (PDMS) sample with a defined indentation modulus of 2.5 MPa was applied additionally. The PDMS sample was scanned and the peak force was increased until an indentation value was reached that was expected for the measurement of the collagen fibrils. Following, the radius of the tip was adjusted to achieve a measured indentation modulus of 2.5 MPa. The calibration took place in the respective environment of the subsequent measurement.

The atomic force microscope was primarily used for the measurement of the modulus of single surface-supported collagen fibrils under the influence of external stimuli in varying liquid environments. The applied mode was the PFQNM tapping mode. Preliminarily, adequate parameters for the measurements had to be evaluated. Starting with experiments performed at ambient conditions, the correct site on a single collagen fibril for the extraction of the modulus was investigated, including the influence of the measurement angle. Going to experiments in a liquid environment, the set point, that was the peak force, was optimised including a consideration of the measured height with varied peak force. After establishing the measurement parameters, the gained values were compared to the literature and an evaluation of the measurement error was done. For the PFQNM AFM measurements, ScanAsyst Fluid cantilever (cf. Table 3.1) were applied and the peak force was kept below 1.5 nN. The frequency was 1 kHz with a Scan rate of 0.5 Hz and a scan size between $1\,\mathrm{x}\,1\,\mu m^2$ and $2\,\mathrm{x}\,2\,\mu m^2$. The experiments should provide a high comparability between the untreated and the treated state (after exposure to UV light or/and elevated temperatures) of the sample. Measuring separated fibrils for the evaluation of both states opens the possibility of introducing uncertainties derived from, *e.g.*, different geometries or number of defects. Thus, the very same fibril was monitored throughout one experiment. The setup is depicted in Figure 3.2. For evaluating the development of the modulus with ongoing exposure, the experiments were performed *in situ* meaning that the measurement of the sample took place while treating it. By that, time-resolved information could be gathered. The samples were irradiated with UV light or/and heated in a liquid environment. Both UV light source and kind of liquid were varied. UV light with a wavelength of 364 nm (UVA), 312 nm (UVB), and 254 nm (UVC) was used for the experiments. The UV-Vis spectra of the UV light sources are displayed in Figure A.1, Figure A.2, and Figure A.3, respectively. During the experiment, the UV

lamps were placed next to the sample so that it was irradiated from the side at a distance of 5 cm. The resulting intensities experienced by the sample were 0.7 mW·cm^{-2}, 0.4 mW·cm^{-2}, and 0.5 mW·cm^{-2} for the UVA, UVB, and UVC lamp, respectively. For heating the samples, a Peltier device was placed under the substrate and connected to it with conductive silver paste. Temperatures were varied between 35 °C and 45 °C. For creating the liquid environment, the AFM cantilever was immersed in approximately 200 µl of the respective fluid.

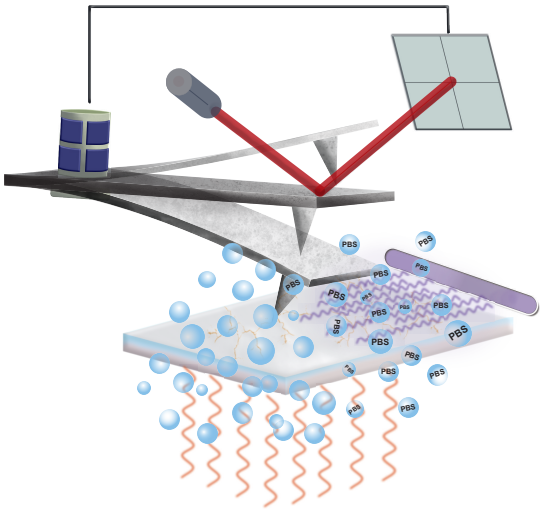

Figure 3.2.: Schematic AFM setup for PFQNM tapping mode experiments. The collagen fibrils were spread on a glass substrate and continuously measured by PFQNM tapping mode. Simultaneously, the sample could be irradiated with UV light from the side or/and heated from beneath. All measurements took place in a liquid environment that was either deionised water or a PBS-based solution. The figure was published in the *Journal of the Mechanical Behavior of Biomedical Materials*, ***88***, *415-421 (2018)*.[284]

The modulus acquired by PFQNM AFM measurements was calculated according to the DMT model or the Sneddon model and will therefore be referred to as DMT modulus or Sneddon modulus (cf. Section 2.2.3.1). As Poisson ratio, a value of 0.5 was applied.[205] All experiments were conducted in a liquid environment. Apart from the thereby controlled state of hydration, the formation of a water meniscus between tip and sample was excluded.

First experiments were used to monitor the development of the modulus over time without any external stimulus. By that, later recorded differing effects during experiments with treatment could be assigned to the treatment. Following up, a reasonable time for a measurement had to be evaluated.

For every measurement, a new sample with single surface supported collagen fibrils was synthesised. After choosing a sample spot, this spot was imaged up to three times for gaining the modulus in the untreated state. The influence of an elevated temperature was investigated by exposing samples to 35, 37, 42, or 45 °C. For each temperature, samples were either immersed in deionised water, 1xPBS, or 10xPBS for at least 60 min, resulting into twelve different treatment conditions. Additionally, samples were immersed in deionised water and exposed

to 45 °C and subsequently immersed in 1xPBS and, again, exposed to 45 °C. Regarding the application of UV light, samples were exposed to either UVA, UVB, or UVC light at room temperature for at least 60 min. For each UV light source, samples were immersed in deionised water or 1xPBS, resulting into six different treatment conditions. Additionally, elevated temperatures and exposure to UV light was combined. Collagen samples were heated to 45 °C, immersed in 1xPBS, and exposed to UVA or UVB light. Every combination was applied for at least two collagen fibrils. The gained results were displayed as changes in percentage with respect to the averaged value of the modulus in the untreated state. This kind of representation was chosen to provide a higher comparability between the samples because of an examination without regarding the varying initial moduli of the fibrils.

For the presented tensile tests, the sample was prepared as described in Section 3.2.3, resulting in freely suspended collagen fibrils. The sample was immersed in deionised water or 1xPBS and irradiated with UVA, UVB, or UVC light, resulting into six different measurement conditions. Data were acquired for 60 min at room temperature. The UV-Vis-spectra of the UV light sources are displayed in Figure A.1 (UVA), Figure A.2 (UVB), and Figure A.3 (UVC) and the resulting intensities experienced by the sample were 0.7 $mW \cdot cm^{-2}$, 0.4 $mW \cdot cm^{-2}$, and 0.5 $mW \cdot cm^{-2}$ for the UVA, UVB, and UVC lamp, respectively. With a calibrated B300-cantilever (cf. Table 3.1), AFM-supported static deflection versus piezo displacement curves were obtained by vertically bending the fibril in its very middle. The approach- and retract-velocity were 1 $\mu m \cdot s^{-1}$ and the maximal applied force was kept below 6 nN. Static deflection versus piezo displacement curves on the freely suspended collagen fibril were recorded before exposure to UV light and simultaneously to it in 5 min steps to obtain the time-dependent tensile modulus. For each measurement the region of interest (ROI) in the middle of the fibril and a point on the substrate were chosen on which the probe rested. By that, a signal coming from fibril bending and a signal from the stiff substrate could be compared to ensure that the sample has not shifted due to drift. Furthermore, the probe was moved away from the ROI to avoid any further interactions than the intended deflection versus piezo displacement curves.

A model was developed that described the extraction of the elongation during the fibril bending for the estimation of the axial tensile modulus. The calculation took place based on a homemade Python (programming language) script that required probe radius, suspended length of the fibril, fibril diameter, and sensitivity and force constant of the cantilever as input parameters, apart from the acquired deflection versus piezo displacement signal. The probe radius was provided by the manufacturer, the suspended length of the fibril was taken from the AFM images, and the diameter of the fibril was obtained from a deconvolution of the tip size with the AFM image of the fibril applying the open source software Gwyddion.[283] In the script, the deflection was converted to a force by the multiplication with the sensitivity of the cantilever and its force constant. The vertical displacement of the fibril during bending was calculated by subtracting the piezo displacement from the deflection signal. An indentation into the fibril was neglected. The resulting force versus fibril displacement curve was converted into a stress versus strain curve. For this conversion, the applied force in the axial direction of the fibril, as well as its axial elongation, were necessary. The acquisition of both quantities was explained by a model that was based on geometrical considerations and is explained in detail in Section 4.2. From the linear region of the stress versus strain curves, the modulus was extracted that reflects the resistance of the collagen fibril towards axial tensile load. The experimental results were compared to finite element analysis (FEA)-based findings.

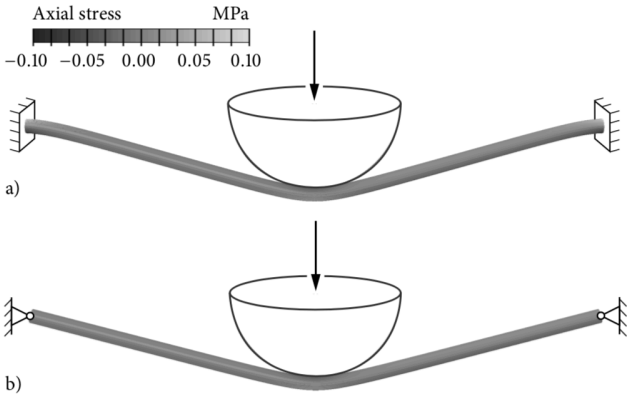

Figure 3.3.: Finite element (FE) models of fibrils with a) fixed and b) simply supported ends. Fibrils of diameters $d_0 = 50\,\text{nm}$ and suspended lengths $l_0 = 2000\,\text{nm}$ were deflected by $\delta = 280\,\text{nm}$ by a rigid indenter of radius $r = 300\,\text{nm}$. Stresses were calculated using a Young's modulus of $E = 1\,\text{N}{\cdot}\text{nm}^{-2}$. Image was provided by courtesy of Philipp L. Rosendahl.

3.4.1 Finite element model

The validation of the applied model was done by employing a finite element representation of the test setup. To model the fibril, shear-deformable beam elements with circular cross section and quadratic shape functions were applied with material properties that were assumed to be linear elastic. The Young's modulus and the Poisson's ratio were set to be $E = 1\,\text{N}{\cdot}\text{nm}^{-2}$ and $\nu = 0.5$, respectively. For the suspension of the fibril, either fixed or simply supported ends were chosen to establish limit cases for the boundary conditions (cf. Figure 3.3). While the fixed ends represent rigid bars to which the fibrils were attached, the assumption of simply supported ends implies a vanishing bending stiffness of the fibril in the vicinity of the bars. In comparison to the fibril, the Young's modulus of the indenter tip was at least one order of magnitude higher, which is why it was modelled rigid. Due to the compliancy of the fibril in transverse direction, the deformation of the indenter was assumed negligible just as the contact between both was assumed frictionless. The deflection of the fibril was determined by the vertical displacement of the indenter, finite deformations and geometric nonlinearity were accounted for, and the fibril was discretised using 2000 elements in axial direction.

The Raman microscope was equipped with a Nd:YAG-Laser with a wavelength of 532 nm and an electron multiplying charge-coupled device (EMCCD) camera. A silicon sample was used for the calibration of the detector. For the Raman spectroscopy of the collagen hydrogels, the samples (cf. Section 3.2.2) were fixed in a quartz glass cuvette, to avoid any movement during the measurement, and a 20x/0.4 Nikon objective was used in the microscope. The cuvette was fully filled with the respective liquid already 1 h before the measurement and it was fixed to the stage of the Raman microscope to keep its position steady. The irradiation of the samples did not take place simultaneously to the measurement, as it has been the case for the AFM measurements (cf. Section 3.3), but alternately. During the irradiation, the head of the microscope needed to be moved upwards to make space for the UV lamp to be positioned above the collagen sample. After irradiation, the microscope head was repositioned. This measurement process was repeated for every irradiation step. Raman spectra were obtained for the untreated state and after every irradiation cycle. In general, the samples were irradiated four times for 15 min each. Measurement parameters such as Laser power, measurement time, and number of accumulations, as well as impact of the Laser power on the collagen sample and influence of the measurement process on the resulting Raman signal, were evaluated. The settings of the measurement were systematically approximated with starting values for the Laser power of 5 and 15 mW, for the measurement time of 30 and 90 s, and for the number of accumulations of 10 and 30. Part of this process was to ensure that the sample was not damaged by the Laser itself. To ensure that, the same spot of the sample was consecutively irradiated with the Laser and spectra were taken before and after 30 and 60 min of irradiation. Eventually, the collagen hydrogels were measured with a Laser power of 10 mW and the Raman spectra were generated from 10 accumulations of 70 sec each. A further possible introduction of errors was the repositioning of the microscope head after the UV irradiation of the samples. Thus, the repositioning was performed without the irradiation and the two resulting Raman spectra were evaluated.

For the SERS measurements of the separated collagen fibrils, an immersion 60x/1.0 Nikon objective was applied and the sample was measured without the cuvette but still fully hydrated. The Laser power was reduced to 1 mW. The measurement process stayed the same with irradiation intervals of 15 min, the positioning of the UV lamp on top of the sample, and a repositioning of the microscope head.

The UVA and UVC light sources were the same as they were for the AFM-based experiments. The UV-Vis-spectra of the UV light sources are displayed in Figure A.1 (UVA) and Figure A.3 (UVC) and the resulting intensities experienced by the sample were 5.2 $mW \cdot cm^{-2}$ and 12 $mW \cdot cm^{-2}$ for the UVA and UVC lamp, respectively. All spectra were treated in the same way with the Project FOUR 4.1 software. After a subtraction of the background, the spectra were normalised with respect to the Si-peak (520 cm^{-1}). The spectra of the untreated

state, 15 min, 30 min, 45 min, and 60 min of irradiation were compared and highlighted for three Raman shift regions: amide region, C–H region, and O–H region.

The general principle of the patterning of collagen hydrogels with UV light is depicted in Figure 3.4. A grid was placed between sample and light source to imprint a UV light pattern on the collagen. The setup was immersed in a liquid environment. The applied combination of UV light source and liquid environment were either UVA and deionised water or UVC and 1xPBS.

For the first attempts (proof of principle) a transmission electron microscopy (TEM) grid was applied on collagen fibrils attached to a glass substrate. The evaluation of the experiment was performed with AFM, which required small periods of the grid to generate a size of UV light exposed and unexposed areas on the sample that could be captured with this method (*e.g.* $< 90\,\mu m$). The applied TEM grids had a 600 mesh. For the patterning of collagen hydrogels, the grid dimensions had to fulfil the same requirement when the treatment was evaluated by AFM. The application of biological cells, however, asked for bigger grid periods so that several cells could fit in the created exposed or unexposed areas. To control the design of the applied structure, the grid and the corresponding sample holder were 3D printed. The 3D printer operated in the bat configuration, applying a UV light lamp as curing source from beneath with a pixel size of $27\,\mu m$. During post-treatment, the printed parts were cleaned in isopropanol and fully cured in a UV light chamber. The resin was provided by the manufacturer. The designs were modelled with AutoCAD. The finalised device was used to irradiate collagen hydrogels that, after exposure, were investigated with AFM to identify exposure-induced variations in the indentation modulus or were used as substrate for the attachment of biological cells to investigate the adhesion behaviour in dependence on the exposure conditions. The dimensions of the grid varied depending on this distinction of the type of experiment. As UV light source for the irradiation of the samples, either the UV lamps were used that have been applied throughout the AFM and Raman spectroscopy measurements, or the Axio Imager.M2m light microscope equipped with a mercury lamp was applied. For the latter, a bandpass filter with a bandwidth of 10 nm was added (365 nm) to single out UVA light from the mercury lamp. The filter was mounted on top of the grid. As alternative for a grid, a quartz glass-based photomask from a Mask Aligner was used.

The light intensity experienced by the sample was measured by placing the respective grid between light source and liquid-covered sensor, adjusting the distances that occurred during the experiments. In the case of a printed part without voids, the light intensity reaching the sensor decreased to zero. Applying the grid that was used for samples subsequently measured by AFM, the sensor showed a light intensity of $0.05\,mW{\cdot}cm^{-2}$, $0.05\,mW{\cdot}cm^{-2}$, and $0.02\,mW{\cdot}cm^{-2}$ for the UVA, UVB, and UVC lamp, respectively.[iv] For the application of the Axio Imager.M2m as UVA light source, the light intensity behind the photomask was $3.6\,mW{\cdot}cm^{-2}$. In the case

[iv] It has to be kept in mind that these values average the intensity over irradiated and non-irradiated areas.

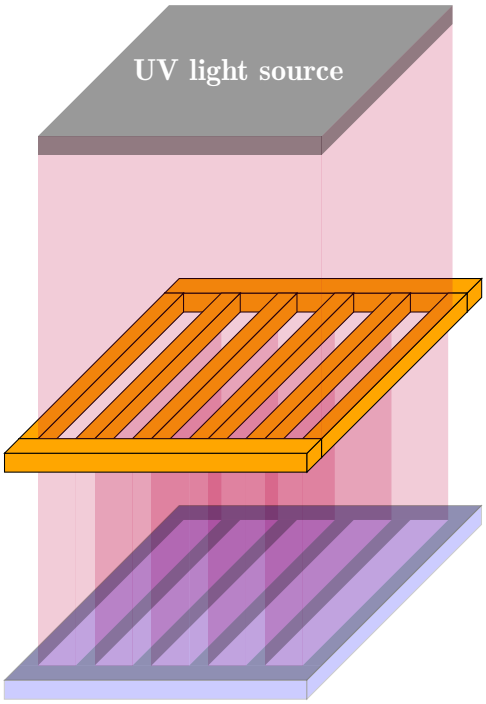

Figure 3.4.: Scheme of the setup that was used for imprinting a pattern on a collagen hydrogel due to UV light exposure. From top to bottom, a UV light source emits light that shines through a grid resulting into exposed and unexposed regions on the sample.

of the grid that was applied for subsequent cell spreading, these values were 0.7 $mW \cdot cm^{-2}$, 1.1 $mW \cdot cm^{-2}$, and 2.7 $mW \cdot cm^{-2}$ for the UVA, UVB, and UVC lamp, respectively. For the application of the Axio Imager.M2m as UVA light source, the light intensity behind the printed grid was measured to be 1.8 $mW \cdot cm^{-2}$.

For the AFM measurements, the samples were treated with the combination of UVA light and deionised water or with the combination of UVB or UVC light and 1xPBS. MLCT-BIO-D and XNC12-A (cf. Table 3.1) cantilever were used during PFQNM AFM measurements with an applied peak force between 0.2 and 2 nN. Scan speed was kept between 0.1 and 0.3 Hz with a peak force amplitude of 300 nm and a peak force frequency of either 125 or 250 Hz. Due to the softness of the samples, the engage step was crucial and required a low engage set point (usually < 1 nN), as well as an avoidance of the fast engage movement. Calibration was done as described in Section 3.3. After exposure of the collagen hydrogels to UV light, AFM was used to monitor whether regions of increased/decreased DMT modulus could be found on the samples, whose dimensions agree with the pattern of the applied grid.

For the experiments with biological cells, the main part of the experiments was done with CV-1 in Origin and carrying the SV40 genes (COS)-7 cells that are fibroblast-like cells from an African green monkey. As culture

medium for the COS-7 cells DMEM[v] supplemented with 10 % fetal bovine serum (FBS) and 1 % penicillin-streptomycin was applied. The culture medium was exchanged every 2 to 3 days, including a rinsing of the adherent cells with PBS. The cells were stored in a humidified incubator with a CO_2 content of 5 % at 37 °C. Before the cells could be placed on a substrate for a subsequent experiment, they had to be detached from the bottom of the cell flask using 1.5 ml of accutase solution. The detached cells were placed on a beforehand UV light exposed collagen hydrogel with a slight amount of culture medium. To avoid the flushing of the cells from the hydrogel during the addition of extra culture medium, the cells were given some hours to attach to the hydrogel before the sample was gently and fully covered. After the attachment of the cells on the UV exposed hydrogels, the samples were recorded by light microscopy images over days. It was investigated whether the UV light exposure created regions in which cell attachment occurred preferentially and whether spreading and growth behaviour were influenced.

[v] Containing L-glutamine, Na-pyruvate, and non-essential amino acid solution (NEAA).

4 Results and discussion

4.1 Indentation modulus of physically treated single collagen fibrils[vi]

4.1.1 Discussion of experimental parameters

AFM on collagen fibrils spread on a stiff substrate resulted in images presenting structures of ordinarily 10 to 20 nm in height, 50 to 300 nm in width, and several micrometres in length (cf. Figure 4.1). The fibrils were individually scattered all over the surface with casual contact points between adjacent structures. The most prominent feature about the collagen fibrils was the periodically alternating height in their axial direction that is the D-band pattern. The periodicity of 65 to 70 nm could be evaluated by AFM. The stiff glass substrate, in comparison, appeared smooth and thus the collagen fibrils were conveniently highlighted. During AFM measurements, a movement of the collagen fibrils was not detected, which proofed a strong adherence of the collagen structures to the glass. A side effect of the strongly attached fibrils might have been their non-circular cross section, which showed a width that can be up to twenty times higher than their height. Surface tensions of the substrate might have acted on these small structures and, thereby, caused this deviation. Merely imaging of collagen fibrils was accomplished with ZEIHR-cantilever possessing a nominal force constant of 28 $N \cdot m^{-1}$ (cf. Table 3.1). The further measurements, however, aimed for the evaluation of mechanical properties of the samples and were conducted in a liquid environment. Cantilever and measurement parameters had to be adjusted according to the requirements of the experiments which resulted in the following preliminary work.

4.1.1.1 Estimation of measurement uncertainties

AFM-based nanomechanical mapping has to deal with several influences, introducing uncertainties into the final results. Beginning with the calibration procedure, an overall error is assumed to be in the range from 20[31] to 39 %[285] regarding the eventually measured quantity. While the estimation of the InvOLS goes along with an uncertainty of only 2 %,[286] the estimation of the tip radius causes the biggest deviations. Wenger *et*

[vi] For the most part, the results presented in Chapter 4.1 are published in the *Journal of Mechanical Behaviour of Biomaterials*.[284] Special thanks go to Melanie Rogge who supported the PFQNM AFM measurements on UV exposed collagen fibrils as a student assistant.

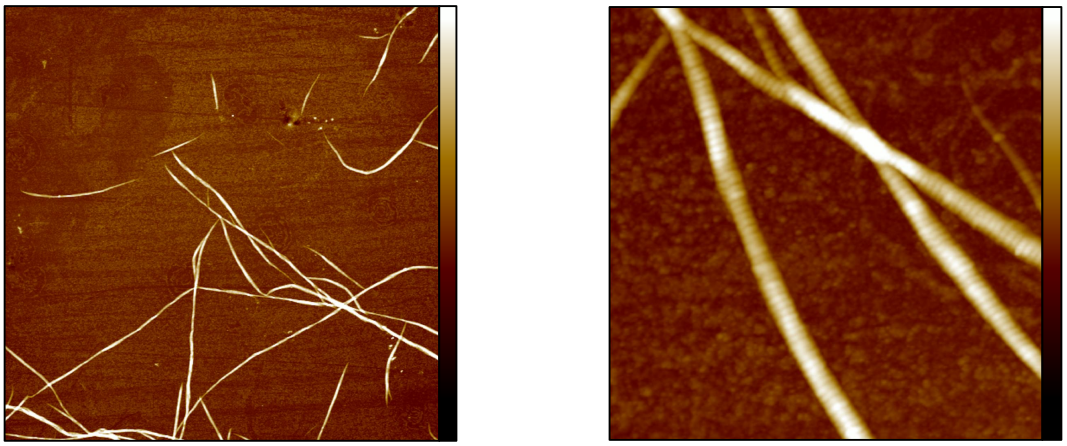

a b

Figure 4.1.: AFM height images of collagen fibrils on a glass substrate obtained in tapping mode showing (a) the distribution of fibrils on the substrate and (b) the D-band pattern in a more detailed image. Measurements were done in air with a ZEIHR cantilever (cf. Table 3.1). Colour bar: -30 to 30 nm. Scan size: (a) $30 \times 30\,\mu m^2$ and (b) $4 \times 4\,\mu m^2$.

al.[31] state that the uncertainties regarding the contact area (cf. Section 4.1.1.2) contribute with 30 %. For the actual recording of the mechanical properties, consecutive measurements of the same ROI on a collagen fibril delivered a deviation of the extracted DMT modulus below 10 %.[vii]

4.1.1.2 PFQNM measurements in air

In contrast to AFM imaging, the measurement of nanomechanical properties needs further consideration regarding the procedure.

First of all, the choice of the peak force has to be discussed. The exerted peak force is decisively responsible for the resulting indentation. According to the 'Bueckle rule',[287] the indentation depth of the probe, during the examination of mechanical properties, may not exceed 10 % of the sample height. Otherwise, the stiffness of the underlying substrate contributes to the measured modulus and, thereby, falsifies the result. Furthermore, plastic deformation of the sample is possible[288] and, thus, has to be avoided. For the air-dried collagen fibrils, the indentation followed the limit of 10 % for the indentation depth for peak forces up to 15 nN, which eased their investigation. Thus, a modulus could be extracted.

For the calculation of the indentation modulus the AFM software offers two contact models: DMT and Sneddon. While the Sneddon model is often preferred for soft samples (*e.g.* biological samples), one requirement for

[vii] These measurements were performed after completing the preparatory measurements described in Section 4.1.1.2 and Section 4.1.1.3.

its application is a sufficient indentation that is said to be beyond 30 nm. The single collagen fibrils, however, did not allow for such an indentation. Thus, the contact area can hardly be modelled by a conical indenter rather than by a spherical. In succession to the small possible indentation depth, the DMT contact model was applied for the evaluation of the indentation experiments. However, the Sneddon modulus was recorded as well to perform a comparison between both (cf. Section B). Figure B.1, Figure B.2, and Figure B.3 show similar qualitative results for the DMT model and the Sneddon model with ongoing time of treatment. However, deviations in the quantitative results were obvious.

The small dimensions of a collagen fibril led to the question from where to extract the mechanical properties in a way that they were representative and reliable. To analyse that, the DMT modulus was measured and averaged over a distance of 300 nm parallel to the axis of the fibril. Two sites (labeled A and B in Figure 4.2) of an air-dried fibril were evaluated and the DMT modulus was analysed at the apex of the fibril and on its respective edges. Additionally, the scanning angle of the AFM image was varied in 45 °-steps (between 0 ° and 360 °) to test possible influences on the resulting DMT modulus. A dependency on the scanning angle was not detected, which allowed the evaluation of fibrils independent of their orientation. For all analysed orientations, the modulus at the apex of the fibril was higher than the values obtained at the edges, as shown in Table 4.1. The difference of the DMT moduli obtained from the apex of the fibril at the two positions was small in comparison to the differences obtained at the same edge of both positions. A reason for the deviation was the effective contact area between the AFM tip and the sample. For the measurements at the apex of the fibril, the AFM tip got in contact with the fibril evenly. For the measurement points on its edge, however, the tip did not indent evenly into the collagen fibril but exhibited an asymmetrical contact due to the shape of the sample. Consequently, the values underlay fluctuations and the reliability was questionable since the applied contact mechanism model requires an even contact area. Internal stresses[230] caused by surface tensions were a further source for deviations between different measurement positions. As a result, the DMT modulus was evaluated along the apex of the single collagen fibrils, which offered the highest accuracy of the values. Additionally, this approach followed the procedure of Baldwin *et al.*[11] who took their data from an area ± 10 % around the apex of the collagen fibril. From a quantitative point of view, the presented values (Table 4.1) were in agreement with moduli published by Wenger *et al.*[31] who found an elastic modulus between 5 and 11.5 GPa for rat tail tendon.

4.1.1.3 PFQNM measurements in liquid

The immersion of collagen fibrils in a liquid environment establishes their fully hydrated state and, thus, is a reasonable action for their investigation since the state of hydration has a major impact on the mechanical properties. Its identification at ambient conditions introduces uncertainties that complicate the comparison of

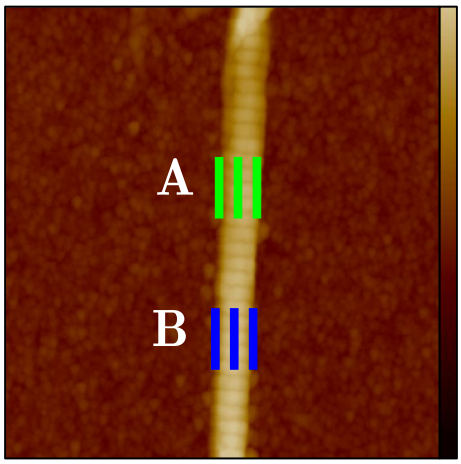

Figure 4.2.: AFM height image of a collagen fibril on a glass substrate obtained in PFQNM tapping mode in air showing the sites A (green) and B (blue) used for the evaluation of a suitable spot for data acquisition. For both sites, three lines are depicted from which cross sections were evaluated for the estimation of the fibril's DMT modulus. Two lines were positioned at the edges of the fibril and one along its apex. ZEIHR cantilever were applied (cf. Table 3.1). Colour bar: 0 to 40 nm. Scan size: $2.1 \times 2.1\ \mu m^2$.

Table 4.1.: Results for the measurement of the DMT modulus and its standard deviation at the evaluation sites A and B (cf. Figure 4.2). The sample was rotated stepwise by 45 ° and the depicted results were averaged over one full rotation.

DMT modulus (GPa) at the...	Site A	Site B
apex of the fibril	9.55 ± 1.90	9.83 ± 1.20
edge (1) of the fibril	6.06 ± 0.80	7.38 ± 1.60
edge (2) of the fibril	5.56 ± 2.30	7.71 ± 1.70

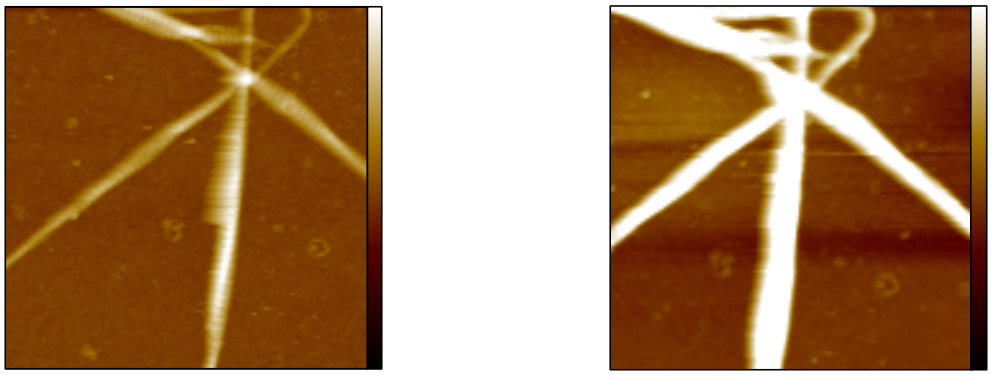

a b

Figure 4.3.: AFM height images of collagen fibrils that were (a) air-dried and (b) immersed in deionised water. Colour bar and measurement site are kept identical to emphasise the swelling of collagen fibrils of rat tail tendon according to the uptake of water. ScanAsyst Fluid cantilever were applied (cf. Table 3.1). Colour bar: -30 to 30 nm. Scan size: $7 \times 7\,\mu m^2$.

results between different measurements. Investigating all collagen samples in a fully hydrated state circumvents this issue and increases the comparability between independent measurements. A further advantage is that collagen in the body is rather in the fully hydrated state than partially or non-hydrated. Obtained results, thus, are more representative for real life conditions. During the immersion of the collagen fibrils in a liquid environment, a swelling was detected (cf. Figure 4.3) that has been described before.[289] The height increased from approximately 10 to 20 nm in the dry state to approximately 30 to 50 nm in the fully hydrated state (Figure 4.4), which led to a loss of the clear identification of the D-band pattern. This increase was in agreement with a report by Grant *et al.*[217] that states a two-fold swelling of the collagen when being immersed in buffer solution in comparison to air. The visual absence of the D-band pattern is supposed to originate from different swelling behaviours of the gap and the overlap region. As the gap regions are said to be softer, they swell stronger than the overlap regions[290] and, thereby, both may have reached a similar height in the end. The origin of the swelling is the osmotic pressure that leads to a water uptake described by the Donnan equilibrium and the least swelling occurs if the pH of the liquid is around the isoelectric point,[291–293] which for collagen is around pH 7. The swelling of the collagen with the visual vanishing of the D-band pattern occurred for measurements in a pH 7 buffer solution as well as for measurements in deionised water and PBS whose pH slightly deviate from the isoelectric point.

Furthermore, the modulus of collagen fibrils decreases when being immersed in a liquid,[238,294] which, from an experimental point of view, makes AFM measurements more delicate since the 'Bueckle rule' is violated more easily. Thus, a softer cantilever had to be chosen, which was done by the application of ScanAsyst Fluid cantilever with a nominal force constant of $0.2\,N \cdot m^{-1}$.

At first, a suitable peak force was identified. For that, several collagen fibrils immersed in deionised water were

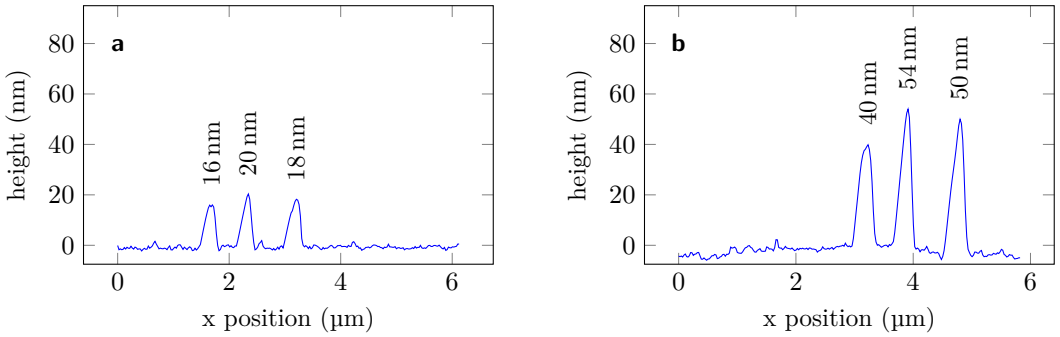

Figure 4.4.: Cross sections of collagen fibrils (a) in air and (b) immersed in deionised water taken from Figure 4.3a and Figure 4.3b, respectively.

sequently imaged while increasing the peak force from 0.5 nN to 15 nN and from 0.5 nN to 5 nN (Figure 4.5). The resulting DMT modulus, deformation, and measured height of the fibril were recorded. With increasing peak force, the resulting DMT modulus also increased. For peak forces above 2 nN in particular the DMT modulus started to distinctly deviate, which rendered comparisons between different fibrils valueless. Lowest deviations between the results were found for peak forces below 2 nN, suggesting that this value should not be exceeded during measurements. This regime was further narrowed by the evaluation of the fibril deformation for which the real height of the sample was estimated by addition of the deformation and the measured height (Figure 4.6). The deformation was increasing with the peak force while the measured height of the fibril was decreasing more rapidly resulting in a drop of the real height. Thus, the real height was systematically underestimated when the applied load was chosen too high. For every peak force, the resulting fraction of the deformation with respect to the real height is stated next to the respective bar, showing that only for peak forces below 1.5 nN could the results be considered reliable. Consequently, the maximum force applied was kept between 0.5 and 1 nN for the following experiments.
It can also be confirmed that the DMT modulus for collagen fibrils immersed in a liquid environment was up to three orders of magnitude smaller (1 to 10 MPa) in comparison to the collagen fibrils measured at ambient conditions (1 to 10 GPa).

A further quantity that influenced the value of the DMT modulus was found in the internal fitting procedure of the PFQNM mode. The synchronisation (synch) distance is the time/distance between the start point of the extend-retract cycle and the point at which the peak force is reached. Thereby, it defines the part of the curve that is used for the fit. A chosen synch distance that is too long includes parts of the retract curve and, thus, results in an incorrect fit. Accordingly, a chosen synch distance that is too short does not contain all the necessary data points for the performance of a reliable fit. The length was defined during the calibration process on the sapphire sample. Due to continuous long-time experiments, drifts might have occurred that required an on-the-fly recalibration of the synch distance. While the glass substrate provided a suitable rigidity to perform

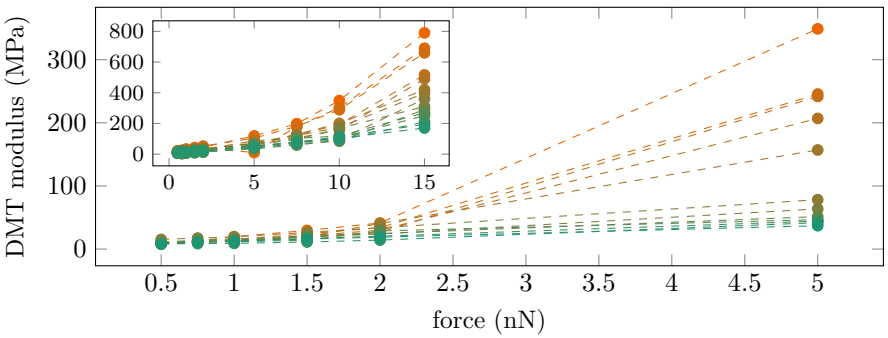

Figure 4.5.: PFQNM AFM measurements of various single collagen fibrils with successively increasing peak force. Every curve shows the development of the resulting DMT modulus for one fibril with a maximum applied force of 5 nN and 15 nN (inset).

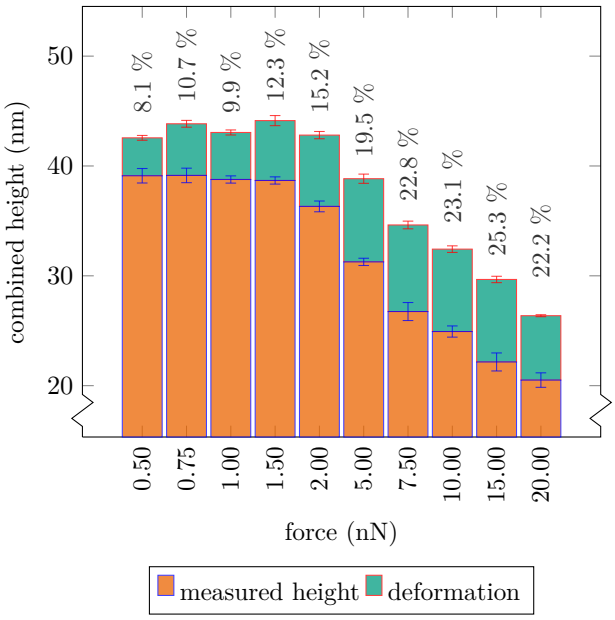

Figure 4.6.: Example of a PFQNM AFM measurement of a single collagen fibril with successively increasing peak force of up to 20 nN. The deformation (green) and the measured height (orange) were recorded and added as measure for the real height, which started to decrease for peak forces > 1.5 nN. The stated numbers depict the percentage of the deformation with respect to the combined height.

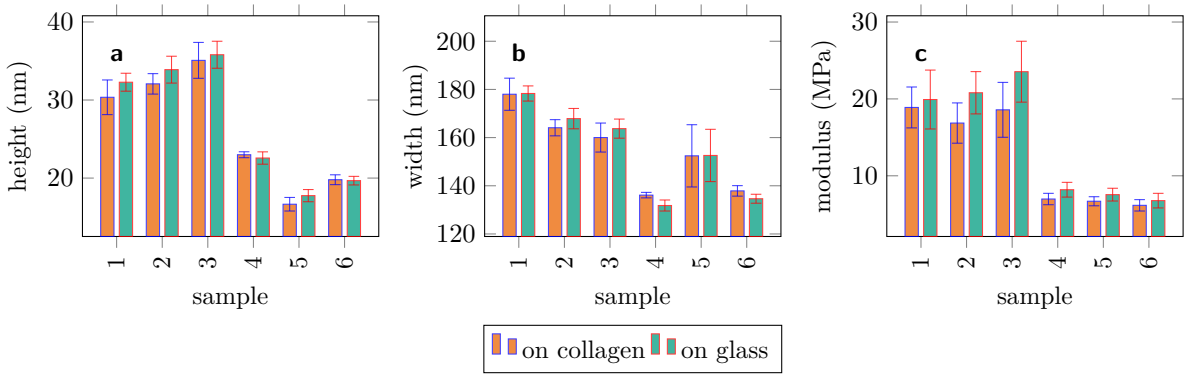

Figure 4.7.: Evaluation of the influence of the AutoConfig-function on the measured (a) height, (b) width, and (c) DMT modulus of six collagen fibrils in dependence on the underlying substrate stiffness. Higher values were recorded for the DMT modulus if the calibration took place on the stiff substrate (glass) in comparison to the soft substrate (collagen). For height and width, such a trend was not stated.

this recalibration, the soft collagen fibrils did not. Resulting differences dependent on the calibration of the synch distance on the glass substrate or on the collagen fibril are displayed in Figure 4.7 by means of fibril height, width, and modulus. Six collagen fibrils were measured twice in deionised water with the same peak force. Once, the calibration of the synch distance was performed on the glass substrate; the second time it took place on the softer collagen fibril. Figure 4.7a and Figure 4.7b show that only slight and random variations between the measured heights and width of the fibrils occurred, which were in the respective error bars. However, they were random and within the respective error bars. In contrast, the DMT modulus (Figure 4.7c) was systematically higher for all samples when the calibration was performed on the glass substrate and, in most cases, the values were also beyond the respective error bars. It can be concluded that, while the geometrical information of the collagen fibrils were not influenced by a variation of the calibration material for the synch distance, the modulus was lower when the softer substrate was applied. Thus, uncontrolled recalibration steps during the measurement have to be avoided.[viii]

For comparing several experiments regarding the DMT modulus, it has to be considered whether inherent properties of the collagen fibrils lead to different DMT moduli of separate but identically treated collagen fibrils. For example, internal defects and kinks may influence the mechanics of the sample. A controversially discussed topic is the influence of the size of a collagen fibril, particularly the cross section area. Heim *et al.*[288] state that fibrils with a diameter between 58 nm and 150 nm do not show a size-dependent radial indentation modulus. However, Wenger *et al.*[294] point out that, when talking about tensile properties, the elastic modulus always behaves inversely proportional to the cross section area. The present results tended to support the idea of a size-dependent DMT modulus (cf. Figure 4.7). The supposable size-dependence of the DMT modulus, as

[viii] Via the 'AutoConfig'-button, the software enables recalibration steps during a measurement.

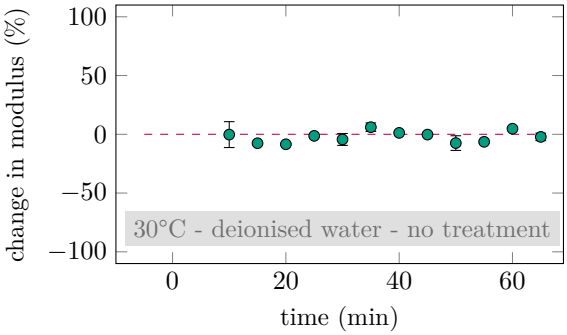

Figure 4.8.: Relative change of the DMT modulus with time of exposure for single surface supported collagen fibrils immersed in deionised water measured by PFQNM AFM. The sample was heated to 30 °C to account for possible heating of the liquid due to the UV lamp but no UV light was applied. Thus, the experiment was established as a reference measurement that showed no significant change of the DMT modulus with time of exposure. The horizontal line depicts the initial DMT modulus of the untreated sample.

well as the possible errors introduced by the calibration procedure (cf. Section 4.1.1.1), resulted in the decision to display the change in DMT modulus with performed treatment in relative terms to the untreated value. This should ease the comparison between separately performed experiments and emphasise the qualitative influence of the treatment on the mechanics of the collagen fibrils.

Since the measurements should display the impact of an external treatment on the evolution of the DMT modulus with time, it was necessary to show the results over time without any treatment. Thus, a collagen fibril was immersed in deionised water and PFQNM AFM measurements were performed for 65 min (Figure 4.8). No UV exposure was applied but the sample was measured at 30 °C to account for possible heating of the sample during application of UV light. Figure 4.8 will be referred to as a reference measurement and it exhibits the style in which most of the results in Section 4.1 will be presented. The change of the DMT modulus in percentage versus the time of treatment is shown. The measurement and the treatment are conducted simultaneously. That is why the measurements can be referred to as *in situ* experiments and the displayed time is the actual time of treatment. The dashed purple line is a guide for the eye and represents the initial DMT modulus in the untreated state. All changes that are given in percentage refer to this initial value. Displayed error bars represent standard deviations when several measurements of the same treatment conditions were averaged. For the reference graph (Figure 4.8), all data points were in close proximity to the initial value. The occurring deviations from that line provided a first idea of the accuracy of the measurements in general. Despite these deviations, the evolution of the DMT modulus did not show any change from the initial value, which showed that the measurement technique itself did not alter the mechanics of the collagen fibrils. Thus, every deviation from this behaviour was be considered as impact from the respectively performed treatment.

4.1.2 Thermal treatment of single collagen fibrils

DHT treatment is a known and applied approach to modify the mechanical properties with the supply of thermal energy. The treatment is conducted with temperatures above 100 °C and continues for several hours while the sample is kept under reduced pressure.[272,273] This time-consuming process is well-established but not very simple. A straightforward solution might be the exposition of the collagen sample to a liquid environment combined with a short heating treatment at moderate temperatures. A decrease of the Young's modulus during heat treatment of collagen fibrils in deionised water at temperatures between 50 and 62 °C has been reported,[11] as well as the increase of the elastic modulus by the addition of NaCl or KCl. Denaturation effects beyond 50 °C were also already discussed[295] leaving the question whether the application of lower temperatures result into similar changes. For the present study, collagen fibrils were immersed in deionised water or PBS-based solutions and heated up to 34, 37, 42, and 45 °C for 60 min. It shall be noted that for the measurements that involved thermal treatment, there were no data points for the first 10 to 15 min of treatment. During this period, the heating of the samples induced drifts of the cantilever that could result in tip or sample damage if the tip was engaged. Additionally, due to the drift, a relocation of the ROI might have been necessary, which also led to a loss of data points.

The experiments at the different temperatures did not deliver a distinct temperature dependency. However, the resulting behaviour of the collagen fibril during the thermal treatment depended on the applied kind of liquid environment. Therefore, the depicted results are an average from all applied temperatures with respect to the varied liquids, which resulted in three curves, as shown in Figure 4.9. While the heated collagen fibrils that were immersed in deionised water exhibited a decrease of the DMT modulus throughout the treatment time of 60 min, the samples immersed in PBS-based solutions suggested an increasing modulus within the first 40 min of treatment followed by a tendency of decreasing values. In comparison to the fibrils immersed in the 10xPBS/$NaHCO_3$, the fibrils immersed in 1xPBS exhibited an increased level of the modulus throughout the treatment time. The maximum value (40 min) and the modulus after 60 min of treatment, however, were similar. The results featured large errors, especially for Figure 4.9b and Figure 4.9c, that questioned the actual impact of the treatment. Figure 4.9 represents the results averaged over several experiments whose number is stated in the figure. While the single experiments agreed on the tendency the temperature treatment introduced - increasing DMT modulus for measurements in 1xPBS and 10xPBS and decreasing DMT modulus for measurements in deionised water - they very much differed in the extent of the changes and their temporal implementation. Figure 4.10 gives the results from four different single measurements confirming that statement. An exemplary trend for collagen fibrils immersed in 1xPBS is shown (Figure 4.10a), as well as the reproducibility for experiments conducted in deionised water with an example (Figure 4.10b) for strongly varying intensities. These results very much confirmed earlier findings that the thermal denaturation of col-

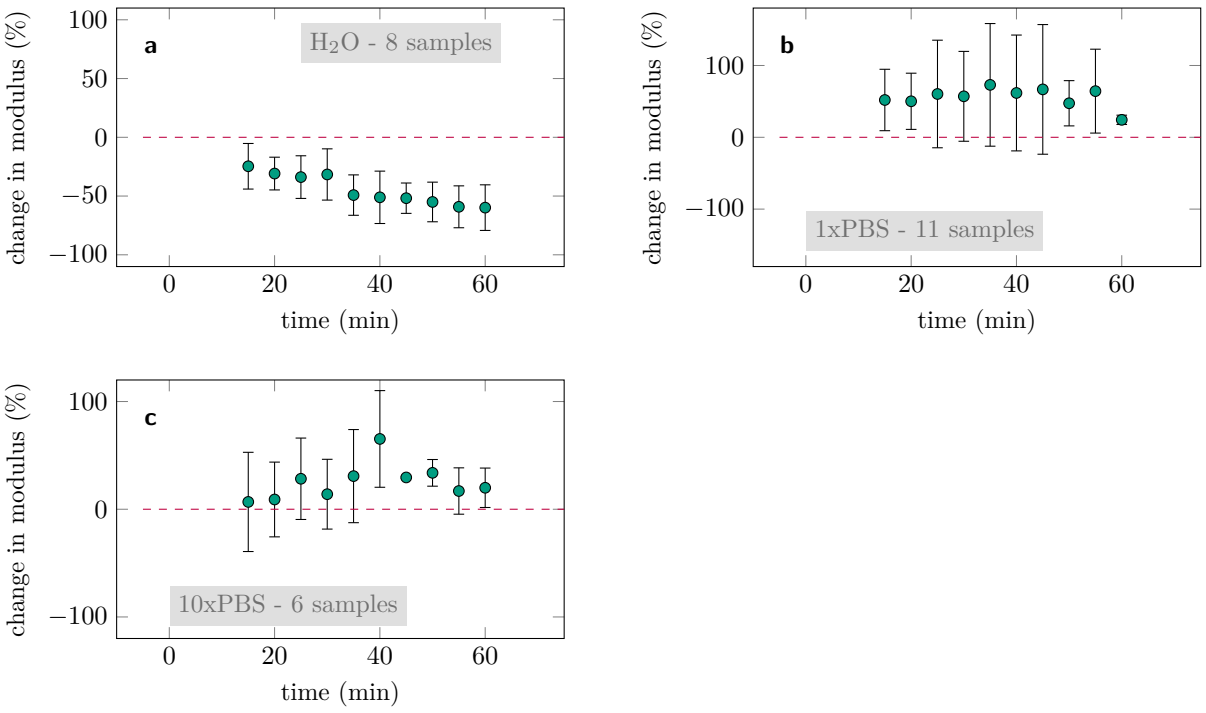

Figure 4.9.: Relative change of the DMT modulus with time of treatment for single surface supported collagen fibrils measured by PFQNM AFM. The data points show averaged results for 60 min of treatment at elevated temperatures (34, 37, 42, and 45 °C) of collagen fibrils immersed in (a) deionised water, (b) 1xPBS, and (c) 10xPBS. The horizontal line depicts the initial DMT modulus of the untreated sample.

lagen depends on the water content and pH of environmental medium. The dependence of the modulus on the liquid environment was also seen earlier.[217] A further important quantity that has to be considered is the degree of crosslinking[24,275,276,296,297] that was most likely the reason for the depicted change in modulus (cf. Section 4.1.5).

4.1.2.1 Thermal treatment with consecutively varied liquid environment

Figure 4.11 shows the change in modulus for a collagen fibril that was successively immersed in deionised water and 1xPBS at elevated temperature. First, a fibril was immersed in deionised water at 23 °C before being monitored for 60 min at 45 °C (section I). Subsequently, the fluid was changed to 1xPBS. After recording three images at 23 °C (section II), the same fibril was monitored for 60 min at 45 °C (section III) in deionised water again. The change in DMT modulus in section I corresponded to the behaviour that was already seen in Figure 4.9a. The drop in DMT modulus that could be seen between section I and section II could most likely be dedicated to thermal impact on the fibril of the time in which the liquid was cooling down from 45 °C to 23 °C. Due to occurring drifts at non-stable temperature conditions, measurements of the modulus could not

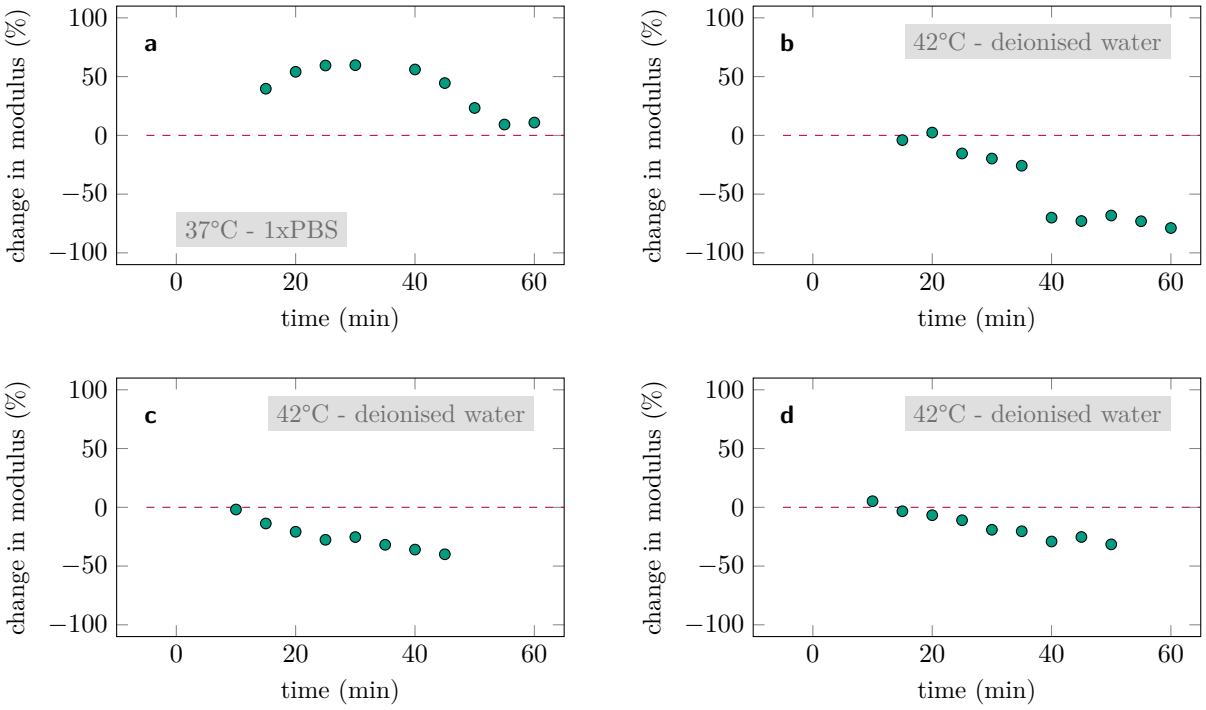

Figure 4.10.: Relative change of the DMT modulus with time of treatment for single surface supported collagen fibrils measured by PFQNM AFM. Four single experiments for 60 min of treatment at elevated temperatures ((a) 37 °C and (b,c,d) 42 °C) of collagen fibrils immersed in (a) 1xPBS and (b,c,d) deionised water were chosen. The horizontal line depicts the initial DMT modulus of the untreated sample.

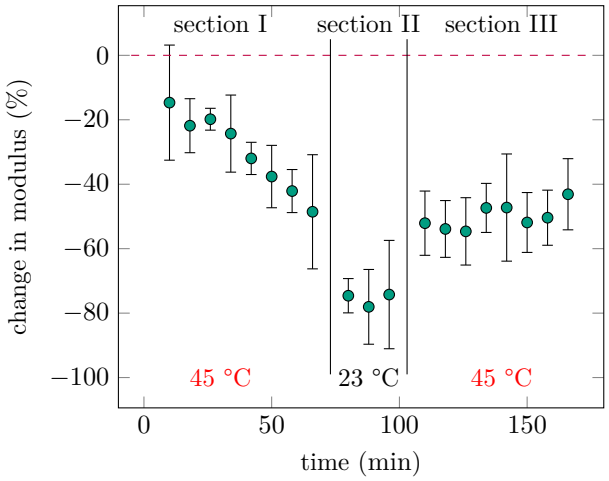

Figure 4.11.: Relative change of the DMT modulus with time of treatment for single surface supported collagen fibrils measured by PFQNM AFM. The fibrils were immersed in deionised water and measured at (section I) 45 °C for 60 min before the medium was changed to 1xPBS followed by an acquisition of three images at (section II) 23 °C and measurements (section III) at 45 °C for 60 min. The horizontal line depicts the initial DMT modulus of the untreated sample.

be performed, but the residual thermal energy was sufficient enough to promote the decrease of the modulus. In section II, the modulus was presented to be stable. The transition to section III went along with a jump towards a higher modulus followed by a slight further increase, including an indicated maximum after 30 min to 40 min of the section III treatment. This experiment did not only show a qualitative agreement with the results presented in Section 4.1.2 but also quantitative similarities were found. The decrease in modulus for fibrils immersed in deionised water was −60 % for the averaged results (cf. Figure 4.9a) and −49 % for the successive immersion in deionised water and PBS after 60 min of treatment (cf. Figure 4.11). The increase for the fibrils immersed in 1xPBS was 73 % for the averaged results (cf. Figure 4.9b) and 100 % for the successive immersion in deionised water and PBS after 60 min (cf. Figure 4.11).

4.1.3 Ultraviolet light exposure of single collagen fibrils

The irradiation of single surface-supported collagen fibrils were conducted similarly to the already described experiments at elevated temperatures. Simultaneously to the measurement, the samples were irradiated and combinations of deionised water or 1xPBS with UVA, UVB, or UVC light were applied.

In Figure 4.12 the impact of UV light on the DMT modulus of collagen fibrils is shown for single experiments. Like for the experiments at elevated temperatures, two different trends were emerging that were closely linked to the applied liquid environment. In PBS, an increasing DMT modulus with treatment time reaching a maximum value with a subsequent decrease was seen, which seemed to become characteristic (cf. Figure 4.12a,

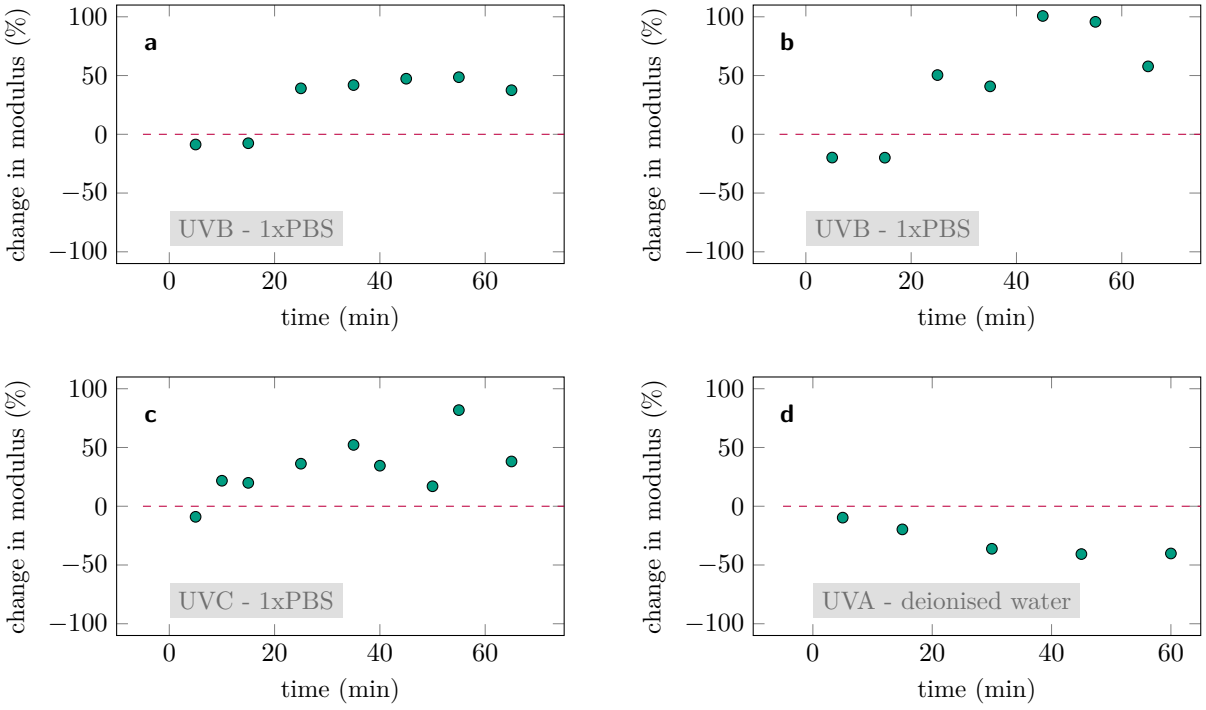

Figure 4.12.: Relative change of the DMT modulus with time of exposure for single surface supported collagen fibrils measured by PFQNM AFM. Four single experiments were chosen showing the impact of UV light for 60 min of exposure for following combinations of UV light source and liquid environment: (a) UVB and 1xPBS, (b) UVB and 1xPBS, (c) UVC and 1xPBS, and (d) UVA and deionised water. The horizontal line depicts the initial DMT modulus of the untreated sample.

Figure 4.12b, and Figure 4.12c). The second was a decreased DMT modulus for measurements performed in deionised water after 60 min of treatment (cf. Figure 4.12d). Figure 4.13 shows the combination of deionised water with UVA and UVB light for 160 min of exposure with averaged data points. The results for the application of UVC light are not displayed for a lack of reproducibility. The trend for the exposure to UVA and UVB light was in agreement with Figure 4.12d. It was found that the maximum change in DMT modulus was approximately −50 %. The error bars indicated that this behaviour was similar for most of the measurements. Figure 4.14 shows the combination of 1xPBS with UVA, UVB, and UVC light for 60 min of exposure with averaged data points. For the application of UVB and UVC light an elevation of the DMT modulus was reached with a maximum value obtained between 30 and 50 min for UVB and between 20 and 40 min for UVC. A subsequent decrease brought the DMT modulus back in the range of the initial value within the 60 min. For the application of UVA light, however, such a behaviour was not seen. Instead, the DMT modulus tended to reach a decreased level of approximately −20 %. The so far depicted results showed that the fluctuations in the results of the deionised water-based measurements are smaller than for the PBS-based measurements.

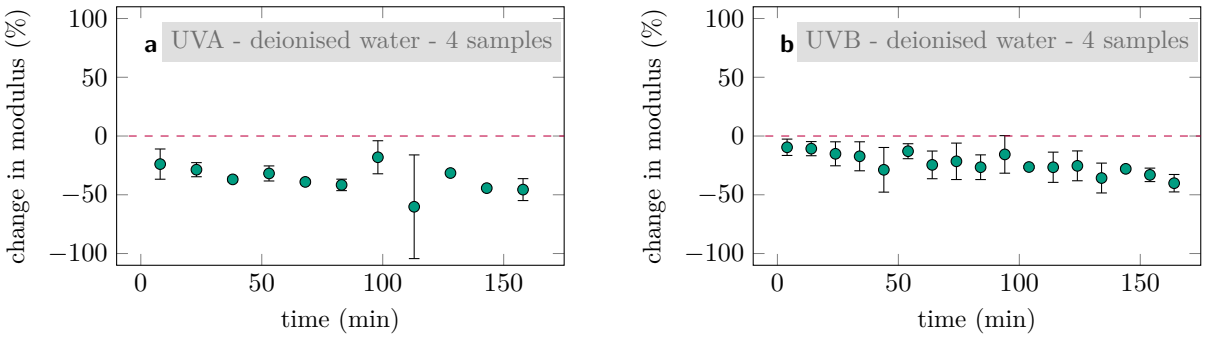

Figure 4.13.: Relative change of the DMT modulus with time of exposure for single surface supported collagen fibrils measured by PFQNM AFM. Every data point was averaged over the stated amount of samples for the irradiation of collagen fibrils immersed in deionised water with (a) UVA and (b) UVB light. The horizontal line depicts the initial DMT modulus of the untreated sample.

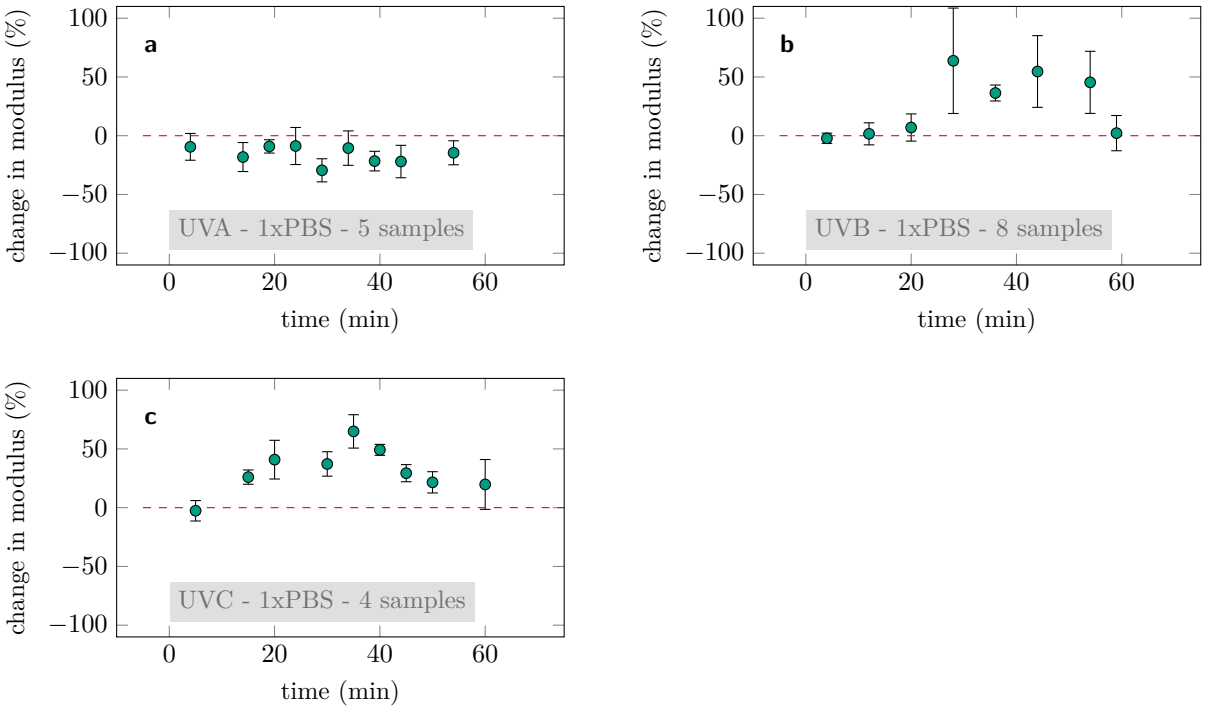

Figure 4.14.: Relative change of the DMT modulus with time of exposure for single surface supported collagen fibrils measured by PFQNM AFM. Every data point was averaged over the stated amount of samples for the irradiation of collagen fibrils immersed in 1xPBS with (a) UVA, (b) UVB, and (c) UVC light. The horizontal line depicts the initial DMT modulus of the untreated sample.

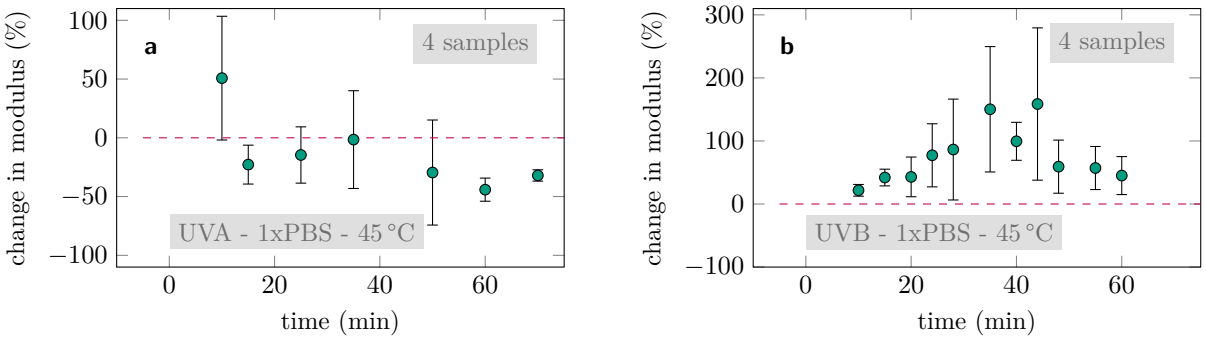

Figure 4.15.: Relative change of the DMT modulus with time of treatment for single surface supported collagen fibrils measured by PFQNM AFM. The fibrils were immersed in 1xPBS and exposed to (a) UVA and (b) UVB light while, at the same time, the temperature was adjusted to 45 °C. The horizontal line depicts the initial DMT modulus of the untreated sample.

4.1.4 Combined ultraviolet light exposure and thermal treatment

The results presented for the thermal treatment (cf. Section 4.1.2) and for the exposure to UV light (cf. Section 4.1.3) raised the question of whether a combination of both methods could amplify the effects. The approach of creating a synergetic effect by combining two methods under the application of their respective optimal parameters has been done before, for example by joining UV light and DHT treatment.[298] Combining UV exposure and thermal treatment, as presented here, might offer an easy and handy method for the modification of mechanics of collagen samples. Under the intention of increasing the DMT modulus, the sample was immersed in 1xPBS, exposed to UVB light, and heated to 45 °C. After the thermal equilibrium was reached the UV light was turned on. Using different UV light sources (UVA and UVB) should reveal whether the temperature or the UV light was the governing mechanism, since the exposure to UVA light resulted in a non-increased DMT modulus (cf. Figure 4.14a) in contrast to the application of UVB light (cf. Figure 4.14b). Figure 4.15a contains the results for the combination with UVA light and did not show an increase of the DMT modulus but rather exhibited a decreasing trend. From that point of view, the governing mechanism was the UV light since the DMT modulus-elevating character of the 45 °C could not be reproduced. The combination of 45 °C, 1xPBS, and UVB light, however, showed the expected increase of the DMT modulus, a maximum value between 30 and 50 min, and the subsequent decrease (Figure 4.15b). In fact, the found maximal value for the change in the DMT modulus was - taking the value for an exposure time of 40 min - 99 % and, thus, outmatched the 55 % of the averaged UVB irradiation experiments (cf. Figure 4.14b) as well as the 73 % of the averaged heating experiments (cf. Figure 4.9b). Regarding the error bars, however, this result did not guarantee a significant increase of the maximum value by the combination of UV light exposure and thermal treatment since the fluctuations within theses measurements were comparably large.

4.1.5 Crosslinking potential of collagen fibrils

As already addressed in Section 4.1.1.3, it could be assumed that separate but identically treated collagen fibrils could already have different mechanics due to inherent properties (*e.g.* defects, kinks). The so far presented results led to the denomination of a further quantity that is the state of crosslinking. The experiments showed that the resistance of the fibril towards radial indentation could be manipulated by the application of elevated temperatures and/or UV light exposure. It is well accepted that the reasons are the occurrence of crosslinking or denaturation processes. Yet, not every collagen fibril -under identical treatment conditions- showed the same behaviour during treatment as it was demonstrated in Figure 4.10b and Figure 4.10d, as well as in Figure 4.12a and Figure 4.12b. Foremost was the extent to which a change in DMT modulus occurred varied. Figure 4.16 attempts to explain this in opposing the initial DMT modulus in the untreated state to the DMT modulus that represents the maximum change during the treatment. Several individual collagen fibrils were investigated. Figure 4.16a shows PFQNM AFM experiments for single collagen fibrils immersed in 1xPBS and irradiated with either UVA, UVB, or UVC light, while Figure 4.16b shows PFQNM AFM experiments for single collagen fibrils immersed in deionised water and irradiated with UVA light as representative for the inducement of a decreasing DMT modulus. Two adjacent chart bars belong to one fibril showing the initial DMT modulus (orange) and the maximum DMT modulus (green) reached throughout the experiment. The results are grouped by the applied UV light and further by the experiment meaning that, for example, in Figure 4.16a the chart bars for 1.1 and 1.2 both belong to the same experiment but represent two individual fibrils. For the PBS-examples, thus, two experiments were evaluated for each UV light source with two fibrils each. Only for the experiment number 5 four fibrils were recorded. Within one experiment, the time for which the maximal DMT value was extracted was the same. The values are ordered in such a way, that within one experiment the fibril with the highest initial DMT modulus is on the left while the fibril with the lowest is on the right. The numbers given in percentage above the bars are the change in DMT modulus for the single fibril between the two designated points in time of exposure.

Keeping in mind that, within one experiment, the bars are sorted by a decreasing initial value from left to right, it was striking that the information on the relative change behaved in an opposite manner (Figure 4.16a). This means that the fibrils with a higher initial DMT modulus exhibited a smaller relative change in modulus than fibrils with a smaller initial DMT modulus, referring to the same experiment. The conclusion is that the latter have a higher potential for a change in their mechanical properties without stating that they were able to achieve a higher absolute value in comparison. Regarding the results obtained for the evolution of the DMT modulus of collagen fibrils that were immersed in 1xPBS, especially for the irradiation with UVB and UVC light, they exhibited a time-dependent evolution of the DMT that was reminiscent of an inverted parabola. As it is seen in Figure 4.9 and Figure 4.14b, the error bars for results averaged over several fibrils were rather

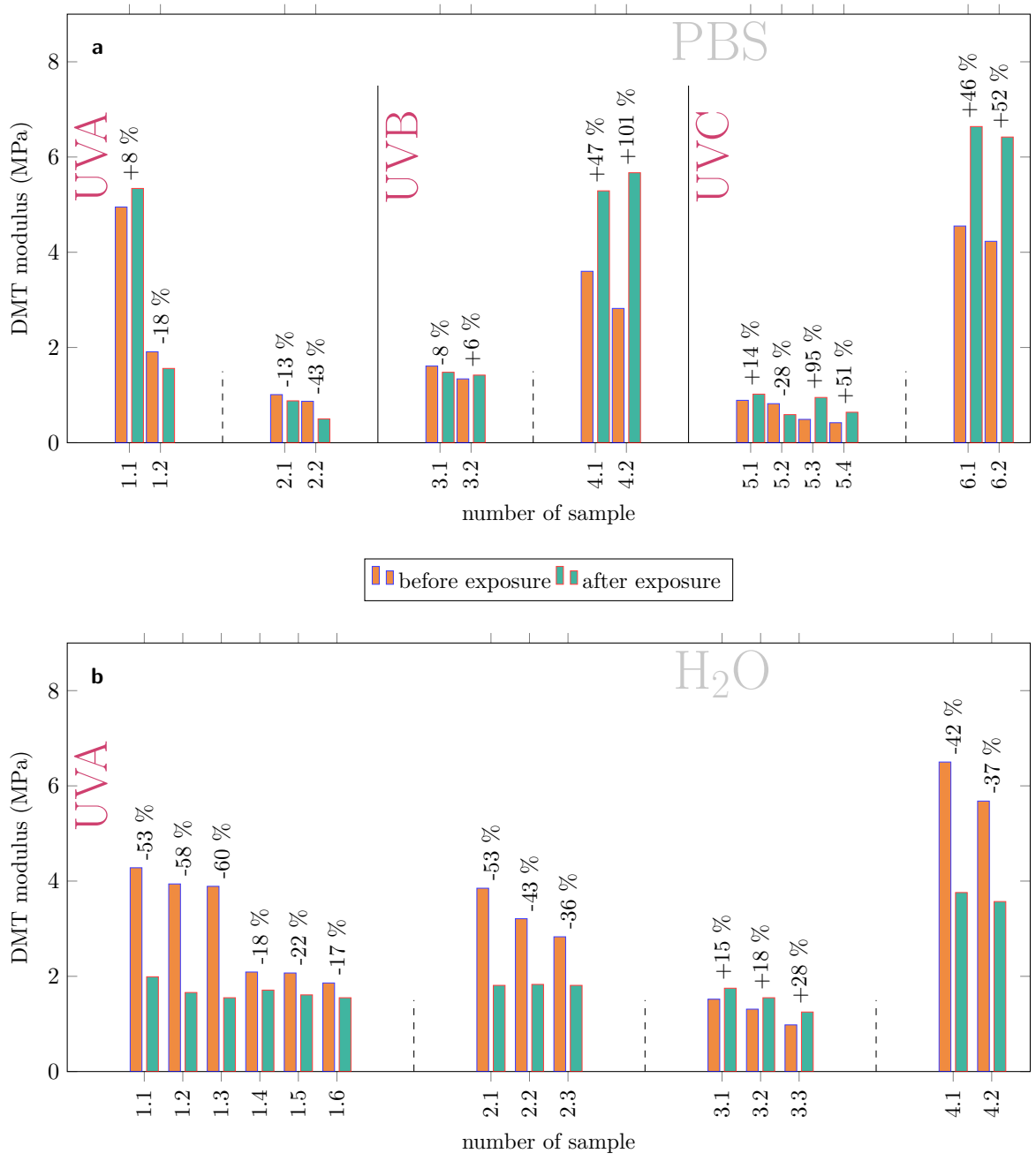

Figure 4.16.: The comparison between the (orange) initial DMT modulus of a single surface supported collagen fibril and its (green) maximal change in DMT modulus after a certain time of UV light exposure is displayed for 30 collagen fibrils. The results were divided into sections according to the applied UV light source (solid vertical lines) and into sections showing results from one experiment (dashed vertical lines). Within one experiment, the fibrils were sorted in decreasing order regarding their DMT modulus. Results are displayed for collagen fibrils immersed in (a) 1xPBS and (b) deionised water and the presented fractions show the change in DMT modulus between the initial value and the moment of maximal change which was the same within each experiment.

high. The explanation was given by the examination of the change in DMT modulus with time for single fibrils (cf. Figure 4.9 and Figure 4.14b) showing that, for the same treatment, they exhibited different extents of relative change and slightly varying temporal behaviour. Transferring these observations to Figure 4.16, an explanation for the behaviour could be suggested. With time, the mechanical properties of every individual collagen fibril, under the application of crosslinking-favouring conditions, followed the behaviour of an approximated inverted parabola. The collagen fibrils in the different experiments presented in Figure 4.16a were, initially, in different states of this cycle. While the fibrils with the initial high DMT modulus were already close to their maximum potential of crosslinking, others were at the very beginning of the cycle. This theory could also explain why the DMT modulus of the samples number 3.1 and number 5.2 was decreasing. In the untreated state, they had already reached or even exceeded their maximal possible state of crosslinking. Further irradiation led to the subsequent decrease of the fibril mechanics due to the break-up of crosslinks. The stated different states of the untreated fibrils, most likely, came from the synthesis. Fibrils that had started growing earlier had more time to crosslink in the collagen solution under the application of 37 °C than fibrils that had started growing later. Figure 4.17 sketches this process. The initial DMT modulus and the corresponding value after 25 min of exposure are plotted for experiment number 3.2 and experiment number 3.3. An inverted parabola connecting all the points was inserted to display the possible trend of the mechanical properties during crosslinking-favouring UV light exposure.

The presented idea could also be transferred to Figure 4.16b. As shown in Figure 4.13, the DMT modulus decreased for irradiation experiments performed in deionised water with a decreasing rate leading to a stabilisation around -50 to −60 % of change in modulus. The comparison of the initial DMT moduli with values after a certain time of UVA light exposure showed a higher relative change for the fibrils with a higher initial DMT modulus (except for experiment number 3). This fits to the presented theory since the so far reported decrease of the DMT modulus for collagen fibrils immersed in deionised water was higher for the beginning of exposure in comparison to longer exposure times. Thus, a high initial DMT modulus bore a high potential for a negative relative change in the number of occurring crosslinks while an already reduced number of crosslinks only allowed for small further changes. Interestingly, the experiments number 1, number 2, and number 4, had a similar final DMT modulus. This supported the observation that the rate with which the reduction in DMT modulus proceeded decreased for longer time of exposure and, thus, favoured an assimilation of the results when treated in deionised water. An exception was depicted by experiment number 3 in Figure 4.16b since positive changes in DMT modulus were reported. The fibrils followed the behaviour described for Figure 4.16a but exhibiting an increase in DMT modulus of up to 30 %. This result showed a further reason for the increased error bars that were discussed earlier and also underlines that every fibril has to be seen as an individual complex protein for which a general reaction towards external influences could be stated but never holds true in every case.

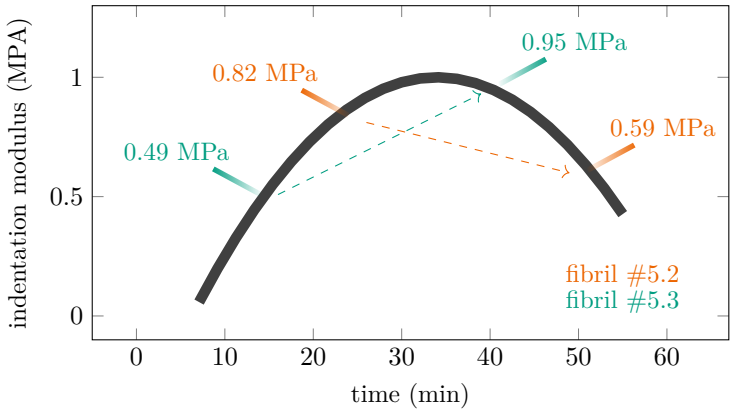

Figure 4.17.: Schematic representation of the theory that the evolution of the DMT modulus, for a crosslinking-favouring exposure, follows an inverted parabola. Two fibrils from experiment number 5 in Figure 4.16a were exemplarily chosen and depicted here in green and orange. The initial DMT modulus (left side of the parabola) and the corresponding value after 25 min of exposure (right side of the parabola) are shown for both data sets and a resulting inverted parabola is plotted to emphasise a possible trend of the mechanical properties during UV light exposure.

4.1.6 Simultaneous and successive ultraviolet light exposure

So far, the exposure of the collagen fibril and the measurement of its DMT modulus have been recorded simultaneously. These *in situ* measurements gave valuable insight into the materials behaviour but they also raised the question whether the effect of exposure depends on the continuity of the irradiation or whether a stepwise application of the UV light would lead to the same effect. For that, collagen fibrils were measured by PFQNM AFM with a successive exposure sequence of 5 min - 5 min - 5 min - 15 min - 30 min for the combination UVA light and deionised water, as well as UVB light and 1xPBS. The results were directly compared to similar measurements that have been conducted in the 'simultaneous' way (Figure 4.18). While the grey data points stand for the comparative measurement, the green data points show the results of the experiments performed according to the 'successive' way. Figure 4.18a exhibited a fairly good agreement for the results of both measurement types. For the measurement in 1xPBS (Figure 4.18b), the data points did not overlap with the same accuracy. However, for the 'successive' measurement, the general expected tendency of an increase in modulus over time of exposure with a subsequent decrease was stated. Consequently, both approaches led to the same impact of UV light on the mechanical properties of collagen fibrils. Furthermore, it can be recorded that the changes induced by the exposure did not immediately get lost as soon as the UV source was turned off and the irradiation of the sample could be interrupted to investigate the current state of the sample and then be resumed. This was helpful for the presented Raman measurements.

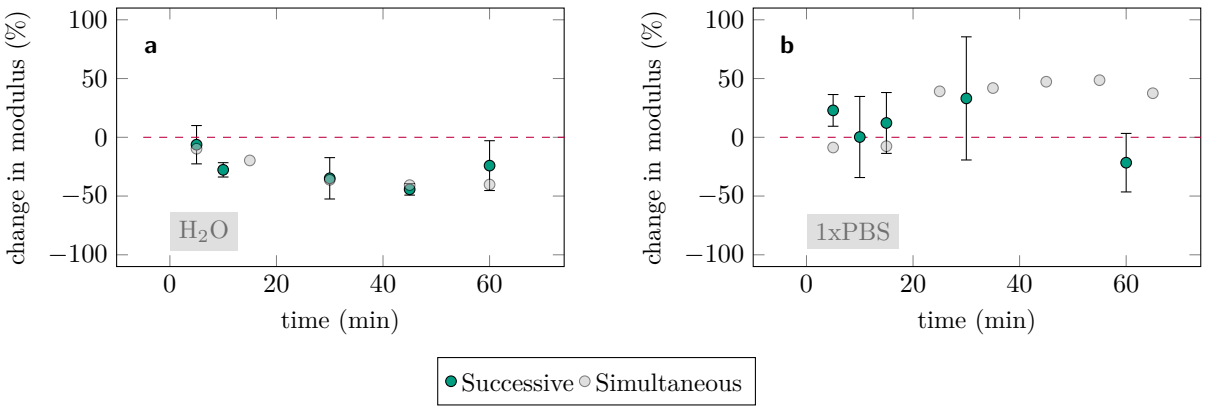

Figure 4.18.: Relative change of the DMT modulus with time of exposure for single surface supported collagen fibrils measured by PFQNM AFM. Comparison of results for (grey) UV light exposure that was done simultaneously to the PFQNM measurements and (green) results obtained by alternating the PFQNM measurement and the UV light exposure. Collagen fibrils were exposed to (a) UVA and (b) UVB light and immersed in (a) deionised water and (b) PBS.

4.1.7 Summary

The aim of Section 4.1 was to describe the impact of UV light irradiation on the radial indentation modulus of fully hydrated and surface supported collagen fibrils by AFM *in situ*. It was shown that AFM is a suitable technique to image single collagen fibrils and measure their DMT modulus. Once a reliable measurement site on the specimens was identified, experiments at ambient conditions were straightforward. Immersing the sample in a liquid, however, induced a fibril swelling and required a more careful choice of measurement parameters, especially of the maximum force applied to the sample, to not overestimate the acquired DMT modulus. Before samples were treated with UV light, measurement of the DMT modulus at temperatures between 34 and 45 °C were performed for samples immersed in deionised water or PBS-based solutions. Averaged results showed that the immersion in the former favoured a decrease in DMT modulus with treatment time while the latter promoted an increase. However, the averaged results also displayed a large deviation range. Focusing on single experiments, it was obvious, that the combination of the liquid environment did, for most cases, set the general tendency of the development but that extent and temporal rhythm varied. Similar tendencies were found for the exposure of collagen fibrils to UV light. UVA, UVB, and UVC light sources were applied in combination with deionised water or PBS. Averaging the results from several experiments showed that especially the combination of PBS and UVB or UVC led to an increase in the DMT modulus within 30 to 40 min followed by a decrease, while collagen fibrils immersed in deionised water tended to lose mechanical stability. From these measurements, two model conditions evolved representing stabilising (PBS and UVB/UVC) and destabilising tendencies (deionised water and UVA). Synergetic effects of UV light and thermal exposure were also investigated. Although the recorded changes were higher than for the

individual treatments, a significant improvement could not be stated due to the high errors. Heating of the sample, however, had not been spotlighted in further measurements, since a central interest was the patterned modification of the specimen‘s mechanical properties that should be achieved by localised exposure of the collagen to UV light.

Questions arose from the gathered results like the origin of the varying quantitative change in modulus induced by treatment. Comparing the treatment-induced change of single fibrils with their respective initial DMT modulus showed a dependency that could be correlated to the sketched development of the fibrils. Since the initial state of crosslinking may have varied, the potential for further crosslinking and bond breaking differs for every collagen fibril. Thus, the change in modulus is fibril-specific, which led to the depicted errors. Furthermore, it was shown that the same impact of the UV light exposure was achieved by both continuously scanning and irradiating the samples and alternating both processes.

The described development of the DMT modulus dependent on the conditions of the UV light exposure was complemented by the investigation of the tensile modulus.

a b

Figure 4.19.: Schematics of the (a) TGZ-500 calibration grid with collagen fibrils stretched over its trenches that was used as substrate in the AFM-based tensile tests and (b) of the applied B300 probe (cf. Table 3.1).

4.2 Tensile tests of collagen fibrils[ix]

4.2.1 Setup for tensile test

Figure 4.19a shows a schematic of the applied TGZ-500 calibration grid as substrate for the AFM-based tensile tests with the collagen fibrils stretched over its trenches and Figure 4.19b shows a schematic of the applied B300 cantilever (cf. Table 3.1). Impressions of the real situation are given in Figure 4.20 depicting PFQNM AFM images of two different collagen fibrils that were stretched over a trench. Both examples were considered for measurement, independent of the angle they have with respect to the trench. Fibrils that were sagged or even in contact with the bottom of the trench (cf. Figure 4.21) were not considered. The collagen fibrils chosen for measurement had a diameter between approximately 40 and 80 nm and a suspended length between 2000 and 2800 nm.

Testing of the tensile modulus requires a firm attachment of the fibril to the bars of the substrate to prevent movement or slipping of the fibril during the experiment. Figure 4.21 shows how, in contrast to the parts that were attached to the bars, the freely suspended part of the fibril was moving during imaging in PFQNM mode with forces that were in the range of the forces applied for the bending experiments. This behaviour suggested that the fibril was firmly attached and its suspension points could be modelled by clamps or similar descriptions. Additionally, no slipping or change in position of the fibril after the experiments was detected.

[ix] The results in Chapter 4.2 emerged from the cooperation with Philipp L. Rosendahl who validated the measurement setup and derived the membrane solution and the non-linear beam solution by FEA and, thereby, takes huge credit for the presented findings. Special thanks go to Achim Bender and Dirk Gründing for fruitful discussion regarding the validation of the to be presented model and support with the error progression, respectively.

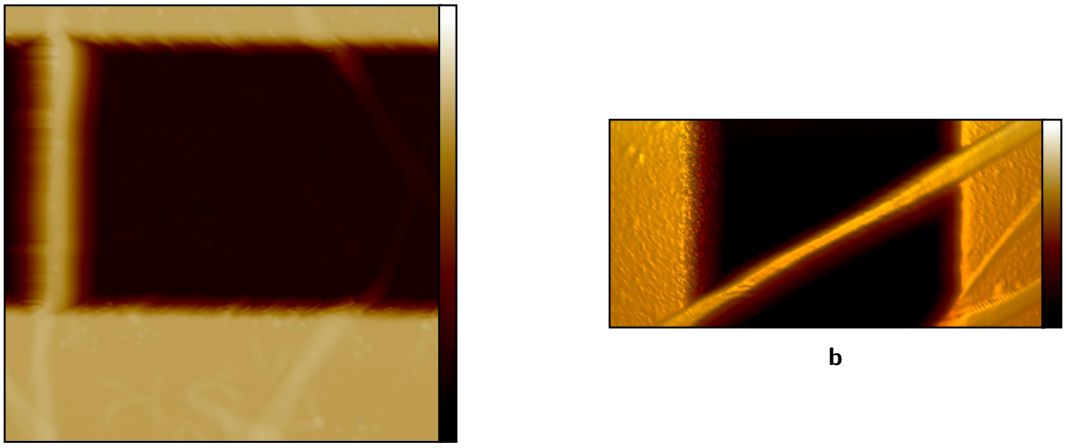

Figure 4.20.: PFQNM AFM height images of two different collagen fibrils that were stretched over the trenches of the TGZ-500 calibration grid in a liquid environment acquired with a ScanAsyst Fluid cantilever (cf. Table 3.1). A (a) two-dimensional and a (b) three-dimensional image with an image ratio of 1:2 of different spots are shown. Colour bar: (a) -500 to 500 nm and (b) -450 to 700 nm. Scan size: (a) $3 \times 3\,\mu m^2$ and (b) $3 \times 1.5\,\mu m^2$.

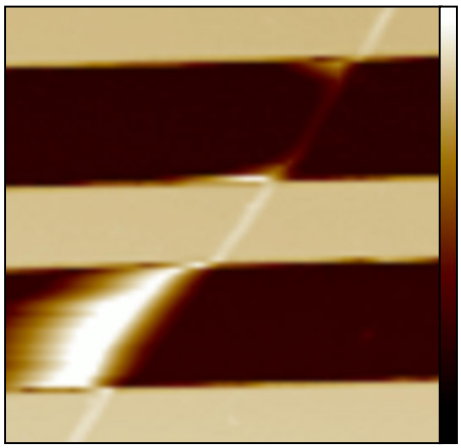

Figure 4.21.: PFQNM AFM height image of a collagen fibril that was stretched over the trenches of the TGZ-500 calibration grid with a scan size of $6.4 \times 6.4\,\mu m^2$ in a liquid environment. For some trenches the fibril was attached to the bottom while for other trenches the fibril was freely suspended with the free part moving during AFM measurement and the fixed part not showing any movement. ScanAsyst Fluid cantilever were applied (cf. Table 3.1). Colour bar: -500 to 500 nm. Scan size: $6.4 \times 6.4\,\mu m^2$.

4.2.2 'Tangent model'

The extraction of Young's modulus E from the linear regime of a stress versus strain curve is a common process. If the material behaviour is assumed to be linear elastic and neither thermal strains nor lateral stresses occur, E can be estimated by Hooke's law

$$\sigma = E \cdot \varepsilon, \tag{4.1}$$

with, for the presented case, the axial fibril stress σ and the axial fibril strain ε. The output of the performed tensile tests on freely suspended collagen fibrils as they are described in Section 3.4, however, was a vertical displacement that was evaluated as fibril deflection δ in the middle of the fibril and the lateral (vertical) indenter force on the fibril $F(\delta)$. The task was to bring these quantities together.
For the case of neglected bending stresses

$$\sigma = \frac{N}{A}, \tag{4.2}$$

is constant across the cross section of the fibril and is derived by the division of the axial normal force N and the cross section area A. Under the consideration that friction between fibril and indenter were neglected, the relationship between F and N is expressed by

$$N = \frac{F}{2 \cdot \sin \phi}, \tag{4.3}$$

with ϕ as the angle between the actual fibril position and its initial rest position (deflection angle of the fibril). Additionally, A depended on ϕ. The calculation of A by

$$A = \frac{\pi \cdot d^2}{4}, \tag{4.4}$$

depended on the fibril diameter d that, in turn, was changing due to lateral contraction of the fibril by

$$d = d_0 \cdot (1 - \nu \cdot \varepsilon), \tag{4.5}$$

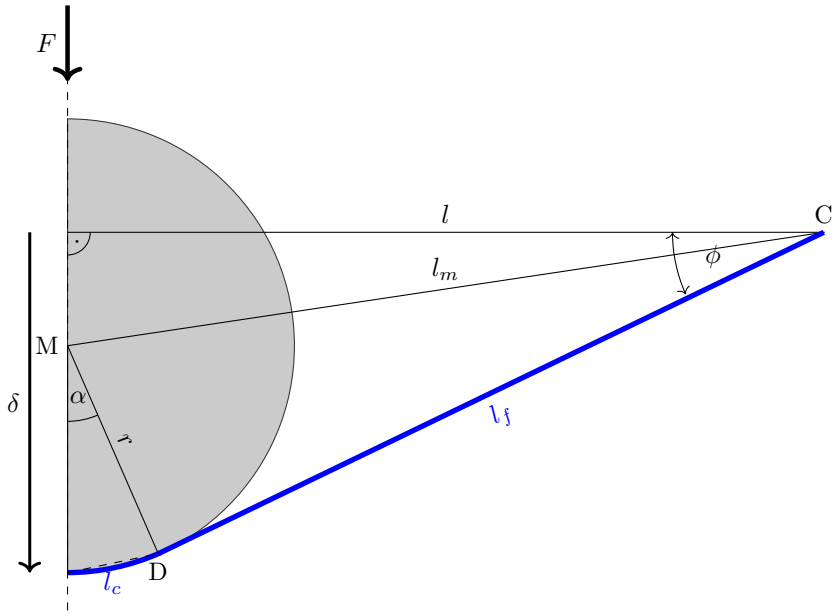

Figure 4.22.: Two-dimensional scheme of the 'tangent model' showing the right half of the measurement setup in which the AFM probe with the radius r deflects a suspended fibril by the vertical distance δ. The AFM probe (half circle, dark grey) bends a fixed fibril with the angle ϕ between the initial position of the fibril with half the length of the suspended fibril l and the deflected fibril with the length $l_f + l_c$. The attachment point of the fibril with the sphere D was the intersection of a straight line running through the suspension point C of the fibril. The angle α between a vertical line through the middle of the AFM probe M and the connection line between M and D, as well as the line l_m connecting C and M are auxiliary values.

with the initial fibril diameter d_0 and the Poisson's ratio ν. The dependence on ϕ was introduced by ε that, in the case of the nominal strain ε_n, was described by

$$\varepsilon_n = \frac{\Delta l}{l} \tag{4.6}$$

where l was half the length of the unperturbed freely suspended fibril and Δl was the elongation due to the deflection of the fibril, which was connected to the deflection of the fibril under load. For the estimation of the deflection, the contact line of the fibril with the indenter had to be known.

The geometrical considerations for the extraction of the elongation was labelled 'tangent model'. The auxiliary line that started from the suspension point of the fibril C behaved to the circle as tangent meaning that there was only one contact point between the two objects (Figure 4.22). For the extraction of the length of the fibril during deflection $l + \Delta l_{tan}$ an auxiliary line l_m was drawn between the suspension point C of the fibril and the centre of the indenter M. It was described by

$$l_m = \sqrt{l^2 + (\delta - r)^2} \tag{4.7}$$

for which the term $\delta - r$ may have become negative and so could the first term in Equation (4.8):

$$\phi = \arcsin \frac{\delta - r}{l_m} + \arcsin \frac{r}{l_m}. \tag{4.8}$$

This, however, was intended. The total deformed length $l + \Delta l_{tan}$ was the sum of

$$l_f = \sqrt{l_m^2 - r^2} \tag{4.9}$$

and

$$l_c = \phi \cdot r \tag{4.10}$$

describing the straight regime and the arc length, respectively. The extraction of ϕ and $l + \Delta l_{tan}$ enabled the conversion of the required data into axial stress versus strain curves.
The presented geometrical considerations were supposed to allow for the extraction of the tensile modulus of freely suspended collagen fibrils from stress versus strain curves that have been derived from static deflection versus piezo displacement curves during bending experiments. Their correctness was validated by FEA.

4.2.3 Validation by finite element analysis

FEA calculations were performed for the validation of the applicability of the presented setup and the evaluation of the obtained results, for which several assumptions were made that are summarised in Table 4.2.

During the FEA-based validation, the application of the nominal strain was compared to the total true strain ε_t obtained by integrating strain increments

$$\mathrm{d}\varepsilon = \frac{\mathrm{d}\hat{l}}{\hat{l}}, \tag{4.11}$$

according to

Table 4.2.: List of the assumptions made for the finite element analysis-based calculations.

Absence of	**Properties of fibril**	**Quantities**	
thermal strains	linear elastic material	Indenter tip radius	300 nm
lateral stresses	incompressible	Suspended length	2000 nm
friction between indenter and fibril		Initial fibril diameter	50 nm
		Poisson's ratio	0.5
	Application of	Moment of inertia	$\approx 3.07 \times 10^{-19}\,\mathrm{mm}^4$
	Euler-Bernoulli beam theory	Ratio EA_0/EI_0	$\approx 6.4 \times 10^{10}\,\mathrm{mm}^2$
	perfectly round indenter		

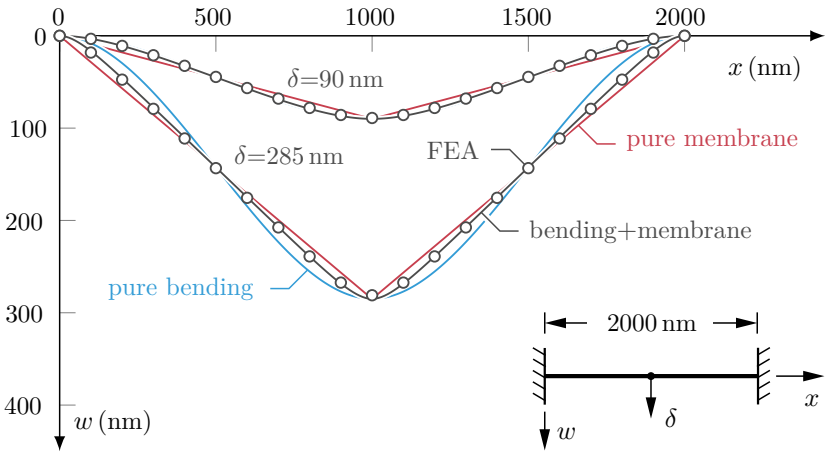

Figure 4.23.: Deflection of a beam with clamped ends and prescribed centre displacement. Analytical solutions were compared to the finite element analysis (FEA, gray dots) reference model introduced in Section 3.4.1 and shown in Figure 3.3a. The geometrically non-linear solution (bending + membrane, gray) is given by Equation (C.20) and the geometrically linear solution (pure bending, blue) by Equation (C.28). The pure membrane solution (red) corresponded to straight lines connecting beam ends and load point. Image was provided by courtesy of Philipp L. Rosendahl.

$$\varepsilon_t = \int_l^{l_0} \mathrm{d}\varepsilon_t = \int_l^{l_0} \frac{\mathrm{d}\hat{l}_0}{\hat{l}_0} = \ln\left(\frac{l_0}{l}\right), \tag{4.12}$$

where l_0 was the deformed length of the fibril ($l + \Delta l_{tan}$).

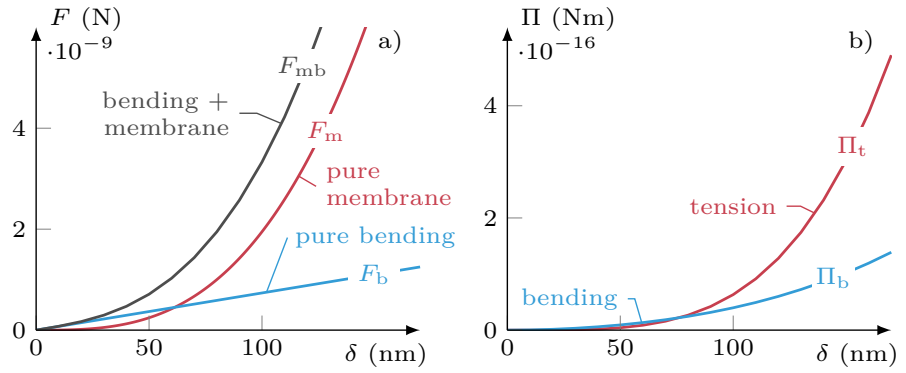

Figure 4.24.: Beam with clamped ends subjected to a prescribed centre displacement δ. a) Comparison of reactions forces from combined bending and membrane F_{mb} (Equation (4.13), gray), pure bending F_{b} (Equation (4.14), blue), and pure membrane F_{m} (Equation (4.18), red) solutions. b) Strain energy contributions originating from bending Π_{b} (Equation (4.20), blue) and tension Π_{t} (Equation (4.21), red). Quantities were given for a Young's modulus of $E = 1\,\mathrm{GPa}$. Images were provided by courtesy of Philipp L. Rosendahl.

4.2.3.1 Membrane solution

Figure 4.23 shows a comparison between the chosen analytical solutions and the FEA reference solution that was introduced in Section 3.4.1, regarding the vertical displacement δ with dependence on the horizontal position of the fibril. The comparison was made for vertical displacements δ in the middle of the fibril of 90 nm and 285 nm. The FEA reference solution was compared to the solutions for the linear beam theory (pure bending), straight segments that connect the load point with the beam ends (pure membrane), and the non-linear beam theory (bending + membrane). In the case of 90 nm, the linear beam solution was in good agreement with the FEA reference solution. For an increased deflection of 285 nm, however, deviations between the FEA reference solution and the linear beam theory became apparent. Instead, axial forces, that are not accounted for in linear beam theory, became relevant and, thus, the pure membrane-approach offered a good description. This was underlined by the calculation of the vertical reaction force at the load point (Figure 4.24a) and the strain energy stored in the deformed fibril (Figure 4.24b) for the linear beam theory, the consideration of straight fibril segments, and the non-linear beam theory. For the latter, considering both bending and membrane contributions, the derivation of the reaction force

$$F_{\mathrm{mb}} = 2 \cdot V_{\mathrm{mb}} \tag{4.13}$$

is referred to in Section 4.2.3.2.

In case of pure bending,[299] however, the reaction force F_b read

$$F_\mathrm{b} = 2 \cdot V_\mathrm{b} = 24 \cdot E \cdot I \cdot \frac{\delta}{l^3}, \tag{4.14}$$

with V_b for the linear beam obtained from Equation (C.29) and with the fibril's moment of inertia $I = \pi d^4/64$, the fibril's diameter d, and the suspended length $2l$. The load point deflection is δ and E is the fibril's Young's modulus.

With the assumption of straight fibril segments, the axial strain

$$\varepsilon = \frac{\Delta l}{l} = \frac{\sqrt{l^2 + \delta^2} - l}{l} \tag{4.15}$$

can be determined from geometry (cf. Figure 4.23). Estimation of the pure membrane reaction force required a statement for the axial force N, that was given by

$$N = \frac{\sqrt{l^2 + \delta^2}}{\delta} \cdot \frac{F}{2}, \tag{4.16}$$

and the elasticity law for pure tension that was considered with

$$N = E \cdot A \cdot \varepsilon. \tag{4.17}$$

Eventually, the combination yielded the pure membrane reaction force

$$F_m = 2 \cdot E \cdot A \frac{\sqrt{l^2 + \delta^2} - l}{l \cdot \sqrt{l^2 + \delta^2}} \cdot \delta, \tag{4.18}$$

where $A = \pi d^2/4$ is the fibril's cross section area. Figure 4.24a shows that the reaction force for the pure bending F_b bore a proportionality to the displacement δ resulting in an adequate description of the freely suspended fibril for small deflections only (approximately $< 50\,\mathrm{nm}$). Focusing on pure axial forces, however, the development of the reaction force with increasing fibril displacement δ agreed well with the force response of the fibril. That comparison hinted to the governing influence of the membrane force throughout the experiments, which suggested that Equation (4.18) was suitable for the estimation of the tensile modulus. The influence of the membrane forces could further be seen in Figure 4.24b showing the total strain energy potential Π versus

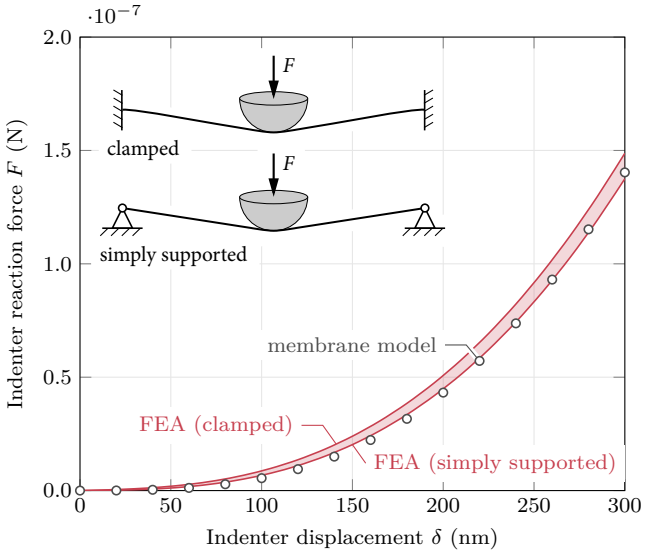

Figure 4.25.: Comparison of the membrane model, Equation (4.18), to finite element analyses. Limit cases assuming a Young's modulus of the fibril of $E = 2.75\,\mathrm{GPa}$. Image was provided by courtesy of Philipp L. Rosendahl.

the fibril displacement δ. For small δ (approximately $< 100\,\mathrm{nm}$) the bending strain energy and the tensile strain energy were similar in value. For higher δ, however, the tensile strain energy increased faster than the bending strain energy and, thus, delivered a higher contribution to the total strain energy that is given by

$$\Pi = \frac{1}{2} \cdot \int_0^{2l} \left(\frac{M^2}{E \cdot I} + \frac{N^2}{E \cdot A} \right) \mathrm{d}x, \tag{4.19}$$

where M denotes the bending moment. Equation (4.19) can be divided into the bending contribution

$$\Pi_\mathrm{b} = \frac{1}{2} \cdot \int_0^{2l} \frac{M^2}{E \cdot I} \, \mathrm{d}x, \tag{4.20}$$

and the tensile contribution

$$\Pi_\mathrm{t} = \frac{1}{2} \cdot \int_0^{2l} \frac{N^2}{E \cdot A} \, \mathrm{d}x. \tag{4.21}$$

Figure 4.25 shows a comparison of the FEA reference model to the membrane solution for the described limit cases (cf. Section 3.4.1) of the boundary conditions. In any case, either simply supported or fixed, Equation (4.18) provided a good description of the reaction force. Thus, it should also be capable of delivering

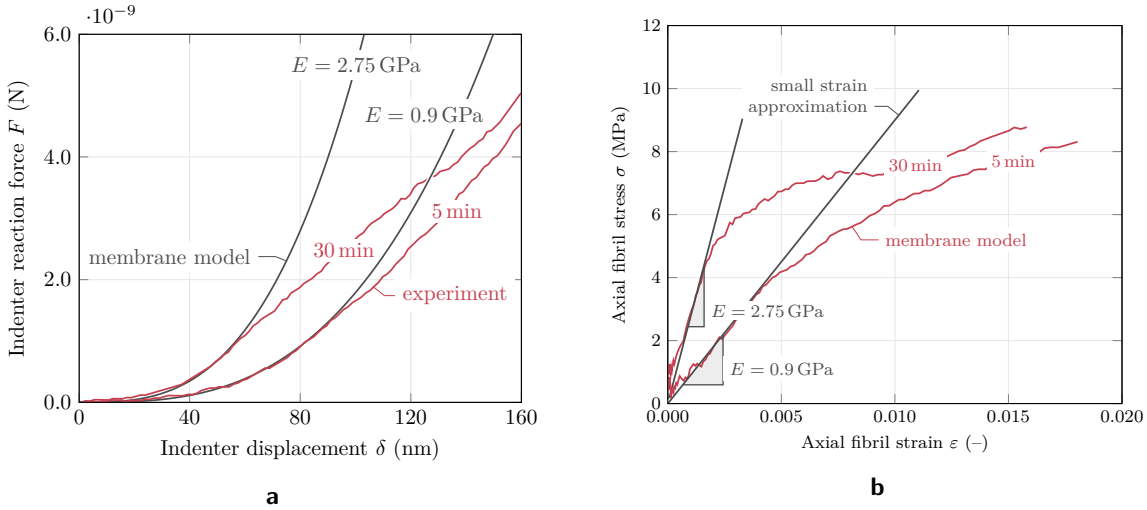

Figure 4.26.: (a) Force versus deflection-signals of a fibril in 1xPBS solution exposed to UVA light for 5 min and 30 min at room temperature, respectively. The initial material response was well represented by the membrane model assuming different Young's moduli. (b) Stress-strain behaviour of a fibril in 1xPBS solution exposed to UVA light for 5 min and 30 min, respectively. The membrane model described the initial linear response of the material and allowed for determining the fibril's axial Young's modulus. Images were provided by courtesy of Philipp L. Rosendahl.

a satisfying description of the experimental data. Figure 4.26a shows two experimentally obtained force versus indentation curves that have been derived from tensile tests on one collagen fibril immersed in 1xPBS after 5 min and 30 min of UVA light exposure at room temperature. The model described the first part of both curves well, resulting in different Young's moduli, as would have been expected. For higher indentations, the model and the experimental curves started to deviate due to the influence of physical non-linearities[x] that have not been accounted for in the model. This could also be seen during the calculation of the fibril's stress versus strain response shown in Figure 4.26b. The axial strain was obtained from Equation (4.15), while the axial stress used $\sigma = N/A$ and Equation (4.16) which resulted in

$$\sigma = \frac{F}{2 \cdot A} \frac{\sqrt{l^2 + \delta^2}}{\delta}. \tag{4.22}$$

The initial linear response, that was seen in Figure 4.26b could be described well by the membrane solution and, thus, allowed an extraction of the tensile modulus.

[x] The membrane solution considered the non-linear geometry, the material behaviour was assumed to be linear elastic.

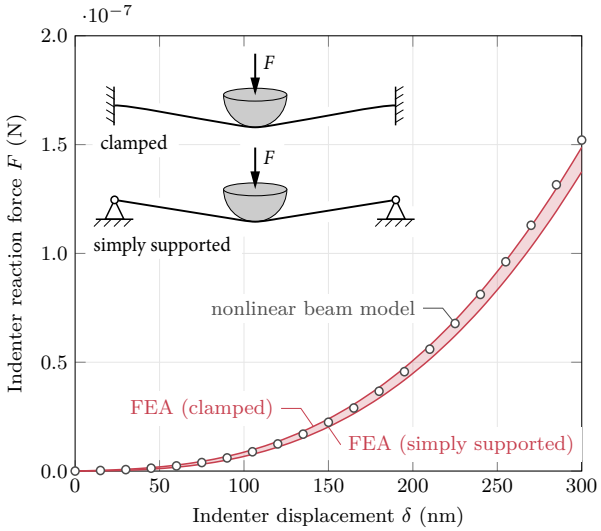

Figure 4.27.: Comparison of the non-linear beam model, Equation (4.13), to finite element analyses. Limit cases assuming a Young's modulus of the fibril of $E = 2.75\,\text{GPa}$. Image was provided by courtesy of Philipp L. Rosendahl.

4.2.3.2 Non-linear beam solution

The so far presented calculations show a dominating influence of the membrane forces on the tensile testing. Yet, this was predominantly correct for fibril displacements δ higher than approximately 100 nm. For $\delta < 50\,\text{nm}$, bending contributions were seen (cf. Figure 4.24a). Although the trend of the reaction force of the pure membrane solution is in better agreement with the experimental data than the pure bending solution, a refinement of the proposed analytical solution seemed appropriate. Applying non-linear beam theory accounting for moderately large rotations (von Kármán non-linearity),[299] considered bending and tension contributions. The term "moderately large rotations" refers to up to approximately 10 times the beam's diameter. The corresponding equations were derived in Section C.

Employing the shear force V_{mb} of the non-linear beam model for the calculation of the indenter reaction (Equation (4.13)) resulted in an excellent agreement with the FEA reference model (cf. Figure 4.27). The application of the non-linear beam theory included the assumption of a centre point load and neglected the radius of the indenter leading to deviations between model and analytical solutions for large deformations. Yet, the non-linear beam solution overcame the uncertainties of the membrane solutions for small δ, providing a better agreement between FEA model and an analytical solution for a broader range of δ. Additionally, computation of stress and strain were more accurate due to the robustness of the solution. The comparison to experimental data (Figure 4.28) showed a good agreement. The resulting values for the tensile modulus were smaller with respect to their evaluation based on the membrane solution (cf. Figure 4.26).

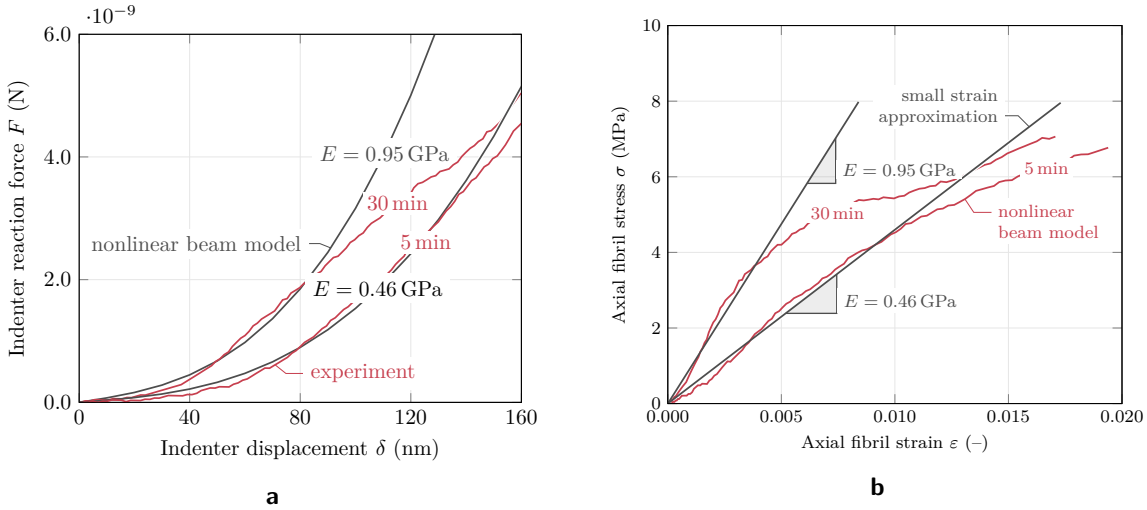

Figure 4.28.: (a) Force versus deflection signals of a fibril in 1xPBS solution exposed to UVA light for 5 min and 30 min at room temperature, respectively. The initial material response was well represented by the non-linear beam model assuming different Young's moduli. (b) Stress-strain behaviour of a fibril in 1xPBS solution exposed to UVA light for 5 min and 30 min, respectively. The non-linear beam model described the initial linear response of the material and allowed for determining the fibril's tensile modulus. Images were provided by courtesy of Philipp L. Rosendahl.

4.2.4 Ultraviolet light exposure

To investigate the influence on the results dependent on the applied analytical solution, the experimental data were evaluated with respect to the membrane solution as well as the non-linear beam solution.

Figure 4.29 shows the results of single tensile experiments for all combinations of three UV light wavelengths (UVA, UVB, UVC) and two liquid environments (deionised water and 1xPBS) based on the membrane solution. The findings are arranged in two columns according to the liquid environment (deionised water on the left, 1xPBS on the right), depicting representative results for the behaviour of the collagen fibrils observed throughout the tensile tests for the respective exposure. In the untreated state, the acquired tensile modulus averaged over the shown six results was 1.49 ± 0.46 GPa. The values after 60 min of exposure differed in dependence on the treatment. For collagen fibrils immersed in deionised water, the final tensile modulus was beneath the untreated value. While for the application of UVA and UVC light, the decrease in tensile modulus was continuous (cf. Figure 4.29a and Figure 4.29e), the application of UVB light showed a rather stepwise drop of the modulus from the initial to the final value after 20 to 30 min of irradiation. UVA and UVB light exposure exhibited a stabilisation of the modulus after 40 to 50 min of exposure which was not the case for UVC irradiation. For the immersion of the collagen fibrils in 1xPBS, and especially for exposure to UVB light (Figure 4.29d) and exposure to UVC light (Figure 4.29f), the final value was in the range of the initial value. In between, however, the tensile modulus was initially increasing with a maximum reached between 20 and 40 min and subsequently decreasing again. By that, the behaviour was similar to the results described for

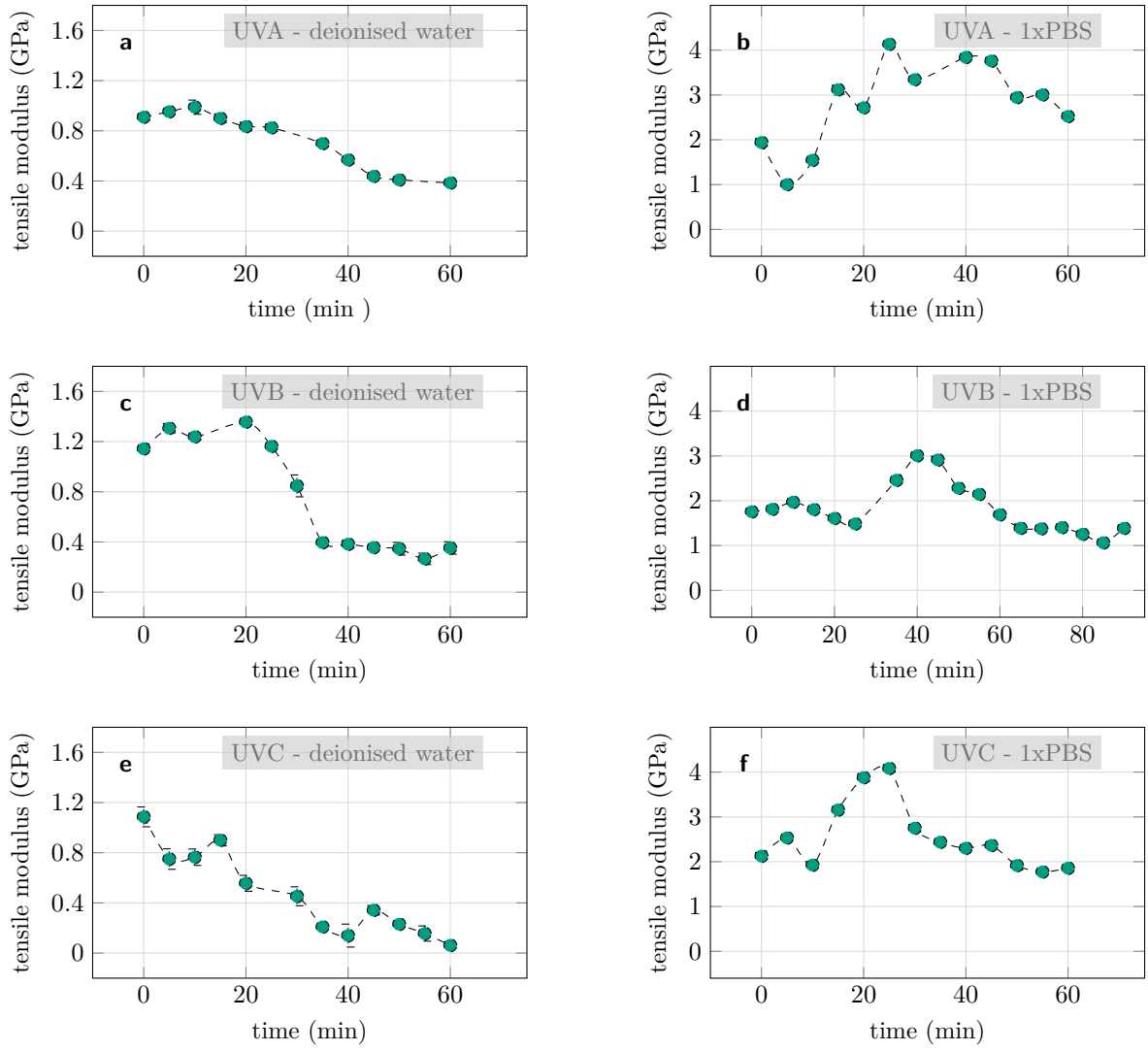

Figure 4.29.: Development of the tensile modulus with time of exposure for freely suspended collagen fibrils measured by static force versus indentation curves and evaluated according to the membrane solution. The experiments were conducted for 60 min (and 90 min for d) investigating all combinations of UVA, UVB, and UVC light with deionised water and 1xPBS as liquid environment.

the indentation experiments (cf. Section 4.1.3). Since the effects of the irradiation did not consequently show stabilised properties within the first 60 min, but still had exhibited the maximum value, the UVB irradiation was displayed for 90 min of exposure (Figure 4.29d). It could be seen that, within the extra 30 min, no relevant changes occurred anymore.

Figure 4.30 shows the results of the same single tensile experiments as in Figure 4.29 for all combinations of three UV light wavelengths (UVA, UVB, UVC) and two liquid environments (deionised water and 1xPBS). This time they were evaluated based on the non-linear beam solution. For both analytical solutions, the overall trends of the tensile modulus during UV light exposure were maintained. Yet, deviations were found in the extent to which the tensile modulus was changing during exposure as well as the quantitative results in general. In the untreated state, the acquired tensile modulus averaged over the shown six results was 0.95 ± 0.36 GPa. A wide range of tensile moduli measured for collagen fibrils in an aqueous environment has been published elsewhere. Starting in the megapascal-range with 32 MPa[212] up to 250 and 450 MPa,[90,238] the numbers extend into the gigapascal-range with tensile moduli between to 2.2 to 3.5 GPa for small strains up to 4.3 GPa for high strains.[209] The presented results agreed with the values reported by Svensson *et al.*[209]

The depicted error bars derived from an error propagation throughout the required calculations for the creation of the stress versus strain curves and the fitting of their linear regime. While the averaged strain error was smaller 5 %, the averaged stress error was 23 %, which came from the uncertainties introduced by the estimation of the fibril diameter. Thus, an improvement in accuracy of the quantitative values could be achieved by a more precise determination of the fibril's cross section area. The diameter was, in case of doubt, rather underestimated. A change in diameter, however, did not impact the qualitative trend of the evolution of the mechanical properties with treatment. Regarding of the qualitative results, the most debatable finding seemed to be the combination of UVA light and 1xPBS. For the indentation measurements (cf. Figure 4.14a), the tendency was rather of a destabilising nature. However, results shown in Figure 4.16a also indicated the occurrence of stabilising effects when collagen fibrils were irradiated with UVA light under the application of a 1xPBS environment. In combination, findings so far showed ambivalent results for this specific combination, which ruled it out as representative condition for a mostly crosslinking-favouring treatment.

As noted in Section 4.1.3, for the results of the indentation experiments, Figure 4.29 and Figure 4.30 also gave the impression that, for the deionised water-based measurements, the trend of the data points was more steady than it was for the PBS-based measurements where the results showed strong fluctuations between data points. Nevertheless, the overall tendency was still accessible.

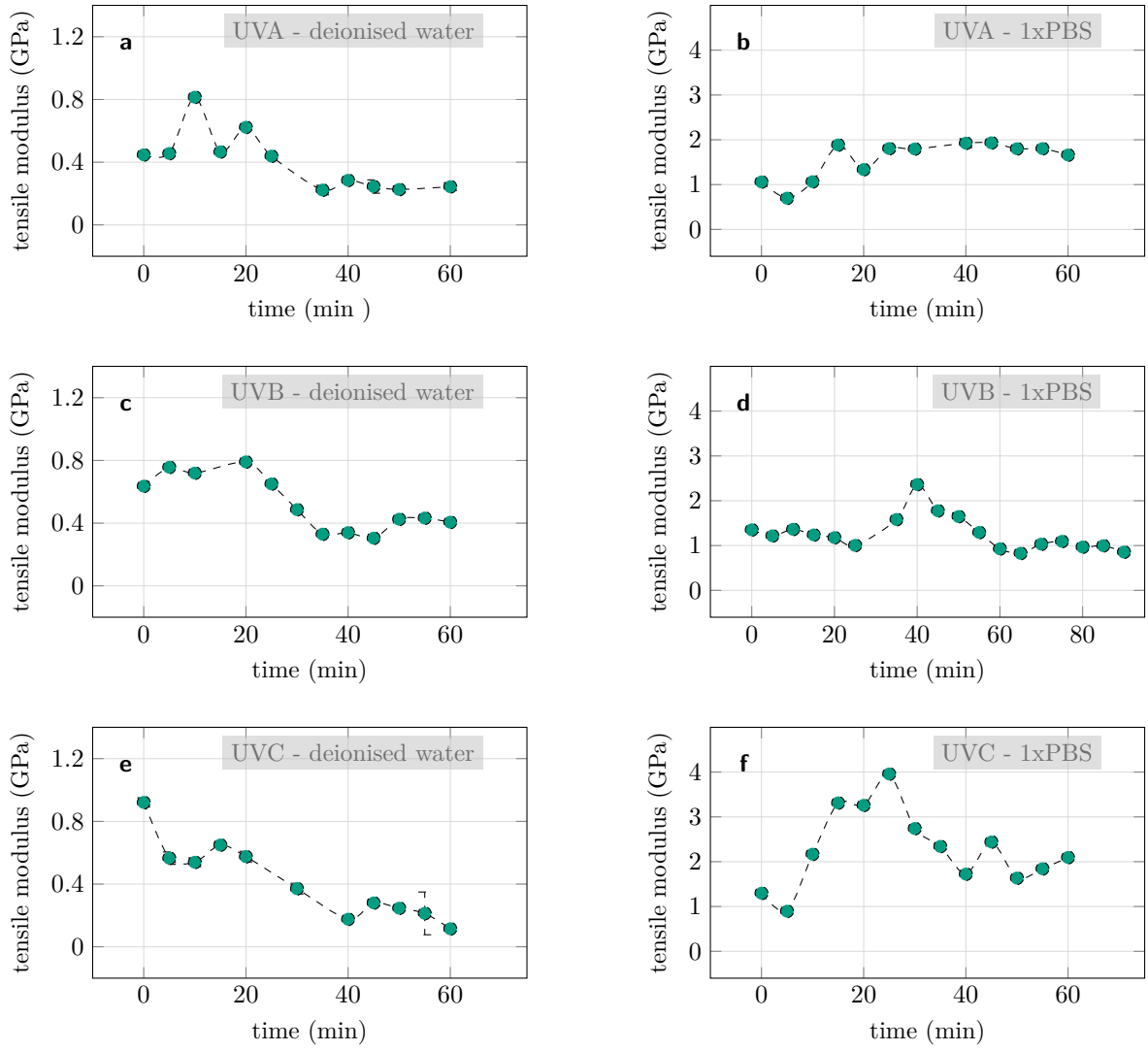

Figure 4.30.: Development of the tensile modulus with time of exposure for freely suspended collagen fibrils measured by static force versus indentation curves and evaluated based on the non-linear beam solution. The experiments were conducted for 60 min (and 90 min for d) investigating all combinations of UVA, UVB, and UVC light with deionised water and 1xPBS as liquid environment.

4.2.5 Summary

The aim of Section 4.2 was to describe of the impact of UV light exposure on the tensile modulus of collagen fibrils for their immersion in varied liquid environments. Although tensile tests on fibril structures with radial dimensions in the nanometre-range have been performed before, their implementation can be laborious and is not suited for an efficient testing of several samples. Thus, the motivation was to design an experiment whose sample preparation is straightforward.

In the style of bending experiments, the collagen fibrils were spread over a substrate containing cavities, in the presented case, a silicon-based AFM calibration grid with regularly occurring trenches. The stretched fibrils were vertically bent in the middle of their freely suspended part by an AFM cantilever with a sphere of defined radius. Starting with the thereby recorded static deflection versus piezo separation curves, stress versus strain curves were derived that represented the properties of the fibril in axial direction and whose linear part was used for the extraction of the tensile modulus. The measurement setup and the evaluation procedure were validated by FEA. As analytical description of the chosen FEA model, the membrane solution was presented, showing the dominance of the membrane forces during the conducted experiments. When it comes to small deflections of the fibril, however, a refinement of the description was required resulting in the introduction of the non-linear beam solution. The experiments were evaluated for both solutions, demonstrating that only quantitative differences were introduced while the qualitative behaviour was the same for both the membrane and the non-linear beam solution. Fibrils immersed in PBS exhibited an increase in tensile modulus with a maximum value reached within 60 min of UV light exposure, while the tensile modulus of specimens immersed in deionised water was decreasing during exposure. The measured tensile modulus averaged over all experiments before exposure was 1.49 ± 0.46 GPa and 0.95 ± 0.36 GPa for the membrane solution and the non-linear beam solution, respectively. These values ranged among the upper limit of the results that have been presented in literature. Improvement was expected by a more accurate estimation of the fibril diameter. Yet, the measurement setup proved itself feasible for the estimation of the tensile modulus of fibrillar structures.

4.3 Structural research on ultraviolet light treated collagen samples[xi]

4.3.1 Discussion of experimental parameters

Raman spectroscopy offers access to structural data of a specimen and it can be applied to biological samples. However, the method requires a certain sample volume to generate a detectable and evaluable signal. Since for conventional Raman spectroscopy single collagen fibrils, that have been investigated so far, do not pose a sufficient amount of collagen to create a reliable Raman signal, collagen hydrogels were used for the first experiments. In a second step, signals were also generated from separated collagen fibrils by the application of SERS. By that, a comparison of the behaviour of separated collagen fibrils and collagen hydrogels could be done. The introduction of collagen hydrogels was not only a consequence of the frame conditions deployed by Raman spectroscopy, but a transition from the experiments on single collagen fibrils to three-dimensional structures that, eventually, could be applied for experiments with living cells. Thus, the Raman spectroscopy experiments were building a bridge by investigating the applicability of the earlier presented findings to higher dimensional structures, which would be the necessity to continue the research.

As for the formerly described experiments, the collagen samples were kept fully hydrated throughout the whole experiment. For that purpose, the samples were stored in a quartz glass-cuvette during measurement. The confined space was filled with the measurement-respective liquid and the quartz glass allowed for the transmission of the UV light, as well as the transmission of the excitation and the emission light.
The non-destructive character of Raman spectroscopy depends on the measurement parameters, as there are the Laser power, measurement time, and number of accumulation cycles. It is obvious that a long irradiation of the sample with a high Laser power leads to the generation of an increasing amount of Stokes and anti-Stokes Raman signals resulting in a distinct spectrum. The downside of these signal-favouring parameters in combination with sensitive samples, *e.g.*, biological samples, is the risk of measurement-induced denaturation or bleaching effects. Since any destructive character of the measurement has to be avoided, the measurement parameters have to be chosen carefully and possible concessions regarding the signal quality have to be made. To obtain meaningful spectra, the described setup required a long measurement time due to the attenuation of the signal by the cuvette and the liquid. The collagen hydrogels also proved themselves to be very stable, which allowed an applied laser power of 10 mW and 10 accumulations with a measurement time of 70 s each. A consecutive irradiation of the sample with only the Laser (2 x 30 min) did not result in any deviations

[xi] The results presented in Chapter 4.3 were gained in cooperation with Annika Stocker who wrote her master's thesis[300] on the topic of the investigation of collagen's molecular structure due to UV irradiation by Raman spectroscopy.

of the collagen signal, which proved the non-destructive character of the applied measurement parameters. The influence of the measurement routine was investigated by repetitive measurements of the same sample spot, without any UV light exposure. By that, no decisive deviations between the spectra were detected. An example for that is shown in Figure 4.31. A spot on the collagen hydrogel was chosen and a spectrum was obtained. Since the Raman measurement and the UV irradiation of the sample took place alternately, the head of the Raman microscope had to be moved upwards to fit the UV lamp above the sample. After irradiation the head was repositioned and the next Raman measurement was done. This process was simulated without irradiation for Figure 4.31 and it can be seen that the normalised spectra were nearly identical. Apart from variations in intensity, no peak shifts or changes in intensity ratios were seen. These occurring deviations were attributed to the accuracy with which the microscope head was repositioned. The measured deviations in peak intensity were taken as threshold values. Deviations between consecutive spectra that were beneath the obtained threshold for the respective peak were not considered as changes induced by UV light exposure. Before normalisation, deviations in intensity of the Si-peak at 520 cm^{-1} were detected. To exclude effects of the UV light on the silicon substrate, that might influence the evaluation, a pure silicon substrate went through the measurement-irradiation cycles. The detected deviations did not show a tendency with time of exposure but were rather arbitrary. Thus, an impact of the UV light on the silicon substrate was excluded and the deviations were assigned to the accuracy of the repositioning of the microscope head.
Figure 4.31 also shows the regions of the Raman shift that were highlighted for evaluation. Their choice is explained in Section 4.3.2. The style of the image was used throughout the evaluation with the amide bands (1150 - 1750 cm^{-1}) in the top frame, the C–H region (2800 to 3100 cm^{-1}) in the left, and the O–H region (3150 to 3550 cm^{-1}) in the right bottom frame.

4.3.2 Identification of Raman spectrum of collagen

The evaluation of the Raman spectroscopy experiments requires an assignment of the occurring single peaks and bands of the Raman spectrum to their corresponding vibration in the collagen sample. Although collagen samples have been investigated by Raman spectroscopy before, the identification of the signal is not completely universal because, *e.g.*, the signal shifts due to several reasons like state of hydration, composition of liquid environment, and chemical environment of the vibration. The immersion of the sample in a liquid environment already induces variations in the Raman signal including a loss of resolution and a reduction of the signal-to-noise ratio. Signals of Raman spectra of the same material can differ up to 19 cm^{-1} when measured in solid or liquid state.[256]

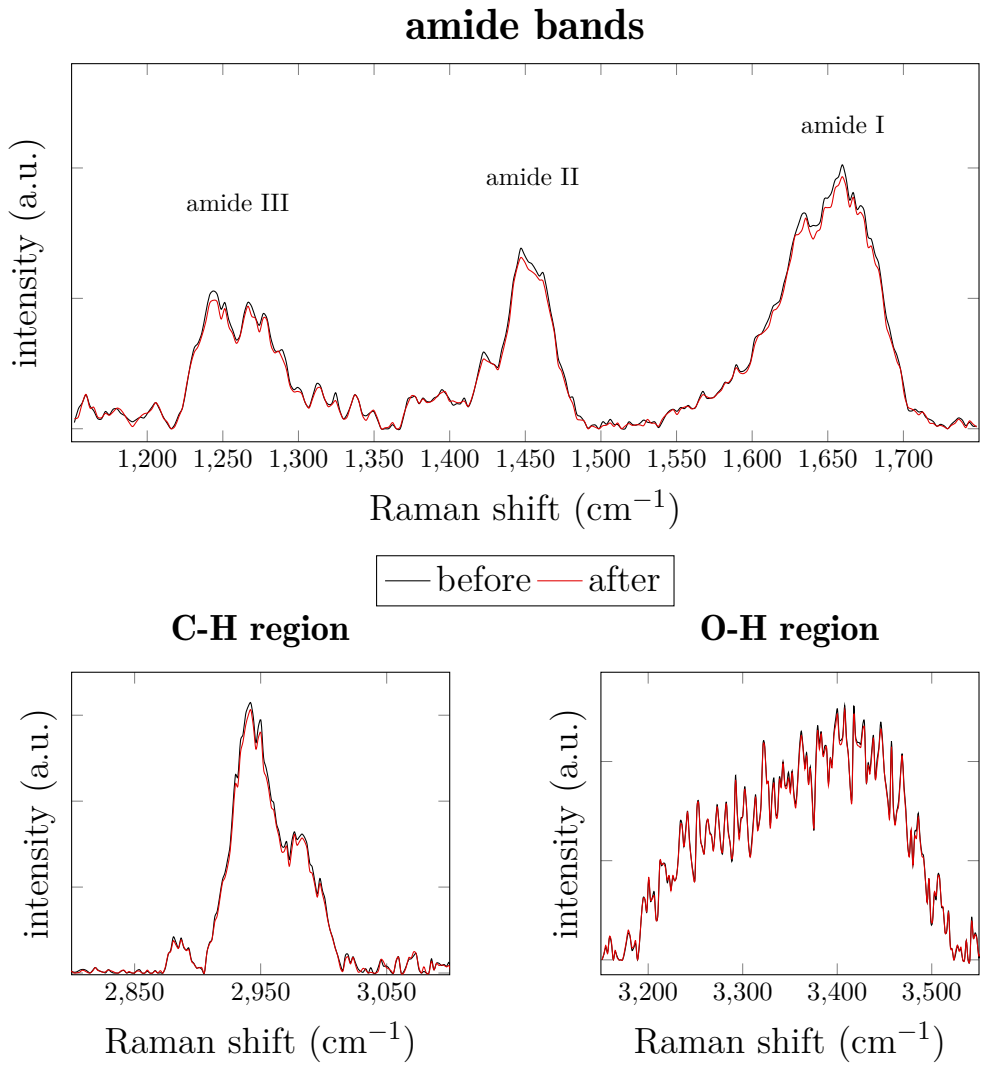

Figure 4.31.: Three regions of Raman spectra of a collagen hydrogel immersed in deionised water without exposure to UV light: amide bands (1150 to 1750 cm^{-1}), C−H stretching (2800 to 3100 cm^{-1}), and O−H vibrations (3150 to 3550 cm^{-1}). The graphs show variations introduced into the Raman spectra due to the withdrawal of the microscope head and the re-approaching of the measurement spot which was necessary for the process of alternating irradiation and measurement. Since no treatment took place, this graph was used as a reference. The black spectrum was before re-approaching of the measurement spot and the red spectrum was after.

The identification of the collagen peaks was based on values from literature in which either collagen or individual components of collagen have been investigated by Raman spectroscopy.[182,239,242,244–253,301] First results obtained during Raman spectroscopy of collagen hydrogels led to the identification of three Raman shift regions that were highlighted throughout the evaluation: 1100 to 1800 cm^{-1} (amide band region), 2800 to 3150 cm^{-1} (C–H fingerprint region), and 3150 to 3550 cm^{-1} (O–H region). Due to the second silicon peak (substrate) between approximately 940 to 1030 cm^{-1}, this region could not be used for the evaluation of characteristic Tyr and Phe peaks. Table 4.3 gives a compendium of the information that has been used for the identification of the collagen Raman spectrum and compares it to the Raman shifts in the measured collagen spectrum that were correlated with these literature values. Table 4.4 gives an overview on further characteristic peaks of a collagen spectrum that could not be found, identified, or properly assigned to the here presented Raman spectra.

4.3.3 Raman spectroscopy on ultraviolet light irradiated collagen hydrogels

In this section, the results for the exposure of collagen hydrogels immersed in deionised water to UVA and of collagen hydrogels immersed in 1xPBS or 10xPBS to UVC light are displayed. Every experiment was evaluated separately by, first, pointing out the most prominent features of the Raman spectra and, second, interpreting the found changes. The highlighted changes were compared to marker of destabilising or stabilising events in collagen or its single components as they already have been presented in literature. In this way, the understanding of displayed changes could be carried to the next experiment, which allowed for an easier access to their meaning.

Figure 4.32 shows the Raman spectra obtained of a collagen hydrogel immersed in deionised water after several 15 min intervals of exposure to UVA light. These findings were most representative for the tendencies that were observed in this measurement series. The most obvious impact of the treatment was the change in intensity of the amide I band. After 15 min of irradiation, the intensity dropped, which was also the case for the amide II and amide III band and was also indicated for the O–H region. A tendency with ongoing exposure was not seen for the C–H region.

A decreasing intensity of the amide I band correlates with a denaturation or even a fragmentation of organic samples, while an increasing intensity indicates the formation of crosslinks.[240,278] This correlation between a decreasing intensity and the degradation of collagen can even be expanded to the whole Raman spectrum of collagen.[241] As the intensity level of the Raman spectrum (cf. Figure 4.32) after 60 min of exposure was predominantly lower than the initial intensity level, the results suggested a destabilising nature of the exposure to UVA light and deionised water. Although not that prominent as in the amide I band, the decreasing intensity was also found for the O–H region. These results were a first hint for the hydrolytic character of the destabilising reactions. Fields *et al.*[244] already suggest to consult the O–H region for the detection of a peptide

Table 4.3.: Compendium of Raman signals in collagen described in literature in comparison to experimentally identified Raman signals of a collagen hydrogel.

Raman shift in literature cm^{-1}	**Raman shift in spectrum** cm^{-1}	**Identification**
622[249]	620	Phe
643[248]	642	Tyr
722[245]	718	C–S stretching
815[245]	815	C–O–C stretching
830[248]	831	Tyr
850[248]	849	Tyr stretching
1031[249]/1033[245]/1035[182]	1031	Phe
1165[61]	1157	Phe
1178[248]	1173	Tyr
1195[61]	1198	Phe
1227 - 1242[182]	1232 - 1257	β-sheet (2nd structure)
1230 - 1300[182]	1210 - 1295	Amide III band
1264 - 1272[182]	1257 - 1280	α-helix (2nd structure)
1480 - 1580[182]	1420 - 1485	Amide II band
1585[61]/1586[249]	1585	Phe
1600 - 1690[182]	1545 - 1715	Amide I band
1640[246]	1641	Ordered structure
1655 - 1662[182]	1655 - 1663	α-helix (2nd structure)
1672 - 1674[182]	1670 - 1677	β-sheet (2nd structure)
2800 - 3100[256]	$\sim$2800 - $\sim$3100	CH stretching
2898[256]	2900	Pro
3000 - 3700[244]	3150 - 3550	OH stretching
3025[256]	3023	Tyr

Table 4.4.: Compendium of literature values for the identification of Raman spectra of collagen. The list presents signals of a Raman spectrum of collagen that have been shown in literature but could not be found (-), clearly identified (ni), or were overlaid (ol) by another signal in the here presented Raman spectra.

Raman shift in literature cm^{-1}	**Raman shift in spectrum** cm^{-1}	**Identification**
510[245]	ol	S–S vibration
540[245]	ol	S–S vibration
855[242]	ni	Pro ring
860[182]	ni	Tyr
875[242,245]	ni	Hydroxyproline ring
920[245]/922[242]	ol	Proline ring
924[182]	ol	Proline
938[245]	ol	C-C stretching, backbone
1004[245,249]	ol	Phe
1007[182]	ol	Phe
1025[61]	ni	Phe
1207[249]	ni	Phe
1210[248]	ni	Tyr
1270[246]	ni	Ordered structure
1340/1360[182]	ni	Tryptophan doublet
1447[61]	-	CH_2
1606[248,249]	ni	Phe
1616[248]	ni	Tyr
2933[61]	ni	CH_3
3220[246]	ni	Collagen bound water
3320[61]	ni	NH stretching
3325[256]	ni	Collagen bound water

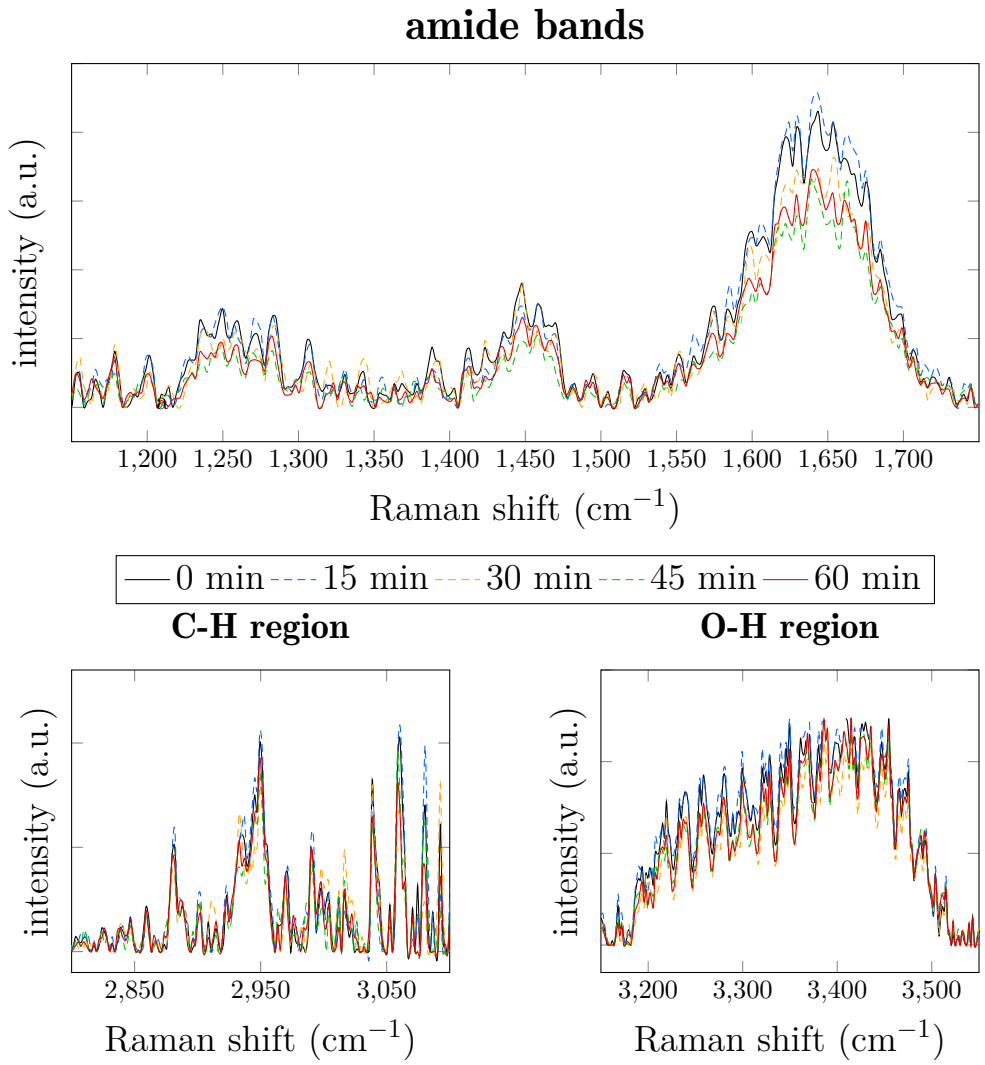

Figure 4.32.: Three regions of Raman spectra of a collagen hydrogel immersed in deionised water and exposed to UVA light: amide bands (1150 to 1750 cm^{-1}), C−H stretching (2800 to 3100 cm^{-1}), and O−H vibrations (3150 to 3550 cm^{-1}). The spectra represent different time steps of exposure: 0 min - black, 15 min - blue, 30 min - orange, 45 min - green, 60 min - red.

bond hydrolysis. As a decreasing intensity was read as marker for a hydrolysis, an increasing intensity was read as marker for a condensation reaction that was related to crosslinking. That a condensation reaction can function as a crosslinker for collagen samples is shown for DHT treatment in which intermolecular crosslinks are formed by esterification or amide formation.[271] Regarding the C–H region, the addressed fluctuation in the intensity was most prominent for Raman shifts between 2995 and 3115 cm^{-1}. For Raman shifts higher than 3000 cm^{-1}, the C–H signals were not exclusively but predominantly correlated with aromatic amino acids.[256] Two representatives for aromatic amino acids are Tyr and Phe that are mostly found in the telopeptides of collagen. Thus, an involvement of the telopeptides in the response of the collagen samples towards the UV light exposure was stated, supporting earlier findings that the telopeptides carry major responsibility for the mechanical stability and structural changes.[33,87,302] To underline that beyond 60 min of exposure, further destabilisation of the sample was the leading mechanism, the Raman spectrum after 180 min of exposure is depicted in Figure D.1 showing the continuous decrease in intensity for all signals.

As a direct comparison, Figure 4.33 shows the findings for a UVC irradiated collagen hydrogel immersed in 1xPBS. The displayed results represent the most distinct changes. As for Figure 4.32, the final intensity of the amide I band decreased in comparison to its initial intensity. However, in comparison to the initial value the intensity reached a maximum value for 30 min and 45 min of irradiation time before it dropped. For the highest intensity, the amide I band was shifted to lower wave numbers. A shift that was recovered after 60 min of exposure. A similar behaviour as seen for the amide I band was observed for the O–H region and the amide III band (without the region around 1260 cm^{-1}). In the amide II band the intensity decreased gradually with increasing exposure time. The C–H region exhibited several tendencies, but for the most prominent band (2800 to 3030 cm^{-1}), the intensity reached a minimum value after 30 min to 45 min followed by an increase below the initial intensity. For the Raman signals above 3100 cm^{-1}, there was a fluctuation in the intensity for the single peaks.

According to the evaluation of Figure 4.32, the increase in intensity of the amide I band and its shift to lower wavenumbers was correlated to the formation of crosslinks. Thus, within the first 60 min of exposure, crosslinks were formed, but then destabilisation became the governing mechanism as indicated by a drop in the intensity. During the decrease in intensity, the amide I band shifted to higher wave numbers, which was interpreted as a destabilisation marker.[240] Regarding the secondary structure, the absolute intensity of the peaks that were expected to represent the α-helix (1655 to 1663 cm^{-1}) and β-sheet (1675 cm^{-1}) in the amide I band showed the same behaviour as stated for the whole amide I band. The relative ratio between the β-sheet and the α-helix peak, however, showed a decreasing value during exposure that was associated with the occurrence of stabilising events. During the destabilising process, the ratio increased again. This agreed with the values obtained during the UVA irradiation of collagen hydrogels immersed in deionised water, where the β-sheet to α-helix peak ratio had an overall increasing tendency. As α-helix and β-sheet are possible

structures of the telopeptides, changes during UV exposure indicated that this region was involved in the stabilisation (and formation) processes of collagen, most likely by formation of covalent links between the triple helices.[64,88,91,303,304] Again there was a correlation between the intensity development of the amide I band with the O–H region. A non-related behaviour of the intensity with advancing exposure was seen for the C–H region. The amide I band-associated crosslinking period was accompanied by a decreasing intensity of the region from 2902 to 3015 cm^{-1}, whereas for the predominantly aromatic amino acid region the trend mostly followed the amide I band. The region from 2902 to 3015 cm^{-1} was mostly associated with the C–H stretching of aromatic and aliphatic amino acids expanded by signals form charged amino acids, Pro, threonine (Thr) and His.[256] The band-like structure mostly prohibited the identification of individual amino acid signals. The increase of the Tyr peak (3023 cm^{-1}) and the Pro peak (2900 cm^{-1}) during the crosslink-phases could be read as a further indication of the involvement of the telopeptide in the stabilising effect promoted by Pro rests. To show that there was no more stabilisation taking place, the Raman spectrum is depicted after 120 min of exposure in Figure D.2. More distinct effects of further destabilisation beyond 60 min of exposure were seen for another sample exposed to UVC light and immersed in 1xPBS (cf. Figure D.3). Although the stabilisation was not as pronounced as in Figure 4.33, it was clearly visible. Additionally, the Raman spectrum acquired after 240 min of UVC exposure exhibited a distinct decay of the sample. The plots of the integral intensity for the Raman spectra of longer exposure times than 60 min are shown in Figure D.4.

Figure 4.34 shows the Raman spectra for a UVC irradiated collagen hydrogel immersed in 10xPBS for 60 min of exposure. As the amide II and the amide III band were already comparatively weak in the untreated state, they nearly disappeared while the intensity of the amide I band was constantly increasing. Its intensity reached a maximum value after 45 min of UVC irradiation with a slight subsequent decrease. The same held true for the O–H region. For the C–H region, the signals got more distinct with advancing time of exposure and beyond 3000 cm^{-1}, the variations from the intensity tendency seen in the amide I band accumulated.
The presented measurement in 10xPBS solution expressed a strong tendency to crosslinking without any strong destabilising effects, as was seen in and Figure 4.32 and Figure 4.33, including the correlation between the amide I band and the O–H region. As for the measurement in 1xPBS, the β-sheet to α-helix peak ratio tended to decrease during the occurrence of crosslinking events and *vice versa*. Apart from the observations made regarding the involvement of the telopeptides, the C–H region did not allow for any further clear interpretation. To summarise the evolution of the peak intensity of the amide I band and the O–H band for the Raman spectroscopy measurements on collagen hydrogels, the integral intensity of both bands was evaluated and compared, which is shown in Figure 4.35. In this way, the described behaviour is displayed more obviously and underlines the evaluation, showing the decrease of the peak intensity for the gel immersed in deionised water and its temporal increase for collagen hydrogels immersed in PBS. Additionally, the similar behaviour of both bands is depicted. It could be seen that not all the Raman spectra exhibited the same de-/stabilisation marker.

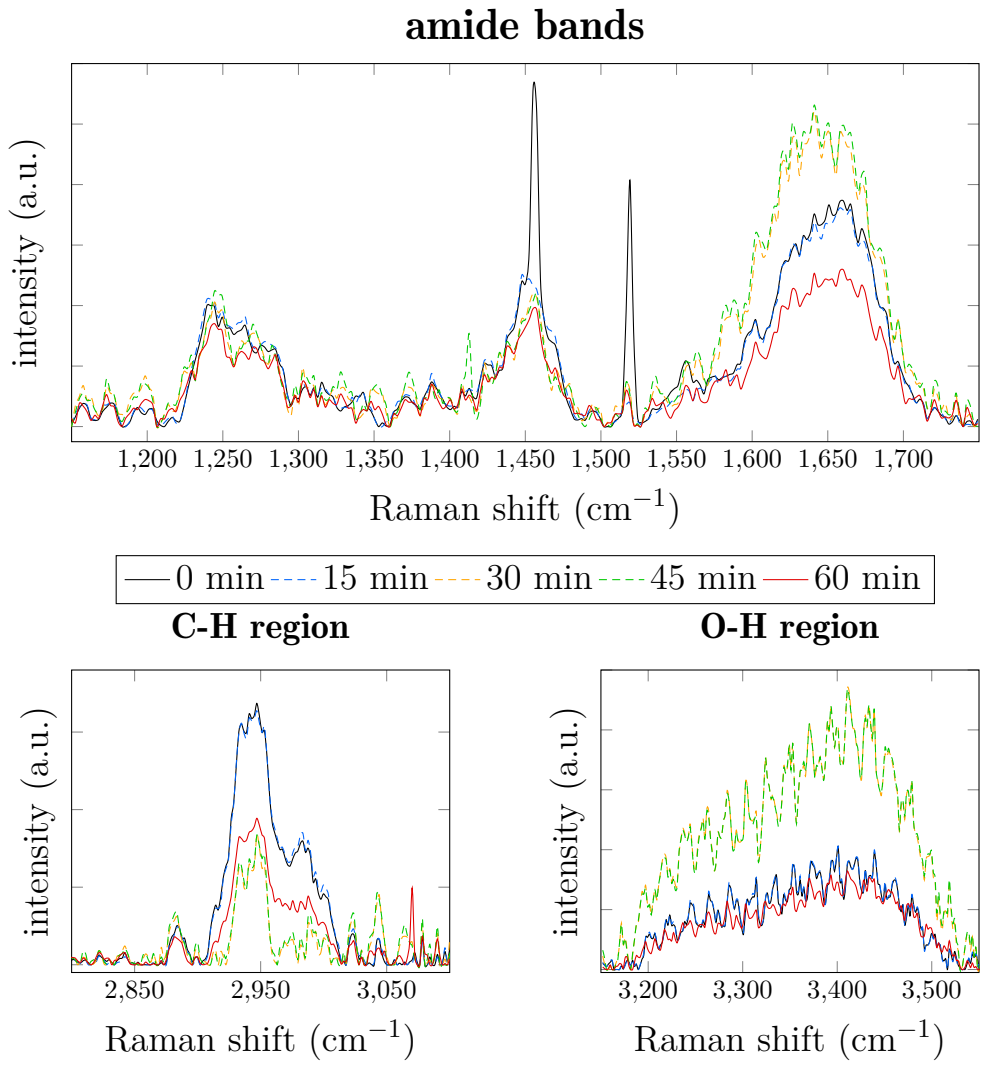

Figure 4.33.: Three regions of Raman spectra of a collagen hydrogel immersed in 1xPBS and exposed to UVC light: amide bands (1150 to 1750 cm^{-1}), C−H stretching (2800 to 3100 cm^{-1}), and O−H vibrations (3150 to 3550 cm^{-1}). The spectra represent different time steps of treatment: 0 min - black, 15 min - blue, 30 min - orange, 45 min - green, 60 min - red.

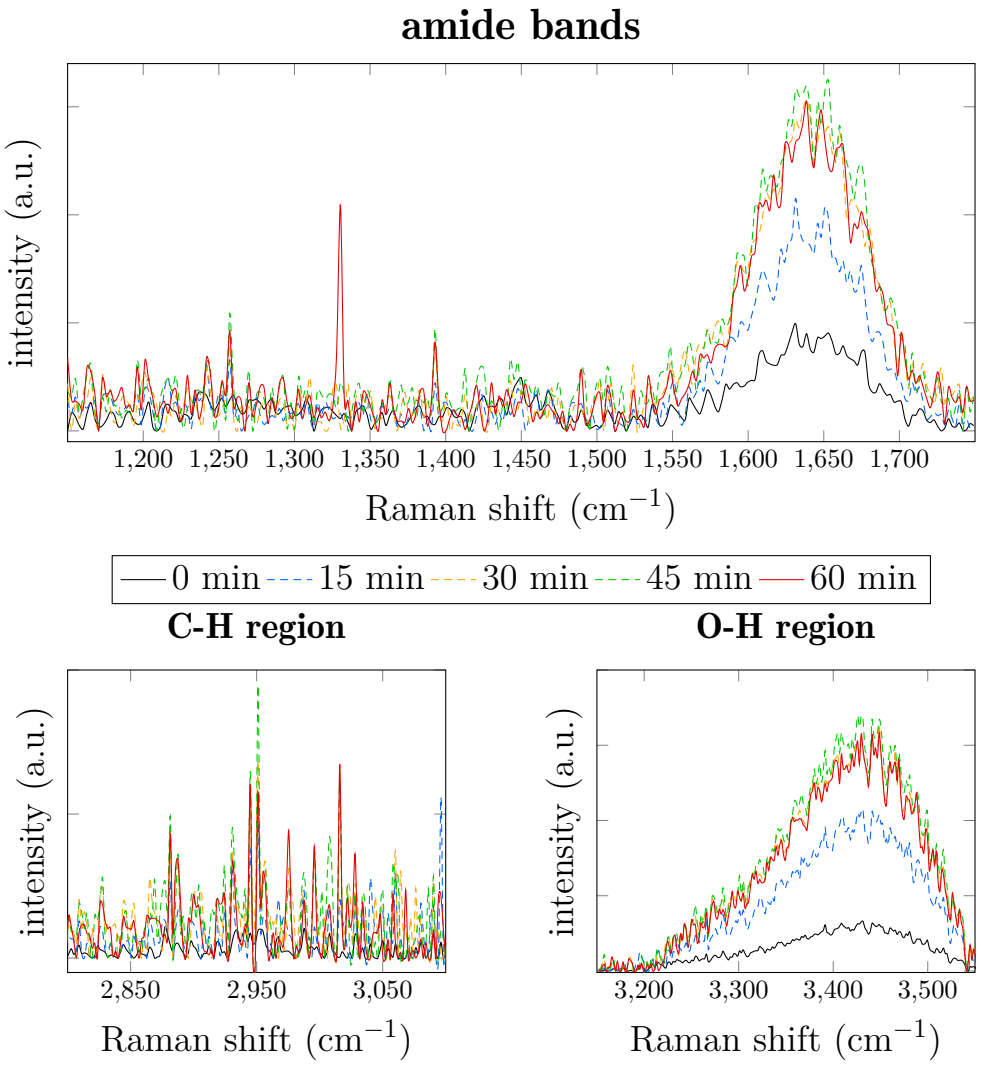

Figure 4.34.: Three regions of Raman spectra of a collagen hydrogel immersed in 10xPBS and exposed to UVC light: amide bands (1150 to 1750 cm^{-1}), C−H stretching (2800 to 3100 cm^{-1}), and O−H vibrations (3150 to 3550 cm^{-1}). The spectra represent different time steps of treatment: 0 min - black, 15 min - blue, 30 min - orange, 45 min - green, 60 min - red.

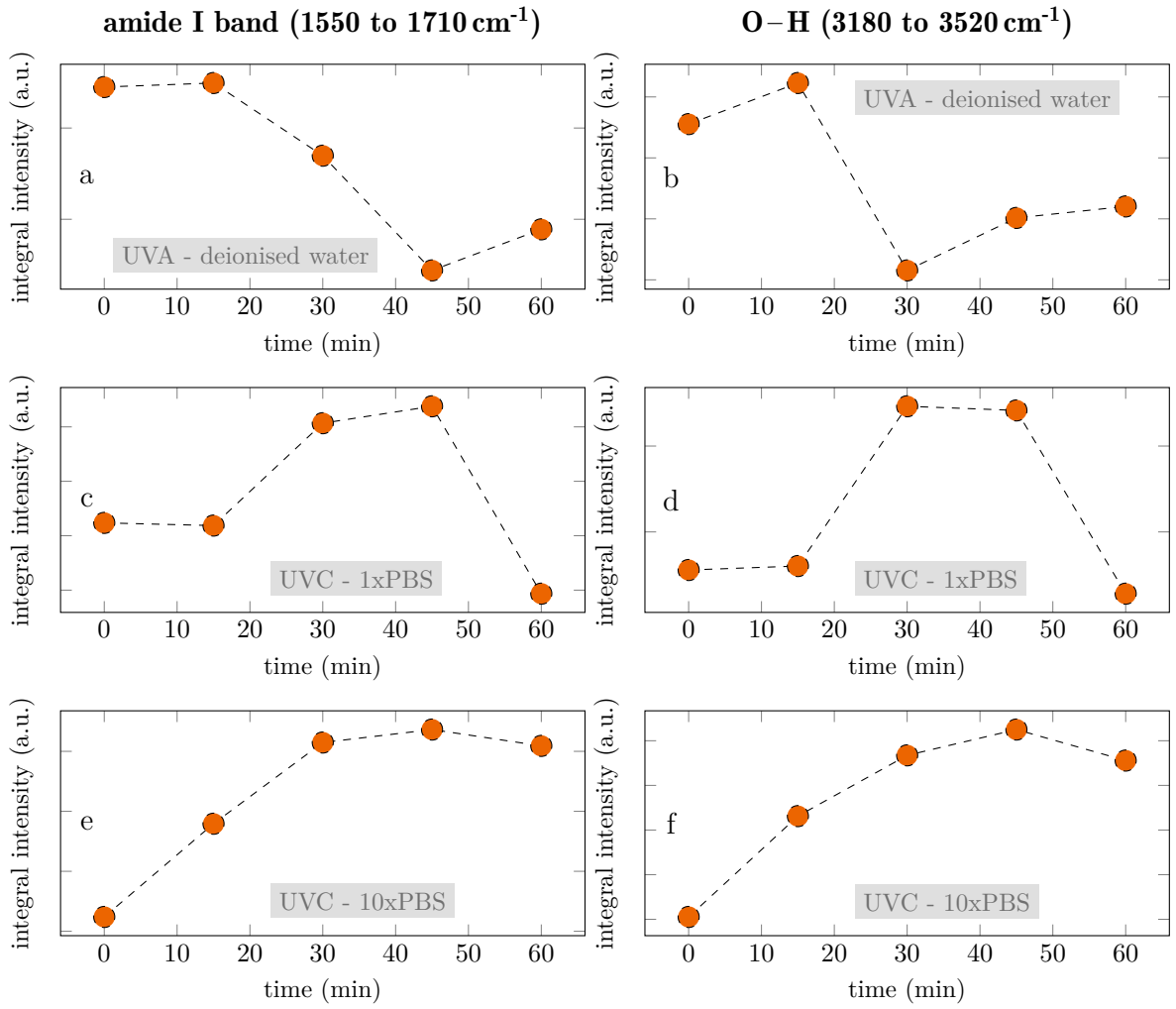

Figure 4.35.: The integral intensities for (a, c, e) the amide I band (1550 to 1710 cm^{-1}) and (b, d, f) the O−H band (3180 to 3520 cm^{-1}) from Figure 4.32 (UVA light and deionised water in a,b), Figure 4.33 (UVC light and 1xPBS in c,d), and Figure 4.34 (UVC light and 10xPBS in e,f) were evaluated from the Raman spectroscopy measurements on the collagen hydrogels to clarify the evolution of the peak intensity with advancing exposure time.

However, the presented findings supported each other and exhibited similarities. It should not be stated that the presented destabilisation or stabilisation marker indicated the exclusive occurrence of one process. It was more likely that stabilising and destabilising processes happened simultaneously with one being the superior part depending on treatment and initial sample conditions. The interplay between these two processes would lead to sample-specific Raman spectra. As further origins for deviations, the heterogeneity of the collagen hydrogels, varying initial states of crosslinking, and the measurement depth were suggested. To show the influence of the measurement point in z-direction and to discuss the penetration depth of the UV exposure, a collagen hydrogel immersed in 1xPBS was exposed to UVC light for 60 min. Spectra were obtained from the surface of the sample and from a depth of approximately 12 µm before and after exposure (Figure 4.36). The comparison revealed that the resulting Raman spectrum depended on the measurement position, which emphasised the necessity of repeatedly measuring the same spot for comparable results. For the measurements at the surface, the depicted amide region answered the findings of the extended experiments with UVC irradiated collagen hydrogels immersed in 1xPBS (cf. Figure 4.33) by showing that there was a general decrease in intensity of the amide I band between the untreated state and 60 min of exposure. The same behaviour was seen for the comparison of the Raman spectra taken in the depth between the untreated state and after 60 min of exposure, leading to the conclusion that the radiation effects penetrated at least 12 µm into the collagen hydrogel.

4.3.4 Further ultraviolet light-liquid combinations

The two presented combinations of UV light source and liquid environment (UVA and deionised water/UVC and 1xPBS) were chosen as examples for the predominant introduction of destabilising and stabilising mechanisms in collagen hydrogels, respectively. By knowing the influence of the exposure conditions on the mechanical properties, the resulting Raman spectra were searched for markers that describe the expected behaviour and compare them to literature. Nevertheless, further measurement conditions were applied and evaluated. Figure 4.37 shows the amide band region for a collagen hydrogel immersed in 1xPBS and exposed to UVA light (Figure 4.37a), a collagen hydrogel that was immersed in deionised water but not rinsed after synthesis and exposed to UVC light (Figure 4.37b), and a collagen hydrogel that was immersed in deionised water but properly rinsed with deionised water and exposed to UVC light. The respective integral intensities over time of exposure are depicted in Figure 4.38. For the sample exposed to UVA light, an overall decrease in peak intensity of the amide I band as well as of the O – H band could be seen indicating destabilising mechanisms. While this did not agree with the results shown for the tensile tests (cf. Figure 4.30b), destabilisation was found during the acquisition of the indentation modulus (cf. Figure 4.14a). On the one hand, this inconsistency supported the choice of the two mentioned model systems (UVA and deionised water; UVC and 1xPBS) as measurements

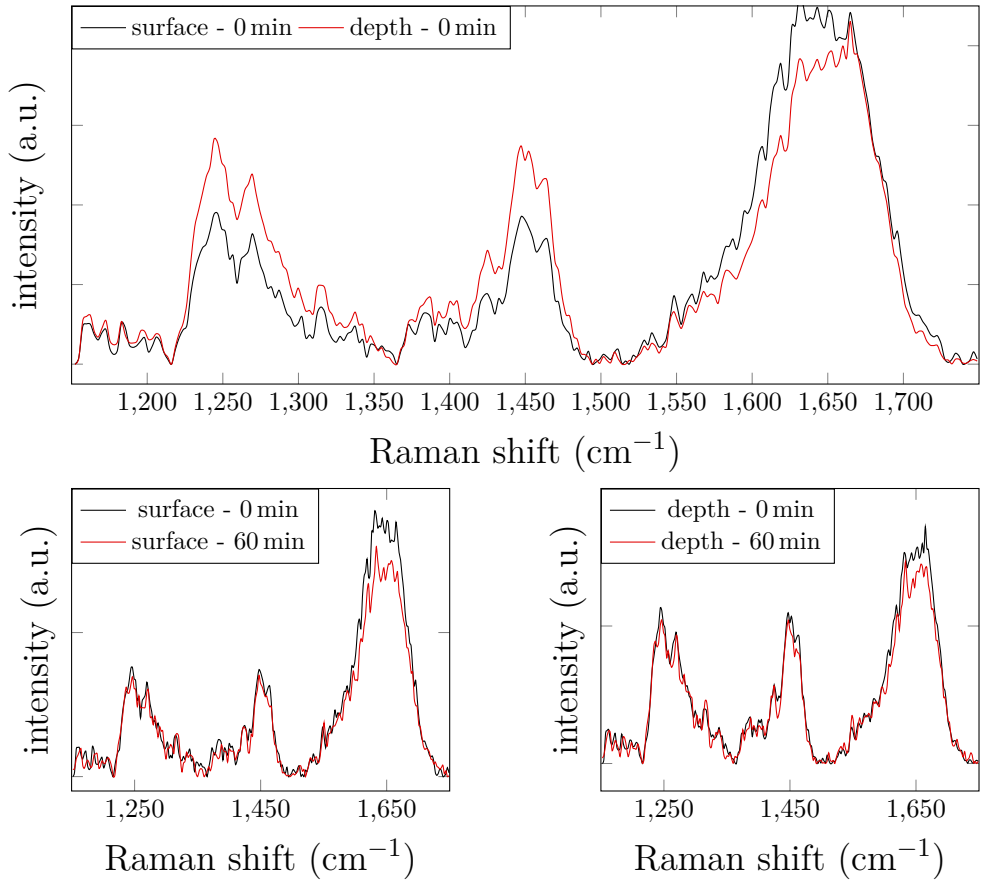

Figure 4.36.: The amide bands region (1150 to 1750 cm^{-1}) of the Raman spectrum of a collagen hydrogel immersed in 1xPBS and irradiated with UVC light is displayed. Raman spectra were obtained at the surface of the sample and at a spot 12 µm below ('depth') to investigate the influence of the measurement depth on the results. The single graphs show a comparison between 'surface' and 'depth' before treatment, the 'surface' spot before and after treatment, and the 'depth' spot before and after treatment.

conditions for the Raman spectroscopy experiments. For both cases, the mechanical response of the collagen fibrils was consistent for the majority of the measurements (cf. Figure 4.14, Figure 4.13, and Figure 4.30). Thus, changes in the Raman spectra could be linked to an increase (UVC and 1xPBS) or a decrease (UVA and deionised water) of the modulus. On the other hand, the results from Raman spectroscopy supported that not only the addition of 1xPBS decided the occurring changes in the collagen sample. The UV light source has also to be taken into account, as shown by the following two experiments. Both samples exposed to UVC light were measured in an environment of deionised water. However, the first sample (cf. Figure 4.37b) was not rinsed with deionised water after synthesis while the second one (cf. Figure 4.37c) was. The first collagen hydrogel exhibited increasing peak intensities for the amide I band and the O−H band associated with occurring stabilising mechanisms. This was ascribed to PBS residues in the gel that had been introduced during synthesis and had not been removed subsequently. For the second sample the trends of the integral intensities of the amide I band and the O−H band were not similar, and the Raman signal did gain more noise with progressing exposure time. The latter effect got more prominent with increasing exposure time, as can be seen in Figure D.5. Additionally, the change of the integral intensities of the amide I band and the O−H band with progressing exposure time are displayed in Figure D.6. Although the increasing noise rendered an evaluation of the peak intensity questionable, the increasing noise itself was explained as sign for sample decomposition. On the one hand, this supported the findings of the mechanical stability of collagen samples with progressing UVC exposure when immersed in deionised water. On the other hand the question of why the increasing noise as a sign for decomposition has not been seen for the Raman spectra of the hydrogel immersed in deionised water and exposed to UVA light arose. At this point, an influence of the UV light source was proposed. Short-wavelength UVC light caused more damage to the collagen when directly being irradiated than the long-wave UVA light. It was suggested that the introduction of PBS generated a shielding effect against this aggressive decomposition.

The Raman spectroscopy of fully hydrated and UV irradiated collagen hydrogels gave some insight into structural changes of three-dimensional system that in similar form were applied as substrate material in tissue engineering. Regarding the presented AFM experiments, it was also of interest to attempt the extraction of the structural information from separated collagen fibrils. As a potential outcome, these measurements could be correlated to the detected changes in the mechanical properties. Additionally, a comparison between three-dimensional and one-dimensional collagen structures could be made.

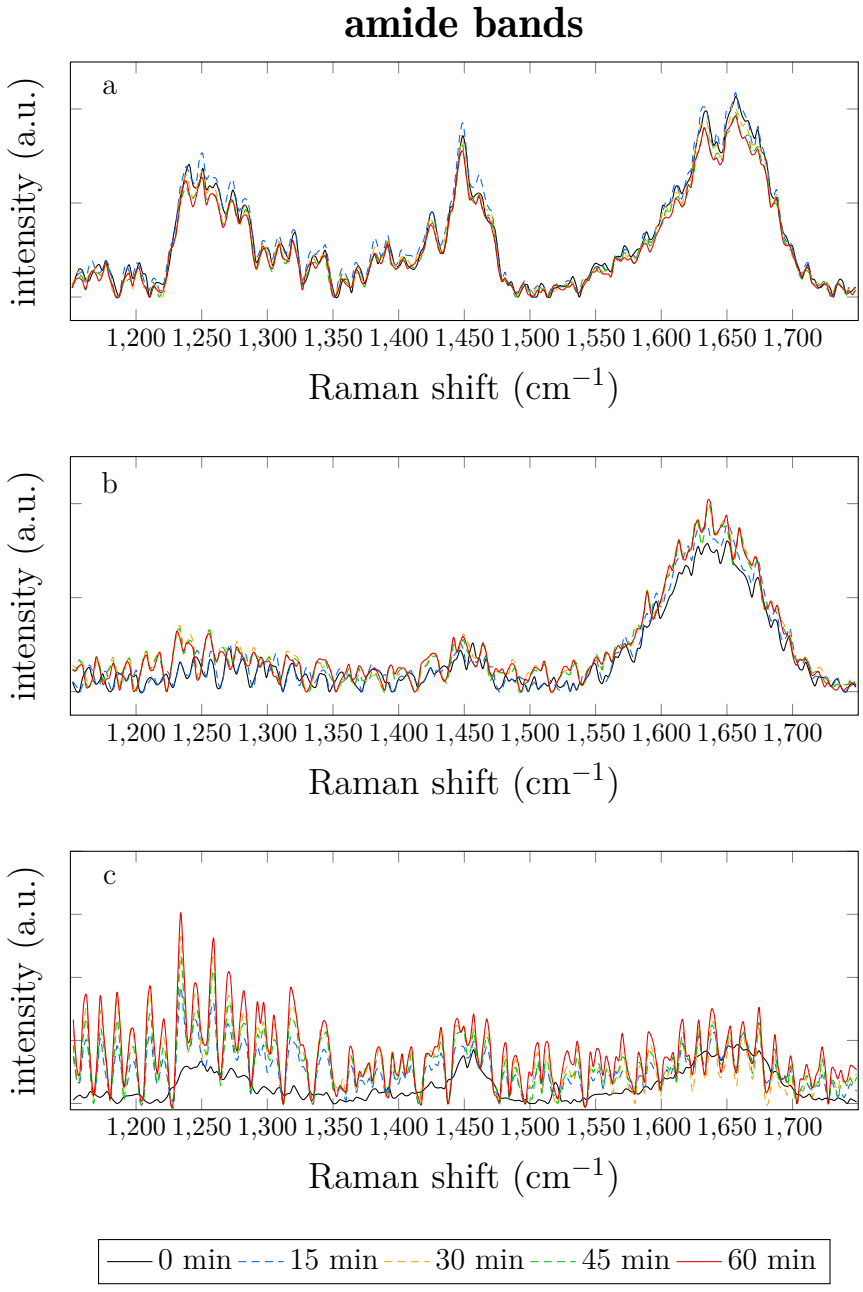

Figure 4.37.: The amide bands (1150 to 1750 cm^{-1}) of Raman spectra of collagen hydrogels immersed in (a) 1xPBS and (b,c) deionised water and exposed to (a) UVA and (b,c) UVC light are displayed. For (c) the collagen hydrogel was rinsed with deionised water after the synthesis while for (b) the collagen hydrogel was not. The spectra represent different time steps of exposure: 0 min - black, 15 min - blue, 30 min - orange, 45 min - green, 60 min - red.

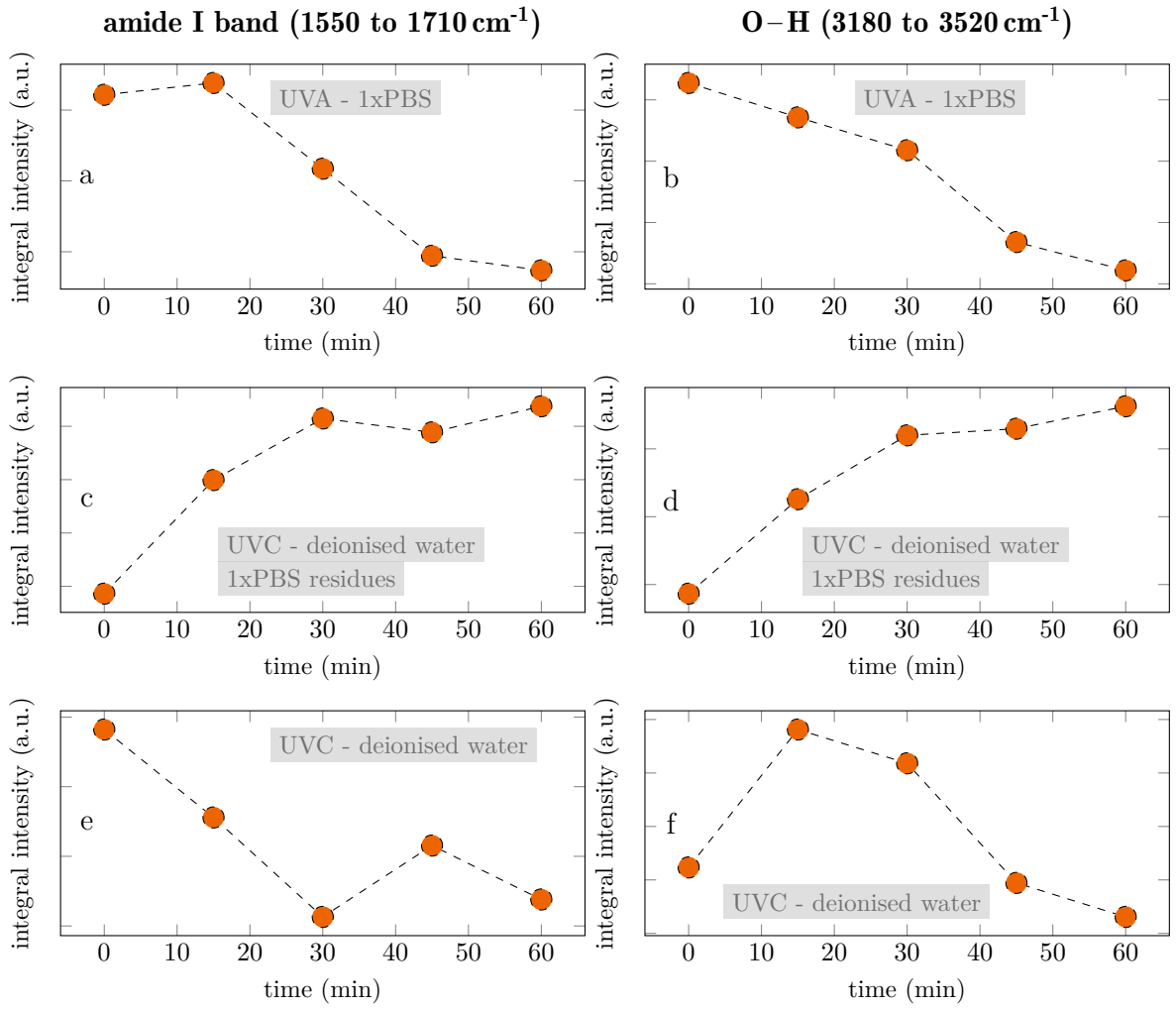

Figure 4.38.: The integral intensities for (a, c, e) the amide I band (1550 to 1710 cm^{-1}) and (b, d, f) the O–H band (3180 to 3520 cm^{-1}) from Figure 4.37 were evaluated from Raman spectroscopy measurements on collagen hydrogels to clarify the evolution of the peak intensity with advancing exposure time. The two bands were compared to illustrate their similar behaviour.

4.3.5 Surface Enhanced Raman Spectroscopy on ultraviolet light exposed collagen fibrils

The separated collagen fibrils were exposed to the same experimental conditions as the collagen hydrogels. Yet, the sample needed to be brought in contact with silver to enable the enhancement of the Raman signal. The application of a silver substrate resulted in an increased background signal that overlaid the Raman signal of the collagen sample and a decreased the signal-to-noise ratio. The corresponding Raman spectrum is shown in the appendix (cf. Figure D.7). As a further option for the realisation of SERS measurements, silver nanoparticle with a diameter of 20 nm were added to the collagen solution before incubation. Preparatory work yielded best results with the addition of 50 µl of silver nanoparticle solution to the collagen solution. The Laser power was reduced to 1 mW.

The addition of silver nanoparticles resulted in evaluable data, as shown in Figure 4.39, for separated collagen fibrils immersed in deionised water and irradiated with UVA light for 60 min. The results of the SERS measurements, again, show the amide band, the C−H, and the O−H region with results of the UV exposure in 15 min intervals. The same information was exhibited as it was the case for the collagen hydrogels, yet, differences were apparent. The intensity ratios of the amide bands varied in comparison to the hydrogels. This effect occurred depending on the x-y-position of the measurement spot on the sample. For the C−H region, the prominent band from 2902 to 3015 cm^{-1} yielded single peaks, and the O−H region generated two bands.
The amide region of the UVA irradiation experiment showed a steadily decreasing signal intensity for the amide I and amide III bands. For the amide II band, an intensity increase after 30 min was detected similar to the measurements of the collagen hydrogel under the same measurement conditions (cf. Figure 4.32). The strong signal after 60 min of exposure, however, was irregular. For the C−H and the O−H region, the intensity equaled the one of the amide I band.
An overall destabilisation of the UVA exposure for collagen fibrils immersed in deionised water could be detected and it was seen that the correlation between the amide I band and the O−H region also held true for the measurements of separated collagen fibrils. Due to the distinct signals in the C−H region, an identification of the corresponding amino acids could be done for the strong signals with the values provided by Howell *et al.*[256] which results in the suggestions seen in Table 4.5, where Raman shifts closest to the found signals are listed. Due to the changed chemical environment, the list could not claim completeness. Since the change in intensity was similar for all the peaks, a deviating behaviour for a special amino acid could not be highlighted.

Figure 4.40 shows the Raman spectra for UVC irradiated separated collagen fibrils immersed in 1xPBS. The amide I and amide III band showed the highest signal intensity for 15 min of exposure with a subsequent decrease. The amide II band showed a similar intensity for the untreated state and 60 min of exposure with lowered intensity levels for the meantime measurements. The O−H region went along with the amide I band.

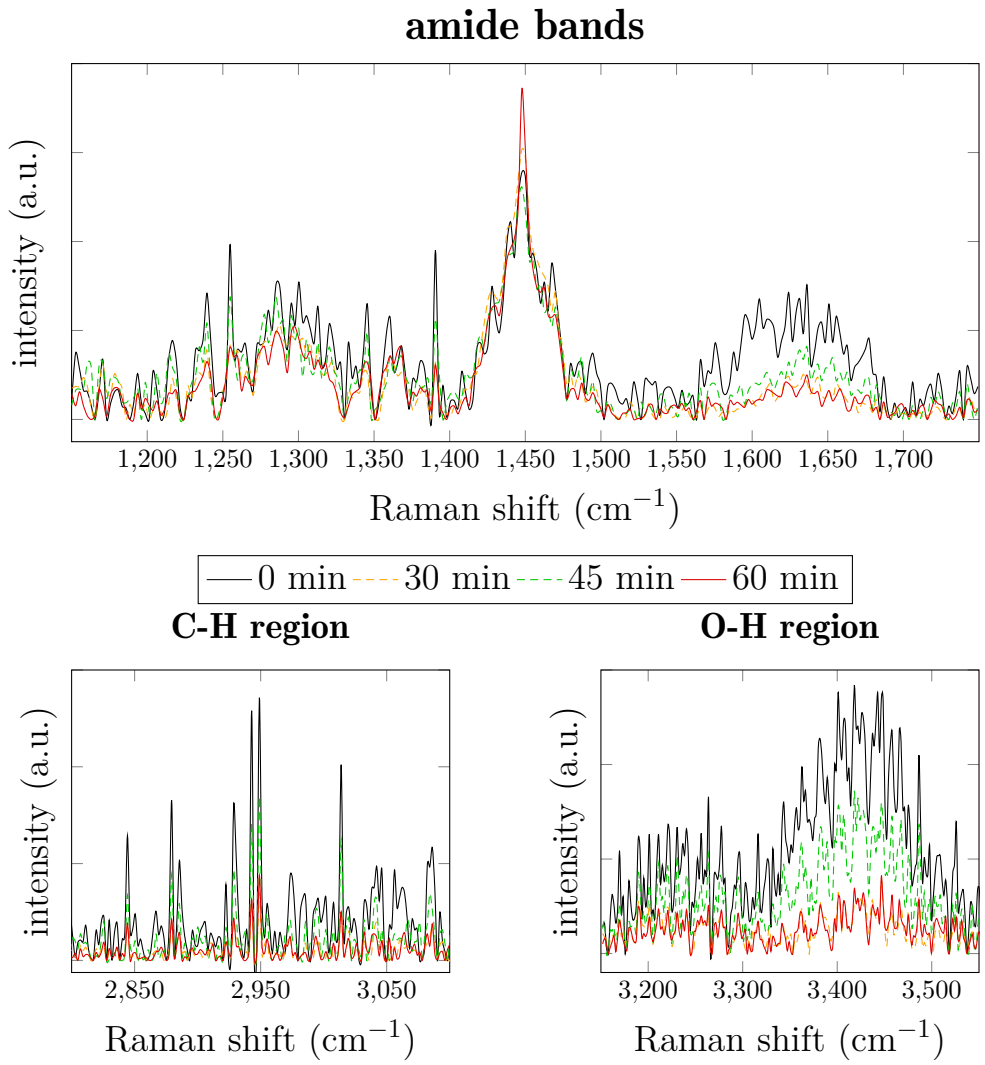

Figure 4.39.: Three regions of SERS spectra of collagen fibrils immersed in deionised water and exposed to UVA light: amide bands (1150 to 1750 cm^{-1}), C−H stretching (2800 to 3100 cm^{-1}), and O−H vibrations (3150 to 3550 cm^{-1}). The spectra represent different time steps of treatment: 0 min - black, 30 min - orange, 45 min - green, 60 min - red.

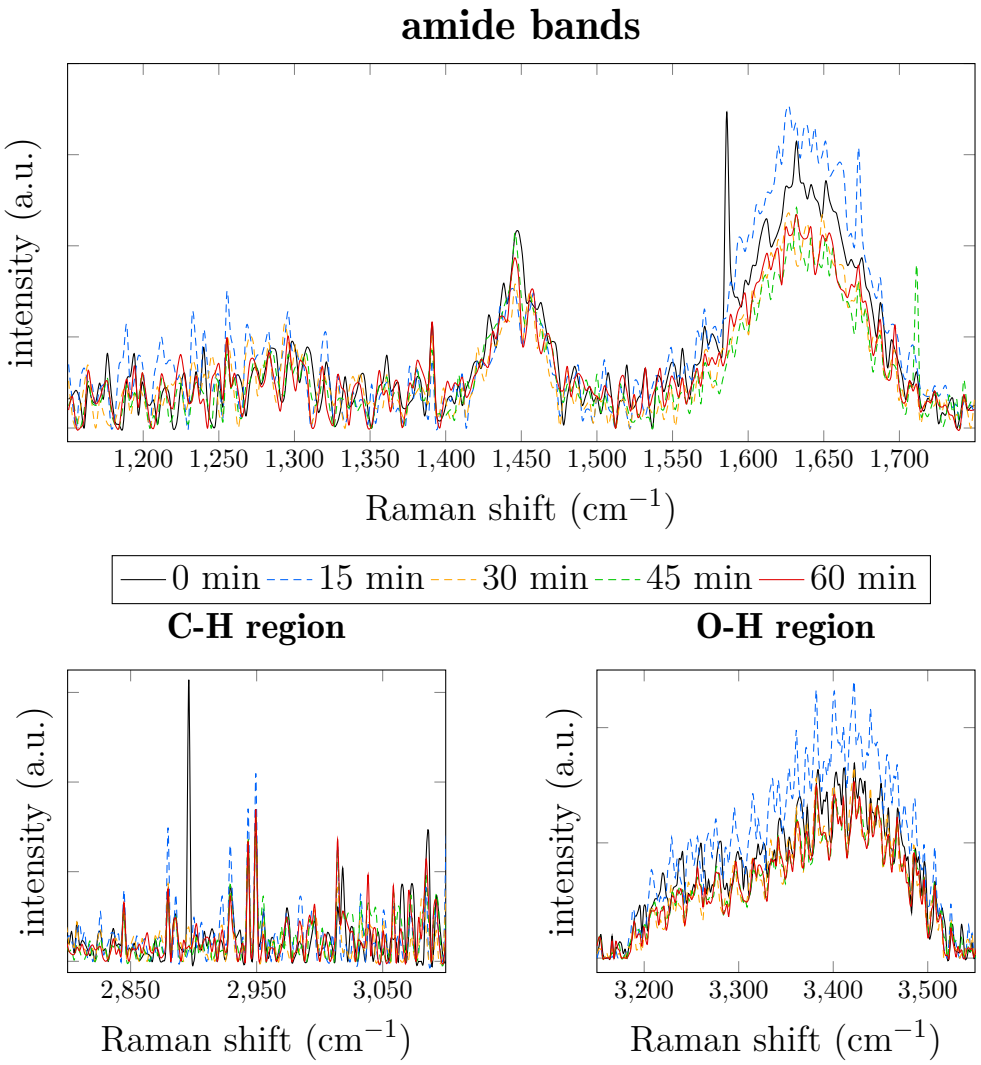

Figure 4.40.: Three regions of SERS spectra of collagen fibrils immersed in 1xPBS and exposed to UVC light: amide bands (1150 to 1750 cm^{-1}), C−H stretching (2800 to 3100 cm^{-1}), and O−H vibrations (3150 to 3550 cm^{-1}). The spectra represent different time steps of treatment: 0 min - black, 15 min - blue, 30 min - orange, 45 min - green, 60 min - red.

Table 4.5.: Measured Raman signals of collagen fibrils immersed in deionised water and irradiated with UVA light during a SERS experiment. The values were compared to identified C−H vibrations of amino acids adapted from Howell *et al.*[256] between 2883 and 3019 cm^{-1}. The intensity of the signals is indicated by w (weak), m (medium), and s (strong).

Raman shift in spectrum cm^{-1}	**Raman shift in literature** cm^{-1}
2880	leucine (Leu) (2883 s)
2885	Lys (2884 m), isoleucine (Ile) (2885 s)
2923	Thr (2923 w), Pro (2925 w)
2929	Ser (2929 w), Ile (2932 s)
2944	cysteine (Cys) (2941 s), Leu (2941 s), Lys (2941 s), Ile (2948 s)
2950	Phe (2951 m), Tyr (2951 m), Glu (2952 s), valine (Val) (2953 s), Pro (2954 s)
3014	Cys (2008 w), Gly (3019 w)

For Raman shifts below 3000 cm^{-1} in the C−H region, the highest intensity is seen after 15 min of exposure. The general development of the Raman spectra suggested initially dominating crosslinking mechanisms (< 30 min of exposure) followed by mostly destabilising effects. The identification of the markers for the secondary structure was not certain and, thus, did not allow for an evaluation. In the C−H region, the same peaks were distinct as for the SERS measurement with the UVA irradiation (cf. Figure 4.39). In general, the recorded changes for this measurement were not distinct which rendered further detailed descriptions questionable.

Figure 4.41 shows the Raman spectra for UVC irradiated separated collagen fibrils immersed in 10xPBS for up to 60 min. Again, the variations in the Raman spectra were, for the most part, not significant, which impeded the derivation of clear tendencies. Yet, the strongest tendency was found for the O−H region supporting the identification of the similar intensity development for the amide I band since their correlation had been established throughout the Raman spectroscopy experiments. Hence, a steady increase in intensity with advancing time of exposure was recorded.
With respect to the signal of the O−H region, a stabilising effect throughout the treatment was suggested, although the strongest intensity of the amide III band was found after an exposure time of 15 min. The distinct peaks in the C−H region were in agreement with the peaks identified in Figure 4.39.

Overall, the presented SERS measurements did not allow for a detailed analysis of the structural changes induced by the UV light exposure, as was the case for the investigation of the collagen hydrogels. This could be attributed to the reduced sample volume whose changes were minor in comparison to changes summed up over several collagen fibrils, as was the case for the measurements of the hydrogels. Yet, the general trends, as

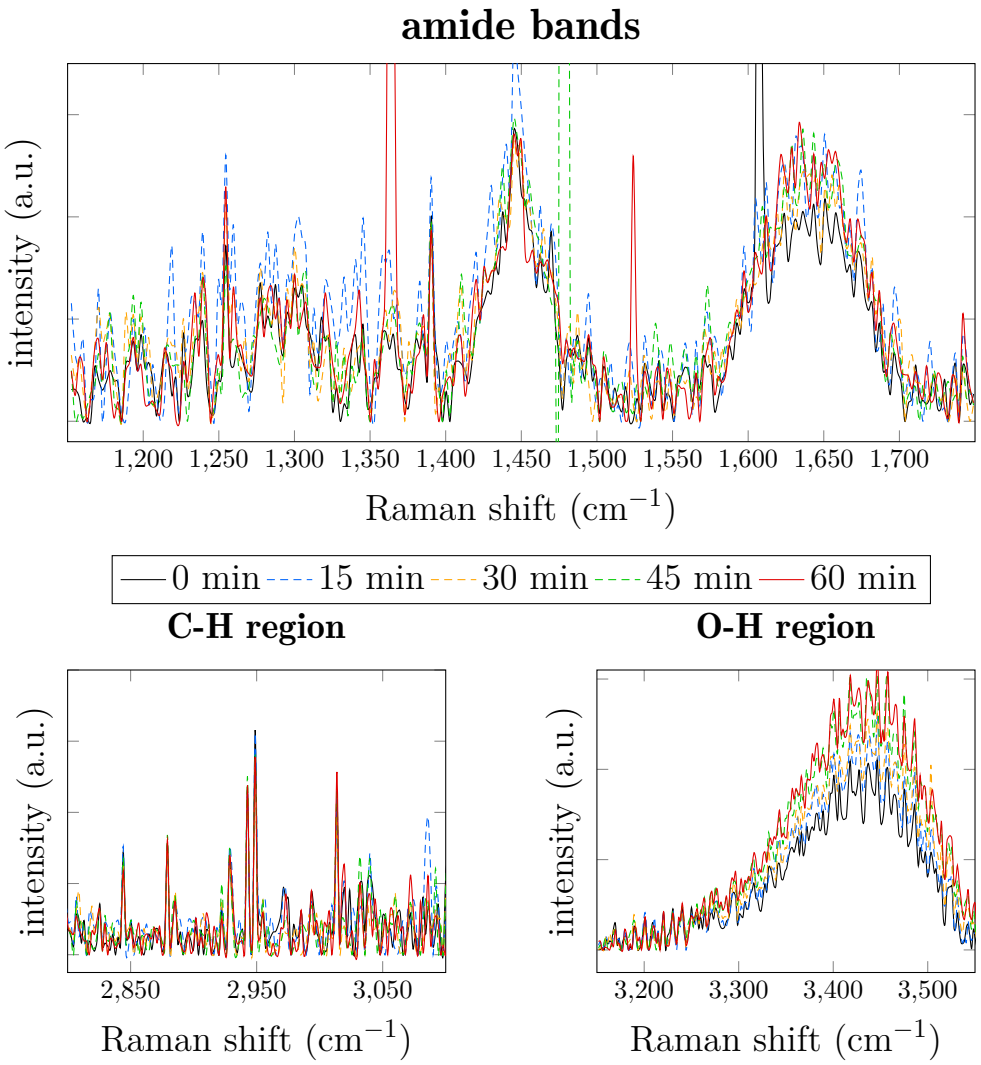

Figure 4.41.: Three regions of SERS spectra of collagen fibrils immersed in 10xPBS and exposed to UVC light: amide bands (1150 to 1750 cm^{-1}), C−H stretching (2800 to 3100 cm^{-1}), and O−H vibrations (3150 to 3550 cm^{-1}). The spectra represent different time steps of treatment: 0 min - black, 15 min - blue, 30 min - orange, 45 min - green, 60 min - red.

they were carved out for the measurements on the hydrogels, could be confirmed. Similar to the evaluation of the Raman spectroscopy measurements of the collagen hydrogels, the integral intensities of the amide I band and the O−H band were evaluated and compared in Figure 4.42 for all investigated combinations. Again, similarities between the evolution of the peak intensities with advancing exposure time for both bands can be stated, as well as the influences of the varied measurement conditions. Deviating behaviour is seen for the exposure of collagen fibrils immersed into 10xPBS to UVC (Figure 4.42e and Figure 4.42f). Although the integral intensity of the amide I band reached a maximum after 30 min exposure time, the integral intensity of the O−H band kept increasing.

4.3.6 Summary

The aim of Section 4.3 was to explain the investigation of structural changes in collagen samples in deionised water or PBS due to UV irradiation with the help of Raman spectroscopy. The samples were irradiated in 15 min steps and the subsequently recorded spectra were compared to each other to evaluate the development of special Raman signals with time of exposure. Hydrogels were measured as representatives for three-dimensional collagen structures and separated collagen fibrils were recorded by SERS. The results should help to understand the observations that were made during the AFM-based experiments.

Special attention was paid to the amide bands (1100 to 1800 cm^{-1}), C−H stretching of the amino acids (2800 to 3150 cm^{-1}), and O−H vibrations (3150 to 3550 cm^{-1}). In general, an increase in signal intensity was associated with stabilising effects occurring in the collagen and *vice versa*. Thus, the comparison of the successively recorded Raman spectra of the hydrogels suggested an overall destabilising effect on the collagen structure when UVA light was applied in combination with deionised water as liquid environment. After 60 min of UVC irradiation of hydrogels immersed in PBS, the signal intensity also tended to be beneath the one of the untreated state. In between, however, signal intensity increased that was suggested to correlate with a strengthening effect of the collagen structure. This was mainly derived from the behaviour of the amide region that describes the peptide bonds which link the amino acids. The amide I band, especially, mostly coming from C=O stretching, exhibited different intensity levels throughout the UV irradiation. The O−H stretching vibrations were interpreted as quantity for the water that was bound or free within the collagen and their behaviour correlated to the properties of the amide I band. It was concluded that the stabilising reactions, derived from the amide I band, were condensation reactions, derived from an increase in the O−H stretching vibrations and that the destabilising reactions possessed a hydrolytic character. While the assignment of the peaks in the C−H region to specific amino acids bore uncertainties and, thus, was not conducted, it could be stated that the Raman shift region in which mostly aromatic amino acids are located showed the highest fluctuations during UV light exposure. From that, it was suggested that the telopeptides played a (special) role

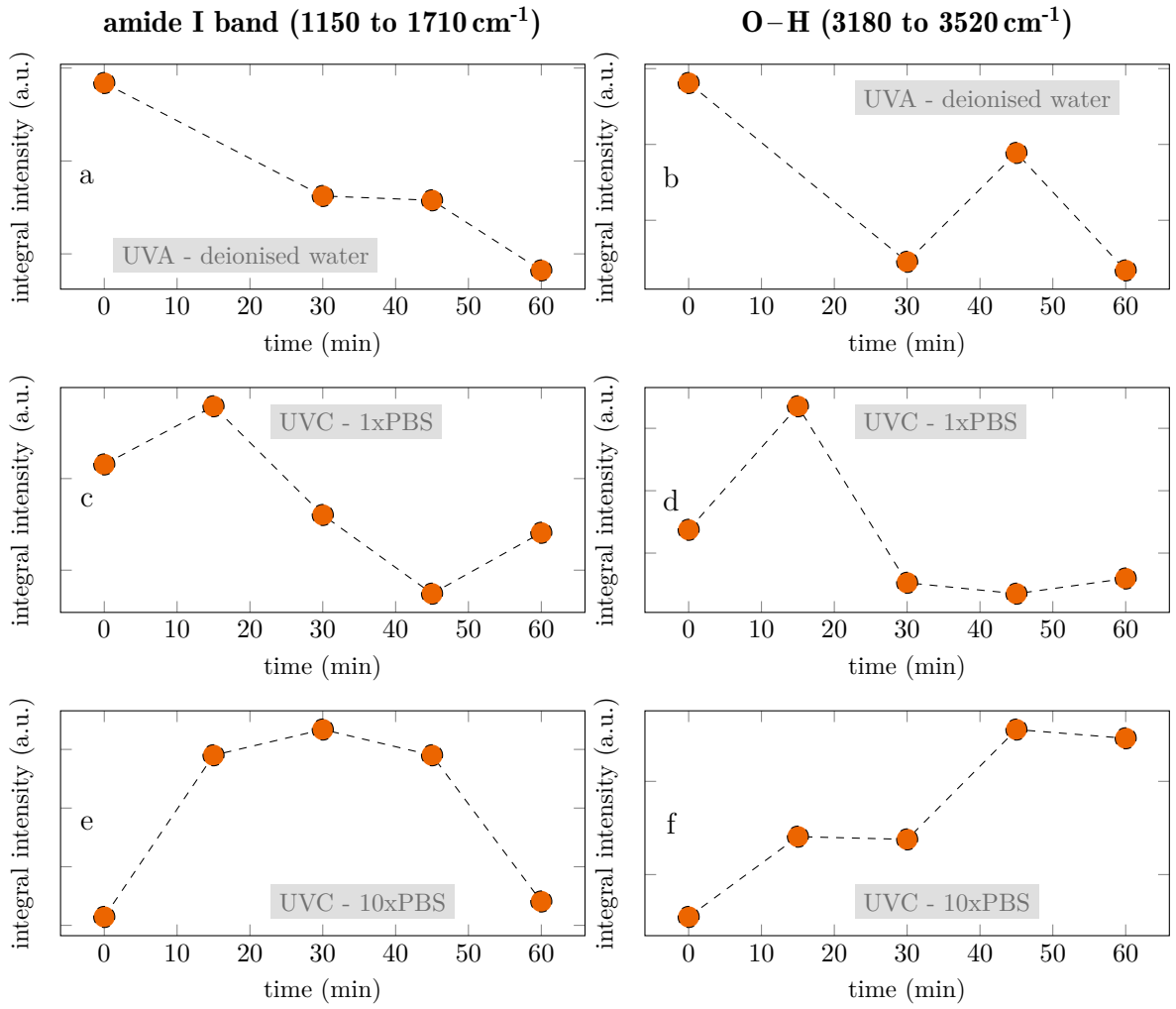

Figure 4.42.: The integral intensities for (a,c,e) the amide I band (1550 to 1710 cm^{-1}) and (b, d, f) the O–H band (3180 to 3520 cm^{-1}) from Figure 4.39 (UVA light and deionised water in a,b), Figure 4.40 (UVC light and 1xPBS in c,d), and Figure 4.41 (UVC light and 10xPBS in e,f) were evaluated from SERS measurements on collagen fibrils to clarify the evolution of the peak intensity with advancing exposure time.

during the stabilising and destabilising processes since the aromatic amino acids were mostly to be found in the non-helical ends of the α-chains. Markers that were related to the secondary structure of collagen showed a decreasing tendency in the β-sheet to α-helix peak ratio during stabilising events and *vice versa*, showing changes in the structure of the telopeptides. For the SERS experiments on separated collagen fibrils, the results looked similar regarding the influence of the different treatments on the general behaviour of the samples. Yet, the individual spectra exhibited differences in comparison to the ones acquired on collagen hydrogels. For the C−H vibrations, distinct peaks were found where, for the hydrogels, the overlapping of signals led to the formation of bands. Additionally, the intensity ratios of the amide bands depended on the measurement site and were not as reproducible as for the experiments on the collagen hydrogels.

The Raman spectroscopy results support the findings of the AFM experiments, concluding that a combination of UVA light and deionised water majorly induced destabilising effects while the application of UVC light and PBS mediated a temporal strengthening of the collagen structure. The comparison between the hydrogels and the separated fibrils was interpreted as the collagen fibrils being the structural component that was majorly influenced by the UV light exposure since both sample types show a similar response. In a hydrogel, interfibrillar bondings were rare due to the distances between the fibrils, although, they were in contact with each other. This supports the hypothesis that the collagen fibrils were the strongest unit in a collagen construct.

The results from the Raman spectroscopy experiments could be correlated to the findings from the before presented AFM experiments since the formation of crosslinks in collagen leads to a higher mechanical stability. Based on this correlation, in particular, the amide I band intensity with time of exposure showed the mechanical response of the collagen sample in a qualitative way. During the Raman spectroscopy experiments and the AFM measurements, a mostly destabilising trend has been recorded for the UVA irradiation of collagen fibrils immersed in deionised water. Similarly, UVC irradiation of collagen fibrils that were immersed in PBS-based solution predominantly exhibited a stabilising phase within the first 60 min of exposure. Furthermore, the Raman spectroscopy results also showed that the behaviour of the separated collagen fibrils towards the treatment conditions could be transferred to collagen hydrogels as three-dimensional structures that are closer to an application as substrate in tissue engineering than the single fibrils. This was convenient for the handling of collagen over several length-scales but, also raised the question why no significant differences between one- and three-dimensional structures occurred. The hypothesis was that, even when brought in close proximity of each other within a confined space, the packing density and the number of connecting points between collagen fibrils in a hydrogel were not sufficient enough to form interfibrillar bonds. This fits to the application principle of DHT treatment in which dehydration of the collagen network forces it to minimise the space between the single collagen units with the goal of crosslink formation. Due to the similar outcome for the one- and the three-dimensional structures, it was concluded that the intrafibrillar bonds were mainly influenced under UV exposure. Mechanical measurements support this impression since single collagen fibrils[209,238] exhibit a higher resistance against load than collagen hydrogels.[224]
The question was whether the so far collected findings led to a theory that might explain them.

The combination of UV light irradiation and deionised water most likely led to destabilisation of the collagen, as seen for the Raman spectroscopy results and for the AFM measurements. The general understanding is that UV light is harmful and causes damage of biological material.[305] Irradiation of collagen samples with UV light has proven that this is true for a lot of measurement conditions. An extensive irradiation leads to destabilisation and the transition from the triple helical structure to a random coil conformation. In this way, an intermediate state is discovered that is correlated with a partial destabilisation of the collagen molecules. While peptide bonds are broken during the scission of the α-chains, the triple helical structure stays intact due to hydrogen bonds. The scission can occur on many sites of the α-chains and takes place randomly, although, some sites are favoured. With ongoing time of exposure, the number of intact α-chains decreases and the triple helix is unfolded eventually, when the α-chains at the C-terminus of the collagen molecule are uncoupled.[27,305] This explanation fits the presented results obtained by Raman spectroscopy, showing a decrease of the amide bands as a marker for destabilisation, without a sign of the unfolding of the triple helix (cf. Figure 4.32).

Radical formation is seen as a major mechanism to introduce scission and, thus, the involvement of radicals in the interaction of UV light with collagen and several mechanisms are proposed.[306] UV radiation can release electrons from Tyr by

$$\mathrm{Tyr} \xrightarrow{+h\nu} \mathrm{Tyr}^{+} + \mathrm{e}^{-}, \tag{4.23}$$

(also applicable to Phe) potentially leading to the formation of hydrogen radicals by

$$\mathrm{e}^{-} + \mathrm{H}^{+} \longrightarrow {}^{\bullet}\mathrm{H}. \tag{4.24}$$

Metreveli *et al.*[306] show that the application of acetic acid as liquid environment in combination with injected electrons leads to formation of an anion-radical

$$\mathrm{e}^{-} + \mathrm{CH_3COOH} \xrightarrow{280\,\mathrm{nm}} \mathrm{CH_3C^{\bullet}O^{-}OH}, \tag{4.25}$$

which, in the case of acetic acid, is unstable but, in general, might be an example for potential reactions. The reaction of the collagen molecule with the produced radicals may lead to the creation of radicals in the collagen by detaching the hydrogen atom from C_α. In general, the combination of UV light with a photosensitising agent can lead to the formation of radicals like singlet oxygen ($^1O_2$), superoxide anion ($O_2{}^{\bullet -}$) and hydroxyl radicals ($^{\bullet}$OH).[307] During UV exposure, primary free radicals gather in the collagen-surrounding water most likely around Pro.[306] UV light does not only interact with photosensitising agents but also with the amino acids of the collagen. Tyr absorbs light at 275 nm[25] leading to a Tyr-derived electron injection. At a wavelength of 253.7 nm Tyr is irreversibly destabilised and Phe is too. In general, the aromatic chains are excited between 270 and 290 nm. From Tyr, oxidising agents create Tyr radicals from which two can link to form a dityrosine in an environment of acetic acid. Another product of direct Tyr-photolysis under exposure to light with a wavelength of 300 nm is 3,4-dihydroxyphenylalanine.[121] It is also stated by Creed[308] that UVC light-based photoionisation leads to phenoxyl radical formation in an aqueous environment, which sets in the photolysis of Tyr and phenols. Several additives, like β-carotene[121] or vitamin E,[117] diminish UV light-induced effects. Vitamin E acts as a UV absorber and radical scavenger.[117]

The results obtained from the AFM measurements have shown that destabilising events were the major effect during the application of UVC light on collagen fibrils immersed in deionised water. So far, the destabilisation was correlated with the UV light-induced scission of the α-chains and the occurrence of certain crosslinks

(*e.g.* dityrosine) was understood as a step during the UV light-induced degradation. The results suggested that the rate of the crosslink-formation could not balance the scissions of the α-chains which led to an overall destabilisation of the collagen structures. It was also questionable whether the number of tyrosine residues is sufficient to produce enough links for the strengthening of the collagen material even if, additionally, Tyr is formed from Phe.[117]

Regarding the exchange of the deionised water with PBS, one of the most striking findings was the introduction of majorly stabilising effects during UV light irradiation of collagen samples - especially for UVB and UVC light. In fact, it is shown that (preferably divalent) phosphate ions bind to positively charged amino acid residues at the collagen molecule. By the connection of two positively charged amino acid residues, salt bridges are formed that exhibit a stabilising character. It is the number of involved binding sites that is discussed, but its dependency on the pH and the salt content of the solution can be stated. Mertz *et al.*[309] published a pattern of axial charge density in type I collagen fibrils, proposing potential binding sites for phosphate ions (*e.g.* Lys^+ and arginine $(Arg)^+$). Not all charged amino acid residues bind to phosphate ions. Spatially close sites of opposite charge will favour an electrostatic interaction. Mertz *et al.*[309] state that competitive binding of, for example, Cl^- ions derived from NaCl, is not excluded but energetically not favourable in comparison to the binding of phosphate ions. Extant ions stay in solution in the interstitial water. PBS is known to promote the collagen fibrillogenesis *in vitro*[310] showing its importance for the formation of stable collagen structures. The formation of salt bridges within the collagen fibrils is an example for intrafibrillar bindings that fits the assumption of the collagen fibrils being the structural component that is mostly influenced by the applied exposure, as shown with the Raman spectroscopy measurements. Yet, these stabilising effects induced by PBS do also occur without the addition of UV light. The simple addition of PBS does not alter IR absorption bands (1200 to 1500 cm^{-1}), indicating that no structural changes take place.[309] Thus, the detection of structural changes in the present study most likely hint at the involvement of further crosslinking mechanisms. Results that, however, could be explained by the formation of salt bridges due to the addition of PBS were the changes in mechanical properties in succession to the application of elevated temperatures (cf. Section 4.1.2). The temperatures above 37 °C and the slightly changed pH in comparison to the collagen solution may have triggered the formation of further salt bridges to reach a full occupation of all possible reaction sites. It may also have led to the creation of new reaction sites since their number depends on, for example, the pH. Coming back to the role of PBS when UV light is applied. Since the absence of PBS predominantly led to destabilising effects, the addition of PBS seemed to have a crosslink-favouring or at least shielding character. The Raman spectroscopy measurements suggested an increase in intensity in the amide I band, as well as in the O–H region that was evaluated as stabilisation. This could be interpreted as a crosslink-forming condensation reaction based on the direct connection of two amino acids as, for example, two Tyr residues. It is reported, that at pH 11, the addition of KBr enhances the formation of dityrosine.[308] A

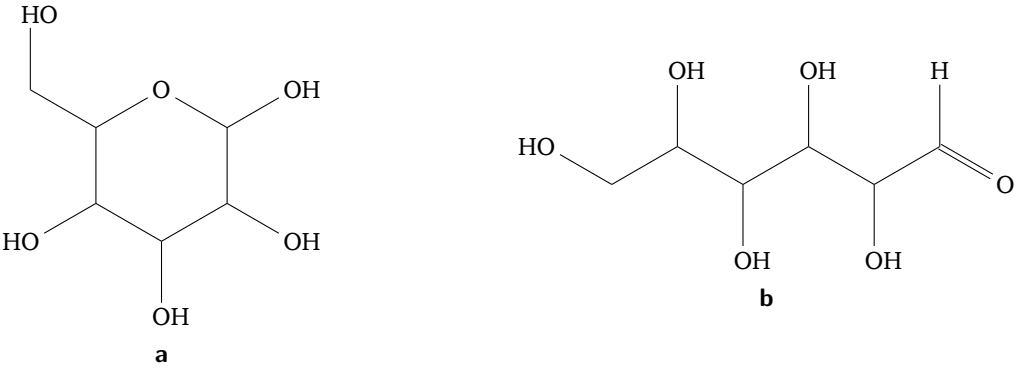

Figure 4.43.: Structure of (a) D-glucose[314] closed and (b) L-glucose[315] open adapted from the *National Center for Biotechnology Information - PubChem Database*.[316]

similar effect could be expected for the NaCl that is included in the PBS solution. Davidenko *et al.*[21] report that a strengthening behaviour is also found for the addition of glucose under the irradiation with UVC light. Glucose forms additional bonds in the collagen molecule and prevents unravelling of the triple helical structure and, therefore, finds application in the crosslinking of biomaterials.[311] Free radicals are required to catalyse the glucose-based reactions,[312] which is why the combination with UV light is promising.[307] For introducing a crosslinking effect, glucose needs to be in its linear form (cf. Figure 4.43), which leads to the exposition of an aldehyde group.[313] Ohan *et al.*[19] state that the aldehyde group reacts with the amine groups under the formation of a Schiff base while Davidenko *et al.*[21] hypothesise that the addition of glucose did not use free amine groups for crosslinking since the free amine groups are required for the bioactivity of the collagen and the cell reactivity was not changed after crosslinking. Nevertheless, the strengthening effects of collagen under the addition of glucose are shown for both cases. Additionally, glucose also diminishes the denaturation of the collagen because it locates crosslinks close to scission sites in the α-chains.[19] PBS could have a similar influence on the collagen in combination with UV light, as the comparison of the chemical structure from PBS (Figure 4.44a) to glucose (Figure 4.43) shows similar functional groups.

In case the light absorption of the Tyr in the UVC range was the initialising step for a crosslinking mechanism, UVB, but especially UVA light, should not have been able to lead to a stabilisation of the collagen by this mechanism. The obtained results from collagen samples exposed to UVA light during their immersion in 1xPBS showed that stabilising (cf. Figure 4.30) and destabilising (cf. Figure 4.14 and Figure 4.38) effects have been recorded. It is reported that UVA light has a stabilising influence on collagen when additives are involved. Examples for these effects of additional substances are manifold with two prominent examples being the addition of riboflavin or glucose[19] that exhibits stabilising effects for an irradiation wavelength of 257 nm[21]. From the literature that proposes chemical reactions for several combinations of additives and UV light exposure of collagen, the following hypothetical ideas were derived to describe the influence of PBS. It is proposed that, UVA especially, requires a photosensitiser, which can be for example, riboflavin[317] or

hematoporphyrin (HP).[120] In combination with the photosensitiser, UVA light produces the oxygen-radical singlet oxygen ($^1O_2$), which initiates crosslinking of the collagen. Ryu *et al.*[120] point out that though many ROS are known, the singlet oxygen is the decisive one in the here discussed mechanisms. Without the addition of the photosensitiser, crosslinking is not observed. The underlying process of a singlet oxygen crosslinking is connected with the possible involvement of the photooxidised amino acid residues of Cys, His, methionine (Met), tryptophan (Trp), and Tyr. The photooxidised histidyl residue is pointed out to be the most likely part in this mechanism to react with other amino acids. Also riboflavin can form singlet oxygen in water under irradiation,[318] as well as hydroxyl radicals ($^{\bullet}OH$) with hydrogen peroxid (H_2O_2) as an intermediate.[319] The creation of crosslinks in collagen is based on covalent bonds between amino acids as a result of aldol condensation or aldimine formation reactions.[122]

Parallels can be drawn to the here presented results. The immersion of collagen in deionised water did not show any signs of distinct crosslinking events during the irradiation of UVA light. This held true for the indentation experiments, tensile tests, and Raman spectroscopy measurements. While no change was detected for the addition of PBS during the indentation tests, the tensile tests did show signs of crosslinking during UVA irradiation. In that sense, the PBS fulfils the same purpose as the photosensitisers. Figure 4.44 shows the chemical structures of riboflavin and PBS. The structure of HP is shown in Figure D.8. Riboflavin and HP carry exposed carbonyl (=O) and hydroxyl (−OH) groups that most likely generate the ROS. PBS also carries both these groups, too, which gives it a similarity to the other structures. Thus, the idea is that PBS, in combination with UVA light also acts as a photosensitiser to crosslink collagen molecules in a way that increases their axial resistance towards load.

The occurrence of crosslinking during the tensile tests but its absence for the indentation experiments might have been derived from the mechanical anisotropy of the collagen fibrils. It might also have been a hint that the crosslinking mechanisms for the UVC irradiation are different from the one for UVA irradiation since the irradiation with UVC light led to an increase in mechanical stability for the indentations experiments, as well as the tensile tests when PBS was added.

Further crosslinking methods were imaginable but some could also be excluded. For example, so far, UV crosslinking is said to be not using free amine groups as crosslink sites since they are required for the bioactivity of the collagen. In case they are blocked by crosslinks, the cell reactivity would be compromised.[21] To exclude any doubts, this has to be tested for the UV crosslinking based on PBS. The function of PBS as photosensitiser is backed by the application of nicotinamide adenine dinucleotide phosphate (NADPH) as photosensitiser, generating ROS especially for the UVA and UVB region.[307,322]

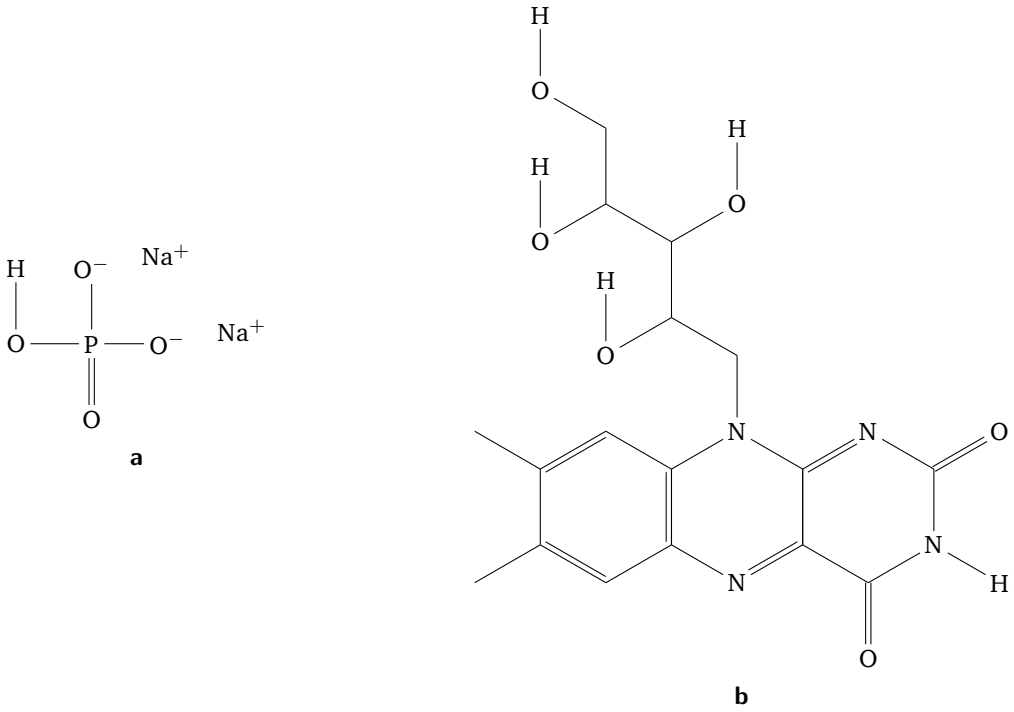

Figure 4.44.: Structure of PBS[320] and riboflavin[321] adapted from the *National Center for Biotechnology Information - PubChem Database*.[316]

4.5 Patterned exposure to ultraviolet light[xii]

4.5.1 Patterned irradiation of collagen fibrils

The requirements of an environment for cell growth that mimics properties of the body are complex and cannot be satisfied by the exposure of a collagen-based substrate to UV light. Nevertheless, to employ the investigated changes of the UV light on collagen for the modification of substrates, it was utilised that light can be selectively shone on a sample by the application of a mask. The idea was to imprint a pattern on a collagen-based substrate by shining UV light through a mask and applying the conditions that have been investigated in Chapter 4.1 and Chapter 4.2.

For the execution of a first test, a copper TEM grid with a 600 mesh was used as a mask for the irradiation of single collagen fibrils spread on a glass substrate. The exposure of the sample to UVB light through the TEM grid took place for 30 min while the sample was immersed in 1xPBS. Subsequently, PFQNM AFM measurements were used to record the indentation modulus of the collagen fibrils. The measures of the TEM grid should result in exposed and unexposed areas on the sample with an edge length in the range of approximately 10 to 25 µm and approximately 15 to 30 µm, respectively. To ensure sufficient data points per fibril and enable a sufficient magnification of them, a scan area of $80 \times 10\ \mu m^2$ was divided into 8 AFM images with a scan size of $10 \times 10\ \mu m^2$ each, as shown in Figure 4.45. The averaged modulus of several fibrils was denoted beneath the respective image and a possible orientation of the TEM grid above the samples was suggested according to the measured DMT moduli. It was seen that in the middle of the image-series the DMT modulus was lower than to its left and right. Considering that the conditions applied to the sample expectably resulted in a stabilisation of the collagen fibrils, the middle of the image-series was interpreted as unexposed area. Thus, the AFM images to its left and right were interpreted as exposed sides. The size of the unexposed area (in x-direction) fit the range of the expected size of the TEM grid bar. However, due to the distance between grid and sample, an identical representation of the TEM grid structure on the sample was not expected. The results showed that a grid could be applied to pattern collagen samples by the application of UV light. Since separated collagen fibrils left too much of the underlying substrate exposed, collagen hydrogels were applied in the further experiments to promote that the seeded biological cells only sensed the collagen as substrate. It was shown that collagen hydrogels, *e.g.*, with a concentration of $2\ mg \cdot ml^{-1}$, are applicable as matrix environment for cells.[323–325] For their UV exposure, a new sample holder had to be designed.

[xii] The results presented in this section were gained in cooperation with Yue Du who wrote his master's thesis on the topic of UV light patterned collagen hydrogels and their influence of cell adhesion behaviour.

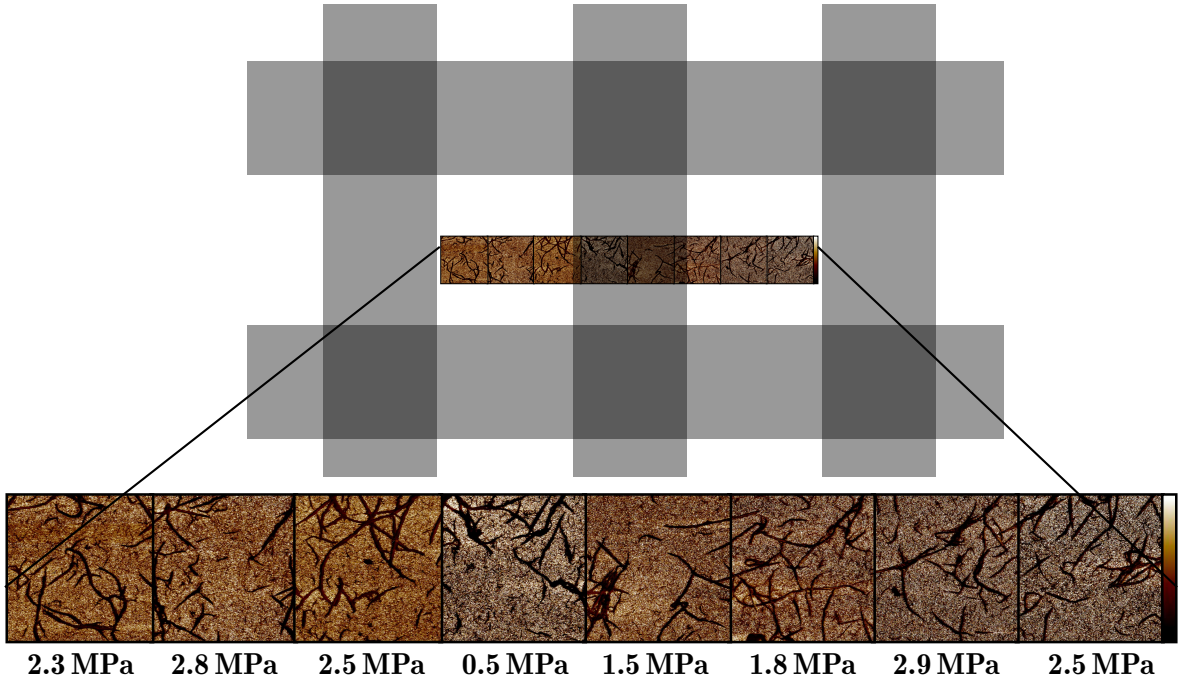

Figure 4.45.: PFQNM AFM images (DMT modulus) of collagen fibrils attached to a glass substrate are lined up next to each other presenting an area of $80 \times 10\,\mu m^2$. The sample was immersed in 1xPBS and exposed to UVB light for 30 min according to the schematic setup presented in Figure 3.4. The presented modulus is an averaged value over several measurement spots of the respective frame and the suggested structure (transparent black) shows a possible orientation of the TEM grid with respect to the measurement site. Colour bar: 0 to 10 MPa. Scan size (single frame): $10 \times 10\,\mu m^2$.

Figure 4.46.: CAD designs of (a) holder and (b) grid for patterned exposure of collagen hydrogels. The width of the grid bars and voids is 750 µm each. Images were provided by courtesy of Yue Du.

4.5.2 Design of sample holder

The sample holder was designed to enable an exchange of the grid-type according to the need of the experiment. Figure 4.46a shows a CAD model of the applied sample holder. Since the sample was supposed to be immersed in a liquid during irradiation, the bottom part had to provide enough room that could be filled with, *e.g.*, deionised water. The actual grid (Figure 4.46b) was placed on top and was held in position by the edgewise notches ensuring a comparable distance to the sample for all experiments. A contact between grid and sample should be avoided. The most applied structure were bars stretching between the two long sides of the grid separated by voids. Another option was to expose only one half of the sample while the other half stayed covered. In case the exposed collagen hydrogel was employed for subsequent measurements with the AFM, usually, the width of bar and void were 180 µm and 80 µm, respectively. Regarding the grids used for the preparation of cell spreading experiments, these values were ultimately increased up to 750 µm (bar) and 750 µm (void) as shown in Figure 4.46b. Additionally photomasks were applied.

4.5.3 Atomic force microscopy measurements on (patterned) collagen hydrogels

Two-dimensional maps of mechanical properties of soft collagen hydrogels immersed in a liquid were obtained. While the combined imaging and recording of mechanical properties for cells in a liquid environment is more common,[200] gels were probed in dry state[326] and mechanical properties of soft matrices for cell growth and thin protein films were extracted by single force versus distance curves[327] or by the application of colloidal probes,[328] respectively. In the hydrated state gels were also imaged[329] or force volume maps[330] were obtained. Nevertheless, PFQNM AFM on soft hydrogels in a liquid environment faces influences as, *e.g.*, noise and a less well defined contact between the probe and the sample.[331] Figure 4.47 shows PFQNM AFM images of a

collagen hydrogel immersed in deionised water. Tracing the topography of the sample resulted in deviations between trace and retrace curves, as can be seen in the height image. Thus, the height image lacked distinct features. The DMT modulus image, however, delivered a good agreement between trace and retrace curves. The sample was exposed to UVA light (UVA lamp) for 80 min and AFM images were recorded simultaneously. Every image that carried information on the DMT modulus was averaged resulting in the respective data points shown in Figure 4.47c. It can be seen that the acquired DMT modulus decreased with progressing exposure time, which was in perfect agreement with the so far presented results. Figure 4.48 shows the same information as Figure 4.47 but for a collagen hydrogel immersed in 1xPBS and exposed to UVC light. The DMT modulus increased during the first 40 min of exposure and subsequently decreased, which was in perfect agreement with the results presented earlier for the exposure of collagen fibrils to 1xPBS and UVC light for 80 min. From these experiments, it can be concluded, that - as it was assumed for the Raman spectroscopy experiments - collagen hydrogels behaved in the same way as collagen fibrils regarding their response to UV light exposure and a varied liquid environment.

Yet, imaging of the collagen hydrogel surface remained challenging. Figure 4.49 shows two examples of collagen hydrogels imaged with PFQNM AFM immersed in deionised water in which trace and retrace were in good agreement and, thus, suggested reliable results. For the height image (Figure 4.49a) a XNC12-A cantilever (cf. Table 3.1) was applied. It can be seen that the collagen hydrogel possessed a rough surface with cavities that were irregular in shape, size, and localisation. The peak force error image (Figure 4.49b) was obtained with a MLCT-Bio-D cantilever (cf. Table 3.1). It shows that the collagen fibrils were rather arbitrarily piled than densely packed, which supported the assumption (c.f. Section 4.3) that interfibrillar bonds were less prominent. Figure 4.49b gave the impression that the collagen islands were embedded in a more amorphous matrix, but this impression could neither be proven nor discarded.

After having shown that collagen hydrogels, in general, react to UV light exposure in the expected way, the idea was to pattern their DMT modulus by the application of a grid. Figure 4.50 shows the DMT modulus and a scheme of a collagen hydrogel immersed in deionised water of which only one half was exposed to UVA light for 120 min. A XNC12-A cantilever was used (cf. Table 3.1). The DMT modulus was measured across the boundary between the exposed and the unexposed area to derive a direct comparison. AFM images with a scan size of 1 µm and an aspect ratio of 1:3 were obtained for several positions along an axis perpendicular to the described boundary. For every scan area, the DMT modulus was averaged, resulting in one data point as they are seen in Figure 4.50a and Figure 4.50b. The data points were related to their acquisition position on the line across the boundary. The position of the boundary could not be assigned exactly (due to the uncertainties of stray light and shadow zones), but it was supposed to be within the length of the measurement region. Both graphs, acquired at two different positions, exhibited lower values for the DMT modulus on their 'left' side, which was interpreted as the exposed area and, thus, a lower modulus was expected.

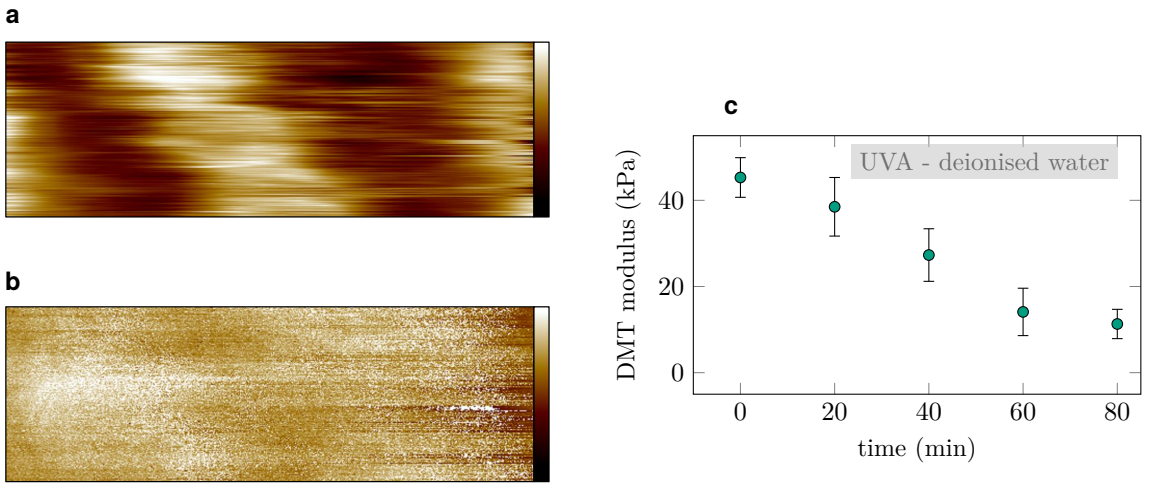

Figure 4.47.: A collagen hydrogel immersed in deionised water was measured by PFQNM AFM with XNC12-A cantilever resulting in (a) the height image and (b) the DMT modulus image. Subsequently, the hydrogel was exposed to UVA light (UV lamp) for 80 min and PFQNM AFM images were obtained simultaneously. In (c) the DMT modulus averaged over each image is depicted over time of exposure. Colour bar: (a) -100 to 70 nm and (b) -50 to 70 kPa. Scan size: $20 \times 6.7\ \mu m^2$.

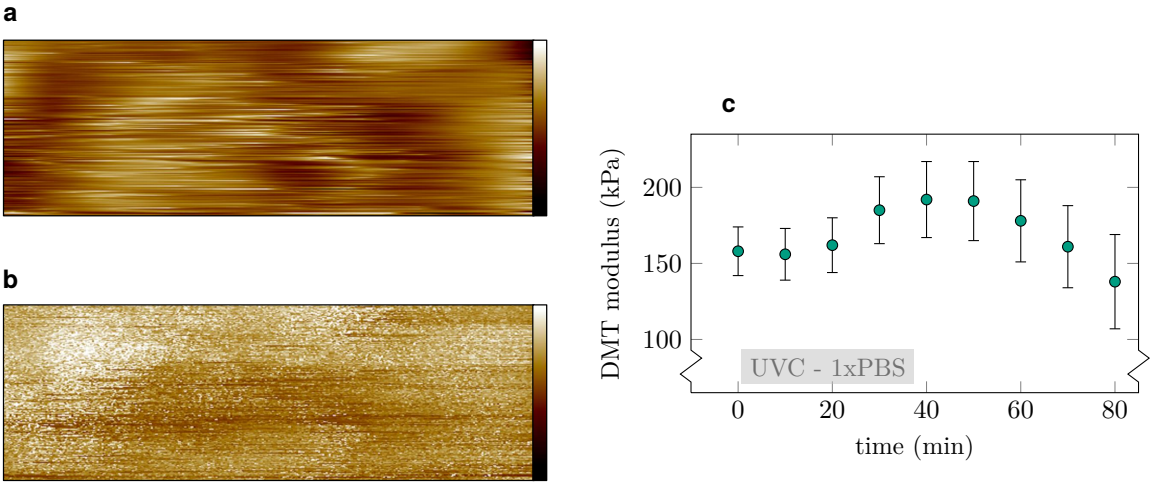

Figure 4.48.: A collagen hydrogel immersed in 1xPBS was measured by PFQNM AFM with XNC12-A cantilever resulting in (a) the height image and (b) the DMT modulus image. Subsequently, the hydrogel was exposed to UVC light (UV lamps) for 80 min and PFQNM AFM images were obtained simultaneously. In (c) the DMT modulus averaged over each image is depicted over time of exposure. Colour bar: (a) -100 to 70 nm and (b) -250 to 300 kPa. Scan size: $20 \times 6.7\ \mu m^2$.

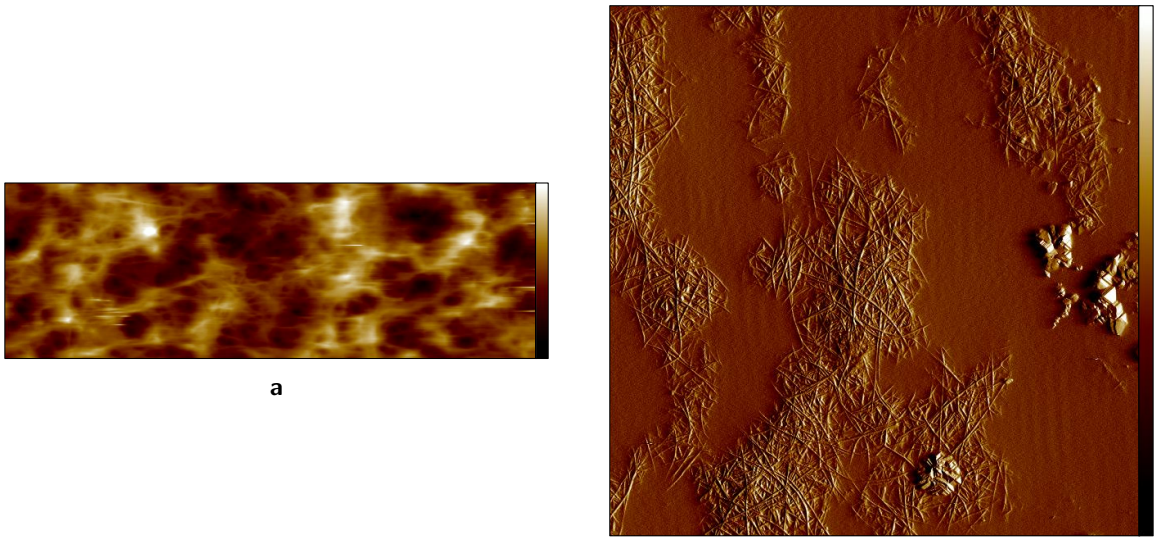

a b

Figure 4.49.: Two collagen hydrogels immersed in deionised water and measured with PFQNM AFM resulting in (a) a height image acquired with a XNC12-A cantilever and (b) a peak force error image acquired with a MLCT-Bio-D cantilever. Colour bar: (a) -1 to 1 µm and (b) -250 to 300 pN. Scan Size: (a) $80 \times 26.7\ \mu m^2$ and (b) $50 \times 50\ \mu m^2$. Image (b) was provided by courtesy of Yue Du.

The results obtained during the exposure of half a collagen hydrogel to UV light were promising but only had a low spatial resolution. Thus, more detailed images of the distribution of the DMT modulus had to be obtained and a more complex grid structure had to be applied. Figure 4.51 shows the DMT modulus of a collagen hydrogel and a scheme of a grid imprinted in a quartz glass-based photomask that had a repeating pattern of alternating bars and voids with increasing width (10, 20, 40, 80, 160, 320, and 500 µm). The images were obtained with a XNC12-A cantilever (cf. Table 3.1). Using the Axio Imager.M2m light microscope as source for UVA light, a collagen hydrogel immersed in deionised water was irradiated through this photomask for 120 min. Figure 4.51a gives an example for how a patterned structure might have been expected to look. This image showed a 20 µm wide bar that locally shielded the DMT modulus of the collagen hydrogel from decreasing, as it has happened for the area to its left and right. Figure 4.51b, however, gives an example of how heterogenous the DMT modulus of the sample surface could be, making it difficult to state whether the origin of an area of high or low DMT modulus was inherent or derived by the UV light exposure. For the investigation, adjacent averaged cross sections, as they are seen in Figure 4.51, were taken perpendicular to the direction of the grid bars; but the expected pattern given by the grid was not doubtlessly identified. An example for that is given in Figure 4.52 showing the assembling of three adjacent averaged cross sections. Areas of a comparatively low DMT modulus are highlighted in red. The thereby revealed pattern, however, could not be fit to the sequence of the grid since a void of 20 µm width would have been followed by a 80 µm bar. Nevertheless, an influence on the patterning can also not be fully excluded.

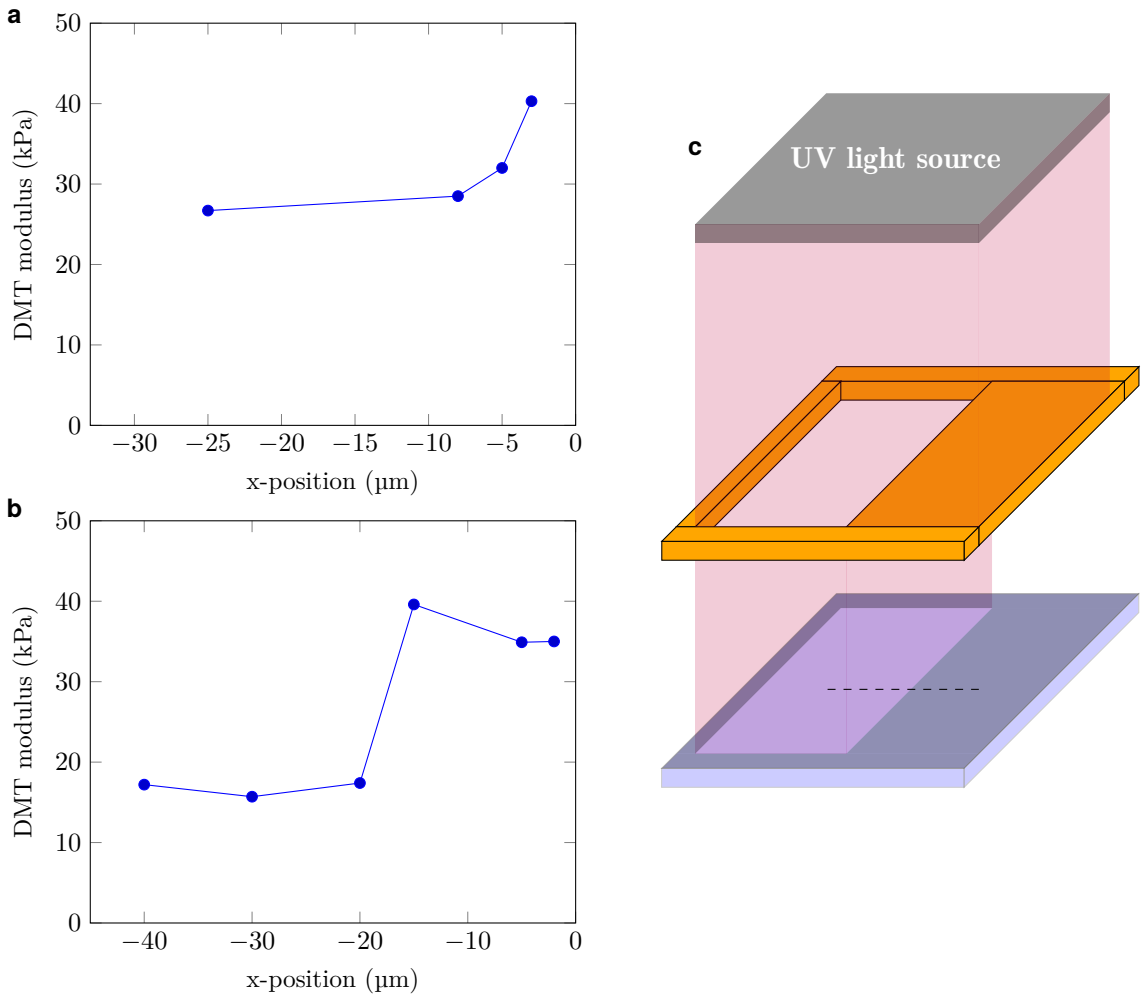

Figure 4.50.: A collagen hydrogel immersed in deionised water was exposed to UVA light for 120 min and, subsequently, the DMT modulus was acquired by PFQNM AFM for several points along a horizontal axis across the boundary of exposed and unexposed regions with a scan size of $1 \times 0.1\,\mu m^2$ each. Each data point in (a) and (b) was averaged over the scan area. A model of the exposure setup (from top to bottom: UV light source, grid, and sample) is shown in (c) highlighting that only half of the sample was exposed to UVA light. The dashed line symbolises a line on which the data points were recorded. The results in (a) and (b) were obtained from different positions on the sample. A XNC12-A cantilever was used for the AFM measurements and the Axio Imager.M2m light microscope was used for UV light exposure.

The experiments presented in Figure 4.50 and Figure 4.51 are two examples for the performed measurements that also involved the 3D printed grids as patterning devices. A more distinct structuring of the modulus of the collagen hydrogels, however, could not be seen. Nevertheless, the results presented so far could also be reflected in the investigations regarding the growth of biological cells on (patterned) collagen hydrogels.

4.5.4 Cells on patterned collagen samples

Figure 4.53 shows light microscopy images of COS-7 cells that were seeded on a collagen hydrogel and have been stored for 24 and 72 h in the incubator at 37 °C and 5 % CO_2. In comparison to the observed growth of the cells in the cell flasks, the cell proliferation on the collagen hydrogels was slow but a confluence could be attained throughout several experiments.

The first attempts for the investigation of the impact of a UV light exposed collagen hydrogel on the behaviour of the seeded cells were done by exposing one half of a collagen hydrogel and shading the other half. By that, a direct comparison of the cell behaviour on the same sample could be performed. Figure 4.54 shows a collagen hydrogel whose one half was exposed to UVB light for 30 min while being immersed in 1xPBS. The comparison of the unexposed side (Figure 4.54a) to the exposed side of the sample (Figure 4.54b) exhibited that, on the latter, the COS-7 cells were less round in shape but, instead, did spread more on the surface. Additionally, the cells seemed to stretch more on the exposed side. This observation would fit the general expectations that cells tend to spread more if the elastic modulus of the substrate is higher which, comparing the unexposed and the exposed side of the sample, should be the case for the exposed side. The opposite case is shown in Figure 4.55 in which one half of a collagen hydrogel was exposed to UVA light while being immersed in deionised water and the other half was not. The COS-7 cells on the unexposed side showed an appearance similar to Figure 4.54a with partial stretching. On the exposed side, however, the cells predominantly appeared to be more round with hardly any stretching. Again, this would fit the expectations, saying that on a softer substrate the cells spread less but are rounder. Due to the combination of UVA light and deionised water, the exposed side was expected to be softer than the unexposed side.

Yet, smaller and more complex structures should be imprinted on the surfaces of the collagen hydrogels. For that, the sample holder and the grid shown in Figure 4.46 were applied, exposing the sample to UVB light while being immersed in 1xPBS. A ROI of this sample for four different storage times can be seen in Figure 4.56. In the middle of the light microscopy images, an island of cells was forming, which was growing throughout the storage time. The image series suggested that this island had a preferred direction of growth, which was indicated by the red line and the corresponding red arrow, and avoided the area highlighted by the red box. With respect to the image size, the highlighted area of no cell propagation had a width of approximately 250 µm and the final measured width of the area covered with cells was approximately 550 µm. The applied grid consisted of alternating bars and voids that both had a width of 750 µm. Thus, the measured quantities of

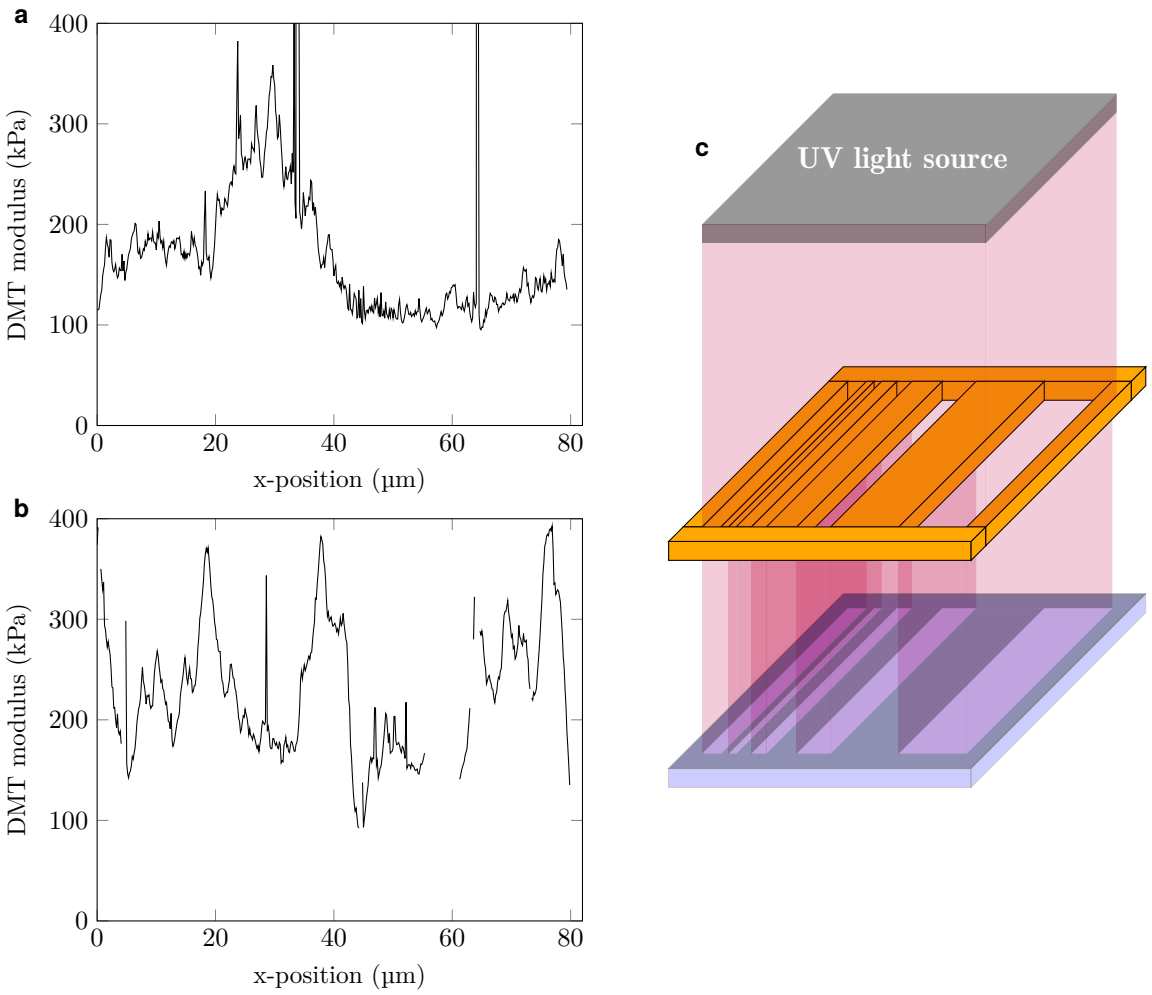

Figure 4.51.: A collagen hydrogel immersed in deionised water was exposed to UVA light (Axio Imager.M2m light microscope) for 120 min and, subsequently, the DMT modulus was acquired by PFQNM AFM for several points along a horizontal axis across the boundary of exposed and unexposed regions with a scan size of $80 \times 27\,\mu m^2$. Cross sections (a) and (b) were averaged over the scan area providing exemplary results along a line perpendicular to the bars represented in (c) where a schematic drawing of the patterning setup with the UV light source, a grid (photomask), and the sample (from top to bottom) is shown. The repeating pattern consisted of alternating bars and voids with a width evolution of 10, 20, 40, 80, 160, 320, and 500 µm. A XNC12-A cantilever was used for the AFM measurements.

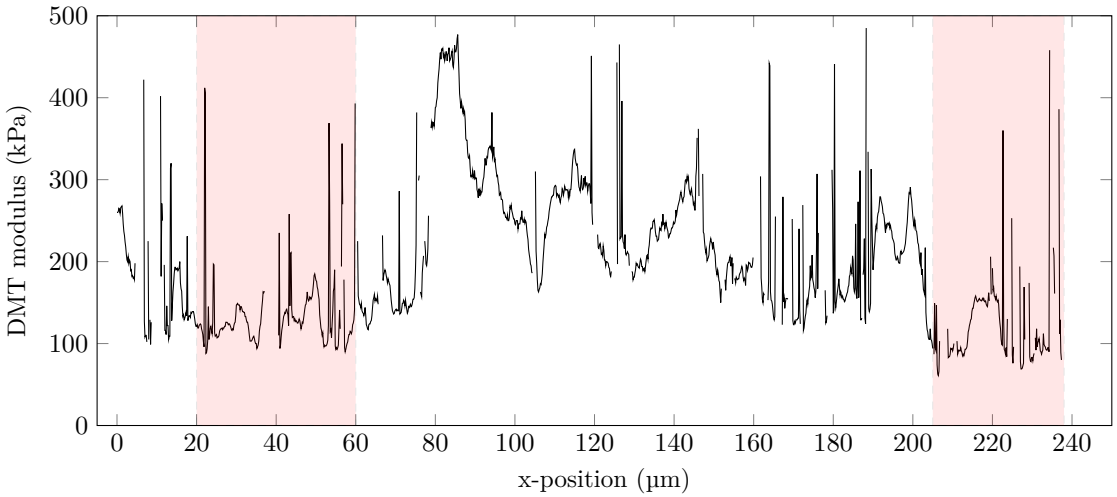

Figure 4.52.: A collagen hydrogel immersed in deionised water was exposed to UVA light for 120 min and, subsequently, the DMT modulus was acquired by PFQNM AFM for several points along a horizontal axis across the boundary of exposed and unexposed regions with a scan size of $80 \times 27\,\mu m^2$. The DMT modulus of every scan area was averaged resulting in one cross section and the averaged cross sections of three adjacent images are shown next to each other. Exposure took place under the application of the photomask shown in Figure 4.51. The red boxes highlight regions of comparatively low DMT modulus. A XNC12-A cantilever was used for the AFM measurements and the Axio Imager.M2m light microscope was used for UV light exposure.

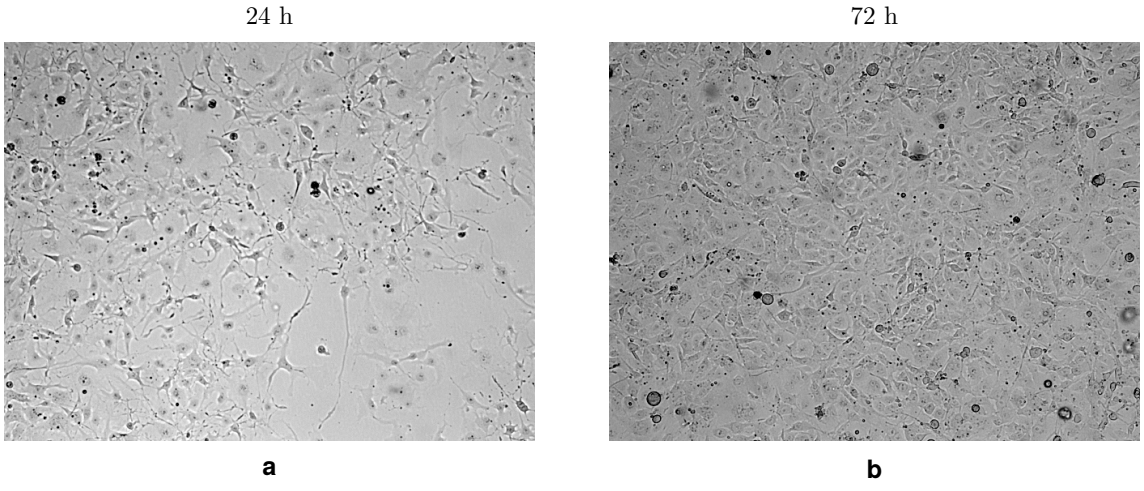

Figure 4.53.: Light microscopy images (5x/0.12 Zeiss-objective) of COS-7 cells on a collagen hydrogel (a) 24 h and (b) 72 h after seeding. The samples, covered with nutrition solution, were stored in an incubator at 37 °C and 5 % CO_2. Image size: $1225 \times 915\,\mu m^2$. Images were provided by courtesy of Yue Du.

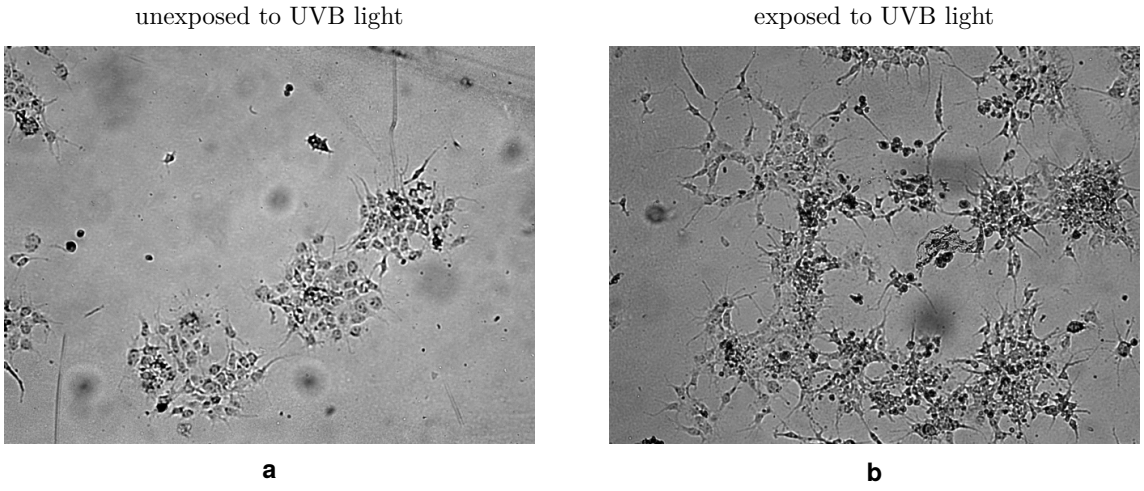

Figure 4.54.: Light microscopy images (5x/0.12 Zeiss-objective) of COS-7 cells on the same collagen hydrogel of which (a) one half was not exposed to UV light and (b) the other half was exposed to UVB light for 30 min while the hydrogel was immersed in 1xPBS. The COS-7 cells were seeded subsequently and the sample, covered with nutrition solution, was stored in an incubator at 37 °C and 5 % CO_2. Image size: 1225 x 915 µm^2. Images were provided by courtesy of Yue Du.

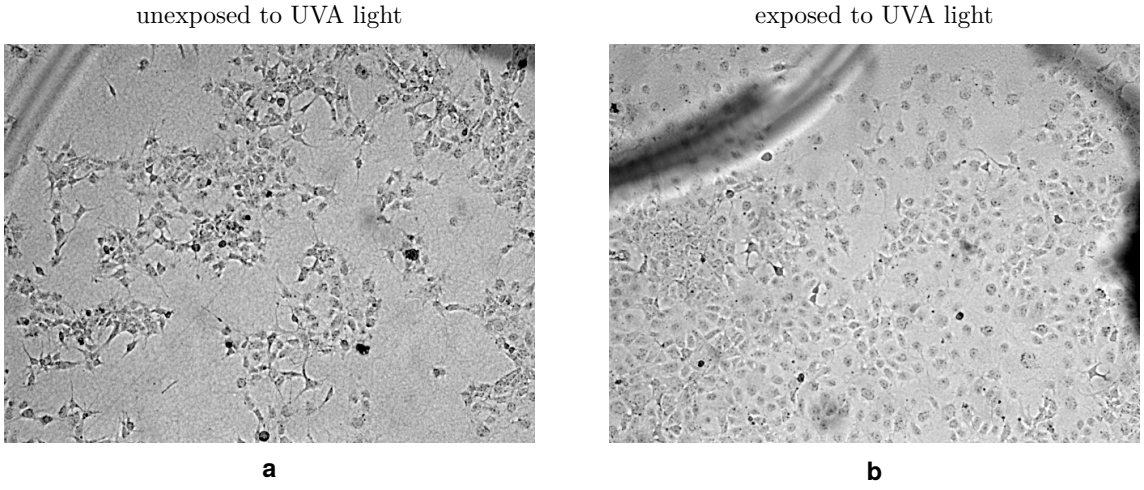

Figure 4.55.: Light microscopy images (5x/0.12 Zeiss-objective) of COS-7 cells on the same collagen hydrogel of which (a) one half was not exposed to UV light and (b) the other half was exposed to UVA light for 60 min while the hydrogel was immersed in deionised water. The COS-7 cells were seeded subsequently and the sample, covered with nutrition solution, was stored in an incubator at 37 °C and 5 % CO_2. Image size: 1225 x 915 µm^2. Images were provided by courtesy of Yue Du.

the light microscopy images of the COS-7 cells did not agree with the default values of the grid. The measured values could get closer to the latter if the area without cells to the left of the red box also belonged to the box and if the cell propagation could have continued in the depicted direction until it had reached 750 µm. Shadow casting or stray light could also have led to deviating values between the dimensions of the grid and the actual pattern on the sample. According to the general assumption that cells prefer stiffer areas for growth and propagation, the area highlighted by the red box was assumed to be covered by a bar of the grid, while the cells preferentially attached beneath a void due to the exposure to UVB while being immersed in 1xPBS. Still, Figure 4.56 could not confirm a successful patterning of the cell growth on a UV light exposed collagen hydrogel.

Similar results are presented in Figure 4.57 showing COS-7 cells that were seeded on a collagen hydrogel which had been exposed to UVA light through a grid for 120 min while being immersed in deionised water. During exposure, the bars of the grid were horizontally oriented regarding the presented images. Again, an area, highlighted by a red box, of lower cell population throughout the time of observation, could be found while the COS-7 cells preferentially propagated in the direction marked by the red arrow. Due to the unevenness of the sample, the propagating cells moved out of the focal plane of the microscope. As for Figure 4.56, the dimensions of the highlighted areas did not exactly fit the dimensions given by the grid. Still there seemed to be some driving force that guided the cell propagation in the specific direction.

Yet, for both samples, the shown behaviour was rather specific for one spot than for the whole sample, which meant that a pattern of alternating areas, according to the pattern of the applied grid, with low and high cell populations could not be found.

4.5.5 Summary

The aim of Section 4.5 was to describe the influence of the growth and propagation behaviour of biological cells by a patterned exposure of a collagen hydrogel substrate to UV light. Changes in the DMT modulus were investigated by PFQNM AFM and the cell behaviour was recorded by light microscopy.

AFM-based monitoring of the DMT modulus of collagen hydrogels during exposure to UV light revealed the same behaviour as has been presented before for collagen fibrils. Collagen hydrogels immersed in deionised water and exposed to UVA exhibited a continuously decreasing DMT modulus while the application of 1xPBS and UVC light resulted in a temporal elevation of the DMT modulus with a subsequent decrease. The next step towards a patterning of the collagen hydrogel was the exposure of half the sample to UV light while the other half stay unexposed. AFM measurements of the DMT modulus allowed the identification of a transition zone from low to high modulus (in agreement with the exposure conditions) that was located in the area of the transition between void and bar of the grid. Increasing the complexity of the grid did not deliver a distribution

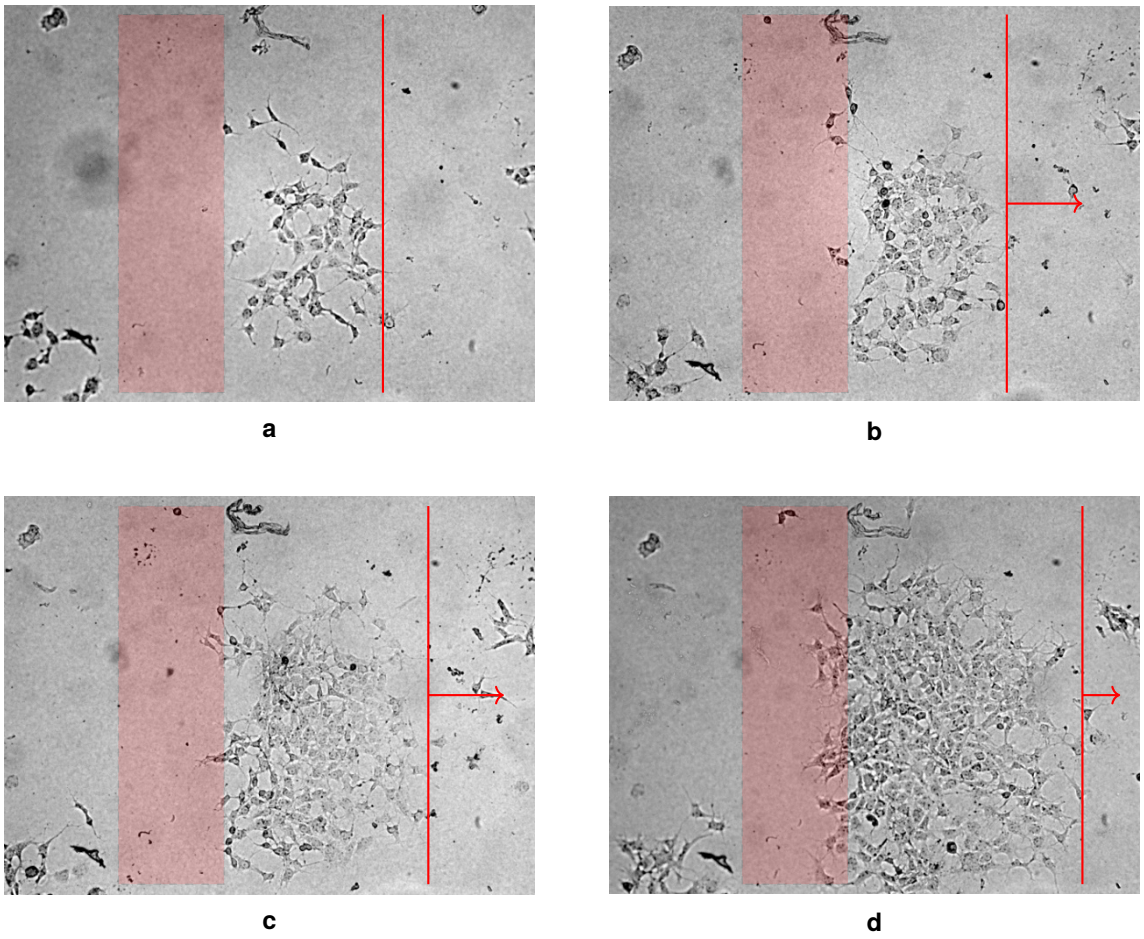

Figure 4.56.: Light microscopy images (5x/0.12 Zeiss-objective) of COS-7 cells on the same spot of a collagen hydrogel after (a) 96 h, (b) 120 h, (c) 144 h, and (d) 168 h. The collagen hydrogel was exposed to UVB light through a grid for 30 min while being immersed in 1xPBS. The COS-7 cells were seeded subsequently and the sample, covered with nutrition solution, was stored in an incubator at 37 °C and 5 % CO_2. The red box highlights an area of minimal cell attachment and the red line highlights a propagation direction of the cell colony. Image size: $1225 \times 915\ \mu m^2$. Images were provided by courtesy of Yue Du.

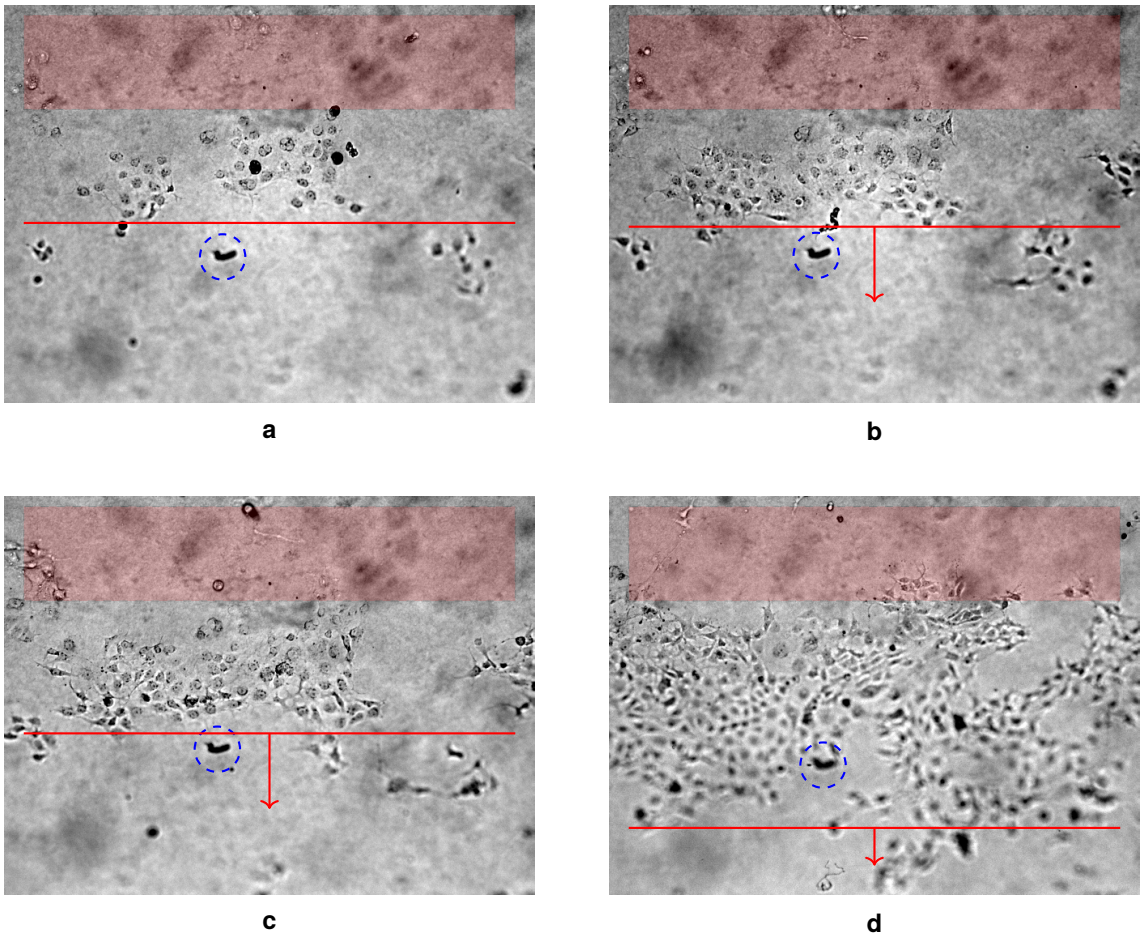

Figure 4.57.: Light microscopy images (5x/0.12 Zeiss-objective) of COS-7 cells on the same spot of a collagen hydrogel after (a) 96 h, (b) 120 h, (c) 144 h, and (d) 168 h. The collagen hydrogel was exposed to UVA light through a grid for 120 min while being immersed in deionised water. The COS-7 cells were seeded subsequently and the sample, covered with nutrition solution, was stored in an incubator at 37 °C and 5 % CO_2. The red box highlights an area of minimal cell attachment and the red line highlights a direction of the cell propagation. The blue, dashed circle highlights a structure as guide for the eye. Image size: 1225 x 915 µm^2. Images were provided by courtesy of Yue Du.

of the DMT modulus that fit to the pattern provided by the grid. While regions of lower and higher modulus could be identified, their dimensions could not be seen in the grid. Similar results could be shown for the behaviour of biological cells that were placed on unexposed and (partially) exposed collagen hydrogels. In general, cells adhered to and proliferated on the provided substrates but reaching confluence either took longer than in cell flasks or was not completed. Differences for the cell behaviour were seen for collagen hydrogels whose one half was exposed to UV light while the other one was not. Light microscopy images showed an increasing cell spreading on regions exposed to UVA during immersion in deionised water over unexposed regions to areas exposed to UVB while being immersed in 1xPBS. This agreed with the expectations that stiffer regions support more cell spreading. Applying more complex grid structures, however, did not display a correlation between the areas of cell adhesion and proliferation and the dimensions of the grid. Although some regions could be identified that showed a directed proliferation of cells in combination with regions of no cell adhesion that agreed with the orientation of the applied grid, a pattern that was represented by the whole sample could not be obtained.

5 Conclusions

The objective of this work was to describe the impact of UV light exposure on collagen samples immersed in various liquid environments with the focus on collagen fibrils. Changes in mechanical properties during UV light exposure were recorded by AFM using indentation experiments for the acquisition of an indentation modulus and a new approach to extract a tensile modulus of collagen fibrils was developed. Raman spectroscopy was applied to track changes in the structure of collagen with progressing UV light exposure. The results were compared regarding the combination of applied UV light wavelength and the kind of liquid the samples were immersed in during exposure. Additionally, collagen hydrogels were exposed to patterned UV light investigating the question of whether the growth behaviour of biological cells could be influenced or even guided by the proposed exposure conditions.

After an evaluation of adequate measurement parameters, the PFQNM AFM experiments revealed an essential dependence of the change in the indentation modulus with progressing UV light exposure on the kind of liquid environment. The quantitative findings showed an indentation modulus that was predominantly in the single-digit megapascal-range and a tensile modulus that was, for the unexposed state, between 0.4 and 1.5 GPa. During measurements in deionised water, the obtained modulus - in comparison to the unexposed state - was predominantly decreasing with advancing UV light exposure independently of the UV light source. Samples that were immersed in PBS-based solutions exhibited an elevated modulus after 30 to 50 min with a subsequent decrease when exposed to UVB or UVC light. A slight difference between UVB and UVC light was found in the exposure time at which the maximum elevation occurred, which tended to be shorter during the irradiation with UVC light. Exposure to UVA light did not result in a temporary elevation of the modulus. A new approach was presented for measuring the tensile modulus. Based on a setup for bending tests, the tensile modulus was extracted during fibril deflection due to the estimation of the axial stress and the axial strain. Similar results were found for the tensile modulus of collagen fibrils regarding the influence of the combination of UV light source and liquid environment during 60 min of exposure, including a sooner achievement of the maximum modulus for samples immersed in PBS when exposed to UVC instead of UVB light. A deviation was recorded for the combination of UVA light and 1xPBS, which, in contrast to the indentation modulus, showed an elevated modulus after approximately 40 min of exposure with a subsequent decrease. Due to the similarities and deviations of the results for the modulus in radial and axial direction, two model combinations of UV light source and kind of liquid environment emerged that predominantly led to either stabilising or destabilising effects in the collagen samples. The combination of UVA light and deionised water was used to induce a continuous

decrease of the modulus (destabilisation) and the combination of UVB/UVC and 1xPBS was used to generate an increasing modulus within the first 30 to 50 min of exposure (stabilisation). Investigating the influence of these model combinations on collagen samples measured by Raman spectroscopy delivered markers that could be associated with destabilising or stabilising effects and allowed for insights in the underlying mechanisms. The model combinations were applied to collagen hydrogels, as well as collagen fibrils. The most prominent changes occurred in the amide I band, describing the bonds between the amino acids, whose behaviour correlated with the band that indicates the O−H stretching vibration. From that, stabilising mechanisms were correlated with condensation reactions while a hydrolytic character was assigned to destabilising mechanisms. Details about the involved amino acids could not be clearly extracted but fluctuations in intensity of the aromatic amino acids hinted at an involvement of the telopeptides. This was supported by measured changes in the ratio of the α-helix to β-sheet configurations, two structures that only occur in the non-helical ends of type I collagen. Identifying the telopeptides as a major participant during stabilisation results in a small and limited number of reaction sites that can be activated during UV light exposure. The SERS spectra of collagen fibrils exhibited more distinct C−H vibration signals of the amino acids in comparison to the spectra of the hydrogels. Overall the trends of the applied stabilising or destabilising treatment conditions were similar to the spectra obtained from collagen hydrogels leading to the assumption that exposure to UV light mainly influenced intrafibrillar bonds and less interfibrillar bonds.

In the case of an induced temporary stabilisation, the quantitative extent to which the modulus changed varied, which led to the assumption that the initial state of crosslinking influenced the outcome of the exposure. The idea was that collagen fibrils containing a low initial degree of crosslinking bare a higher potential for an increase in modulus due to a limited number of potential crosslinking sites. Yet, every collagen fibril forms (all) possible crosslinks before destabilising effects prevail. Even on the same sample, not every collagen fibril contained the same initial conditions. The presented results suggested that the addition of PBS to the liquid environment during UV exposure seemed to be a necessary condition to achieve majorly stabilising mechanisms, but not a sufficient condition. Comparing the structure of PBS to substances that verifiably promote stabilising reactions in collagen or exhibit shielding effects revealed similarities that supported the finding of PBS being a decisive component. Apart from the formation of salt bridges, the stabilising mechanisms vary depending on the UV light source.

The interest in UV light exposure-induced changes in the mechanical properties of collagen samples is derived from their applicability as substrates for cell growth in the discipline of tissue engineering. Apart from a higher stability of the substrate, variations in its mechanics also have the potential to modify and guide cell growth, which is necessary for the creation of more promising and long-lasting implants. Thus, collagen hydrogels were exposed to UV light by applying a mask and, subsequently, COS-7 cells were seeded on the samples. Although changes in the mechanical properties of the collagen hydrogel due to exposure to UV light could be seen and

they were in agreement with the previously mentioned behaviour, the impact was not sufficient to generate clearly distinguishable regions of favoured and unfavoured cell growth.

The studies gave insights into the changes of the anisotropic mechanical properties of collagen fibrils due to UV light exposure *in situ*. By monitoring the same collagen fibril during the exposure, the initial state of the fibril was taken into account and a time-resolved evolution of the modulus was obtained. The presented approach for the evaluation of the tensile modulus bears the potential to accelerate the data acquisition in comparison to conventional AFM-based tensile test setups for cylindrical structures with radial dimensions in the lower nanometre-range. The findings regarding the changes in the mechanical properties could be correlated to the Raman spectroscopy measurements. Gaining an understanding of the underlying mechanisms confirmed earlier findings, stating that an introduced stabilisation is limited and, in case of UV exposure, is small compared to chemical treatment. The results showed that, in the case of samples immersed in 1xPBS, the exposure time to reach the maximum elevation can be influenced by the UV light source but the change in modulus will most likely be in the range as is stated in these studies. The measurements also confirmed that decisive changes in modulus can be reached within 60 min of exposure, proving the irradiation with UV light to be a fast method. The growth of cells on the exposed substrates underlined that the biocompatibility of the collagen hydrogels was not harmed by the exposure.

Exposure of collagen samples to UV light is a straightforward, handy, and timesaving method to modify their mechanical properties. Preserving biocompatibility, the outcome of the exposure can be tuned by varying the combination of applied UV light source and the kind of liquid environment.

6 Outlook

The presented studies depict small and defined problems dealing with the interplay of collagen and UV light. Although the tasks were concluded, they are the origin for a variety of follow-up questions and further research.

A general question is how collagen from a different source would react to the applied exposure conditions. The difference between collagen from solution (as used in these studies) and fresh collagen is especially of interest. Further aspects such as, *e.g.*, age of the sample, could be considered. Another way of changing the source is changing the type of collagen. In this case, the impact of UV exposure on collagen samples could be investigated for non-fibrillar collagen types or collagen types that do not exhibit a telopeptide. In the end, it would matter most to test the collagen that is actually applied in medical procedures.

Apart from a change in sample, a change in the AFM mode is also possible with the goal of recording more information on the mechanical properties of collagen fibrils within one measurement and, thus, considering their anisotropy. A recently presented AFM mode combines the torsional oscillation of an AFM cantilever with the depth-resolved acquisition of the indentation modulus, creating three-dimensional maps of the elastic modulus in vertical and lateral direction simultaneously.[332] Applying this mode to collagen fibrils before and after UV light exposure could provide information on their mechanical properties with a high spatial resolution in three dimensions. It bears the possibility to gain the elastic modulus in radial and axial[xiii] direction with one measurement and the resulting images could give hints on whether the change in modulus due to UV light exposure is a homogeneously occurring effect or maybe bound to certain regions in the fibril. This approach could also help to answer the question of whether the deviating behaviour between the indentation and the tensile experiments regarding the measurements of collagen in 1xPBS and exposed to UVA light was due to a reduced reproducibility of the sample behaviour under the applied conditions or due to different underlying mechanisms. With or without that mentioned AFM mode, the origin for this uncertainty could be of interest.

Regarding the experiments with biological cells, sample preparation provided room for improvement. First, the mechanical properties of the collagen hydrogel need to be more homogenous. Otherwise, inherent differences

[xiii] Depending on the orientation of the fibrils towards the torsional oscillation of the AFM tip.

already create an arbitrary pattern on the surface that cannot be broken by an external patterned exposure. Second, the elastic modulus of the collagen hydrogel needs to be more similar to the tissue the cells experience in their natural environment. While the measured elastic moduli of the collagen hydrogels used in this study were predominantly above 50 kPa, distinct differences between soft and stiff substrates have been reported for substrates with elastic moduli far below 10 kPa. The proposal is that the (patterned) exposure of such soft gels to UV light may create real difference in cell behaviour for which, on the one side, the hydrogel samples have to be softer (*e.g.* via thickness) and, on the other side, the applied cell line has to be more fitting to the achieved elastic modulus.

Several further ideas and tasks appeared throughout the research:

- Expanding the evaluation script of the tensile tests so that the bending modulus can be evaluated simultaneously.
- Applying different kinds of salts (instead of PBS) to see whether the final stabilisation will be influenced.
- Using a UV light source with a significantly higher light intensity to induce stronger destabilising effects in collagen hydrogels and test the reaction of cells towards these regions.
- Reaching confluence of seeded cells on a collagen hydrogel before exposing the sample to patterned UVC light and, thus, imprinting a pattern on the sample by guided degradation of cells.

The bottom line of these studies is that an understanding of how exposure to UV light impacts the mechanical properties of collagen fibrils is essential because the results can be transferred to collagen hydrogels. Therefore, it is important to investigate the microscopic properties of the small collagen units, as well as the macroscopic interactions between collagen hydrogels and biological cells. Pursuing both research directions, microscopic and macroscopic, should be the key to enabling admission of an UV light exposed collagen-based product to medical applications.

Bibliography

[1] J. Skopinska-Wisniewska, A. Sionkowska, A. Kaminska, A. Kaznica, R. Jachimiak, and T. Drewa, *Surface characterization of collagen/elastin based biomaterials for tissue regeneration*, Applied Surface Science **255**, 8286–8292 (2009).

[2] A. Sionkowska and T. Wess, *Mechanical properties of UV irradiated rat tail tendon (RTT) collagen*, International Journal of Biological Macromolecules **34**, 9–12 (2004).

[3] K. Matsumoto, T. Nakamura, Y. Shimizu, H. Ueda, T. Sekine, Y. Yamamoto, T. Kiyotani, and Y. Takimoto, *A novel surgical material made from collagen with high mechanical strength - a collagen sandwich membrane*, Asaio Journal **45**, 288–292 (1999).

[4] M. Stolz, R. Raiteri, A. U. Daniels, M. R. VanLandingham, W. Baschong, and U. Aebi, *Dynamic elastic modulus of porcine articular cartilage determined at two different levels of tissue organization by indentation-type atomic force microscopy*, Biophysical Journal **86**, 3269–3283 (2004).

[5] M. Stolz, R. Gottardi, R. Raiteri, S. Miot, I. Martin, R. Imer, U. Staufer, A. Raducanu, M. Duggelin, W. Baschong, A. U. Daniels, N. F. Friederich, A. Aszodi, and U. Aebi, *Early detection of aging cartilage and osteoarthritis in mice and patient samples using atomic force microscopy*, Nature Nanotechnology **4**, 186–192 (2009).

[6] D. Xia, S. Zhang, J. O. Hjortdal, Q. Li, K. Thomsen, J. Chevallier, F. Besenbacher, and M. D. Dong, *Hydrated human corneal stroma revealed by quantitative dynamic atomic force microscopy at nanoscale*, ACS Nano **8**, 6873–6882 (2014).

[7] T. Hassenkam, H. L. Jorgensen, M. B. Pedersen, A. H. Kourakis, L. Simonsen, and J. B. Lauritzen, *Atomic force microscopy on human trabecular bone from an old woman with osteoporotic fractures*, Micron **36**, 681–687 (2005).

[8] J. M. Wallace, B. Erickson, C. M. Les, B. G. Orr, and M. M. B. Holl, *Distribution of type I collagen morphologies in bone: Relation to estrogen depletion*, Bone **46**, 1349–1354 (2010).

[9] T. Hassenkam, G. E. Fantner, J. A. Cutroni, J. C. Weaver, D. E. Morse, and P. K. Hansma, *High-resolution AFM imaging of intact and fractured trabecular bone*, Bone **35**, 4–10 (2004).

[10] S. J. Lee, S. Choi, M. S. Kim, Y. Cheong, H. W. Kwak, H. K. Park, and K. H. Jin, *Short-term effect of cryotherapy on human scleral tissue by atomic force microscopy*, Scanning **35**, 302–307 (2013).

[11] S. J. Baldwin, A. S. Quigley, C. Clegg, and L. Kreplak, *Nanomechanical mapping of hydrated rat tail tendon collagen I fibrils*, Biophysical Journal **107**, 1794–1801 (2014).

[12] A. Gautieri, S. Vesentini, A. Redaelli, and M. J. Buehler, *Hierarchical structure and nanomechanics of collagen microfibrils from the atomistic scale up*, Nano Letters **11**, 757–766 (2011).

[13] Q. Z. Chen, S. E. Harding, N. N. Ali, A. R. Lyon, and A. R. Boccaccini, *Biomaterials in cardiac tissue engineering: Ten years of research survey*, Materials Science & Engineering R-Reports **59**, 1–37 (2008).

[14] F. J. O'Brien, *Biomaterials & scaffolds for tissue engineering*, Materials Today **14**, 88–95 (2011).

[15] C. M. Lo, H. B. Wang, M. Dembo, and Y. L. Wang, *Cell movement is guided by the rigidity of the substrate*, Biophysical Journal **79**, 144–152 (2000).

[16] D. P. McDaniel, G. A. Shaw, J. T. Elliott, K. Bhadriraju, C. Meuse, K. H. Chung, and A. L. Plant, *The stiffness of collagen fibrils influences vascular smooth muscle cell phenotype*, Biophysical Journal **92**, 1759–1769 (2007).

[17] R. G. Wells, *The role of matrix stiffness in regulating cell behavior*, Hepatology **47**, 1394–1400 (2008).

[18] T. Yeung, P. C. Georges, L. A. Flanagan, B. Marg, M. Ortiz, M. Funaki, N. Zahir, W. Y. Ming, V. Weaver, and P. A. Janmey, *Effects of substrate stiffness on cell morphology, cytoskeletal structure, and adhesion*, Cell Motility and the Cytoskeleton **60**, 24–34 (2005).

[19] M. P. Ohan, K. S. Weadock, and M. G. Dunn, *Synergistic effects of glucose and ultraviolet irradiation on the physical properties of collagen*, Journal of Biomedical Materials Research **60**, 384–391 (2002).

[20] J. E. Gough, C. A. Scotchford, and S. Downes, *Cytotoxicity of glutaraldehyde crosslinked collagen/poly(vinyl alcohol) films is by the mechanism of apoptosis*, Journal of Biomedical Materials Research **61**, 121–130 (2002).

[21] N. Davidenko, D. V. Bax, C. F. Schuster, R. W. Farndale, S. W. Hamaia, S. M. Best, and R. E. Cameron, *Optimisation of UV irradiation as a binding site conserving method for crosslinking collagen-based scaffolds*, Journal of Materials Science-Materials in Medicine **27**, 14 (2016).

[22] A. Sionkowska, *Thermal denaturation of UV-irradiated wet rat tail tendon collagen*, International Journal of Biological Macromolecules **35**, 145–149 (2005).

[23] T. Miyata, T. Sohde, A. L. Rubin, and K. H. Stenzel, *Effects of ultraviolet irradiation on native and telopeptide-poor collagen*, Biochimica Et Biophysica Acta **229**, 672–80 (1971).

[24] A. Sionkowska and A. Kaminska, *Thermal helix-coil transition in UV irradiated collagen from rat tail tendon*, International Journal of Biological Macromolecules **24**, 337–340 (1999).

[25] E. Fujimori, *Changes induced by ozone and ultraviolet-light in type-I collagen - bovine achilles-tendon collagen versus rat tail tendon collagen*, European Journal of Biochemistry **152**, 299–306 (1985).

[26] A. Kaminska and A. Sionkowska, *The effect of UV radiation on the thermal parameters of collagen degradation*, Polymer Degradation and Stability **51**, 15–18 (1996).

[27] C. A. Miles, A. Sionkowska, S. L. Hulin, T. J. Sims, N. C. Avery, and A. J. Bailey, *Identification of an intermediate state in the helix-coil degradation of collagen by ultraviolet light*, Journal of Biological Chemistry **275**, 33014–33020 (2000).

[28] A. Stylianou and D. Yova, *Surface nanoscale imaging of collagen thin films by atomic force microscopy*, Materials Science & Engineering C-Materials for Biological Applications **33**, 2947–2957 (2013).

[29] A. Y. Wang, X. Mo, C. S. Chen, and S. M. Yu, *Facile modification of collagen directed by collagen mimetic peptides*, Journal of the American Chemical Society **127**, 4130–4131 (2005).

[30] K. Gelse, E. Poschl, and T. Aigner, *Collagens - structure, function, and biosynthesis*, Advanced Drug Delivery Reviews **55**, 1531–1546 (2003).

[31] M. P. E. Wenger, L. Bozec, M. A. Horton, and P. Mesquida, *Mechanical properties of collagen fibrils*, Biophysical Journal **93**, 1255–1263 (2007).

[32] A. L. Rubin, R. R. Riggio, R. L. Nachman, G. H. Schwartz, T. Miyata, and K. H. Stenzel, *Collagen materials in dialysis and implantation*, Transactions American Society for Artificial Internal Organs **14**, 169 (1968).

[33] M. D. Shoulders and R. T. Raines, *Collagen structure and stability*, Annual Review of Biochemistry **78**, 929–958 (2009).

[34] M. Gasior-Glogowska, M. Komorowska, J. Hanuza, M. Ptak, and M. Kobielarz, *Structural alteration of collagen fibres - spectroscopic and mechanical studies*, Acta of Bioengineering and Biomechanics **12**, 55–62 (2010).

[35] F. H. Silver and W. J. Landis, *Viscoelasticity, energy storage and transmission and dissipation by extracellular matrices in vertebrates*, Collagen: Structure and Mechanics (P. Fratzl, ed.), Ch. 6, pp. 133–154, Springer US, New York, 2008.

[36] K. E. Kadler, C. Baldock, J. Bella, and R. P. Boot-Handford, *Collagens at a glance*, Journal of Cell Science **120**, 1955–1958 (2007).

[37] E. D. Hay, *Extracellular-matrix*, Journal of Cell Biology **91**, S205–S223 (1981).

[38] M. M. Chen, Y. Q. Huang, H. Guo, Y. Liu, J. H. Wang, J. L. Wu, and Q. Q. Zhang, *Preparation, characterization, and potential biomedical application of composite sponges based on collagen from silver carp skin*, Journal of Applied Polymer Science **131**, 40998 (2014).

[39] Z. Q. Zhang, Y. W. Zhang, and H. J. Gao, *On optimal hierarchy of load-bearing biological materials*, Proceedings of the Royal Society B-Biological Sciences **278**, 519–525 (2011).

[40] G. Janani, M. M. Pillai, R. Selvakumar, A. Bhattacharyya, and C. Sabarinath, *An in vitro 3D model using collagen coated gelatin nanofibers for studying breast cancer metastasis*, Biofabrication **9**, 015016 (2017).

[41] M. Venturoni, T. Gutsmann, G. E. Fantner, J. H. Kindt, and P. K. Hansma, *Investigations into the polymorphism of rat tail tendon fibrils using atomic force microscopy*, Biochemical and Biophysical Research Communications **303**, 508–513 (2003).

[42] Y. Henrotin, S. Addison, V. Kraus, and M. Deberg, *Type II collagen markers in osteoarthritis: What do they indicate?*, Current Opinion in Rheumatology **19**, 444–450 (2007).

[43] P. Kannu, J. Bateman, and R. Savarirayan, *Clinical phenotypes associated with type II collagen mutations*, Journal of Paediatrics and Child Health **48**, E38–E43 (2012).

[44] D. J. Taatjes, A. S. Quinn, and E. G. Bovill, *Imaging of collagen type III in fluid by atomic force microscopy*, Microscopy Research and Technique **44**, 347–352 (1999).

[45] S. W. Tsai, Y. H. Cheng, Y. Chang, H. L. Liu, and W. B. Tsai, *Type I collagen structure modulates the behavior of osteoblast-like cells*, Journal of the Taiwan Institute of Chemical Engineers **41**, 247–251 (2010).

[46] A. L. Plant, K. Bhadriraju, T. A. Spurlin, and J. T. Elliott, *Cell response to matrix mechanics: Focus on collagen*, Biochimica Et Biophysica Acta-Molecular Cell Research **1793**, 893–902 (2009).

[47] Z. Keresztes, P. G. Rouxhet, C. Remacle, and C. Dupont-Gillain, *Supramolecular assemblies of adsorbed collagen affect the adhesion of endothelial cells*, Journal of Biomedical Materials Research Part A **76A**, 223–233 (2006).

[48] F. Malfait, R. J. Wenstrup, and A. De Paepe, *Clinical and genetic aspects of Ehlers-Danlos syndrome, classic type*, Genetics in Medicine **12**, 597–605 (2010).

[49] C. E. Kashtan and A. F. Michael, *Alport syndrome*, Kidney International **50**, 1445–1463 (1996).

[50] F. Rauch and F. H. Glorieux, *Osteogenesis imperfecta*, Lancet **363**, 1377–1385 (2004).

[51] S. F. A. Grant, D. M. Reid, G. Blake, R. Herd, I. Fogelman, and S. H. Ralston, *Reduced bone density and osteoporosis associated with a polymorphic Sp1 binding site in the collagen type I alpha 1 gene*, Nature Genetics **14**, 203–205 (1996).

[52] O. G. Andriotis, S. W. Chang, M. Vanleene, P. H. Howarth, D. E. Davies, S. J. Shefelbine, M. J. Buehler, and P. J. Thurner, *Structure-mechanics relationships of collagen fibrils in the osteogenesis imperfecta mouse model*, Journal of the Royal Society, Interface **12**, 20150701 (2015).

[53] S. Lehoux, Y. Castier, and A. Tedgui, *Molecular mechanisms of the vascular responses to haemodynamic forces*, Journal of Internal Medicine **259**, 381–392 (2006).

[54] L. Kass, J. T. Erler, M. Dembo, and V. M. Weaver, *Mammary epithelial cell: Influence of extracellular matrix composition and organization during development and tumorigenesis*, International Journal of Biochemistry & Cell Biology **39**, 1987–1994 (2007).

[55] M. J. Bissell and M. A. LaBarge, *Context, tissue plasticity, and cancer: Are tumor stem cells also regulated by the microenvironment?*, Cancer Cell **7**, 17–23 (2005).

[56] M. J. Paszek, N. Zahir, K. R. Johnson, J. N. Lakins, G. I. Rozenberg, A. Gefen, C. A. Reinhart-King, S. S. Margulies, M. Dembo, D. Boettiger, D. A. Hammer, and V. M. Weaver, *Tensional homeostasis and the malignant phenotype*, Cancer Cell **8**, 241–254 (2005).

[57] G. N. Ramachandran and G. Kartha, *Structure of collagen*, Nature **176**, 593–595 (1955).

[58] G. N. Ramachandran, *Structure of collagen*, Nature **177**, 710–711 (1956).

[59] A. Ambrogelly, S. Palioura, and D. Soll, *Natural expansion of the genetic code*, Nature Chemical Biology **3**, 29–35 (2007).

[60] D. Vnucec, A. Kutnar, and A. Gorsek, *Soy-based adhesives for wood-bonding - a review*, Journal of Adhesion Science and Technology **31**, 910–931 (2017).

[61] C. Gullekson, L. Lucas, K. Hewitt, and L. Kreplak, *Surface-sensitive Raman spectroscopy of collagen I fibrils*, Biophysical Journal **100**, 1837–1845 (2011).

[62] M. J. Buehler, *Hierarchical nanomechanics of collagen fibrils: Atomistic and molecular modeling*, Collagen: Structure and Mechanics (P. Fratzl, ed.), Ch. 8, pp. 175–247, Springer US, New York, 2008.

[63] B. Brodsky and J. A. M. Ramshaw, *The collagen triple-helix structure*, Matrix Biology **15**, 545–554 (1997).

[64] A. George, J. P. Malone, and A. Veis, *The secondary structure of type I collagen N-telopeptide as demonstrated by Fourier transform IR spectroscopy and molecular modeling*, Proceedings of the Indian Academy of Sciences-Chemical Sciences **111**, 121–131 (1999).

[65] T. J. Wess, *Collagen fibrillar structure and hierachies*, Collagen: Structure and Mechanics (P. Fratzl, ed.), Ch. 3, pp. 49–80, Springer US, New York, 2008.

[66] B. G. Hudson, S. T. Reeders, and K. Tryggvason, *Type-IV collagen - structure, gene organization, and role in human-diseases - molecular-basis of goodpasture and alport syndromes and diffuse leiomyomatosis*, Journal of Biological Chemistry **268**, 26033–26036 (1993).

[67] S. L. Hostikka and K. Tryggvason, *The complete primary structure of the alpha-2 chain of human type-IV collagen and comparison with the alpha-1 (IV) chain*, Journal of Biological Chemistry **263**, 19488–19493 (1988).

[68] D. J. S. Hulmes, *Collagen diversity, synthesis and assembly*, Collagen: Structure and Mechanics (P. Fratzl, ed.), Ch. 2, pp. 15–47, Springer US, New York, 2008.

[69] J. Parkinson, K. E. Kadler, and A. Brass, *Self-assembly of rodlike particles in 2 dimensions - a simple-model for collagen fibrillogenesis*, Physical Review E **50**, 2963–2966 (1994).

[70] J. W. Smith, *Molecular pattern in native collagen*, Nature **219**, 157 (1968).

[71] D. J. S. Hulmes and A. Miller, *Quasi-hexagonal molecular packing in collagen fibrils*, Nature **282**, 878–880 (1979).

[72] B. L. Trus and K. A. Piez, *Compressed microfibril models of the native collagen fibril*, Nature **286**, 300–301 (1980).

[73] J. A. Petruska and A. J. Hodge, *Subunit model for tropocollagen macromolecule*, Proceedings of the National Academy of Sciences of the United States of America **51**, 871 (1964).

[74] B. Erickson, M. Fang, J. M. Wallace, B. G. Orr, C. M. Les, and M. M. B. Holl, *Nanoscale structure of type I collagen fibrils: Quantitative measurement of D-spacing*, Biotechnology Journal **8**, 117 (2013).

[75] J. P. R. O. Orgel, T. C. Irving, A. Miller, and T. J. Wess, *Microfibrillar structure of type I collagen in situ*, Proceedings of the National Academy of Sciences of the United States of America **103**, 9001–9005 (2006).

[76] D. J. S. Hulmes, T. J. Wess, D. J. Prockop, and P. Fratzl, *Radial packing, order, and disorder in collagen fibrils*, Biophysical Journal **68**, 1661–1670 (1995).

[77] D. A. D. Parry, *The molecular and fibrillar structure of collagen and its relationship to the mechanical-properties of connective-tissue*, Biophysical Chemistry **29**, 195–209 (1988).

[78] M. Minary-Jolandan and M. F. Yu, *Nanomechanical heterogeneity in the gap and overlap regions of type I collagen fibrils with implications for bone heterogeneity*, Biomacromolecules **10**, 2565–2570 (2009).

[79] J. Myllyharju, J. Brinckmann, H. Notbohm, and P. K. Muller, *Intracellular post-translational modifications of collagens*, Topics in Current Chemistry, vol. 247, pp. 115–147, Springer-Verlag Berlin, Berlin, 2005.

[80] M. L. Chu, T. C. Pan, D. Conway, B. Saitta, D. Stokes, H. J. Kuo, R. W. Glanville, R. Timpl, K. Mann, and R. Deutzmann, *The structure of type-VI collagen*, Annals of the New York Academy of Sciences **580**, 55–63 (1990).

[81] P. E. Shamhart and J. G. Meszaros, *Non-fibrillar collagens: Key mediators of post-infarction cardiac remodeling?*, Journal of Molecular and Cellular Cardiology **48**, 530–537 (2010).

[82] G. N. Ramachandran, M. Bansal, and Bhatnagar R., *A hypothesis on the role of hydroxyproline in stabilizing collagen structure*, Biochimica Et Biophysica Acta (BBA) - Protein Structure **322**, 166–171 (1973).

[83] P. M. Cowan, S. McGavin, and A. C. T. North, *Polypeptide chain configuration of collagen*, Nature **176**, 1062–1064 (1955).

[84] A. Rich and F. H. C. Crick, *Molecular structure of collagen*, Journal of Molecular Biology **3**, 483 (1961).

[85] J. Bella, B. Brodsky, and H. M. Berman, *Hydration structure of a collagen peptide*, Structure **3**, 893–906 (1995).

[86] R. Berisio, L. Vitagliano, L. Mazzarella, and A. Zagari, *Crystal structure of the collagen triple helix model (Pro-Pro-Gly)(10) (3)*, Protein Science **11**, 262–270 (2002).

[87] L. Knott and A. J. Bailey, *Collagen cross-links in mineralizing tissues: A review of their chemistry, function, and clinical relevance*, Bone **22**, 181–187 (1998).

[88] S. G. M. Uzel and M. J. Buehler, *Molecular structure, mechanical behavior and failure mechanism of the C-terminal cross-link domain in type I collagen*, Journal of the Mechanical Behavior of Biomedical Materials **4**, 153–161 (2011).

[89] M. L. Tanzer, *Crosslinking of collagen*, Science **180**, 561–566 (1973).

[90] L. Yang, K. O. Van der Werf, C. F. C. Fitie, M. L. Bennink, P. J. Dijkstra, and J. Feijen, *Mechanical properties of native and cross-linked type I collagen fibrils*, Biophysical Journal **94**, 2204–2211 (2008).

[91] D. L. Helseth and A. Veis, *Collagen self-assembly invitro - differentiating specific telopeptide-dependent interactions using selective enzyme modification and the addition of free amino telopeptide*, Journal of Biological Chemistry **256**, 7118–7128 (1981).

[92] R. Langer and J. P. Vacanti, *Tissue engineering*, Science **260**, 920–926 (1993).

[93] Q. Z. Chen, S. L. Liang, and G. A. Thouas, *Elastomeric biomaterials for tissue engineering*, Progress in Polymer Science **38**, 584–671 (2013).

[94] J. E. Lee, J. C. Park, Y. S. Hwang, J. K. Kim, J. G. Kim, and H. Suh, *Characterization of UV-irradiated dense/porous collagen membranes: Morphology, enzymatic degradation, and mechanical properties*, Yonsei Medical Journal **42**, 172–179 (2001).

[95] K. Fujioka, M. Maeda, T. Hojo, and A. Sano, *Protein release from collagen matrices*, Advanced Drug Delivery Reviews **31**, 247–266 (1998).

[96] B. P. Chan, O. C. M. Chan, and K. F. So, *Effects of photochemical crosslinking on the microstructure of collagen and a feasibility study on controlled protein release*, Acta Biomaterialia **4**, 1627–1636 (2008).

[97] J. M. Dang and K. W. Leong, *Natural polymers for gene delivery and tissue engineering*, Advanced Drug Delivery Reviews **58**, 487–499 (2006).

[98] P. A. J. Enever, D. I. Shreiber, and R. T. Tranquillo, *A novel implantable collagen gel assay for fibroblast traction and proliferation during wound healing*, Journal of Surgical Research **105**, 160–172 (2002).

[99] N. Rajan, J. Lagueux, F. Couet, W. Pennock, D. Mantovani, and A. Sionkowska, *Low doses of ultraviolet radiation stimulate cell activity in collagen-based scaffolds*, Biotechnology Progress **24**, 884–889 (2008).

[100] C. C. Yao, P. Yao, H. Wu, and Z. G. Zha, *Absorbable collagen sponge combined with recombinant human basic fibroblast growth factor promotes nerve regeneration in rat sciatic nerve*, Journal of Materials Science-Materials in Medicine **18**, 1969–1972 (2007).

[101] J. Habermehl, J. Skopinska, F. Boccafoschi, A. Sionkowska, H. Kaczmarek, G. Laroche, and D. Mantovani, *Preparation of ready-to-use, stockable and reconstituted collagen*, Macromolecular Bioscience **5**, 821–828 (2005).

[102] M. T. Sheu, J. C. Huang, G. C. Yeh, and H. O. Ho, *Characterization of collagen gel solutions and collagen matrices for cell culture*, Biomaterials **22**, 1713–1719 (2001).

[103] L. Besseau, B. Coulomb, C. Lebreton-Decoster, and M. M. Giraud-Guille, *Production of ordered collagen matrices for three-dimensional cell culture*, Biomaterials **23**, 27–36 (2002).

[104] B. Jiang, Z. H. Wu, H. C. Zhao, F. Y. Tang, J. Lu, Q. R. Wei, and X. D. Zhang, *Electron beam irradiation modification of collagen membrane*, Biomaterials **27**, 15–23 (2006).

[105] M. R. Cunha, A. R. Santos, G. Goissis, and S. C. Genari, *Implants of polyanionic collagen matrix in bone defects of ovariectomized rats*, Journal of Materials Science - Materials in Medicine **19**, 1341–1348 (2008).

[106] S. Yunoki, E. Marukawa, T. Ikoma, S. Sotome, H. S. Fan, X. D. Zhang, K. Shinomiya, and J. Tanaka, *Effect of collagen fibril formation on bioresorbability of hydroxyapatite/collagen composites*, Journal of Materials Science: Materials in Medicine **18**, 2179–2183 (2007).

[107] S. R. Frenkel, B. Toolan, D. Menche, M. I. Pitman, and J. M. Pachence, *Chondrocyte transplantation using a collagen bilayer matrix for cartilage repair*, Journal of Bone and Joint Surgery - British Volume **79B**, 831–836 (1997).

[108] X. L. Wang, L. Sang, D. M. Luo, and X. D. Li, *From collagen-chitosan blends to three-dimensional scaffolds the influences of chitosan on collagen nanofibrillar structure and mechanical property*, Colloids and Surfaces B: Biointerfaces **82**, 233–240 (2011).

[109] K. M. Brouwer, P. van Rensch, V. E. M. Harbers, P. J. Geutjes, M. J. W. Koens, R. M. H. Wijnen, W. F. Daamen, and T. H. van Kuppevelt, *Evaluation of methods for the construction of collagenous scaffolds with a radial pore structure for tissue engineering*, Journal of Tissue Engineering and Regenerative Medicine **5**, 501–504 (2011).

[110] J. Glowacki and S. Mizuno, *Collagen scaffolds for tissue engineering*, Biopolymers **89**, 338–344 (2008).

[111] I. V. Yannas, E. Lee, D. P. Orgill, E. M. Skrabut, and G. F. Murphy, *Synthesis and characterization of a model extracellular-matrix that induces partial regeneration of adult mammalian skin*, Proceedings of the National Academy of Sciences of the United States of America **86**, 933–937 (1989).

[112] E. Fujimori, *Ultraviolet light-induced change in collagen macromolecules*, Biopolymers **3**, 115–119 (1965).

[113] E. Fujimori, *Ultraviolet light irradiated collagen macromolecules*, Biochemistry **5**, 1034–1040 (1966).

[114] D. R. Cooper and R. J. Davidson, *Effect of ultraviolet irradiation on soluble collagen*, Biochemical Journal **97**, 139–147 (1965).

[115] Y. Kato, K. Uchida, and S. Kawakishi, *Oxidative-degradation of collagen and its model peptide by ultraviolet-irradiation*, Journal of Agricultural and Food Chemistry **40**, 373–379 (1992).

[116] A. Sionkowska, *Modification of collagen films by ultraviolet irradiation*, Polymer Degradation and Stability **68**, 147–151 (2000).

[117] A. Torikai and H. Shibata, *Effect of ultraviolet radiation on photodegradation of collagen*, Journal of Applied Polymer Science **73**, 1259–1265 (1999).

[118] A. Sionkowska, A. Kaminska, C. A. Miles, and A. J. Bailey, *The effect of UV radiation on the structure and properties of collagen*, Polimery **46**, 379–389 (2001).

[119] E. Fujimori, *Cross-linking of collagen CNBr peptides by ozone or UV-light*, FEBS Letters **235**, 98–102 (1988).

[120] A. Ryu, E. Naru, K. Arakane, T. Masunaga, K. Shinmoto, T. Nagano, M. Hirobe, and S. Mashiko, *Cross-linking of collagen by singlet oxygen generated with UV-A*, Chemical & Pharmaceutical Bulletin **45**, 1243–1247 (1997).

[121] A. Sionkowska and A. Kaminska, *Changes induced by ultraviolet light in fluorescence of collagen in the presence of beta-carotene*, Journal of Photochemistry and Photobiology A: Chemistry **120**, 207–210 (1999).

[122] M. Kohlhaas, *Collagen crosslinking with riboflavin and UVA-light in keratoconus*, Ophthalmologe **105**, 785–793 (2008).

[123] N. N. Fathima, J. R. Rao, and B. U. Nair, *Effect of UV irradiation on the physico-chemical properties of iron crosslinked collagen*, Journal of Photochemistry and Photobiology B: Biology **105**, 203–206 (2011).

[124] V. Au and S. A. Madison, *Effects of singlet oxygen on the extracellular matrix protein collagen: Oxidation of the collagen crosslink histidinohydroxylysinonorleucine and histidine*, Archives of Biochemistry and Biophysics **384**, 133–142 (2000).

[125] A. S. McCall, S. Kraft, H. F. Edelhauser, G. W. Kidder, R. R. Lundquist, H. E. Bradshaw, Z. Dedeic, M. J. C. Dionne, E. M. Clement, and G. W. Conrad, *Mechanisms of corneal tissue cross-linking in response to treatment with topical riboflavin and long-wavelength ultraviolet radiation (UVA)*, Investigative Ophthalmology & Visual Science **51**, 129–138 (2010).

[126] K. Wand, R. Neuhann, A. Ullmann, K. Plank, M. Baumann, R. Ritter, M. Griffith, C. P. Lohmann, and K. Kobuch, *Riboflavin-UV-A crosslinking for fixation of biosynthetic corneal collagen implants*, Cornea **34**, 544–549 (2015).

[127] O. Richoz, A. Hammer, D. Tabibian, Z. Gatzioufas, and F. Hafezi, *The biomechanical effect of corneal collagen cross-linking (cxl) with riboflavin and UV-A is oxygen dependent*, Translational Vision Science & Technology **2**, 6 (2013).

[128] K. S. Weadock, E. J. Miller, L. D. Bellincampi, J. P. Zawadsky, and M. G. Dunn, *Physical cross-linking of collagen-fibers - Comparison of ultraviolet-irradiation and dehydrothermal treatment*, Journal of Biomedical Materials Research **29**, 1373–1379 (1995).

[129] C. H. Lee, A. Singla, and Y. Lee, *Biomedical applications of collagen*, International Journal of Pharmaceutics **221**, 1–22 (2001).

[130] J. M. Menter, A. M. Patta, R. M. Sayre, J. Dowdy, and I. Willis, *Effect of UV irradiation on type I collagen fibril formation in neutral collagen solutions*, Photodermatology Photoimmunology & Photomedicine **17**, 114–120 (2001).

[131] N. Metreveli, L. Namicheishvili, K. Jariashvili, G. Mrevlishvili, and A. Sionkowska, *Mechanisms of the influence of UV irradiation on collagen and collagen-ascorbic acid solutions*, International Journal of Photoenergy **2006**, 76830 (2006).

[132] N. N. Fathima, R. Suresh, J. R. Rao, and B. U. Nair, *Effect of UV irradiation on the physicochemical properties of collagen stabilized using aldehydes*, Journal of Applied Polymer Science **104**, 3642–3648 (2007).

[133] E. Ruoslahti and M. D. Pierschbacher, *New perspectives in cell-adhesion - RGD and integrins*, Science **238**, 491–497 (1987).

[134] G. Penners, Z. Priel, and A. Silberberg, *Irreversible adsorption of triple-helical soluble collagen monomers from solution to glass and other surfaces*, Journal of Colloid and Interface Science **80**, 437–444 (1981).

[135] C. C. Dupont-Gillain, E. Pamula, F. A. Denis, V. M. De Cupere, Y. F. Dufrene, and P. G. Rouxhet, *Controlling the supramolecular organisation of adsorbed collagen layers*, Journal of Materials Science: Materials in Medicine **15**, 347–353 (2004).

[136] F. A. Denis, P. Hanarp, D. S. Sutherland, J. Gold, C. Mustin, P. G. Rouxhet, and Y. F. Dufrene, *Protein adsorption on model surfaces with controlled nanotopography and chemistry*, Langmuir **18**, 819–828 (2002).

[137] E. Pamula, V. De Cupere, Y. F. Dufrene, and P. G. Rouxhet, *Nanoscale organization of adsorbed collagen: Influence of substrate hydrophobicity and adsorption time*, Journal of Colloid and Interface Science **271**, 80–91 (2004).

[138] H. L. Chen, X. B. Huang, M. M. Zhang, F. Damanik, M. B. Baker, A. Leferink, H. P. Yuan, R. Truckenmuller, C. van Blitterswijk, and L. Moroni, *Tailoring surface nanoroughness of electrospun scaffolds for skeletal tissue engineering*, Acta Biomaterialia **59**, 82–93 (2017).

[139] C. Wirth, B. Grosgogeat, C. Lagneau, N. Jaffrezic-Renault, and L. Ponsonnet, *Biomaterial surface properties modulate in vitro rat calvaria osteoblasts response: Roughness and or chemistry?*, Materials Science & Engineering C: Biomimetic and Supramolecular Systems **28**, 990–1001 (2008).

[140] S. Park, S. H. Ahn, H. J. Lee, U. S. Chung, J. H. Kim, and W. G. Koh, *Mesoporous Tio(2)as a nanostructured substrate for cell culture and cell patterning*, RSC Advances **3**, 23673–23680 (2013).

[141] A. I. Neto, C. A. Custodio, W. L. Song, and J. F. Mano, *High-throughput evaluation of interactions between biomaterials, proteins and cells using patterned superhydrophobic substrates*, Soft Matter **7**, 4147–4151 (2011).

[142] J. Robertus, W. R. Browne, and B. L. Feringa, *Dynamic control over cell adhesive properties using molecular-based surface engineering strategies*, Chemical Society Reviews **39**, 354–378 (2010).

[143] S. F. Zhou, S. Gopalakrishnan, Y. H. Xu, S. K. Y. To, A. S. T. Wong, S. W. Pang, and Y. W. Lam, *Substrates with patterned topography reveal metastasis of human cancer cells*, Biomedical Materials **12**, 055001 (2017).

[144] J. S. Park, J. S. Chu, A. D. Tsou, R. Diop, Z. Y. Tang, A. J. Wang, and S. Li, *The effect of matrix stiffness on the differentiation of mesenchymal stem cells in response to TGF-beta*, Biomaterials **32**, 3921–3930 (2011).

[145] C. A. Mullen, T. J. Vaughan, K. L. Billiar, and L. M. McNamara, *The effect of substrate stiffness, thickness, and cross-linking density on osteogenic cell behavior*, Biophysical Journal **108**, 1604–1612 (2015).

[146] D. H. Kim, E. A. Lipke, P. Kim, R. Cheong, S. Thompson, M. Delannoy, K. Y. Suh, L. Tung, and A. Levchenko, *Nanoscale cues regulate the structure and function of macroscopic cardiac tissue constructs*, Proceedings of the National Academy of Sciences of the United States of America **107**, 565–570 (2010).

[147] C. Imashiro, Y. Kurashina, and K. Takemura, *Cell patterning method using resonance vibration of a metallic cell cultivation substrate*, Advanced Biomedical Engineering **5**, 142–148 (2016).

[148] M. T. Lam, S. Sim, X. Y. Zhu, and S. Takayama, *The effect of continuous wavy micropatterns on silicone substrates on the alignment of skeletal muscle myoblasts and myotubes*, Biomaterials **27**, 4340–4347 (2006).

[149] C. T. Ho, R. Z. Lin, R. J. Chen, C. K. Chin, S. E. Gong, H. Y. Chang, H. L. Peng, L. Hsu, T. R. Yew, S. F. Chang, and C. H. Liu, *Liver-cell patterning lab chip: Mimicking the morphology of liver lobule tissue*, Lab on a Chip **13**, 3578–3587 (2013).

[150] F. Larramendy, S. Yoshida, L. Jalabert, S. Takeuchi, and O. Paul, *Surface modification for patterned cell growth on substrates with pronounced topographies using sacrificial photoresist and parylene-C peel-off*, Journal of Micromechanics and Microengineering **26**, 095017 (2016).

[151] K. B. Lee, L. Kelbauskas, A. Brunner, and D. R. Meldrum, *A versatile method for dynamically controlled patterning of small populations of epithelial cells on substrates via non-contact piezoelectric inkjet printing*, PLOS ONE **12**, e0176079 (2017).

[152] P. Occhetta, N. Sadr, F. Piraino, A. Redaelli, M. Moretti, and M. Rasponi, *Fabrication of 3D cell-laden hydrogel microstructures through photo-mold patterning*, Biofabrication **5**, 035002 (2013).

[153] C. Credi, C. De Marco, E. Molena, M. M. Nava, M. T. Raimondi, M. Levi, and S. Turri, *Direct photopatterning of hyaluronic acid baits onto a fouling-release perfluoropolyether surface for selective cancer cell capture and immobilization*, Materials Science & Engineering C: Materials for Biological Applications **62**, 414–422 (2016).

[154] P. Henriet, Z. D. Zhong, P. C. Brooks, K. I. Weinberg, and Y. A. DeClerck, *Contact with fibrillar collagen inhibits melanoma cell proliferation by up-regulating p27(KIP1)*, Proceedings of the National Academy of Sciences of the United States of America **97**, 10026–10031 (2000).

[155] I. Mercier, J. P. Lechaire, A. Desmouliere, F. Grill, and M. Aumailley, *Interactions of human skin fibroblasts with monomeric or fibrillar collagens induce different organization of the cytoskeleton*, Experimental Cell Research **225**, 245–256 (1996).

[156] G. Binnig and H. Rohrer, *Scanning tunneling microscopy*, Helvetica Physica Acta **55**, 726–735 (1982).

[157] G. Binnig, C. F. Quate, and C. Gerber, *Atomic force microscope*, Physical Review Letters **56**, 930–933 (1986).

[158] S. Kasas, G. Longo, and G. Dietler, *Mechanical properties of biological specimens explored by atomic force microscopy*, Journal of Physics D: Applied Physics **46**, 133001 (2013).

[159] D. Passeri, M. Rossi, E. Tamburri, and M. L. Terranova, *Mechanical characterization of polymeric thin films by atomic force microscopy based techniques*, Analytical and Bioanalytical Chemistry **405**, 1463–1478 (2013).

[160] K. L. Sorokina and A. L. Tolstikhina, *Atomic force microscopy modified for studying electric properties of thin films and crystals. review*, Crystallography Reports **49**, 476–499 (2004).

[161] K. C. Neuman and A. Nagy, *Single-molecule force spectroscopy: Optical tweezers, magnetic tweezers and atomic force microscopy*, Nature Methods **5**, 491–505 (2008).

[162] D. J. Muller and Y. F. Dufrene, *Atomic force microscopy as a multifunctional molecular toolbox in nanobiotechnology*, Nature Nanotechnology **3**, 261–269 (2008).

[163] Y. F. Dufrene, *Atomic force microscopy, a powerful tool in microbiology*, Journal of Bacteriology **184**, 5205–5213 (2002).

[164] Y. F. Dufrene, T. Ando, R. Garcia, D. Alsteens, D. Martinez-Martin, A. Engel, C. Gerber, and D. J. Muller, *Imaging modes of atomic force microscopy for application in molecular and cell biology*, Nature Nanotechnology **12**, 295–307 (2017).

[165] M. Li, D. Dang, L. Q. Liu, N. Xi, and Y. C. Wang, *Atomic force microscopy in characterizing cell mechanics for biomedical applications: A review*, IEEE Transactions on Nanobioscience **16**, 523–540 (2017).

[166] A. A. Tseng, *Advancements and challenges in development of atomic force microscopy for nanofabrication*, Nano Today **6**, 493–509 (2011).

[167] A. McPherson, A. J. Malkin, Y. G. Kuznetsov, and M. Plomp, *Atomic force microscopy applications in macromolecular crystallography*, Acta Crystallographica Section D: Biological Crystallography **57**, 1053–1060 (2001).

[168] J. L. Toca-Herrera, *Atomic force microscopy meets biophysics, bioengineering, chemistry, and materials science*, ChemSusChem **12**, 603–611 (2019).

[169] H. J. Butt, B. Cappella, and M. Kappl, *Force measurements with the atomic force microscope: Technique, interpretation and applications*, Surface Science Reports **59**, 1–152 (2005).

[170] J. E. Sader, J. W. M. Chon, and P. Mulvaney, *Calibration of rectangular atomic force microscope cantilevers*, Review of Scientific Instruments **70**, 3967–3969 (1999).

[171] H. J. Butt and M. Jaschke, *Calculation of thermal noise in atomic-force microscopy*, Nanotechnology **6**, 1–7 (1995).

[172] B. Pittenger, N. Erina, and C. Su, *Quantitative mechanical property mapping at the nanoscale with PeakForce QNM*, Application Note 128, Bruker Nano Surfaces Division, https://www.bruker.com/fileadmin/user_upload/8-PDF-Docs/SurfaceAnalysis/AFM/ApplicationNotes/Quantitative_Mechanical_Property_Mapping_at_the_Nanoscale_with_PeakForceQNM-AN128-RevB0-AppNote.pdf, 2012.

[173] B. Pittenger, A. Slade, A. Berquand, P. Milani, A. Boudaoud, O. Hamant, and M. Radmacher, *Toward quantitative nanomechanical measurements on live cells with peakforce QNM*, Application Note 141, Bruker Nano Surfaces Division, https://www.bruker.com/fileadmin/user_upload/8-PDF-Docs/SurfaceAnalysis/AFM/ApplicationNotes/AN141-RevA0-Quantitative_Nanomechanical_Measurements_on_Live_Cells_with_PeakForce_QNM-Datasheet.pdf, 2013.

[174] H. Hertz, *Über die Berührung fester elastischer Körper (on the contact of elastic solids)*, Journal für die reine und angewandte Mathematik **92**, 156–171 (1881).

[175] V. L. Popov, *Qualitative treatment of contact problems – normal contact without adhesion*, Contact Mechanics and Friction, Ch. 2, pp. 9–25, Springer-Verlag Berlin Heidelberg, Berlin, Germany, 2010.

[176] K. L. Johnson, K. Kendall, and A. D. Roberts, *Surface energy and contact of elastic solids*, Proceedings of the Royal Society of London. Series A, Mathematical and Physical Sciences **324**, 301 (1971).

[177] B. V. Derjaguin, V. M. Muller, and Y. P. Toporov, *Effect of contact deformations on adhesion of particles*, Journal of Colloid and Interface Science **53**, 314–326 (1975).

[178] I. N. Sneddon, *The relation between load and penetration in the axisymmetric boussinesq problem for a punch of arbitrary profile*, International Journal of Engineering Science **3**, 47–57 (1965).

[179] P. Vandenabeele, *Theoretical aspects*, Practical Raman Spectroscopy - An Introduction, Ch. 1, pp. 1–38, John Wiley & Sons, Ltd., Sussex, United Kingdom, 2013.

[180] E. Smith and G. Dent, *Introduction, basic theory and principles*, Modern raman spectroscopy - A practical approach, Ch. 1, pp. 1–20, John Wiley & Sons, Ltd, West Sussex, England, 2004.

[181] M. Baia, S. Astilean, and T. Iliescu, *Fundamentals of infrared and Raman spectroscopy, SERS, and theoretical simulations*, Raman and SERS Investigations of Pharmaceuticals, Ch. 2, pp. 9–29, Springer-Verlag Berlin Heidelberg, Berlin, Germany, 2009.

[182] A. Rygula, K. Majzner, K. M. Marzec, A. Kaczor, M. Pilarczyk, and M. Baranska, *Raman spectroscopy of proteins: a review*, Journal of Raman Spectroscopy **44**, 1061–1076 (2013).

[183] J. M. Sequaris and E. Koglin, *Subnanogram colloid surface-enhanced Raman-spectroscopy (SERS) of methylated guanine on silica-gel plates*, Fresenius Zeitschrift Für Analytische Chemie **321**, 758–759 (1985).

[184] J. A. Dieringer, A. D. McFarland, N. C. Shah, D. A. Stuart, A. V. Whitney, C. R. Yonzon, M. A. Young, X. Y. Zhang, and R. P. Van Duyne, *Surface enhanced Raman spectroscopy: New materials, concepts, characterization tools, and applications*, Faraday Discussions **132**, 9–26 (2006).

[185] T. Ichimura, S. Fujii, P. Verma, T. Yano, Y. Inouye, and S. Kawata, *Subnanometric near-field Raman investigation in the vicinity of a metallic nanostructure*, Physical Review Letters **102**, 186101 (2009).

[186] J. P. Camden, J. A. Dieringer, J. Zhao, and R. P. Van Duyne, *Controlled plasmonic nanostructures for surface-enhanced spectroscopy and sensing*, Accounts of Chemical Research **41**, 1653–1661 (2008).

[187] K. Kneipp, Y. Wang, H. Kneipp, L. T. Perelman, I. Itzkan, R. Dasari, and M. S. Feld, *Single molecule detection using surface-enhanced Raman scattering (SERS)*, Physical Review Letters **78**, 1667–1670 (1997).

[188] S. M. Nie and S. R. Emery, *Probing single molecules and single nanoparticles by surface-enhanced Raman scattering*, Science **275**, 1102–1106 (1997).

[189] J. J. Carcamo, A. E. Aliaga, E. Clavijo, C. Garrido, J. S. Gomez-Jeria, and M. M. Campos-Vallette, *Proline and hydroxyproline deposited on silver nanoparticles. A Raman, SERS and theoretical study*, Journal of Raman Spectroscopy **43**, 750–755 (2012).

[190] W. R. Premasiri, Y. Chen, P. M. Williamson, D. C. Bandarage, C. Pyles, and L. D. Ziegler, *Rapid urinary tract infection diagnostics by surface-enhanced Raman spectroscopy (SERS): identification and antibiotic susceptibilities*, Analytical and Bioanalytical Chemistry **409**, 3043–3054 (2017).

[191] D. A. Guzonas, D. E. Irish, and G. F. Atkinson, *Evidence for a photon-driven charge-transfer enhancement in the surface-enhanced Raman-scattering of 1,4-diazabicyclo 2.2.2 octane at a silver electrode*, Langmuir **6**, 1102–1112 (1990).

[192] A. Otto, *Surface-enhanced Raman-scattering of adsorbates*, Journal of Raman Spectroscopy **22**, 743–752 (1991).

[193] A. Otto, I. Mrozek, H. Grabhorn, and W. Akemann, *Surface-enhanced Raman-scattering*, Journal of Physics - Condensed Matter **4**, 1143–1212 (1992).

[194] K. Imai, K. Yoshimura, M. Tomitori, O. Nishikawa, R. Kokawa, M. Yamamoto, M. Kobayashi, and A. Ikai, *Scanning tunneling and atomic-force microscopy of T4-bacteriophage and tobacco mosaic-virus*, Japanese Journal of Applied Physics Part 1 - Regular Papers Short Notes & Review Papers **32**, 2962–2964 (1993).

[195] Y. L. Lyubchenko, P. I. Oden, D. Lampner, S. M. Lindsay, and K. A. Dunker, *Atomic force microscopy of DNA and bacteriophage in air, water and propanol - the role of adhesion forces*, Nucleic Acids Research **21**, 1117–1123 (1993).

[196] F. Zenhausern, M. Adrian, R. Emch, M. Taborelli, M. Jobin, and P. Descouts, *Scanning force microscopy and cryoelectron microscopy of tobacco mosaic-virus as a test specimen*, Ultramicroscopy **42**, 1168–1172 (1992).

[197] B. Samori, C. Nigro, V. Armentano, S. Cimieri, G. Zuccheri, and C. Quagliariello, *DNA supercoiling imaged in 3 dimensions by scanning force microscopy*, Angewandte Chemie - International Edition **32**, 1461–1463 (1993).

[198] H. G. Hansma, D. E. Laney, M. Bezanilla, R. L. Sinsheimer, and P. K. Hansma, *Applications for atomic-force microscopy of DNA*, Biophysical Journal **68**, 1672–1677 (1995).

[199] N. H. Thomson, S. Kasas, B. Smith, H. G. Hansma, and P. K. Hansma, *Reversible binding of DNA to mica for AFM imaging*, Langmuir **12**, 5905–5908 (1996).

[200] L. Stühn, A. Fritschen, J. Choy, M. Dehnert, and C. Dietz, *Nanomechanical sub-surface mapping of living biological cells by force microscopy*, Nanoscale **11**, 13089–13097 (2019).

[201] S. V. Kontomaris, D. Yova, A. Stylianou, and G. Balogiannis, *The effects of UV irradiation on collagen D-band revealed by atomic force microscopy*, Scanning **37**, 101–111 (2015).

[202] S. Yamamoto, J. Hitomi, M. Shigeno, S. Sawaguchi, H. Abe, and T. Ushiki, *Atomic force microscopic studies of isolated collagen fibrils of the bovine cornea and sclera*, Archives of Histology and Cytology **60**, 371–378 (1997).

[203] L. Yang, K. O. van der Werf, P. J. Dijkstra, J. Feijen, and M. L. Bennink, *Micromechanical analysis of native and cross-linked collagen type I fibrils supports the existence of microfibrils*, Journal of the Mechanical Behavior of Biomedical Materials **6**, 148–158 (2012).

[204] D. A. Cisneros, C. Hung, C. A. Franz, and D. J. Muller, *Observing growth steps of collagen self-assembly by time-lapse high-resolution atomic force microscopy*, Journal of Structural Biology **154**, 232–245 (2006).

[205] C. A. Grant, D. J. Brockwell, S. E. Radford, and N. H. Thomson, *Effects of hydration on the mechanical response of individual collagen fibrils*, Applied Physics Letters **92**, 233902 (2008).

[206] S. Strasser, A. Zink, M. Janko, W. M. Heckl, and S. Thalhammer, *Structural investigations on native collagen type I fibrils using AFM*, Biochemical and Biophysical Research Communications **354**, 27–32 (2007).

[207] L. Yang, K. O. van der Werf, B. F. J. M. Koopman, V. Subramaniam, M. L. Bennink, P. J. Dijkstra, and J. Feijen, *Micromechanical bending of single collagen fibrils using atomic force microscopy*, Journal of Biomedical Materials Research Part A **82A**, 160–168 (2007).

[208] A. J. Heim, T. J. Koob, and W. G. Matthews, *Low strain nanomechanics of collagen fibrils*, Biomacromolecules **8**, 3298–3301 (2007).

[209] R. B. Svensson, H. Mulder, V. Kovanen, and S. P. Magnusson, *Fracture mechanics of collagen fibrils: Influence of natural cross-links*, Biophysical Journal **104**, 2476–2484 (2013).

[210] A. S. Quigley, S. Bancelin, D. Deska-Gauthier, F. Legare, S. P. Veres, and L. Kreplak, *Data descriptor: Combining tensile testing and structural analysis at the single collagen fibril level*, Scientific Data **5**, 180229 (2018).

[211] J. B. Thompson, J. H. Kindt, B. Drake, H. G. Hansma, D. E. Morse, and P. K. Hansma, *Bone indentation recovery time correlates with bond reforming time*, Nature **414**, 773–776 (2001).

[212] J. S. Graham, A. N. Vomund, C. L. Phillips, and M. Grandbois, *Structural changes in human type I collagen fibrils investigated by force spectroscopy*, Experimental Cell Research **299**, 335–342 (2004).

[213] R. B. Svensson, T. Hassenkam, C. A. Grant, and S. P. Magnusson, *Tensile mechanical measurements on individual collagen fibrils*, Biophysical Journal **100**, 482–482 (2011).

[214] R. B. Svensson, T. Hassenkam, P. Hansen, and S. P. Magnusson, *Viscoelastic behavior of discrete human collagen fibrils*, Journal of the Mechanical Behavior of Biomedical Materials **3**, 112–115 (2010).

[215] C. A. Grant, M. A. Phillips, and N. H. Thomson, *Dynamic mechanical analysis of collagen fibrils at the nanoscale*, Journal of the Mechanical Behavior of Biomedical Materials **5**, 165–170 (2012).

[216] Y. J. Park, G. J. Choi, S. H. Kim, J. Hahn, T. G. Lee, W. J. Lee, and D. W. Moon, *Nanoscale characterization of acid and thermally treated collagen fibrils*, Acta Biomaterialia **8**, 3381–3391 (2012).

[217] C. A. Grant, D. J. Brockwell, S. E. Radford, and N. H. Thomson, *Tuning the elastic modulus of hydrated collagen fibrils*, Biophysical Journal **97**, 2985–2992 (2009).

[218] M. Janko, A. Zink, A. M. Gigler, W. M. Heckl, and R. W. Stark, *Nanostructure and mechanics of mummified type I collagen from the 5300-year-old Tyrolean Iceman*, Proceedings of the Royal Society B: Biological Sciences **277**, 2301–2309 (2010).

[219] T. W. Tombler, C. W. Zhou, L. Alexseyev, J. Kong, H. J. Dai, L. Lei, C. S. Jayanthi, M. J. Tang, and S. Y. Wu, *Reversible electromechanical characteristics of carbon nanotubes under local-probe manipulation*, Nature **405**, 769–772 (2000).

[220] J. P. Salvetat, G. A. D. Briggs, J. M. Bonard, R. R. Bacsa, A. J. Kulik, T. Stockli, N. A. Burnham, and L. Forro, *Elastic and shear moduli of single-walled carbon nanotube ropes*, Physical Review Letters **82**, 944–947 (1999).

[221] T. Namazu, Y. Isono, and T. Tanaka, *Evaluation of size effect on mechanical properties of single crystal silicon by nanoscale bending test using AFM*, Journal of Microelectromechanical Systems **9**, 450–459 (2000).

[222] A. Kis, S. Kasas, B. Babic, A. J. Kulik, W. Benoit, G. A. D. Briggs, C. Schonenberger, S. Catsicas, and L. Forro, *Nanomechanics of microtubules*, Physical Review Letters **89**, 248101 (2002).

[223] B. A. Roeder, K. Kokini, J. E. Sturgis, J. P. Robinson, and S. L. Voytik-Harbin, *Tensile mechanical properties of three-dimensional type I collagen extracellular matrices with varied microstructure*, Journal of Biomechanical Engineering-Transactions of the Asme **124**, 214–222 (2002).

[224] C. S. Osborne, J. C. Barbenel, D. Smith, M. Savakis, and M. H. Grant, *Investigation into the tensile properties of collagen/chondroitin-6-sulphate gels: the effect of crosslinking agents and diamines*, Medical & Biological Engineering & Computing **36**, 129–134 (1998).

[225] X. N. Wang, X. D. Li, and M. J. Yost, *Microtensile testing of collagen fibril for cardiovascular tissue engineering*, Journal of Biomedical Materials Research Part A **74A**, 263–268 (2005).

[226] K. Takaku, T. Ogawa, T. Kuriyama, and I. Narisawa, *Fracture behavior and morphology of spun collagen fibers*, Journal of Applied Polymer Science **59**, 887–896 (1996).

[227] G. D. Pins and F. H. Silver, *A self-assembled collagen scaffold suitable for use in soft and hard tissue replacement*, Materials Science & Engineering C: Biomimetic and Supramolecular Systems **3**, 101–107 (1995).

[228] F. H. Silver, D. Christiansen, P. B. Snowhill, Y. Chen, and W. J. Landis, *The role of mineral in the storage of elastic energy in turkey tendons*, Biomacromolecules **1**, 180–185 (2000).

[229] Hiroshi Miyazaki and Kozaburo Hayashi, *Tensile tests of collagen fibers obtained from the rabbit patellar tendon*, Biomedical Microdevices **2**, 151–157 (1999).

[230] Z. L. L. Shen, M. R. Dodge, H. Kahn, R. Ballarini, and S. J. Eppell, *In vitro fracture testing of submicron diameter collagen fibril specimens*, Biophysical Journal **99**, 1986–1995 (2010).

[231] Z. L. Shen, M. R. Dodge, H. Kahn, R. Ballarini, and S. J. Eppell, *Stress-strain experiments on individual collagen fibrils*, Biophysical Journal **95**, 3956–3963 (2008).

[232] S. J. Eppell, B. N. Smith, H. Kahn, and R. Ballarini, *Nano measurements with micro-devices: Mechanical properties of hydrated collagen fibrils*, Journal of the Royal Society Interface **3**, 117–121 (2006).

[233] Y. L. Sun, Z. P. Luo, A. Fertala, and K. N. An, *Direct quantification of the flexibility of type I collagen monomer*, Biochemical and Biophysical Research Communications **295**, 382–386 (2002).

[234] Y. L. Sun, Z. P. Luo, A. Fertala, and K. N. An, *Stretching type II collagen with optical tweezers*, Journal of Biomechanics **37**, 1665–1669 (2004).

[235] R. B. Svensson, S. T. Smith, P. J. Moyer, and S. P. Magnusson, *Effects of maturation and advanced glycation on tensile mechanics of collagen fibrils from rat tail and achilles tendons*, Acta Biomaterialia **70**, 270–280 (2018).

[236] F. Hang, D. Lu, R. J. Bailey, I. Jimenez-Palomar, U. Stachewicz, B. Cortes-Ballesteros, M. Davies, M. Zech, C. Bodefeld, and A. H. Barber, *In situ tensile testing of nanofibers by combining atomic force microscopy and scanning electron microscopy*, Nanotechnology **22**, 365708 (2011).

[237] F. Hang and A. H. Barber, *Nano-mechanical properties of individual mineralized collagen fibrils from bone tissue*, Journal of the Royal Society Interface **8**, 500–505 (2011).

[238] J. A. J. van der Rijt, K. O. van der Werf, M. L. Bennink, P. J. Dijkstra, and J. Feijen, *Micromechanical testing of individual collagen fibrils*, Macromolecular Bioscience **6**, 697–702 (2006).

[239] Y. J. Hwang and J. G. Lyubovitsky, *The structural analysis of three-dimensional fibrous collagen hydrogels by raman microspectroscopy*, Biopolymers **99**, 349–356 (2013).

[240] L. Xing, K. Lin, X. G. Zhou, S. L. Liu, and Y. Luo, *Multistate mechanism of lysozyme denaturation through synchronous analysis of Raman spectra*, Journal of Physical Chemistry B **120**, 10660–10667 (2016).

[241] M. Votteler, D. A. C. Berrio, M. Pudlas, H. Walles, U. A. Stock, and K. Schenke-Layland, *Raman spectroscopy for the non-contact and non-destructive monitoring of collagen damage within tissues*, Journal of Biophotonics **5**, 47–56 (2012).

[242] L. D. N. Caetano, T. D. Mendes, E. Bagatin, H. A. Miot, J. L. M. Soares, Mmses Enokihara, and A. A. Martin, *In vivo confocal Raman spectroscopy for intrinsic aging and photoaging assessment*, Journal of Dermatological Science **88**, 199–206 (2017).

[243] T. T. Nguyen, T. Happillon, J. Feru, S. Brassart-Passco, J.-F. Angiboust, M. Manfait, and O. Piot, *Raman comparison of skin dermis of different ages: Focus on spectral markers of collagen hydration*, Journal of Raman Spectroscopy **44**, 1230–1237 (2013).

[244] M. Fields, N. Spencer, J. Dudhia, and P. F. McMillan, *Structural changes in cartilage and collagen studied by high temperature Raman spectroscopy*, Biopolymers **107**, e23017 (2017).

[245] T. T. Nguyen, C. Gobinet, J. Feru, S. Brassart-Pasco, M. Manfait, and O. Piot, *Characterization of type I and IV collagens by raman microspectroscopy: Identification of spectral markers of the dermo-epidermal junction*, Spectroscopy - An International Journal **27**, 421–427 (2012).

[246] C. D. Flanagan, M. Unal, O. Akkus, and C. M. Rimnac, *Raman spectral markers of collagen denaturation and hydration in human cortical bone tissue are affected by radiation sterilization and high cycle fatigue damage*, Journal of the Mechanical Behavior of Biomedical Materials **75**, 314–321 (2017).

[247] G. Y. Zhu, X. Zhu, Q. Fan, and X. L. Wan, *Raman spectra of amino acids and their aqueous solutions*, Spectrochimica Acta Part A: Molecular and Biomolecular Spectroscopy **78**, 1187–1195 (2011).

[248] B. Hernandez, Y. M. Coic, F. Pfluger, S. G. Kruglik, and M. Ghomi, *All characteristic Raman markers of tyrosine and tyrosinate originate from phenol ring fundamental vibrations*, Journal of Raman Spectroscopy **47**, 210–220 (2016).

[249] B. Hernandez, F. Pfluger, S. G. Kruglik, and M. Ghomi, *Characteristic Raman lines of phenylalanine analyzed by a multiconformational approach*, Journal of Raman Spectroscopy **44**, 827–833 (2013).

[250] G. D. Fleming, J. J. Finnerty, M. Campos-Vallette, F. Celis, A. E. Aliaga, C. Fredes, and R. Koch, *Experimental and theoretical Raman and surface-enhanced Raman scattering study of cysteine*, Journal of Raman Spectroscopy **40**, 632–638 (2009).

[251] B. Sjoberg, S. Foley, B. Cardey, and M. Enescu, *An experimental and theoretical study of the amino acid side chain Raman bands in proteins*, Spectrochimica Acta Part A: Molecular and Biomolecular Spectroscopy **128**, 300–311 (2014).

[252] J. De Gelder, K. De Gussem, P. Vandenabeele, M. Vancanneyt, P. De Vos, and L. Moens, *Methods for extracting biochemical information from bacterial Raman spectra: Focus on a group of structurally similar biomolecules - fatty acids*, Analytica Chimica Acta **603**, 167–175 (2007).

[253] M. D. Morris and W. F. Finney, *Recent developments in Raman and infrared spectroscopy and imaging of bone tissue*, Spectroscopy - An International Journal **18**, 155–159 (2004).

[254] I. V. Rubtsov, J. P. Wang, and R. M. Hochstrasser, *Vibrational coupling between amide-I and amide-A modes revealed by femtosecond two color infrared spectroseopy*, Journal of Physical Chemistry A **107**, 3384–3396 (2003).

[255] C. David, *Raman spectroscopy for proteins*, Webinar, HORIBA, Ltd., http://www.horiba.com/fileadmin/uploads/Scientific/Documents/Raman/HORIBA_webinar_proteins.pdf, 2012.

[256] N. K. Howell, G. Arteaga, S. Nakai, and E. C. Y. Li-Chan, *Raman spectral analysis in the C-H stretching region of proteins and amino acids for investigation of hydrophobic interactions*, Journal of Agricultural and Food Chemistry **47**, 924–933 (1999).

[257] S. B. Bandini, J. A. Spechler, P. E. Donnelly, K. Lim, C. B. Arnold, J. E. Schwarzbauer, and J. Schwartz, *Perforation does not compromise patterned two-dimensional substrates for cell attachment and aligned spreading*, ACS Biomaterials Science & Engineering **3**, 3123–3127 (2017).

[258] L. H. Jin, B. Y. Yang, L. Zhang, P. L. Lin, C. Cui, and J. Tang, *Patterning of HeLa cells on a micro-fabricated Au-coated ITO substrate*, Langmuir **25**, 5380–5383 (2009).

[259] D. Ayibaike, M. Y. Cui, and J. Q. Wei, *Single-cell patterning based on immunocapture and a surface modified substrate*, Applied Sciences - Basel **8**, 2152 (2018).

[260] M. N. Yousaf, B. T. Houseman, and M. Mrksich, *Using electroactive substrates to pattern the attachment of two different cell populations*, Proceedings of the National Academy of Sciences of the United States of America **98**, 5992–5996 (2001).

[261] M. Winkelmann, J. Gold, R. Hauert, B. Kasemo, N. D. Spencer, D. M. Brunette, and M. Textor, *Chemically patterned, metal oxide based surfaces produced by photolithographic techniques for studying protein- and cell-surface interactions I: Microfabrication and surface characterization*, Biomaterials **24**, 1133–1145 (2003).

[262] J. Vaillancourt, H. Y. Zhang, P. Vasinajindakaw, H. T. Xia, X. J. Lu, X. L. Han, D. C. Janzen, W. S. Shih, C. S. Jones, M. Stroder, M. Y. H. Chen, H. Subbaraman, R. T. Chen, U. Berger, and M. Renn, *All ink-jet-printed carbon nanotube thin-film transistor on a polyimide substrate with an ultrahigh operating frequency of over 5 GHz*, Applied Physics Letters **93**, 243301 (2008).

[263] S. P. Wang, X. Q. Cai, L. H. Wang, J. Li, Q. Li, X. L. Zuo, J. Y. Shi, Q. Huang, and C. H. Fan, *DNA orientation-specific adhesion and patterning of living mammalian cells on self-assembled DNA monolayers*, Chemical Science **7**, 2722–2727 (2016).

[264] F. D. Delapierre, G. Mottet, V. Taniga, J. Boisselier, J. L. Viovy, and L. Malaquin, *High throughput micropatterning of interspersed cell arrays using capillary assembly*, Biofabrication **9**, 015015 (2017).

[265] G. Burgstaller, B. Oehrle, I. Koch, M. Lindner, and O. Eickelberg, *Multiplex profiling of cellular invasion in 3D cell culture models*, PLOS ONE **8**, e63121 (2013).

[266] A. van der Smissen, V. Hintze, D. Scharnweber, S. Moeller, M. Schnabelrauch, A. Majok, J. C. Simon, and U. Anderegg, *Growth promoting substrates for human dermal fibroblasts provided by artificial extracellular matrices composed of collagen I and sulfated glycosaminoglycans*, Biomaterials **32**, 8938–8946 (2011).

[267] D. Y. S. Chau, R. J. Collighan, E. A. M. Verderio, V. L. Addy, and M. Griffin, *The cellular response to transglutaminase-cross-linked collagen*, Biomaterials **26**, 6518–6529 (2005).

[268] S. Matsuda, H. Iwata, N. Se, and Y. Ikada, *Bioadhesion of gelatin films crosslinked with glutaraldehyde*, Journal of Biomedical Materials Research **45**, 20–27 (1999).

[269] M. E. Nimni, D. Cheung, B. Strates, M. Kodama, and K. Sheikh, *Chemically modified collagen - a natural biomaterial for tissue replacement*, Journal of Biomedical Materials Research **21**, 741–771 (1987).

[270] I. M. McPherson, S. Sawamura, and R. Armstrong, *An examination of the biologic response to injectable, glutaraldehyde cross-linked collagen implants*, Journal of Biomedical Materials Research **20**, 93–107 (1986).

[271] M. G. Haugh, M. J. Jaasma, and F. J. O'Brien, *The effect of dehydrothermal treatment on the mechanical and structural properties of collagen-GAG scaffolds*, Journal of Biomedical Materials Research Part A **89A**, 363–369 (2009).

[272] C. M. Tierney, M. G. Haugh, J. Liedl, F. Mulcahy, B. Hayes, and F. J. O'Brien, *The effects of collagen concentration and crosslink density on the biological, structural and mechanical properties of collagen-GAG scaffolds for bone tissue engineering*, Journal of the Mechanical Behavior of Biomedical Materials **2**, 202–209 (2009).

[273] K. S. Weadock, E. J. Miller, E. L. Keuffel, and M. G. Dunn, *Effect of physical crosslinking methods on collagen-fiber durability in proteolytic solutions*, Journal of Biomedical Materials Research **32**, 221–226 (1996).

[274] E. Khor, *Methods for the treatment of collagenous tissues for bioprostheses*, Biomaterials **18**, 95–105 (1997).

[275] R. Usha and T. Ramasami, *The effects of urea and n-propanol on collagen denaturation: Using DSC, circular dicroism and viscosity*, Thermochimica Acta **409**, 201–206 (2004).

[276] A. Bigi, G. Cojazzi, N. Roveri, and M. H. J. Koch, *Differential scanning calorimetry and X-ray-diffraction study of tendon collagen thermal-denaturation*, International Journal of Biological Macromolecules **9**, 363–367 (1987).

[277] K. Vizarova, D. Bakos, M. Rehakova, and V. Macho, *Modification of layered atelocollagen by ultraviolet-irradiation and chemical cross-linking - structure stability and mechanical-properties*, Biomaterials **15**, 1082–1086 (1994).

[278] R. X. Dong, X. L. Yan, X. F. Pang, and S. G. Liu, *Temperature-dependent Raman spectra of collagen and DNA*, Spectrochimica Acta Part A: Molecular and Biomolecular Spectroscopy **60**, 557–561 (2004).

[279] J. Bella, M. Eaton, B. Brodsky, and H. M. Berman, *Crystal and molecular structure of a collagen-like peptide at 1.9 Å resolution*, Science **266**, 75–81 (1994).

[280] P. L. Privalov, *Stability of proteins - proteins which do not present a single cooperative system*, Advances in Protein Chemistry **35**, 1–104 (1982).

[281] S. Leikin, V. A. Parsegian, W. H. Yang, and G. E. Walrafen, *Raman spectral evidence for hydration forces between collagen triple helices*, Proceedings of the National Academy of Sciences of the United States of America **94**, 11312–11317 (1997).

[282] J. Rosenblatt, B. Devereux, and D. G. Wallace, *Injectable collagen as a pH-sensitive hydrogel*, Biomaterials **15**, 985–995 (1994).

[283] D. Necas and P. Klapetek, *Gwyddion: An open-source software for SPM data analysis*, Central European Journal of Physics **10**, 181–188 (2012).

[284] M. Schulze, M. Rogge, and R. W. Stark, *Atomic force microscopy measurements probing the mechanical properties of single collagen fibrils under the influence of UV light in situ*, Journal of the Mechanical Behavior of Biomedical Materials **88**, 415–421 (2018).

[285] K. Sweers, K. van der Werf, M. Bennink, and V. Subramaniam, *Nanomechanical properties of alpha-synuclein amyloid fibrils: A comparative study by nanoindentation, harmonic force microscopy, and peakforce QNM*, Nanoscale Research Letters **6**, 270 (2011).

[286] S. Cook, T. E. Schaffer, K. M. Chynoweth, M. Wigton, R. W. Simmonds, and K. M. Lang, *Practical implementation of dynamic methods for measuring atomic force microscope cantilever spring constants*, Nanotechnology **17**, 2135–2145 (2006).

[287] G. Persch, C. Born, and B. Utesch, *Nano-hardness investigations of thin-films by an atomic-force microscope*, Microelectronic Engineering **24**, 113–121 (1994).

[288] A. J. Heim, W. G. Matthews, and T. J. Koob, *Determination of the elastic modulus of native collagen fibrils via radial indentation*, Applied Physics Letters **89**, 181902 (2006).

[289] P. Fratzl and A. Daxer, *Structural transformation of collagen fibrils in corneal stroma during drying - an X-ray-scattering study*, Biophysical Journal **64**, 1210–1214 (1993).

[290] E. C. Spitzner, S. Roper, M. Zerson, A. Bernstein, and R. Magerle, *Nanoscale swelling heterogeneities in type I collagen fibrils*, ACS Nano **9**, 5683–5694 (2015).

[291] J. H. Bowes and R. H. Kenten, *The swelling of collagen in alkaline solutions. 1. Swelling in solutions of sodium hydroxide*, Biochemical Journal **46**, 1–8 (1950).

[292] D. Jordan Lloyd, R. H. Marriott, and W. B. Pleass, *The swelling of protein fibres. Part I. The swelling of collagen*, Transactions of the Faraday Society **29**, 554–563 (1933).

[293] H. R. Elden, *Rate of swelling of collagen*, Science **128**, 1624–1625 (1958).

[294] M. P. E. Wenger and P. Mesquida, *The NanoBeamBalance: A passive, tensile-test device for the atomic force microscope*, Review of Scientific Instruments **82**, 053908 (2011).

[295] C. A. Miles, T. V. Burjanadze, and A. J. Bailey, *The kinetics of the thermal-denaturation of collagen in unrestrained rat tail tendon determined by differential scanning calorimetry*, Journal of Molecular Biology **245**, 437–446 (1995).

[296] P. J. Flory and R. R. Garrett, *Phase transitions in collagen and gelatin systems*, Journal of the American Chemical Society **80**, 4836–4845 (1958).

[297] M. Luescher, M. Ruegg, and P. Schindler, *Effect of hydration upon thermal-stability of tropocollagen and its dependence on presence of neutral salts*, Biopolymers **13**, 2489–2503 (1974).

[298] D. H. Lew, P. H. T. Liu, and D. P. Orgill, *Optimization of UV cross-linking density for durable and nontoxic collagen GAG dermal substitute*, Journal of Biomedical Materials Research Part B: Applied Biomaterials **82B**, 51–56 (2007).

[299] J. N. Reddy, *Mechanics of laminated composite plates and shells: Theory and analysis*, 2nd ed., CRC Press, Boca Raton, FL, 2003.

[300] Annika Stocker, *Raman Spektroskopie an UV-bestrahlten Kollagenproben*, Master's thesis, Technische Universität Darmstadt (Germany) (2018).

[301] G. J. Thomas, *Raman spectroscopy of protein and nucleic acid assemblies*, Annual Review of Biophysics and Biomolecular Structure **28**, 1 (1999).

[302] K. Kar, S. Ibrar, V. Nanda, T. M. Getz, S. P. Kunapuli, and B. Brodsky, *Aromatic interactions promote self-association of collagen triple-helical peptides to higher-order structures*, Biochemistry **48**, 7959–7968 (2009).

[303] D. J. Prockop and A. Fertala, *Inhibition of the self-assembly of collagen I into fibrils with synthetic peptides - demonstration that assembly is driven by specific binding sites on the monomers*, Journal of Biological Chemistry **273**, 15598–15604 (1998).

[304] J. P. Malone, A. George, and A. Veis, *Type I collagen N-telopeptides adopt an ordered structure when docked to their helix receptor during fibrillogenesis*, Proteins - Structure Function and Genetics **54**, 206–215 (2004).

[305] K. Jariashvili, B. Madhan, B. Brodsky, A. Kuchava, L. Namicheishvili, and N. Metreveli, *UV damage of collagen: Insights from model collagen peptides*, Biopolymers **97**, 189–198 (2012).

[306] N. Metreveli, L. Namicheishvili, K. Jariashvili, M. Dgebuadze, E. Chikvaidze, and A. Sionkowska, *Identification of free radicals induced by UV irradiation in collagen water solutions*, Journal of Photochemistry and Photobiology B: Biology **93**, 61–65 (2008).

[307] M. D. Carbonare and M. A. Pathak, *Skin photosensitizing agents and the role of reactive oxygen species in photoaging*, Journal of Photochemistry and Photobiology B: Biology **14**, 105–124 (1992).

[308] D. Creed, *The photophysics and photochemistry of the near-UV absorbing amino-acids II. tyrosine and its simple derivatives*, Photochemistry and Photobiology **39**, 563–575 (1984).

[309] E. L. Mertz and S. Leikin, *Interactions of inorganic phosphate and sulfate anions with collagen*, Biochemistry **43**, 14901–14912 (2004).

[310] J. A. Uquillas, V. Kishore, and O. Akkus, *Effects of phosphate-buffered saline concentration and incubation time on the mechanical and structural properties of electrochemically aligned collagen threads*, Biomedical Materials **6**, 035008 (2011).

[311] T. S. Girton, T. R. Oegema, and R. T. Tranquillo, *Exploiting glycation to stiffen and strengthen tissue equivalents for tissue engineering*, Journal of Biomedical Materials Research **46**, 87–92 (1999).

[312] K. V. Chace, R. Carubelli, and R. E. Nordquist, *The role of nonenzymatic glycosylation, transition-metals, and free-radicals in the formation of collagen aggregates*, Archives of Biochemistry and Biophysics **288**, 473–480 (1991).

[313] H. F. Bunn and P. J. Higgins, *Reaction of monosaccharides with proteins - possible evolutionary significance*, Science **213**, 222–224 (1981).

[314] National Center for Biotechnology Information. PubChem Database., *D-glucose, CID=5793*, https://pubchem.ncbi.nlm.nih.gov/compound/D-Glucose, Accessed: 06.06.2019.

[315] National Center for Biotechnology Information. PubChem Database., *L-glucose, CID=10954115*, https://pubchem.ncbi.nlm.nih.gov/compound/L-Glucose, Accessed: 06.06.2019.

[316] S. Kim, J. Chen, T. J. Cheng, A. Gindulyte, J. He, S. Q. He, Q. L. Li, B. A. Shoemaker, P. A. Thiessen, B. Yu, L. Zaslavsky, J. Zhang, and E. E. Bolton, *PubChem 2019 update: Improved access to chemical data*, Nucleic Acids Research **47**, D1102–D1109 (2019).

[317] G. Wollensak, E. Spoerl, and T. Seiler, *Riboflavin/ultraviolet-A-induced collagen crosslinking for the treatment of keratoconus*, American Journal of Ophthalmology **135**, 620–627 (2003).

[318] R. Huang, E. Choe, and D. B. Min, *Kinetics for singlet oxygen formation by riboflavin photosensitization and the reaction between riboflavin and singlet oxygen*, Journal of Food Science **69**, C726–C732 (2004).

[319] S. Sel, N. Nass, S. Potzsch, S. Trau, A. Simm, T. Kalinski, G. I. W. Duncker, F. E. Kruse, G. U. Auffarth, and H. J. Bromme, *UVA irradiation of riboflavin generates oxygen-dependent hydroxyl radicals*, Redox Report **19**, 72–79 (2014).

[320] National Center for Biotechnology Information. PubChem Database., *Phosphate-buffered saline, CID=24978514*, https://pubchem.ncbi.nlm.nih.gov/compound/24978514, Accessed: 04.06.2019.

[321] National Center for Biotechnology Information. PubChem Database., *Riboflavin, CID=493570*, https://pubchem.ncbi.nlm.nih.gov/compound/Riboflavin, Accessed: 04.06.2019.

[322] M. L. Cunningham, J. S. Johnson, S. M. Giovanazzi, and M. J. Peak, *Photosensitized production of superoxide anion by monochromatic (290-405 nm) ultraviolet-irradiation of NADH and NADPH coenzymes*, Photochemistry and Photobiology **42**, 125–128 (1985).

[323] E. Bell, B. Ivarsson, and C. Merrill, *Production of a tissue-like structure by contraction of collagen lattices by human-fibroblasts of different proliferative potential invitro*, Proceedings of the National Academy of Sciences of the United States of America **76**, 1274–1278 (1979).

[324] N. J. F. Dodd, S. L. Schor, and G. Rushton, *The effects of a collagenous extracellular-matrix on fibroblast membrane organization - an electron-spin-resonance spin label study*, Experimental Cell Research **141**, 421–431 (1982).

[325] F. Grinnell, M. F. Zhu, M. A. Carlson, and J. M. Abrams, *Release of mechanical tension triggers apoptosis of human fibroblasts in a model of regressing granulation tissue*, Experimental Cell Research **248**, 608–619 (1999).

[326] S. H. Um, J. B. Lee, N. Park, S. Y. Kwon, C. C. Umbach, and D. Luo, *Enzyme-catalysed assembly of DNA hydrogel*, Nature Materials **5**, 797–801 (2006).

[327] A. J. Engler, S. Sen, H. L. Sweeney, and D. E. Discher, *Matrix elasticity directs stem cell lineage specification*, Cell **126**, 677–689 (2006).

[328] P. J. Nowatzki, C. Franck, S. A. Maskarinec, G. Ravichandran, and D. A. Tirrell, *Mechanically tunable thin films of photosensitive artificial proteins: Preparation and characterization by nanoindentation*, Macromolecules **41**, 1839–1845 (2008).

[329] E. K. Dimitriadis, F. Horkay, J. Maresca, B. Kachar, and R. S. Chadwick, *Determination of elastic moduli of thin layers of soft material using the atomic force microscope*, Biophysical Journal **82**, 2798–2810 (2002).

[330] J. Solon, I. Levental, K. Sengupta, P. C. Georges, and P. A. Janmey, *Fibroblast adaptation and stiffness matching to soft elastic substrates*, Biophysical Journal **93**, 4453–4461 (2007).

[331] M. Galluzzi, C. S. Biswas, Y. H. Wu, Q. Wang, B. Du, and F. J. Stadler, *Space-resolved quantitative mechanical measurements of soft and supersoft materials by atomic force microscopy*, NPG Asia Materials **8**, e327 (2016).

[332] C. Dietz, *Sensing in-plane nanomechanical surface and sub-surface properties of polymers: Local shear stress as function of the indentation depth*, Nanoscale **10**, 460–468 (2018).

[333] National Center for Biotechnology Information. PubChem Database., *Hematoporphyrin, CID=11103*, https://pubchem.ncbi.nlm.nih.gov/compound/Hematoporphyrin, Accessed: 04.06.2019.

Appendices

A Ultraviolet lamp spectra

Figure A.1, Figure A.2, and Figure A.3 show the emission spectrum of the applied UVA, UVB, and UVC light source, respectively. The ROI is highlighted in an inset spectrum. The emission spectra of the UV light sources were recorded with an UV spectrometer.

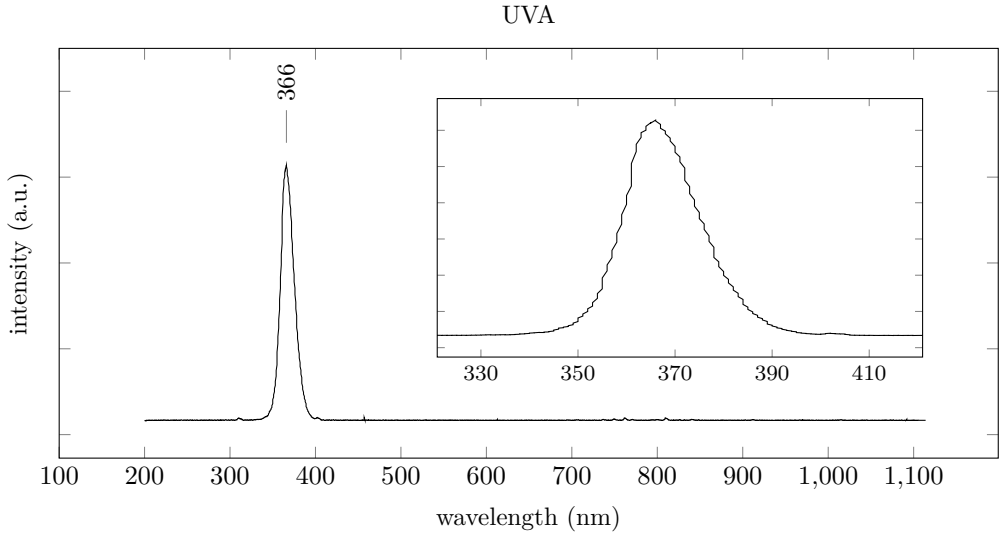

Figure A.1.: Emission spectrum of the light source used for all exposures to UVA light with the decisive wavelength regime highlighted.

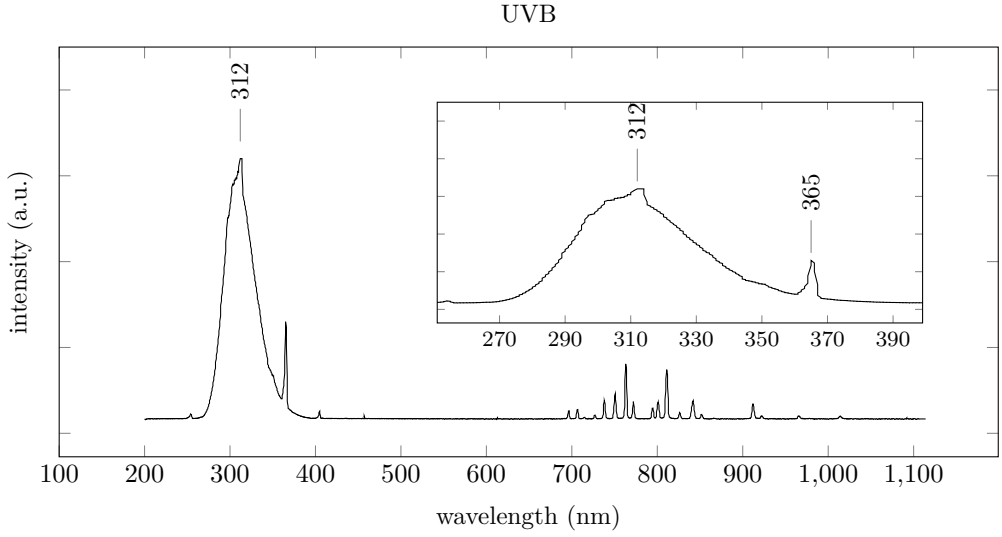

Figure A.2.: Emission spectrum of the light source used for all exposures to UVB light with the decisive wavelength regime highlighted.

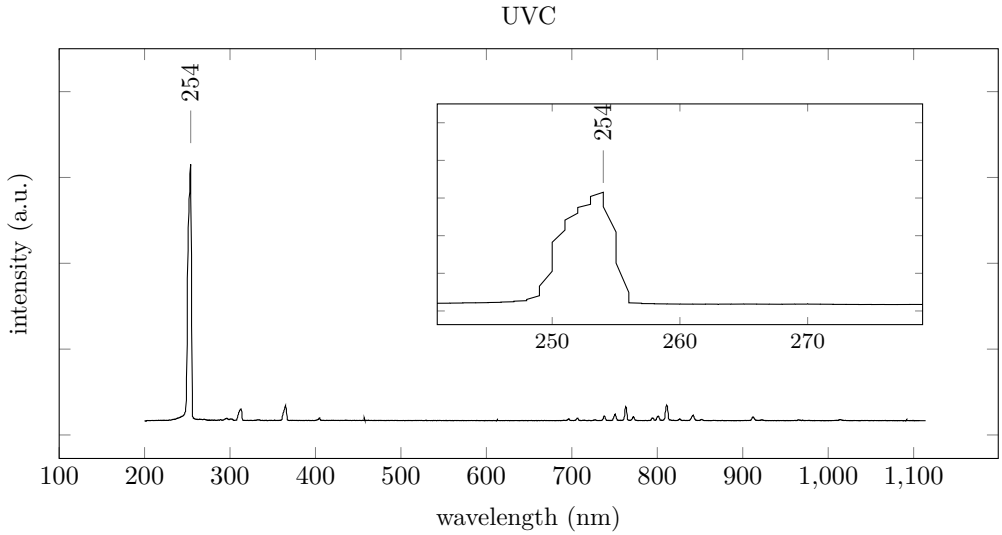

Figure A.3.: Emission spectrum of the light source used for all exposures to UVC light with the decisive wavelength regime highlighted.

B Comparison of DMT and Sneddon

The AFM software offers two contact models for the calculation of the elastic modulus: DMT and Sneddon. While the Sneddon modulus is often more applicable to softer samples (*e.g.* biological samples) one requirement for its application is a sufficient indentation that is said to be beyond 30 nm (manufacturer). The single collagen fibrils, however, did not allow for such an indentation. In succession to the small possible indentation depth, the DMT contact model was applied for the evaluation of the indentation experiments described in Section 4.1. However, the Sneddon modulus was recorded, as well, to perform a comparison between both. This comparison is depicted in Figure B.1 for the averaged UV irradiation results of collagen fibrils immersed in deionised water, in Figure B.2 for the averaged UV irradiation results of collagen fibrils immersed in PBS, and in Figure B.3 for the exposure of UV irradiation at elevated temperatures. For the majority of the results, the Sneddon and the DMT modulus exhibited the same trends and the changes in modulus were either very similar or at least within the error bar of each other. Scattered deviations can be seen for Figure B.1a but the overall tendency was not altered.

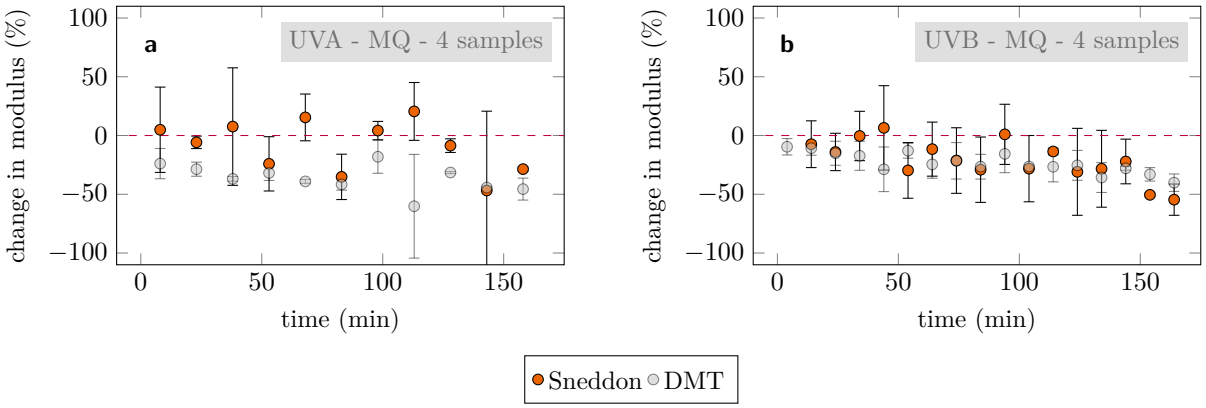

Figure B.1.: Relative change of the (gray) DMT and the (orange) Sneddon modulus with time of exposure for single surface supported collagen fibrils measured by PFQNM AFM. Every data point was averaged over the stated amount of samples for the exposure of collagen fibrils immersed in deionised water to (a) UVA and (b) UVB light. The horizontal line depicts the initial modulus of the untreated sample.

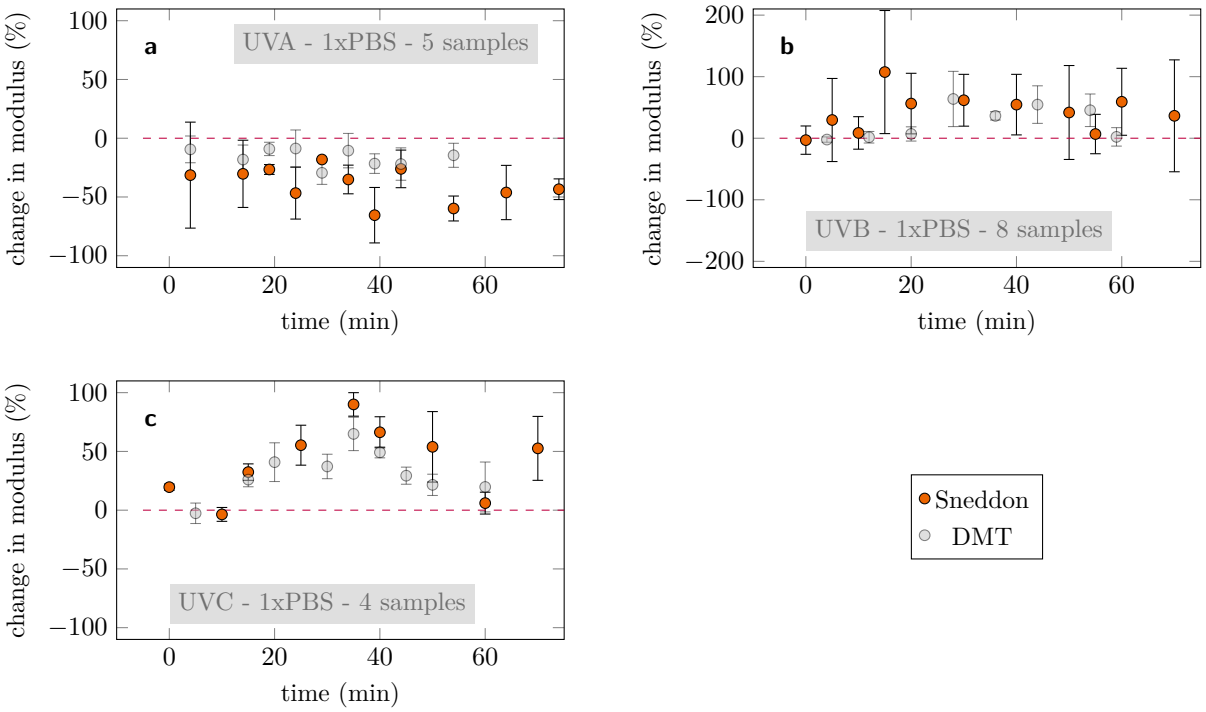

Figure B.2.: Relative change of the (gray) DMT and the (orange) Sneddon modulus with time of exposure for single surface supported collagen fibrils measured by PFQNM AFM. Every data point was averaged over the stated amount of samples for the exposure of collagen fibrils immersed in 1xPBS to (a) UVA, (b) UVB, and (c) UVC light. The horizontal line depicts the initial DMT modulus of the untreated sample.

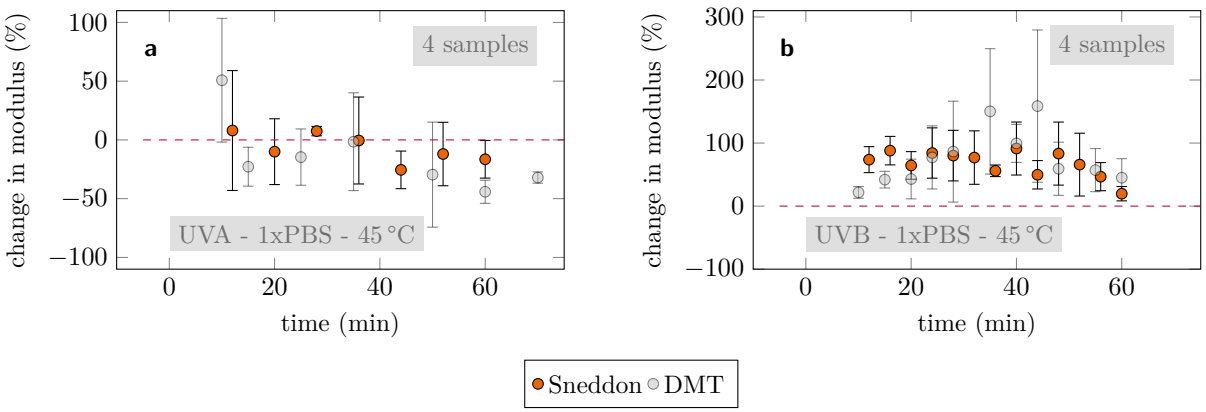

Figure B.3.: Relative change of the (gray) DMT and (orange) Sneddon modulus with time of exposure for single surface supported collagen fibrils measured by PFQNM AFM. The fibrils were immersed in 1xPBS and exposed to (a) UVA and (b) UVB while, at the same time, the temperature was adjusted to 45 °C. The horizontal line depicts the initial DMT modulus of the untreated sample.

C Tensile test

The results presented in Section C *Beam theory for moderately large rotations* have been contributed by Philipp L. Rosendahl.

Beam theory for moderately large rotations

In the case of nonlinear deformations, the axial beam strain is derived from the Green–Lagrange strain tensor according to

$$\varepsilon = \frac{\mathrm{d}u}{\mathrm{d}x} + \frac{1}{2}\left(\frac{\mathrm{d}w}{\mathrm{d}x}\right), \tag{C.1}$$

where x is the axial beam coordinate, u is the horizontal displacement and w the beam deflection (see Fig. C.1). When finite rotations are present, the axial section forces N and Q are rotated against the original coordinate system. In order to formulate equilibrium conditions with respect to the reference coordinate system, let us consider effective horizontal and vertical forces

$$H = N \cdot \cos\psi - Q \cdot \sin\psi = N, \tag{C.2}$$

$$V = N \cdot \sin\psi + Q \cdot \cos\psi = N \cdot \psi + Q, \tag{C.3}$$

where we assume moderately large rotations so that $\sin\psi \approx \psi$ and $\cos\psi \approx 1$ (Fig. C.1). We neglect $Q\sin\psi$ because the shear force is much smaller than the normal force $Q \ll N$ and additionally multiplied by a small number. Equilibrium of horizontal forces H, vertical forces V and bending moments M yields

$$0 = \frac{\mathrm{d}H}{\mathrm{d}x}, \tag{C.4}$$

$$0 = \frac{\mathrm{d}V}{\mathrm{d}x}, \tag{C.5}$$

$$0 = \frac{\mathrm{d}M}{\mathrm{d}x} + H\frac{\mathrm{d}w}{\mathrm{d}x} - V. \tag{C.6}$$

Using Euler-Bernoulli beam kinematics $\psi = \mathrm{d}w/\mathrm{d}x$ and Eqs. (C.2) and (C.3) yields modified equilibrium equations

$$0 = \frac{\mathrm{d}N}{\mathrm{d}x}, \tag{C.7}$$

$$0 = \frac{\mathrm{d}Q}{\mathrm{d}x} + N\frac{\mathrm{d}^2w}{\mathrm{d}x^2} = 0, \tag{C.8}$$

$$0 = \frac{\mathrm{d}M}{\mathrm{d}x} - Q = 0.. \tag{C.9}$$

The nonlinear term in Eq. (C.8) vanishes for small deflections or if the axial force is zero. Differentiating Eq. (C.9) and inserting Eq. (C.8) yields

$$\frac{\mathrm{d}^2M}{\mathrm{d}x^2} + N \cdot \frac{\mathrm{d}^2w}{\mathrm{d}x^2} = 0, \tag{C.10}$$

where the bending moment can be expressed by

$$M = -E \cdot I \cdot \frac{\mathrm{d}^2w}{\mathrm{d}x^2}, \tag{C.11}$$

with the material's Young's modulus E and the cross section's moment of inertia I. Replacing the bending moment in Eq. (C.10) using Eq. (C.11) finally yields the governing differential equation for the present nonlinear bending problem:

$$\frac{\mathrm{d}^4w}{\mathrm{d}x^4} - \lambda^2 \cdot \frac{\mathrm{d}^2w}{\mathrm{d}x^2} = 0, \tag{C.12}$$

where

$$\lambda = \sqrt{\frac{N}{E \cdot I}}. \tag{C.13}$$

A general solution for the above problem is given by

$$w(x) = C_1 + C_2 \cdot x + C_3 \cdot \cosh(\lambda \cdot x) + C_4 \cdot \sinh(\lambda \cdot x), \tag{C.14}$$

where C_1, C_2, C_3 and C_4 are free constants which must be determined from specific boundary conditions. From Eq. (C.7) we know that the unknown axial force N is constant. It is obtained inserting Eq. (C.1) into $N = EA\varepsilon$ and integrating both sides which yields

$$\frac{N \cdot l}{E \cdot A} = \Delta u + \frac{1}{2} \cdot \int_0^l \left(\frac{\mathrm{d}w}{\mathrm{d}x}\right)^2 \mathrm{d}x, \tag{C.15}$$

where A is the beam's cross section and Δu the difference in horizontal displacement between the beam's left and right ends.

Let us denote derivatives with respect to x as $(\,\cdot\,)'$. Consider the beam of length $2l$ with clamped ends subjected to a prescribed centre deflection δ shown in Fig. C.2. Beam deflection w and inclination w' must vanish at the beam ends. Owing to the symmetry of the problem, the inclination w' also vanishes in the beam centre. Inserting the general solution Eq. (C.14) into the boundary conditions for this symmetric problem

$$\begin{aligned} w(0) &= 0, & w'(0) &= 0, \\ w(l) &= \delta, & w'(l) &= 0, \end{aligned} \tag{C.16}$$

yields a linear system of equations. Solving for the free constants yields

$$\begin{aligned} C_1 &= -Z_1, & C_2 &= Z_2 \cdot \lambda, \\ C_3 &= Z_1, & C_4 &= -Z_2, \end{aligned} \tag{C.17}$$

where

$$Z_1 = \frac{\delta \cdot \sinh\left(\frac{\lambda l}{2}\right)}{\lambda \cdot l \cdot \cosh\left(\frac{\lambda l}{2}\right) - 2 \cdot \sinh\left(\frac{\lambda l}{2}\right)}, \tag{C.18}$$

$$Z_2 = \frac{\delta \cdot \sinh(\lambda l)}{2 - 2 \cdot \cosh(\lambda \cdot l) - \lambda \cdot l \cdot \sinh(\lambda \cdot l)}. \tag{C.19}$$

Finally, the deflection of the left half of the beam is given by

$$w(x) = \frac{\lambda \cdot x \cdot \cosh\left(\frac{\lambda \cdot l}{2}\right) - \sinh\left(\frac{\lambda \cdot l}{2}\right) + \sinh\left(\lambda \cdot \frac{l-2 \cdot x}{2}\right)}{\lambda \cdot l \cdot \cosh\left(\frac{\lambda \cdot l}{2}\right) - 2 \cdot \sinh\left(\frac{\lambda \cdot l}{2}\right)} \cdot \delta. \tag{C.20}$$

A fifth boundary conditions is given by the fixed axial displacements at the beam ends which yields

$$\Delta u = 0. \tag{C.21}$$

Inserting

$$w'(x) = \frac{\cosh\left(\frac{\lambda \cdot l}{2}\right) - \cosh\left(\lambda \cdot \frac{l-2 \cdot x}{2}\right)}{\lambda \cdot l \cosh\left(\frac{\lambda \cdot l}{2}\right) - 2 \cdot \sinh\left(\frac{\lambda \cdot l}{2}\right)} \cdot \lambda \cdot \delta, \tag{C.22}$$

and Eq. (C.21) into Eq. (C.15) allows for equating the axial force N and hence λ. The vertical reaction force in the beam centre is then obtained from

$$V_{\text{mb}} = N \cdot w'(l) + Q(l) = -E \cdot I \cdot w'''(l), \tag{C.23}$$

where $w'(l) = 0$ and the subscripts mb indicate that both membrane and bending contributions are accounted for. The third derivative of the deflection reads

$$w'''(x) = -\frac{\cosh\left(\lambda \cdot \frac{l-2 \cdot x}{2}\right)}{\lambda \cdot l \cdot \cosh\left(\frac{\lambda \cdot l}{2}\right) - 2 \cdot \sinh\left(\frac{\lambda \cdot l}{2}\right)} \cdot \lambda^3 \cdot \delta. \tag{C.24}$$

In the case of pure bending ($N = 0$), the second term in Eq. (C.12) vanished an we recover the linear problem

$$\frac{\mathrm{d}^4 v}{\mathrm{d}x^4} = 0, \tag{C.25}$$

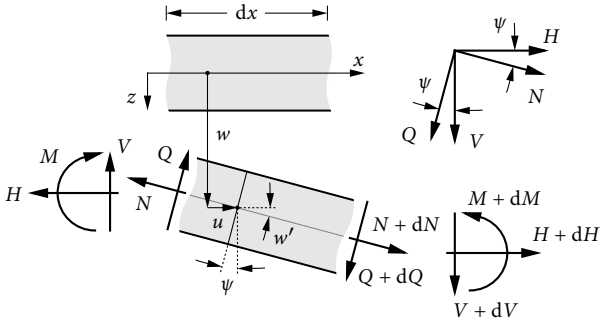

Figure C.1.: Beam kinematics and equilibrium of section forces and moments. Image was provided by courtesy of Philipp L. Rosendahl.

where ν denoted deflections of the geometrically linear beam. The corresponding general solution read

$$\nu(x) = D_1 + D_2 \cdot x + D_3 \cdot x^2 + D_4 \cdot x^3. \tag{C.26}$$

Again, using the boundary conditions given in Eq. (C.16) yields

$$D_1 = 0, \quad D_2 = 0, \quad D_3 = 3 \cdot \frac{\delta}{l^2}, \quad D_4 = -2 \cdot \frac{\delta}{l^3}, \tag{C.27}$$

and we obtain

$$\nu(x) = \frac{x^2}{l^3}(3 \cdot l - 2 \cdot x) \cdot \delta, \tag{C.28}$$

as the pure bending solution for the left half of a beam with clamped ends and prescribed centre displacement δ. The corresponding shear force reads

$$V_\mathrm{b} = -E \cdot I \cdot \nu'''(l) = 12 \cdot E \cdot I \cdot \frac{\delta}{l^3}, \tag{C.29}$$

where the subscript b denotes pure bending.

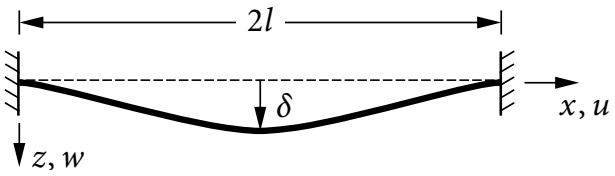

Figure C.2.: Beam with clamped ends and prescribed centre displacement. Image was provided by courtesy of Philipp L. Rosendahl.

D Raman spectroscopy

Measurements longer then 60 min

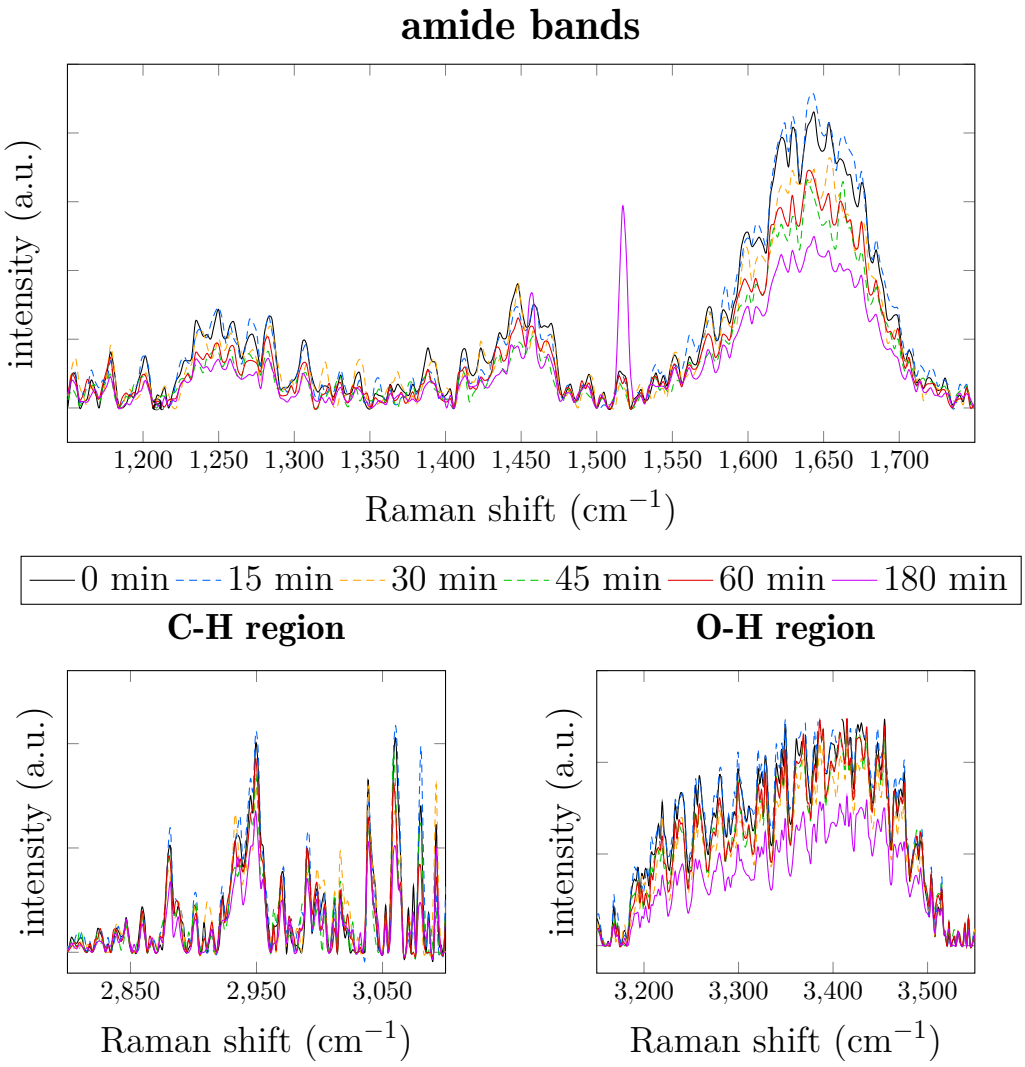

Figure D.1.: Three regions of a Raman spectrum of a collagen hydrogel immersed in deionised water and exposed to UVA light: amide bands (1150 to 1750 cm^{-1}), C−H stretching (2800 to 3100 cm^{-1}), and O−H vibrations (3150 to 3550 cm^{-1}). The spectra represent different time steps of treatment: 0 min - black, 15 min - blue, 30 min - orange, 45 min - green, 60 min - red, 180 min - purple.

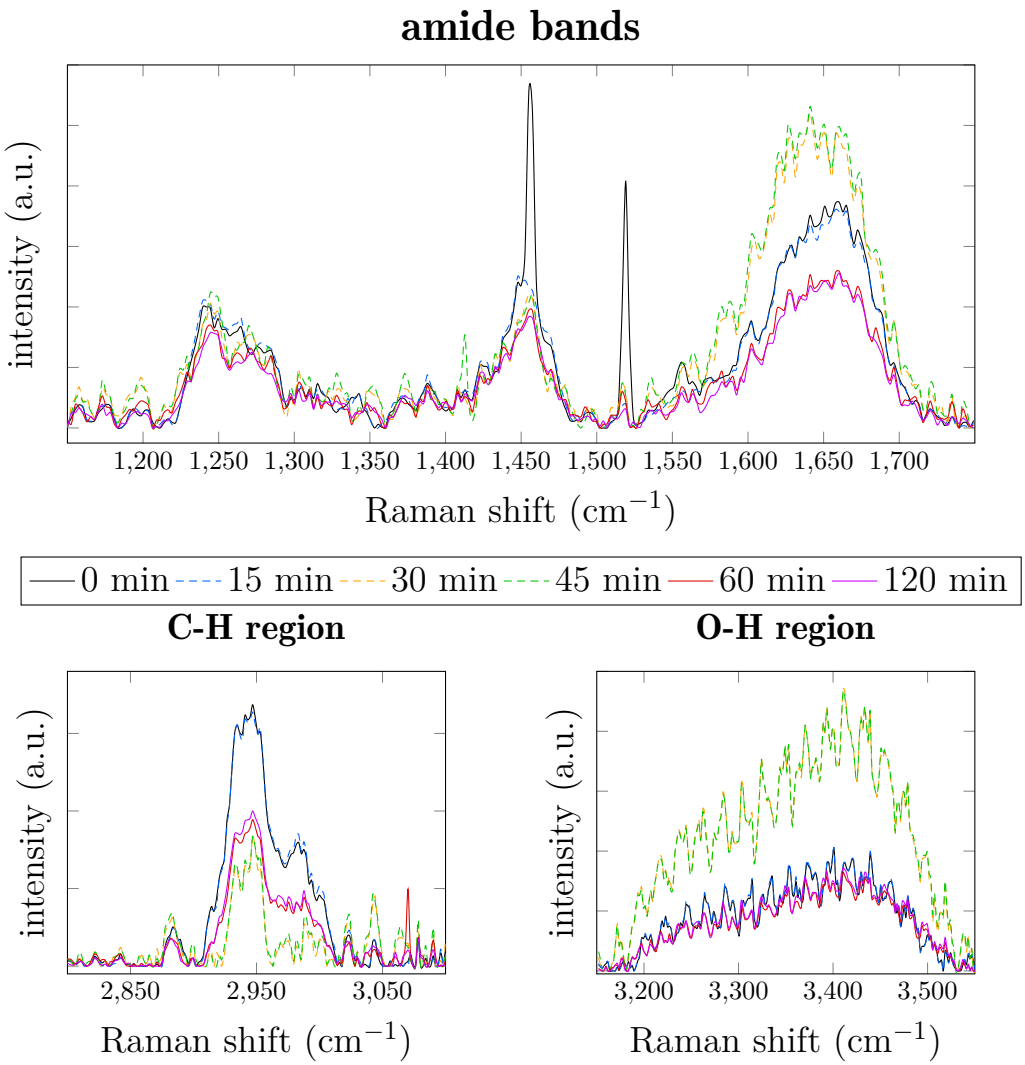

Figure D.2.: Three regions of a Raman spectrum of a collagen hydrogel immersed in 1xPBS and exposed to UVC light: amide bands (1150 to 1750 cm^{-1}), C−H stretching (2800 to 3100 cm^{-1}), and O−H vibrations (3150 to 3550 cm^{-1}). The spectra represent different time steps of treatment: 0 min - black, 15 min - blue, 30 min - orange, 45 min - green, 60 min - red, 120 min - purple.

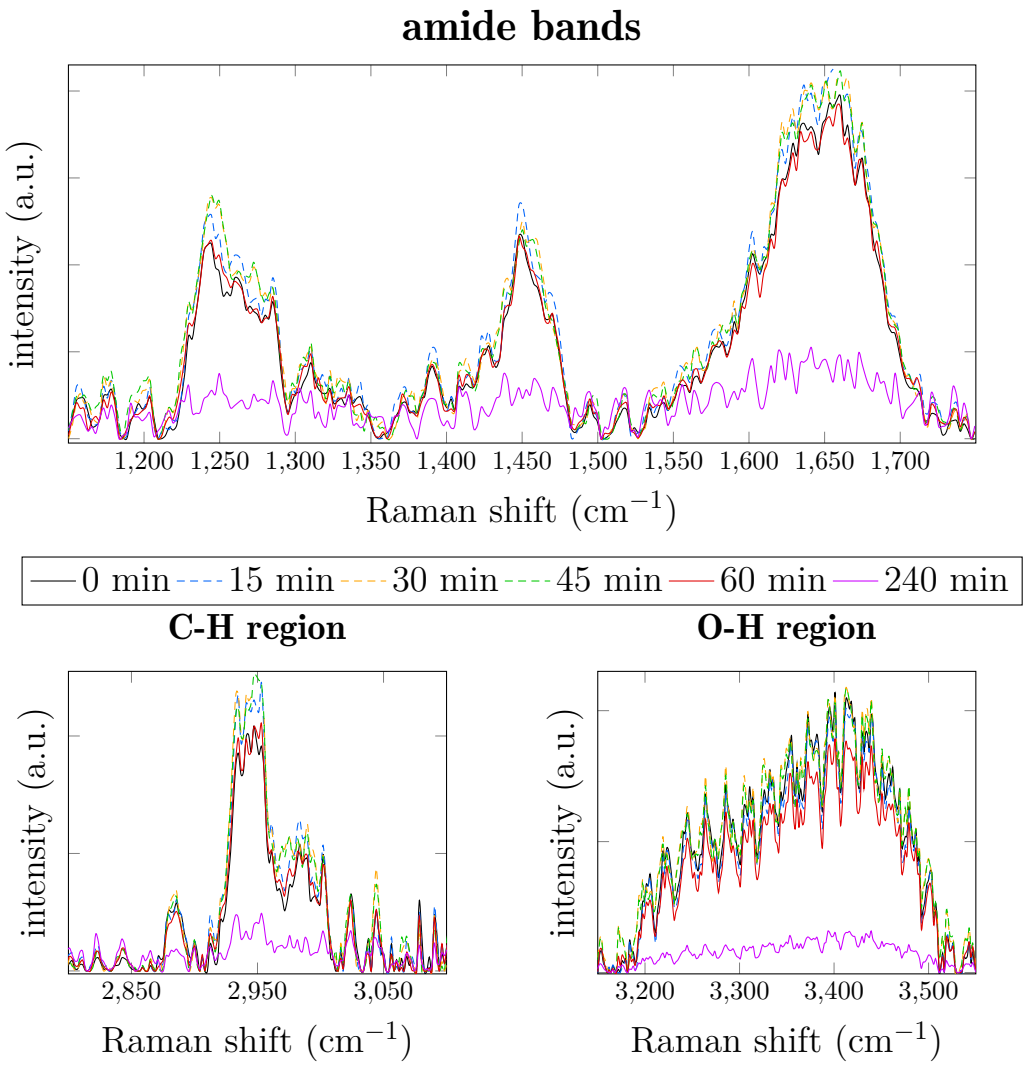

Figure D.3.: Three regions of a Raman spectrum of a collagen hydrogel immersed in 1xPBS and exposed to UVC light: amide bands (1150 to 1750 cm^{-1}), C−H stretching (2800 to 3100 cm^{-1}), and O−H vibrations (3150 to 2550 cm^{-1}). The spectra represent different time steps of treatment: 0 min - black, 15 min - blue, 30 min - orange, 45 min - green, 60 min - red, 240 min - purple.

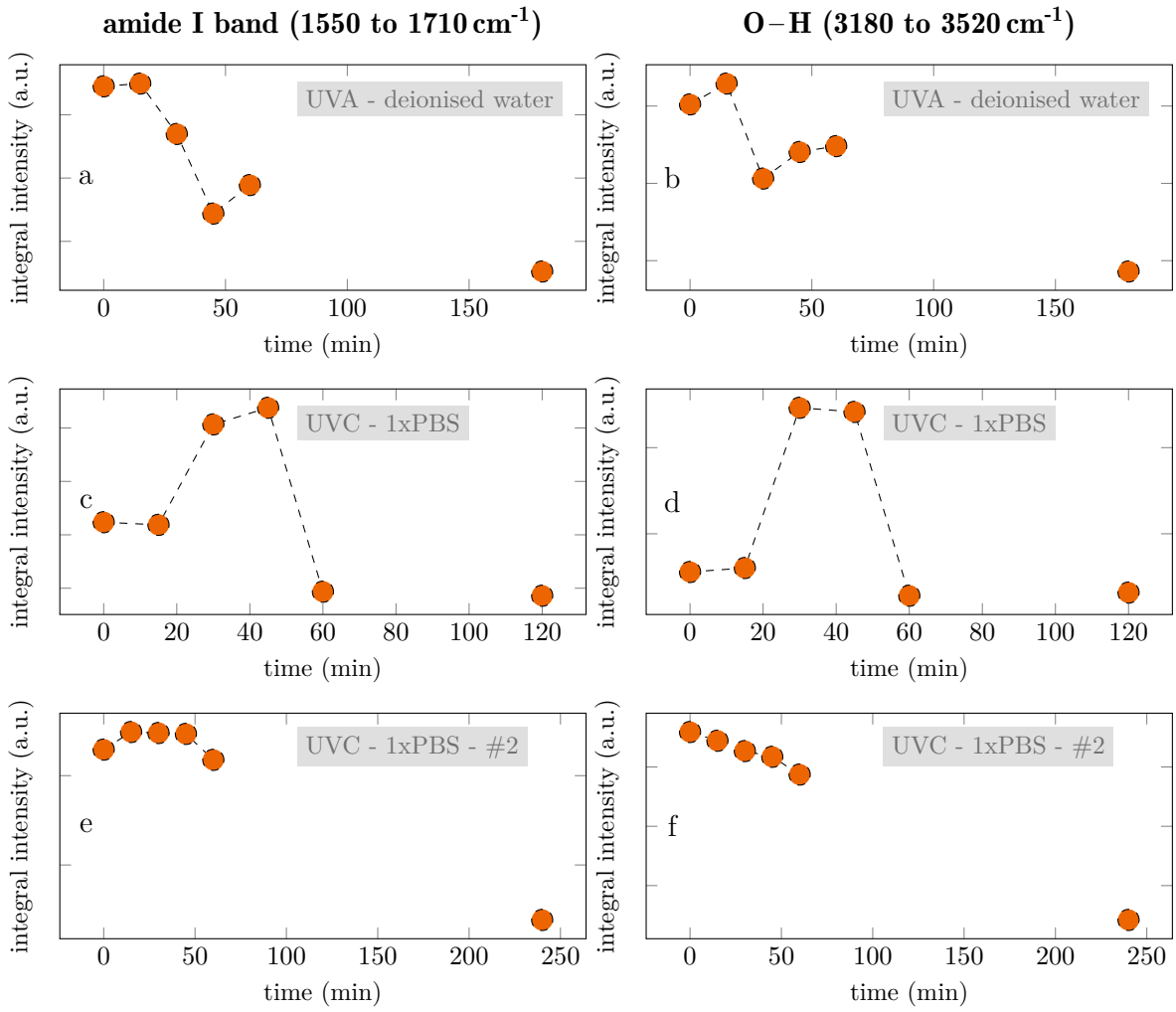

Figure D.4.: The integral intensities for (a,c,e) the amide I band (1550 to 1710 cm^{-1}) and (b, d, f) the O−H band (3180 to 3520 cm^{-1}) from Figure D.1 (UVA light and deionised water in a,b), Figure D.2 (UVC light and 1xPBS in c,d), and Figure D.3 (UVC light and 10xPBS in e,f) were evaluated from the Raman spectroscopy measurements on the collagen hydrogels to clarify the evolution of the peak intensity with advancing exposure time.

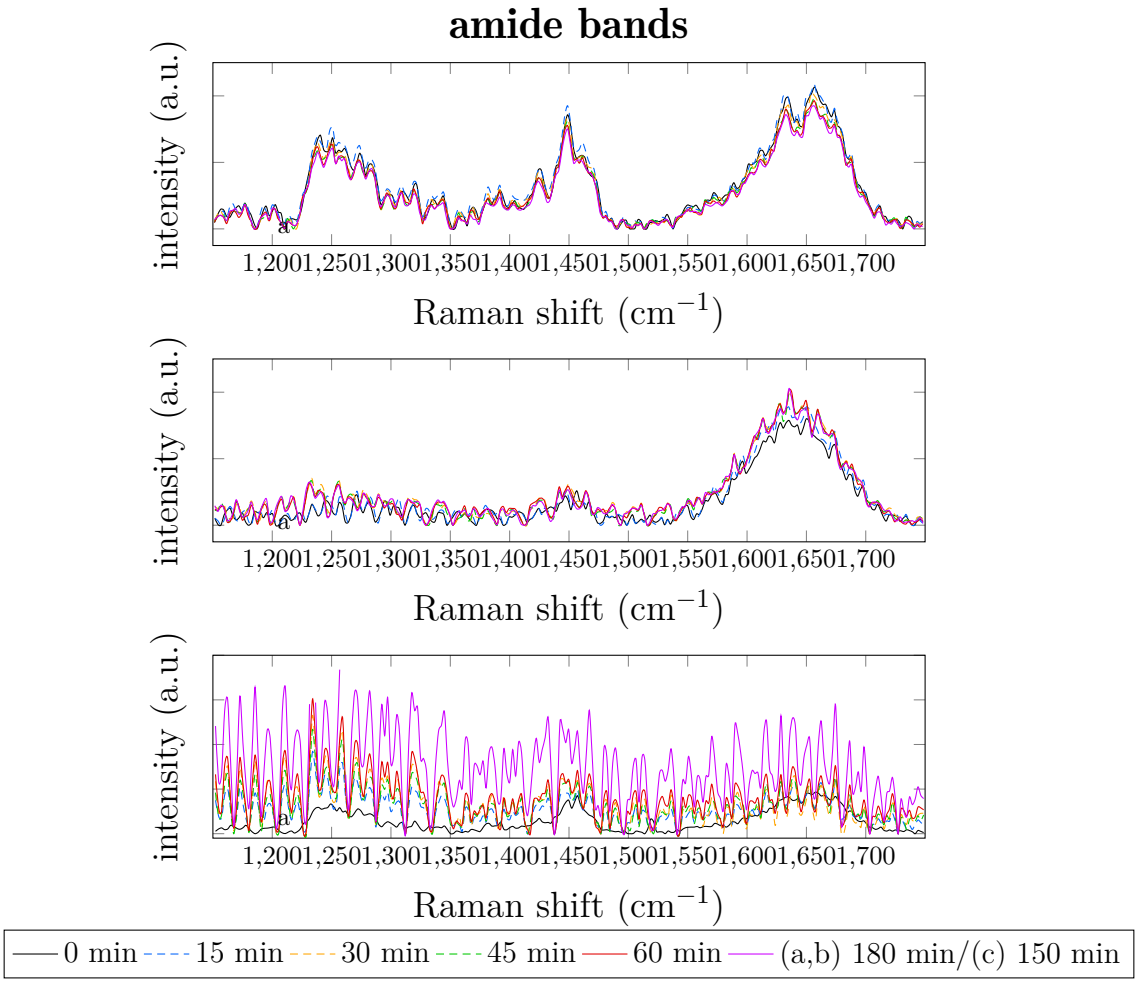

Figure D.5.: The amide bands (1150 to 1750 cm^{-1}) of Raman spectra of collagen hydrogels immersed in (a) 1xPBS and (b,c) deionised water and exposed to (a) UVA and (b,c) UVC light are displayed. For (c) the collagen hydrogel was rinsed with deionised water after the synthesis while for (c) the the collagen hydrogel was not. The spectra represent different time steps of exposure: 0 min - black, 15 min - blue, 30 min - orange, 45 min - green, 60 min - red, (a,b) 180 min/(c) 150 min - purple.

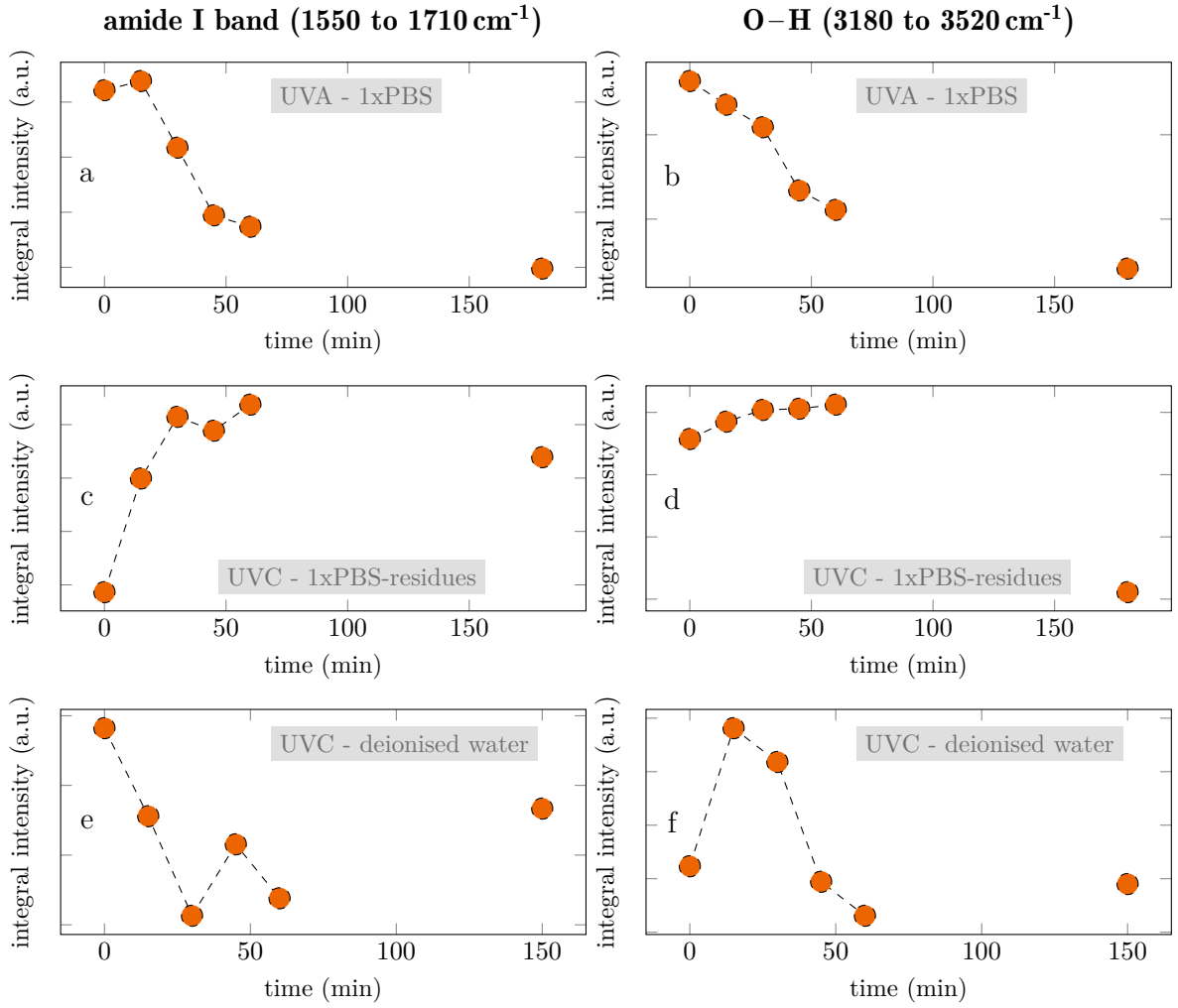

Figure D.6.: The integral intensities for (a,c,e) the amide I band (1550 to 1710 cm^{-1}) and (b, d, f) the O−H band (3180 to 3520 cm^{-1}) from Figure 4.37 were evaluated from Raman spectroscopy measurements on collagen hydrogels to clarify the evolution of the peak intensity with advancing exposure time.

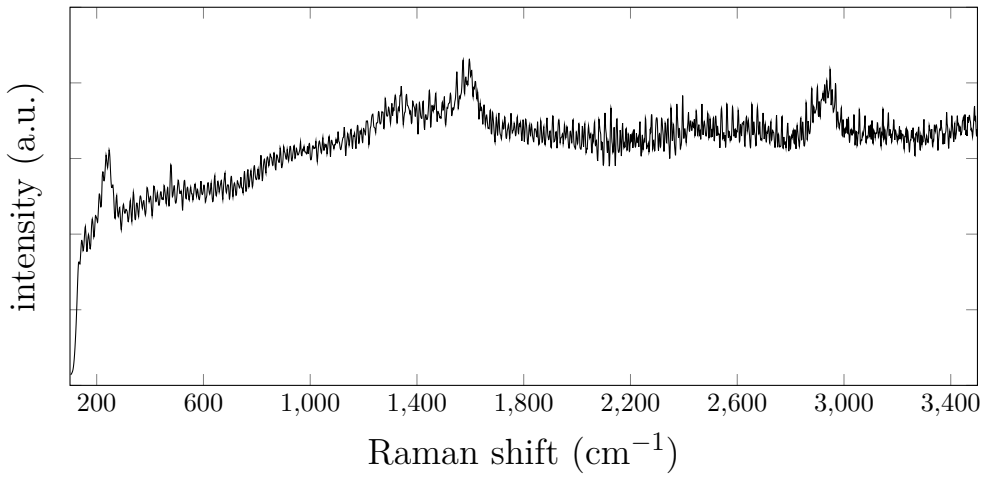

Figure D.7.: Raman spectrum of collagen fibrils attached to a silver-coated substrate suitable for SERS measurements.

Chemical structure of hematoporphyrin

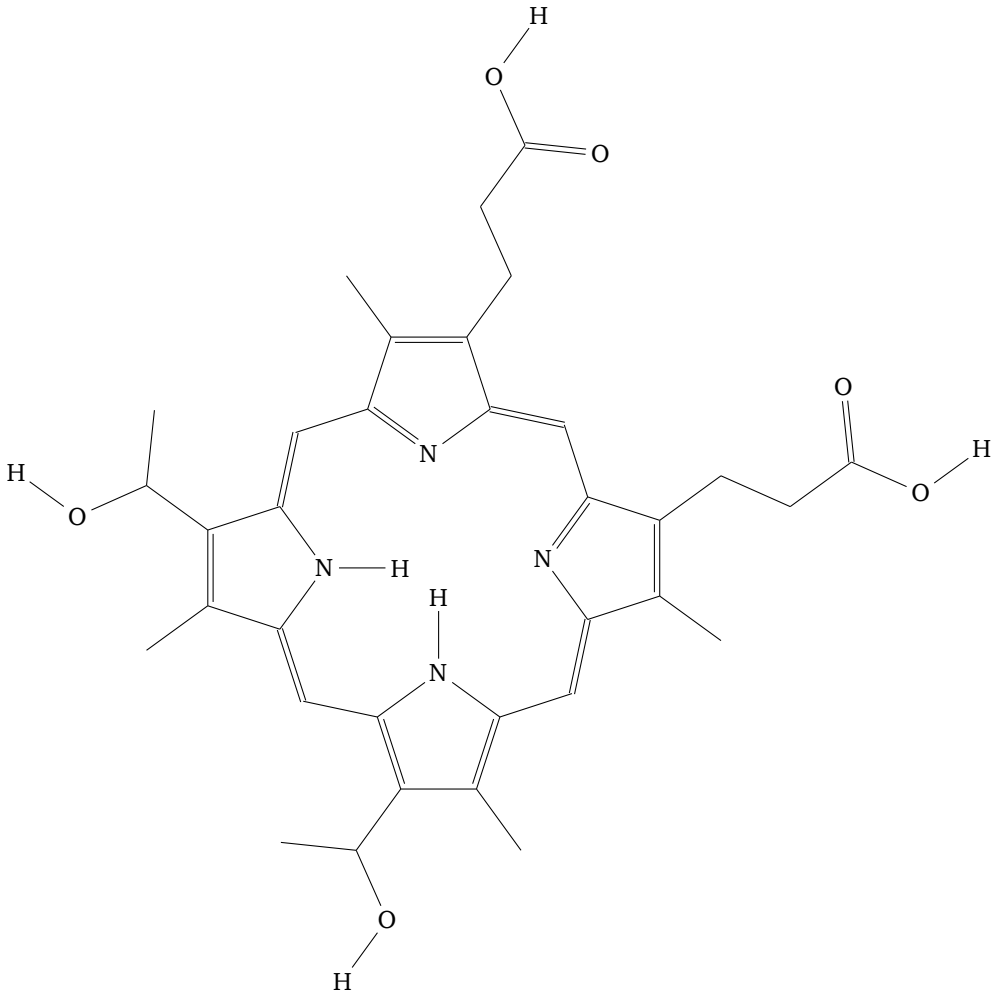

Figure D.8.: Structure of hematoporphyrin[333] adapted from the *National Center for Biotechnology Information - PubChem Database*.[316]

While this document is handed in by only one person, far more people share the gratitude and acknowledgement for this script, which is not only the work of 6 months writing, but rather a consummation of more than a decade of my life with the university as one central hub.

Professor Dr. **Robert W. Stark** is to be thanked for the consistent trust in me to conduct research in his division, his council, and his efforts to provide a positive working environment. This allowed me to get in contact with a variety of scientific tasks and challenges and also to develop and bring in my own ideas.

Dr. **Christian Dietz** has always supported and encouraged me from the very beginning, which also means that he has never turned down a request for advice or assistance. He is a big support for the division and he is to be thanked for all of it.

When it comes to the contribution of individual people to this work, I want to start with former and recent members of the *Physics of Surfaces*-division. I want to thank Dr. **Marek Janko** who has dealt with collagen for his PhD thesis, as well and whose advice helped me to kick off and I want to thank **Asma Siddique** who introduced me to the synthesis of collagen. **Alena Bell** shared her Raman spectroscopy and 3D printer-experience with me, as **Lukas Stühn** did with his AFM-experience and his knowledge regarding cell cultivation. Both always engaged with me in scientific discussions that pushed my work and led to new and more elaborated approaches that I could pursue.

Several materials science students shared parts of my way and contributed to this work. **Patrick Burrichter** and **Michael Spann** did their bachelor's theses during an early stage of this PhD thesis and contributed regarding the correlation of synthesis of collagen fibrils and resulting mechanical properties, as well as setting up experiments for the exposure of collagen fibrils to UV light. **Melanie Rogge** supported me as a student assistant during the indentation experiments on UV light exposed collagen fibrils which, eventually, resulted in a peer-reviewed publication. **Annika Stocker** did her master's thesis on the Raman spectroscopy of UV exposed collagen samples whose results were fundamental for our joined manuscript. Although the UV light induced patterning of collagen hydrogels was an endeavour with uncertain outcome, **Yue Du** decided to supported me with his master's thesis on that topic. I am very grateful for the interest of all of you in my work and for your huge support and I wish every single one the very best for your future.

Outside of the *Physics of Surfaces*-division, **Achim Bender** and **Dirk Gründing** counselled me during the tensile tests of collagen fibrils regarding the applicability of the chosen setup and the error propagation during the evaluation. **Jona Schuch** provided me with equipment for the heating of the biological cells outside of the incubator and Dr. **Constanze Kalcher** solved all my Python and LaTex troubles. Thank you for providing your time and expertise. Special thanks go to **Philipp L. Rosendahl** who helped me with the evaluation of the chosen setup for the tensile tests of collagen fibrils. With enthusiasm, he provided me with all the FEA

based simulations, derivation of the membrane solution and the non-linear beam solution, and his knowledge on engineering mechanics enabled a foundation for the evaluation of these measurements.
I also want to thank the Deutsche Forschungsgemeinschaft under grant STA 1026/7-1 for financial support.

Special thanks go to the members of the examination commission, Prof. Dr. **Regine von Klitzing**, Prof. Dr. **Oliver Clemens**, and Prof. Dr. **Ralph Krupke**, who took the time to prepare the examination and engage into a scientific discussion.

Ohne die genannten Personen und deren wissenschaftliche Beiträge, könnte diese Arbeit in der hier vorgestellten Form nicht existieren. Dies gilt auch für all diejenigen Leistungen, die nicht zwangsläufig wissenschaftlicher Natur waren aber ebenso unersetzlich. So gilt mein Dank den aktuellen und auch ehemaligen Kollegen des *Physics of Surfaces*-Fachgebietes, die die tägliche Beschäftigung zu mehr als nur einem Arbeitsplatz gemacht haben. Die ehemaligen Promovierenden **Kim Phuong Lieu**, **Na Liu** und **Agnieszka Voß** haben mich herzlich aufgenommen und mir stets mit Rat und Tat zur Seite gestanden. Dazu gehört auch mein erster "Büro-Kollege" **Simon Schiwek**, der nicht nur Teil vieler wissenschaftlicher Diskussionen war sondern auch immer für gute Laune gesorgt hat. Das gilt nicht weniger für die aktuelle Besetzung des Büros 206 mit **Alena Bell** und **Lukas Stühn**. Ihre Motivation und Kollegialität war nicht nur eine Bereicherung für meine Arbeit, sondern auch für mich persönlich und für die gesamte Arbeitsgruppe. Dies ist auch zutreffend für den Beitritt von **Julia Auernhammer** und **Anna Lisa Hawlitschek** zu unserem Team. Großer Dank geht an **Simone Liesenberg** und **Melanie Schulze-Wenck**, die uns stets den Rücken freigehalten haben.
Danken möchte ich **Irini Losoff** für das Korrekturlesen und auch **Sascha Seils**, der mich auf das Studium der Materialwissenschaften überhaupt erst aufmerksam gemacht und die Arbeit Korrektur gelesen hat. Es gibt noch viele liebe Menschen, die ich hier nennen könnte, von denen jeder auf seine Art und Weise für mich in den letzten Jahren da gewesen ist. Besonders danken möchte ich noch meinen **Eltern**, meiner **Schwester** und meinen **Großeltern** für ihre Unterstützung.
Und Conny. Für Alles.

Curriculum Vitae

Personal information

Name	Marcus Schulze
Place of birth	Görlitz, Germany

Education

Feb. 2016 - Dec. 2019	**Technische Universität Darmstadt, Materials science department** Research associate and PhD candidate *Physics of Surfaces* division, Prof. Dr. rer. nat. R. W. Stark Topic: *Impact of exposure to ultraviolet light on the nanomechanical properties of collagen probed by atomic force microscopy and Raman spectroscopy*
Jan. 2015 - Jan. 2016	**Technische Universität Darmstadt, Materials science department** Research associate *Physics of Surfaces* division, Prof. Dr. rer. nat. R. W. Stark Topic: *Horizontal oscillation of AFM tips for nanotribology*
Oct. 2011 - Nov. 2014	**Technische Universität Darmstadt, "Materials science" studies** Completion with academic degree: Master of Science *Physics of Surfaces* division, Prof. Dr. rer. nat. R. W. Stark Topic: *The influence of alkali metal cations on the properties of polymer brushes*
Aug. 2012 - Dec. 2012	**Seoul National University, "Materials science" studies** Semester abroad
Oct. 2008 - Aug. 2011	**Technische Universität Darmstadt, "Materialwissenschaften" studies** Completion with academic degree: Bachelor of Science *Physics of Surfaces* division, Prof. Dr. rer. nat. R. W. Stark Topic: *Microstructured polyelectrolyte-films*
Aug. 1998 - Jun. 2007	**Überwald Gymnasium, Wald-Michelbach** Completion with higher education entrance qualification (Abitur)

Peer-reviewed publications

1 Schulze, Marcus; Rogge, Melanie; Stark, Robert W.; *Atomic force microscopy measurements probing the mechanical properties of single collagen fibrils under the influence of UV light in situ*, Journal of the Mechanical Behavior of Biomedical Materials **88**, 415 - 421 (2018)

Conference Contributions

3 Schulze, Marcus; Rogge, Melanie; Stark, Robert W.

Mechanical properties of UV-irradiated collagen fibrils studied with atomic force microscopy

DPG Spring Meeting of the Condensed Matter Section Apr. 2019, Regensburg (Germany) - **Talk**

2 Schulze, Marcus; Rogge, Melanie; Stocker, Annika; Stark, Robert W.

Impact of UV light on the mechanical properties of collagen fibrils probed by Raman spectroscopy and Atomic Force Microscopy

DPG Spring Meeting of the Condensed Matter Section Mar. 2018, Berlin (Germany) - **Poster**

1 Schulze, Marcus; Rogge, Melanie; Stark, Robert W.

Atomic Force Microscopy measurements probing the mechanical properties of collagen fibrils under the influence of UV light in situ

Annual meeting of the german society of biomaterials (DGBM) Nov. 2017, Würzburg (Germany) - **Talk**

3 Bachmann, Svenja; Schulze, Marcus; Krell, Lisa; Merz, Rolf; Wahl, Michael; Stark, Robert W.; *Ultra-Low Friction on Tetrahedral Amorphous Diamons-Like Carbon (ta-C) Lubricated with Ethylene Glycol*, Lubricants **6(3)**, 59 (2018)

2 Kumari, Bharti; John, Daniel; Hoffmann, Paul; Spende, Anne, Toimil-Molares, Maria Eugenia; Trautmann, Christina; Hess, Christian; Ruff, Philip; Schulze, Marcus; Stark, Robert W.; Buntkowsky, Gerd; Andrieu-Brunsen, Annette; Gutmann, Torsten; *Surface Enhanced DNP Assisted Solid-State NMR of Functionalized SiO2 Coated Polycarbonate Membranes*, Zeitschrift für Physikalische Chemie, **232(7-8)**, 1173-1186 (2018)

1 Bachmann, Svenja; Schulze, Marcus; Morasch, Jan; Hesse, Sabine; Hussein, Laith; Krell, Lisa; Schnagl, Johann; Stark, Robert W.; Narayan, Suman; *Aging of oxygen and hydrogen plasma discharge treated a-C:H and ta-C coatings*, Applied Surface Science **371**, 613-623 (2016)